A NUMERICAL INVESTIGATION OF MAGNETIC FIELDS IN LASER-PRODUCED PLASMAS

by

Robert Stephen Craxton

Imperial College

London

Thesis submitted for the degree of Doctor of Philosophy to

The University of London

August 1976

To My Parents

ABSTRACT

The spontaneous generation of magnetic fields in laser-plasma interactions has stimulated considerable interest because a proper understanding of their effects is essential to the interpretation of experimental results and to the development of theoretical models. Large magnetic fields, typically of the order of a mega-Gauss, may arise in both plane and spherical target experiments; the extent to which they may inhibit the classically strong electron thermal conduction is highly pertinent to the problem of obtaining spherically - symmetric implosions for laser-driven fusion. The production of energetic ablating ions is related. The present work is concerned with the development of a computer code (LASERB) and its application to these phenomena.

LASERB is a two-dimensional, cylindrically symmetric, Eulerian code which integrates a set of magneto-hydrodynamic fluid equations for six variables - density, radial and axial velocities, electron and ion temperatures, and azimuthal magnetic field. The hydrodynamics is treated explicity by the Lax-Wendroff method, and the thermal diffusion implicitly by a technique involving the iterative inversion of a quindiagonal matrix. Two algorithms for this matrix inversion are described and compared; they are the Peachman-Rachford Alternating Direction Implicit method, and the less well-known Strongly Implicit method which is preferred.

The code is used to investigate various laser-target configurations, including thin films. Results are presented, and their dependence on parameters such as the laser flux density and the initial plasma state is discussed. An important new phenomenon is that, due to the reduction in the electron thermal conductivity, hot spots in the electron temperature distribution may appear in regions characterized by strong absorption from the laser and large magnetic fields.

The physical and computational limitations of the present code are discussed. Possibilities for the improvement of the numerical technique and for the inclusion of more sophisticated physics are outlined.

CONTENTS

ACKNOWLEDGMENTS

It is a pleasure to acknowledge the support and encouragement that I have received from the Imperial College Plasma Physics Group over the past few years. In particular, M.G. Haines (my supervisor) has taken a keen interest in all aspects of this work and made many helpful suggestions.

I would also like to thank:
A.E. Dangor, J.D. Kilkenny, J.S. Pearlman and J. McGill, who have read and commented on some of the later chapters;
R.J. Wright for performing the eigenvalue calculations of Chapter 6;
A.J. Davey for drawing my attention to the Strongly Implicit method;
A.R. Edmonds and P.A. Ashworth for useful discussions; and
M.G. Drouet, A.W. Ehler, J.F. Kephart, R.C. Malone, J.S. Pearlman and F. Schwirzke for permission to reproduce their diagrams.

Miss Valerie Collins typed most of the manuscript; I am greatly indebted to her for her hard work, patience and sound judgment.

The Imperial College Computer Centre and the University of London Computer Centre have provided an efficient and reliable service; I have always found their staff most helpful. The I.C.C.C. Graphics Section made available the source of the perspective plotting subroutine "MPLT". A generous carrel allocation from the Lyon

Playfair Library was also appreciated.

This work was started while I was a recipient of an S.R.C. research studentship, and completed under a Culham Laboratory contract (CUL/926) for which I am most grateful.

CHAPTER 1

INTRODUCTION

In the past few years advances in laser technology have made possible the irradiation of small targets by very short and intense pulses of highly focussed laser energy.

The physics of these interactions is as interesting as it is difficult to elucidate. Experimentally the plasmas produced evolve on picosecond* timescales and micron† lengthscales, calling for the greatest sophistication of diagnostic techniques if temporal and spatial resolution is to be obtained. Theoretically the complexity and non-linearity of the competing processes believed to be present lead inevitably to computational modelling. This in turn has its limitations; in particular the applicability of a fluid model is assumed and the treatment of small scale phenomena is restricted by the finite size of the mesh.

In practice these three approaches must, and do, advance together. Experimental results are interpreted by comparison with the predictions of computational models which are at best as good as the physics they contain.

The purpose of this work is therefore twofold - to describe a simple computational model, and to outline the experimental and theoretical work in the context of which the results of the model should be understood. Very briefly, Chapters 2-4 discuss the experimental and theoret-

---

* 1 picosecond $= 10^{-12}$ sec

† 1 micron (μm) $= 10^{-6}$ m

ical background, Chapters 5-6 the model and Chapters 7-9 the results.

In Chapter 2 we survey the main physical processes believed to be important in laser-plasma interactions and outline some recent experimental results. An understanding of the physics of laser-plasma interactions is a prerequisite for the ultimate goal, laser fusion.

In Chapter 3 we describe briefly the laser-target configurations which we attempt to simulate, and list the equations needed to specify our fluid model.

In Chapter 4 we discuss the physics of laser-plasma interactions with reference to these equations, making use of the timescales and other characteristic parameters pertinent to a typical configuration. Also we describe the theory of magnetic field generation.

In Chapter 5 we attempt to give a complete specification of the code LASERB. For the reader who is content to believe in LASERB as a "black-box" integrator of the fluid equations listed in Chapter 3 it suffices to read the short Section 5.1 and skip to Chapter 7. The details of the "black-box" are to be found in the extensive Section 5.2, where we also discuss at some length the treatment of the diffusion equation.

In Chapter 6 we describe two methods for solving the quindiagonal matrix equations arising from the implicit

two-dimensional diffusion equation. They are compared with respect to two matrices encountered in the main run of Chapter 7. We show that the Strongly Implicit method has some advantages over the Alternating Direction Implicit method.

In Chapter 7 we present results illustrating some consequences of magnetic field generation: the reduction of the electron thermal conductivity leads to the formation of hot spots in the electron temperature distribution and to the ablation of fast ions.

In Chapter 8 we present results for a different configuration in which $\underline{J} \times \underline{B}$ forces provide ablating ions with additional acceleration.

In Chapter 9 we consider the interaction of a short laser pulse with a thin polystyrene film. We compare our predictions with experimental results, for the energy spectrum of ablating ions and for the percentage of laser light transmitted through the film. Our model is approximate, physically because we do not allow for the presence of more than one charged species and numerically because of the difficulties of representing a thin film on a regular Eulerian mesh; however some agreement with experiment is obtained.

In the conclusion (Chapter 10) we suggest directions in which this work might be extended.

The code LASERB runs either on the CDC 7600 at the

University of London Computer Centre (ULCC) or on the CDC 6400 at the Imperial College Computer Centre (ICCC). In a two minute job on the 7600 between 100 and 200 timesteps may be integrated, depending on the number of mesh points used and on the rate of convergence of the quindiagonal matrix inversion (which consumes typically 50-60% of the overall time).

Development of the code and the interpretation of its results would have been impossible without the microfilm facility available. Each run generates about 25 frames, each containing four plots, the data for which is stored on magnetic tape for future reference. Microfilm generated at ULCC returns within two days, an acceptable turnaround for production runs. Plots generated from test runs at ICCC are available immediately after program execution for interrogation on the ICCC interactive graphics system. The great virtue of the "perspective plots" to be presented is that they allow one to see at a glance exactly what is on the mesh, no more and no less.

CHAPTER 2

LASER-PLASMA INTERACTIONS

Although the physics of the interaction of high-power lasers with matter is in its own right a proper area of investigation , the basic motivation for the research effort in this field is the possibility of obtaining controlled thermonuclear fusion through the spherical compression of laser-heated targets. The aim of this chapter is therefore to discuss recent laser-target experiments in the context of laser fusion.

Section 2.1 provides an introduction to the basic features of the physics of laser fusion, from the theoretical point of view, with the emphasis placed on the absorption, thermal transport and compression processes rather than on the thermonuclear burn. The material covered is all well-known. Section 2.2 reviews the experimental work performed in the last few years, by no means exhaustively, but sufficiently to indicate both current trends and the rôle of magnetic fields. We have resisted the temptation to discuss only those experiments relating to magnetic fields as that would have made impossible a fair assessment of their importance; however we have attempted to cover most of the experiments dedicated specifically to their study.

2.1 LASER FUSION

Work on the interaction of high-power lasers with

matter received a major boost from the declassification of theoretical American work at Livermore [1] and Los Alamos [2] on the compression of small pellets of deuterium and tritium by specially tailored laser pulses. An alternative route to controlled fusion was opened up, based on inertial confinement rather than magnetic containment.

The computer calculations of Nuckolls et al.[1] suggested that a gain of 100 might be obtained with a 1 MJ laser and a compression to about 10^4 times liquid density; a 10kJ laser and a compression of 10^3 might give break-even. A large gain is necessary because of low thermal and laser efficiencies; overall breakeven corresponds to a gain of about 25 of which 15 ends as waste heat and 10 pumps the laser. A commercial reactor burning ten pellets per second in each of ten explosion chambers, each micro-explosion yielding 10^7J, might produce 300 MW; however major advances in laser technology are clearly required before this goal is attained.

Four main processes may be identified in a typical interaction: the absorption of the laser energy in the low density plasma atmosphere surrounding the pellet, the transport of this energy to the spherically converging compression front, the compression itself and the thermonuclear burn. We shall proceed to review the first three of these processes in turn, outlining the basic physics involved. The thermonuclear burn[3] is of little concern to us here.

An alternative approach to inertial confinement involves the use of relativistic electron beams instead of lasers.[4]

2.1.1 Absorption

Initially of course there is no atmosphere; whether the initial absorption proceeds via collisional ionization, multi-photon ionization or some other mechanism is not of importance to us because very rapidly a plasma with an electron number density (n_e) in excess of the critical density (n_c) corresponding to the laser wavelength (λ_{las}) will be created, and electromagnetic radiation will no longer be able to propagate through this region. For example, for Nd-glass lasers (λ_{las}= 1.06μm), the energy required to ionize a layer of deuterium ten wavelengths thick to the critical density ($n_c \simeq 10^{21} cm^{-3}$) is contained within the first picosecond of a pulse of a modest intensity (I) of 3×10^{12} W/cm^2. For this reason theoretical work assumes an initially ionized plasma and concentrates on the absorption of laser energy at densities less than or equal to the critical density.

At sub-critical densities absorption by inverse bremsstrahlung is well understood, and known to be ineffective at the high (keV) temperatures currently attainable. At the critical density, however, the plasma supports natural oscillations at the laser frequency which give rise to various non-linear interactions. These include two absorptive

instabilities, namely the parametric decay instability in which a photon decays into an electron plasma wave and an ion acoustic wave, and the related oscillating two-stream instability in which the ion wave does not propagate but is purely growing. Both of these occur at the critical density; in a third absorptive instability, the two plasmon instability, the photon decays into two electron plasma waves at a quarter the critical density. There are also two important reflective instabilities, Raman and Brillouin backscattering, in which the incident wave decays into a reflected wave and, respectively, an electron or an ion-acoustic wave; although some energy is coupled into the electrostatic wave these instabilities should be avoided because of the loss of energy in the reflected wave.

All of the above instabilities may occur when the laser is incident normally. The motion of the plasma electrons in the incident field is, apart from the relativistic corrections arising from the $\underline{V} \times \underline{B}$ force, perpendicular to the plasma density gradient. In contrast a further mechanism, resonant absorption, requires a finite but small angle of incidence θ_i; the incident wave is refracted out of the plasma along a curved path with a turning point where the electron density is $n_c \cos^2\theta_i$, as is easily obtained from Snell's Law and the familiar dispersion relation

$$\omega^2 = \omega_p^2 + c^2k^2 \qquad (2.1)$$

from which the refractive index μ is given by

$$\mu = \sqrt{1 - \omega_p^2/\omega^2} \qquad (2.2)$$

If the laser is polarized in the plane of incidence the electric field at the turning point is directed into the plasma and drives plasma waves which absorb energy.

An instability related to resonant absorption is the self-focussing of the laser light, alternatively known as filamentation. If there exists an initial perturbation in the electron number density with wave vector perpendicular to the direction of the laser beam, light will be refracted preferentially into the lower density channels where, from (2.2), the refractive index is greater; the associated radiation pressure will then force more plasma out of these channels until an equilibrium is reached in which the radiation and plasma pressures balance.[5] Such density perturbations may result in locally finite angles of incidence at the critical density surface thereby allowing resonant absorption to occur even when the laser beam is normal to the target.[6]

Simulations of these instabilities follow the motions of large numbers of charged particles in the oscillating fields of the incident laser and the self-consistent electrostatic or electromagnetic fields of the plasma. A general feature is the production of electron distribution functions with energetic, non-Maxwellian, suprathermal tails. Because

of the short overall timescales of these simulations (typically several hundred electron plasma oscillations amounting to 1 psec in total), these distribution functions may be used as inputs to hydrodynamic codes (containing several velocity groups) operating on longer timescales.

There are serious problems associated with the effective absorption of laser energy. Ideally the absorptive instabilities and resonant absorption, grouped together with other as yet undiscovered processes as "anomalous mechanisms", will absorb 100% of the incident energy as an "energy dump" in the region of the critical density. However energy absorbed into suprathermal electrons, which have very long mean free paths, is decoupled from the thermal energy that drives the compression of the core; also, the suprathermal electrons may cross the compression front to be absorbed within the dense core, "preheating" it and thereby requiring extra work to be done in subsequent compression. Possible schemes for mitigating these effects include the use of structured pellets with layers of high z material, to absorb the suprathermal electrons[7] and/or to enhance the efficacy of inverse bremsstrahlung (which absorbs energy into thermal electrons). The choice of laser is also pertinent: long wavelength lasers, such as the CO_2 gas laser (λ_{las}= 10,6μm) which may potentially deliver more energy more efficiently than the Nd laser, have the twin disadvantages of depositing their energy further from the pellet and producing more suprathermals.

2.1.2 Thermal transport

In order to transport energy between the critical density region and the compression front good thermal conduction is obviously essential. The electron mean free path λ_e depends on the electron temperature T_e, the ion number density n_i and the ionic charge Z as

$$\lambda_e \propto T_e^2 / n_i Z^2, \qquad (2.3)$$

and is therefore large in the low density high temperature atmosphere. Because of this the classical (Spitzer) electron thermal conductivity K_e [8] is a strongly increasing function of T_e ($\propto T_e^{5/2}$) and should ensure effective transport at the high temperatures of interest. Also, a good spherically-symmetric compression requires sufficient thermal conduction in the spherical θ and ϕ directions to smooth out spatial non-uniformities in the laser irradiation such as may be caused by the use of several overlapping beams or by imperfect beam quality.

The derivation of the Spitzer conductivity breaks down when T_e becomes sufficiently large for λ_e to exceed the temperature scale-length. Thermal transport is then believed to change from a diffusive to an advective process, with the heat flux limited to some multiple of the thermal velocity times the energy density. This we discuss further in Section 4.4; at present we remark that ideally the electrons heated at the critical density should arrive at

the compression front after travelling just enough mean free paths to ensure a sufficiently uniform implosion. Anything that might significantly reduce the electron thermal conductivity, such as large magnetic fields, should be avoided.

2.1.3 Compression

A very simple model of the compression process, which is physically incomplete but nevertheless illustrative, considers the implosion of a fixed mass of fuel of radius $R(t)$, pressure $P(t)$ and temperature $T(t)$ [2]. The implosion velocity of the surface, $\dot{R}(t)$, is assumed proportional to the perfect gas sound speed:

$$\dot{R}(t) = \dot{R}_o (T/T_o)^{\frac{1}{2}} \tag{2.4}$$

where $\dot{R}_o$ is the initial velocity and T_o the initial temperature. The rate at which work is done is equated to the instantaneous laser power $\dot{E}(t)$:

$$4\pi R^2 P\dot{R} = -\dot{E}, \tag{2.5}$$

where we are neglecting the energy necessarily lost in ablation. Adiabatic compression and the perfect gas equation of state give

$$PR^{3\gamma} = P_o R_o^{3\gamma} \tag{2.6}$$

and

$$\left(\frac{P}{P_o}\right)\left(\frac{R}{R_o}\right)^3 = \left(\frac{T}{T_o}\right) \tag{2.7}$$

where P_o and R_o are the initial pressure and radius.

Solving (2.4)-(2.7) one obtains the implosion history

$$R(t) = R_o\ (1 - t/t_1)^{2/(3\gamma-1)} \tag{2.8}$$

and the laser pulse shape

$$\dot{E}(t) = \dot{E}_o\ (1 - t/t_1)^{-s}, \tag{2.9}$$

where $\dot{E}_o$ is the initial laser power and where

$$t_1 = \frac{2}{3\gamma-1}\ \frac{R_o}{-\dot{R}_o} \tag{2.10}$$

and

$$s = \frac{9\gamma-7}{3\gamma-1}\ . \tag{2.11}$$

For example, for $\gamma = 5/3$ we have $s=2$ and

$$R(t) = R_o(1-t/t_1)^{\frac{1}{2}} \tag{2.12}$$

$$\dot{E}(t) = \dot{E}_o(1-t/t_1)^{-2}\ . \tag{2.13}$$

The singular time t_1 may be determined from $\dot{E}_o$ instead of $\dot{R}_o$; from (2.10), (2.5) and (2.11) we may obtain the simple relation

$$\dot{E}_o\ t_1 = (s-1)\ U_o \tag{2.14}$$

where U_o is the initial internal energy

$$U_o = \frac{4}{3}\ \pi R_o^{\,3} P_o/(\gamma-1)\ . \tag{2.15}$$

The total energy E delivered up to the final time t_f is given from (2.9) and (2.14) by

$$E = U_o\left\{(1- \frac{t_f}{t_1})^{\ 1-s} - 1\right\}, \tag{2.16}$$

$$= U_o \left(\frac{T_f}{T_o}\right) - U_o \qquad (2.17)$$

from (2.6)-(2.8) and (2.11), hardly a surprising result because all the laser energy has gone into increasing the internal energy of the compressed pellet.

Some idea of the implications of these formulae may be gained from a numerical example. Consider a deuterium-tritium (DT) pellet of radius 400μm, density $0.2 gm/cm^3$, $\gamma = 5/3$ and initial temperature 21eV. This corresponds to the core which is to be compressed by a laser of energy E = 60kJ; the pellet atmosphere which absorbs the laser light and is ablated is not considered here. The initial temperature is chosen to make

$$U_o = 10^{-8/3} E \; ; \qquad (2.18)$$

therefore from (2.17), (2.6) and (2.7) the peak compression will be 10^4 in density. The final temperature will be 10keV and the final radius 19μm. The pressure will rise from 3×10^6 to 1.5×10^{13} atm. If we choose t_1 = 25nsec , the laser power will rise from 5×10^9 to 10^{15} Watts, 50% of the laser energy will be delivered in the last 54 psec of the pulse, and the pulse will terminate 54 psec before 25 nsec.

We have omitted the constant relating $\dot{R}_o$ to the sound speed in (2.4); this would determine t_1 from (2.10).

This model is grossly over-simplified as we have neglected, at least, realistic equations of state and the Fermi-degeneracy of electrons at high densities. The core

is not compressed homogeneously, but a high density imploding shell developes which compresses a lower density central region. The laser energy certainly does not all go into compression; over 90% may be lost by ablation of the outer layers of the pellet.[9] These and other physical effects are taken into account in computer compression codes, of which LASNEX[1],[9] is the best known.

LASNEX results[1] for the 10^4- fold compression of a 400 μm radius DT liquid droplet by a 60 kJ shaped laser pulse with t_1 = 25 psec are compared with the results obtained above in Table 2-1. After specifying that the compression be 10^4- fold, which is equivalent to choosing

Table 2-1 Comparison of simple model and LASNEX results

	Simple Model	LASNEX
Initial $\dot{E}$	5×10^9 Watts	10^{11} Watts
Final $\dot{E}$	10^{15} Watts	10^{15} Watts
s	2	15/8
Initial $\dot{R}$	8×10^5 cm/sec	10^6 cm/sec
Final $\dot{R}$	2×10^7 cm/sec	3×10^7 cm/sec
Initial pressure	3×10^6 atm	10^6 atm
Final pressure	1.5×10^{13} atm	10^{11} atm
Initial temperature	21 eV	
Final temperature	10 keV	30 keV
Final radius	19 μm	∿ 10 μm

the initial temperature T_o, there are no free parameters left which might be varied to provide a fit. T_o is initial in that it refers to the start of the adiabatic compression treated by the model. Prior to this the droplet has been non-adiabatically heated to this temperature by a weak first shock generated at the start of the laser pulse.[2]

In view of the naïvety of the model and the complexity of LASNEX the agreement is remarkable, with the exception of the final pressure where like is probably not being compared with like. The orders of magnitude are characteristic; the implosion velocity is generally less than the ablative velocities of the pellet atmospheres which we shall find in later chapters, and temperatures in excess of 10 keV are required for effective thermonuclear burning. In the final stages energy has to be symmetrically transported from an ablating atmosphere of about 1mm radius to the compressed sphere of radius about 10μm. The index s was found to be 15/8 on the basis of Fermi-degenerate electrons[1]; that this is so close to our value of 2 is not merely because $\gamma = 5/3$ in both cases - Nuckolls et al. give, instead of (2.11),

$$s = \frac{3\gamma}{\gamma+1} . \qquad (2.19)$$

The justification for our describing this model is that it introduces some typical orders of magnitude and illustrates some of the basic features of laser compression, in particular the singular pulse shape (2.13). During most

of the 25 nsec pulse the power changes very little, and then the bulk of the energy is rapidly released at the end. Such pulse-shaping is believed to be technically feasible.

The early stages of the pulse require intensities lower than the high intensities ($\gtrsim 10^{16} W/cm^2$) currently available from Nd lasers, but the latter are only obtained over small focal areas (diameter $\sim$ 50μm) and small time-scales ($\lesssim$ 1 nsec). The laser pulses considered in our results chapters correspond more to experimental pulses than to these specially shaped pulses.

A series of calculations was performed at Los Alamos[2] for the compression of DT spheres and shells using CO_2 laser light. The yield ratio Y was optimized for spheres and shells as a function of the input energy E, the target mass m, and the three parameters ($\dot{E}_o$, t_1 and s) which determine the pulse shape through (2.9). These quantities should be chosen according to the following considerations:

(a) Y is relatively insensitive to s in the range $1.5 < s < 2.5$, and t_1 in the range $0.5 < t_1/t_o < 3$, where t_o is the transit time for the first shock to reach the centre of the sphere.

(b) E/m should be close to 0.7 kJ/μg.

(c) Y is very sensitive to $\dot{E}_o$, particularly for small m. $\dot{E}_o$ should be proportional to m^ν where ν=1.50 for spheres and 1.38 for shells.

(d) m should be as large as is feasible as $Y \propto E^{0.45}$ (for E > 8kJ).

(e) Spheres are preferred to shells.

The thermonuclear yields in these calculations depend on the compression being largely adiabatic. The yield will be seriously degraded if suprathermal electrons or photons produced in the absorption region penetrate and therefore preheat the high density core. This may possibly be avoided by the use of a structured pellet, with a low Z outer layer (the "ablator") to minimise the generation of line and recombination radiation and enhance thermal conduction, and a high Z inner layer (the "pusher") to absorb suprathermal electrons.[10] The core will also be preheated if the thermal conduction front overtakes the compression front, but this may be avoided with suitable pulse-shaping.[10] In our simulations, where we do not use tailored pulses, we shall see the distinction between compression and thermal fronts; temperature gradients are needed to drive compression, but if the thermal front propagates too fast, such as in the thin film runs of Chapter 9, no compression is obtained.

Another important consideration is the hydrodynamic stability of an implosion. Are Rayleigh-Taylor instabilities stabilized by the hot ablating atmosphere?[11],[12]

Except inasmuch as symmetrical compression requires good thermal conductivity in the pellet atmosphere this work is not concerned with compression and we shall not pursue it further.

2.2 LASER-TARGET EXPERIMENTS

Although most of the interest in laser-plasma interactions has centred on laser fusion, most of the experiments that have been reported have not been directed specifically at obtaining compression as described in Section 2.1.3. Rather, the emphasis has been on acquiring a better understanding of the physical processes involved, and for these purposes a single beam and a plane target usually suffice.

The lasers are almost invariably Nd-glass or CO_2. Pulses contain typically 1-200J, with a full width at half maximum (FWHM) ranging from 25 psec to a few nanoseconds. These quantities are easily measured; the key parameter, however, is generally considered to be the peak laser intensity I_o because it is this which determines the peak oscillating electric fields in the plasma. I_o is difficult to determine because of its dependence on the spatial profile of the focussed laser beam, which is characterized (but not specified) by the spot diameter. Care should be taken in interpreting figures given for the spot diameter: one of the smallest spots reported, that of the Nd laser at the U.S. Naval Research Laboratory (NRL) [13], has a diameter of 12μm at half intensity, but 30μm at half energy (by which we mean that 50% of the energy lies outside 30μm). Spot diameters are generally within 100μm, and the resulting intensity I_o varies typically in

the range 10^{13} - 10^{16} W/cm^2; soon, no doubt, larger intensities will become available. These parameters are similar for Nd and CO_2, but because CO_2 pulse widths do not fall below 1 nsec these lasers tend to produce peak intensities below 10^{15}W/cm^2.

What happens when such a laser pulse is incident upon a plane target? Without doubt a plasma atmosphere is very rapidly blown off the surface, ionized to at least the critical electron number density but probably not much more. The underdense atmosphere is heated by inverse bremsstrahlung, again very rapidly, until it becomes too hot for this process to continue being effective ($T_e \gtrsim$ 100eV); from now on the laser light reaches the critical density region without suffering much attenuation and nonlinear interactions may set in.

Some of this light is specularly reflected (i.e. as off a mirror) from the critical density surface, which in general is not perpendicular to the laser axis; some is backscattered (i.e. back along the laser path); some is scattered (i.e. not back into the focussing optics); and some is absorbed, by parametric instabilities, resonant absorption or possibly other mechanisms. The absorbed energy is shared mainly among thermal and suprathermal ("fast") electrons, with most of the energy going into the fast component according to Brueckner.[14] X-rays are produced, from the bremsstrahlung of fast electrons ($h\nu \sim$10-100keV) and thermal electrons ($h\nu \sim$ 1-10 keV),

and from line and recombination radiation depending on the target material. Magnetic fields are "spontaneously" generated in the clockwise azimuthal direction about the axis of the incident laser beam, and are believed to be typically of the order of a mega-Gauss. Conventional current loops are directed towards the target on and near the axis and close at larger radii.

Some of the fast electrons leave the plasma immediately, setting up a charge-separation electric field which prevents further loss but which accelerates the plasma ions outwards. In this way both fast and thermal electrons transfer their energy to ablating ions which often contain "fast" components. The regions of large electron temperature spread through thermal conduction; and the large associated electron pressures cause general damage to solid targets, including some compression and vaporization, and the penetration of thin films. Ions are heated through equipartition from the electrons, compression if any, and possibly from turbulent electrostatic fields in the absorption region.

Sometimes the target is placed not in an evacuated chamber but in a background gas, in which case the plasma expansion is not as described above. Such a background must be below the threshold density for breakdown by the incident laser, but it may be photoionized by energetic photons emanating from the hot plasma and contain

the return current paths for the magnetic fields. Sometimes the target is in fact a pre-formed plasma, used to study absorption processes for example. Finally, in the minority of experiments that attempt to compress spherical targets containing deuterium and tritium, thermonuclear reactions may take place producing neutrons.

We believe we have summarized the main features of the interactions of current high power lasers with matter. In practice no experiment covers all of these phenomena, and although some overlap is inevitable we shall attempt in the remainder of this chapter to survey the published experimental work under the following headings: magnetic fields, absorption and backscattering, fast ions, x-ray emission, and compression. The relative positioning of magnetic fields and compression in this list is not intended to indicate their relative importance, but rather to remind the reader, who may by now have forgotten, that this work is about magnetic fields.

2.2.1 Magnetic fields

The first observations of spontaneously-generated magnetic fields, also described as "self-generated", "thermally-generated", "pressure-generated" and "thermoelectrically-generated", were reported in 1966 by Korobkin and Serov [15] for the breakdown of air at the focal spot of a ruby laser (2J, 30 nsec). In 1971 Stamper et al. [16] reported the first observation of the effect for a solid target. These

authors focussed a Nd laser (60J, 30 nsec) onto a small Lucite ($C_5H_8O_2$) target in a background of nitrogen, and measured the fields with small magnetic probes up to about 5 mm from the target. They were observed to be primarily azimuthal, and to propagate as pulses with the same velocity as the interaction region between the plasma and the background gas. In the plane of the target, perpendicular to the laser beam, the peak magnetic field B_o was found to scale as $r^{-\nu}$, wher r is the radius measured from the focal spot and $\nu = 1.4$ for $r <$ 1cm and 4.2 for $r >$ 1cm: for $r >$1cm the laser pulse was over before the front reached the probe.

Stamper et al.[16] and Stamper[17] explained these magnetic fields in terms of the pressure gradient term in the generalized Ohm's law, as we shall detail in Section 4.2.1. They occur when gradients of electron temperature and number density are non-parallel, they are in the direction of $\nabla T_e \times \nabla n_e$ (see Fig.2-1), they are convected with the fluid, and in general they decay only very slowly through resistivity. On the basis of a simple model where the azimuthally symmetric fields are generated at a point source and convected outwards by a spherically symmetric expansion[16], B_o should vary as r^{-1}. If we extrapolate the experimental result (B_o = 1kG at r = 1cm) to the focal spot radius of 100μm, we infer a field there of 0.1 MG using the theoretical index $\nu = 1$, or 0.6 MG if we use the experimental $\nu = 1.4$. Serov and Richardson[23]

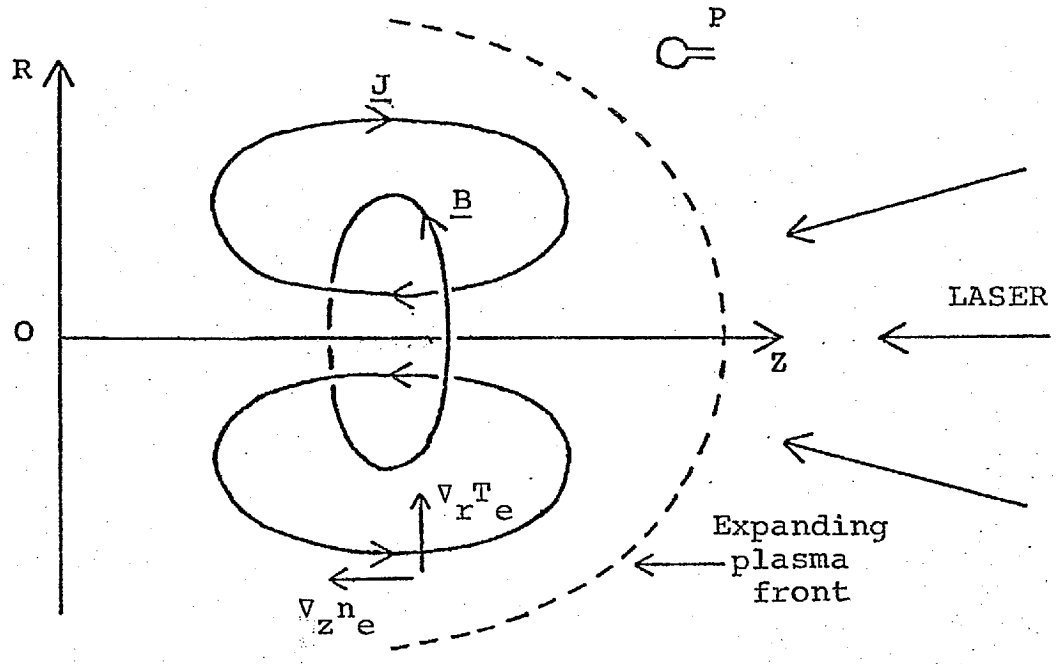

Fig.2-1 Orientation of the self-generated magnetic field and current. The probe at P lies outside the plasma and detects no field.

find $\nu = 2$ for a CO_2 laser (0.2J, 1nsec) focussed onto an aluminium target, and measure a field of 1kG at r=3mm. From this they infer fields of several hundred kilogauss at the focal spot (120μm diameter).

Clearly such extrapolations over two orders of magnitude can no more than indicate what fields might be present at the focal spot; indeed it is possible that the fields may be even greater than estimated, as may be seen from Fig. 2-1. Integrating Ampère's law over a disc in the (r, θ) plane extending to the point P, no field will be

recorded by the probe until the expanding plasma front reaches P because the current loops close within the plasma. (We have assumed cylindrical symmetry and neglected the displacement current for this non-transient phenomenon). The presence of a background gas, converted into a low density plasma through photoionization, allows the current loops to close further from the target; larger magnetic fields may also be generated from steep gradients of density and/or temperature at the front between the main plasma and the background plasma.

Extensive experiments on targets in background gases were carried out at the Naval Postgraduate School, Monterey, as reported by Bird et al.[18], McKee et al.[19], Case and Schwirzke[20], and Schwirzke[21] (who also gives a good introduction to spontaneously-generated magnetic fields). Small inductive probes were used to map the magnetic field contours in the expanding plasma and background gas over a region defined approximately by $\{ 0.4 \leq r \leq 2\text{cm} , 0.6 \leq z \leq 2\text{cm} \}$, for various times, background pressures, targets and laser powers. Such a plot of magnetic field is shown in Fig.2-2, together with the current density computed from Ampère's law. A graph of the pressure dependence of the peak magnetic field (Fig.2-3) showed three regions, interpreted as follows:

(a) low pressure - the magnetic field is unaffected by the background;

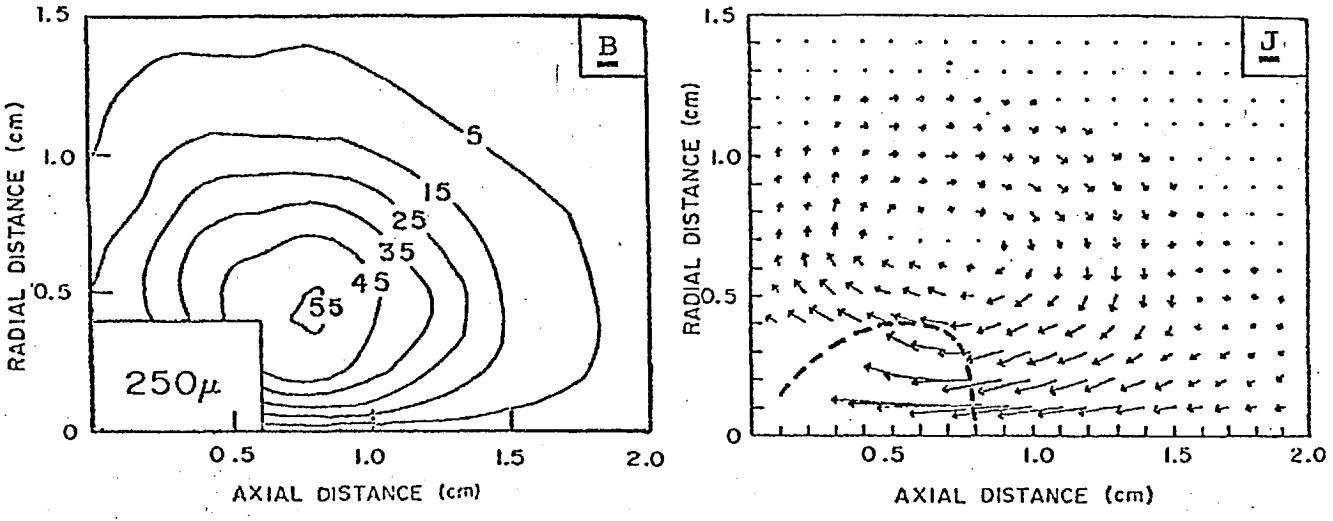

Fig.2-2 Magnetic field (Gauss) and current (max 612 Amp/cm^2) at 120 nsec for a mylar target in 250 mTorr of nitrogen. Dashed line indicates front of expanding laser plasma.(21)

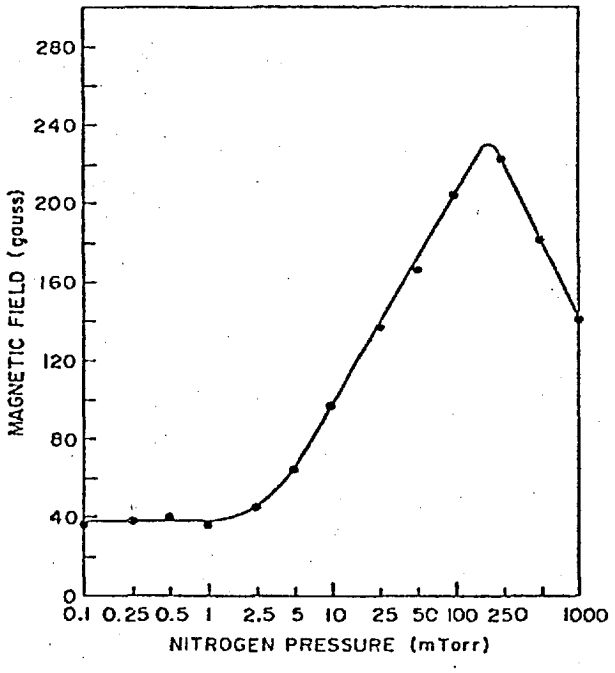

Fig.2-3 Maximum azimuthal magnetic field as a function of nitrogen background pressure at z=4mm, r=3mm for a mylar target.(21)

(b) intermediate pressure - the magnetic field is amplified by steep gradients at the plasma - background front and/or a larger current is able to flow through the background [21] [18];

(c) high pressure - the magnetic field decreases. Long after the end of the laser pulse the sign of $\nabla n_e \times \nabla T_e$ at the expanding front reverses.

Olsen and Mendel [22] measured magnetic fields ($\lesssim$50 Gauss) to within about 0.4cm from their targets, and in some cases also observed small field reversals at late times.

Case and Schwirzke [20] also found an almost instantaneous early time magnetic signal, with a propagation velocity $\gtrsim 10^8$ cm/sec, as distinct from the "pressure gradient" signal just discussed. This was of the same sign but significantly smaller in magnitude ($\sim$ 1-10 Gauss), and was attributed to a stream of thermal electrons emitted in a cone about the target normal of half-angle around 40°. The peak signal occurred at a background pressure of about 1mTorr; below this the background was not sufficiently dense to allow a return path for the current, while above this the electron mean free path decreased so as to close some of the current loops at lower radii than the probes.

Serov and Richardson [23] obtained results similar to Schwirzke [21] for the pressure-generated magnetic field, but (to within about 1 nsec) did not observe a delay in the

initial rise of the magnetic field signal for distances up to several millimeters. The arrival time of the peak magnetic field varied from ∿ 10 nsec at a pressure of a few hundred Torr to ∿ 1nsec at 4000 Torr. At pressures below 20 mTorr a small magnetic field ($\lesssim$ 10 Gauss) of opposite polarity was observed, corresponding to a conventional current flow out of the target. This is in disagreement with Case and Schwirzke [20], and apart from the late time field reversal already described is the only observation known to the author of magnetic fields being generated in the "wrong" direction. The mechanism for this is unclear, although the radiation pressure source described in Section 4.2.2 should not be ruled out.

Currents presumed associated with the self-generated magnetic fields have recently been directly measured by Drouet and Bolton [24], and Drouet and Pépin [25], who respectively focus a Nd laser (4J, 30nsec) and a CO_2 laser (0.1 to 4.5J, 1nsec) onto a flat copper target containing an embedded wire probe, as in Fig. 2-4. By varying the position of the laser relative to the probe from shot to shot the spatial distribution of current was mapped, and was found to be qualitatively in agreement with the theory as indicated by the current paths in Fig. 2-4. They note that the conducting target actively participates in the current flow process, in contrast to the schematic of Fig. 2-1. They note a short precursor current signal [24] whose sign is a

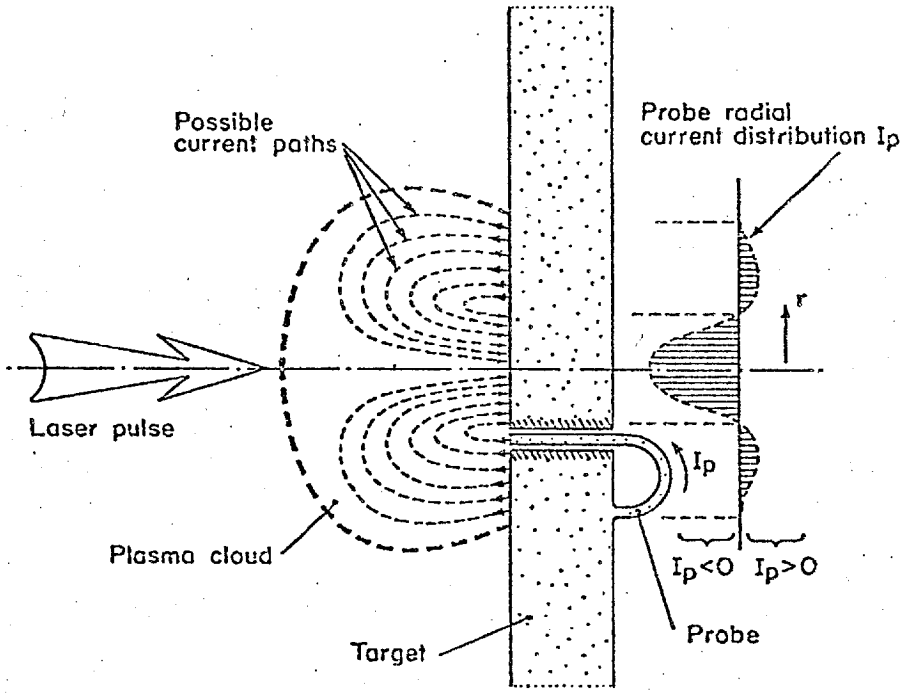

Fig. 2-4 : Diagram showing the target with the wire probe sampling part of the current flow through the plasma target interface.[24]

function of the operating conditions, but which still corresponds to closed-path flow. Because no details are given of this effect we do not classify it as a second example of the magnetic field being created in the"wrong" direction.

We now return to the difficult but important problem of measuring the magnetic fields actually present in the focal region. This has been performed by Stamper and Ripin[26] using two independent methods based on Faraday rotation; in each they inferred values for the peak magnetic field of a few mega-Gauss. They used a Nd laser (2J,100 psec) which gave an intensity of about 10^{15} W/cm^2.

In their first experiment some light was split off

from the main beam, frequency doubled, delayed until after the main pulse, passed through the plasma perpendicular to the plane of Fig. 2-1, and focussed onto a photographic film. The image of the film corresponded to the whole of the area of Fig. 2-1 including the target and some of the region behind the target. By varying the angle of a polarizing sheet placed between the plasma and the camera, until (say) a bright region in the lower half of the film was reduced to minimum intensity, Faraday rotation angles typically of around 10^{o} were obtained. Both the incident and probe beams were vertically polarized.

In the second experiment no probe beam was used. The angle of incidence was 45^{o}, the plane of incidence horizontal and the laser vertically polarized. The specularly reflected light, originating from the critical density region and therefore able to sample the largest magnetic fields, was analysed into (time-integrated) vertically and horizontally polarized components. The detector-assembly was rotated until the signal on the horizontal channel was a minimum and typical rotations of 22.5^{o} were obtained.

The determination of a value for the magnetic field is not at all straightforward as assumptions have to be made about the spatial variations of density and magnetic field. Guided by simple models, computer calculations and experimental results they estimate fields of 4.8 MG from the first experiment and 1.6 MG from the second, to within factors of 3 or 4. In the second experiment there is a

further difficulty: suppose the field configuration is primarily as in Fig.2-1, but with the laser incident in the (r,z) plane at 45° to the z-axis. The angle θ between the magnetic field and both the incident and specularly reflected rays will always be 90° and no Faraday rotation will occur. Stamper and Ripin suggest that fields generated by radiation pressure (see Section 4.2.2), though smaller, will lack this symmetry; and in any case the configuration is not symmetric about the target normal. They use 80° as a reasonable approximation for θ.

Despite this uncertainty the direct measurement of magnetic fields by Faraday rotation represents a significant advance, and we await further such results with interest.

2.2.2 Absorption and Backscattering

The main phenomena of interest under this heading are, as mentioned earlier,

(a) three absorptive instabilities - parametric decay, oscillating two-stream and two plasmon;

(b) two backscattering instabilities - Raman and Brillouin;

(c) resonant absorption; and

(d) filamentation (self-focussing).

Much theoretical work, analytical and computational, has been done in this area, but relatively little is known experimentally.

In general it is only possible to make inferences about these sub-picosecond processes from their analytically

predicted consequences for larger timescales, and it is often difficult to isolate competing processes; also, theoretical work performed for homogeneous plasmas may well be strictly inapplicable for the steep density gradients often encountered in laser - target experiments. However some progress has been made.

Information may be obtained from the spectrum of backscattered light. In particular, a small red-shift by an amount that may reasonably be interpreted as the ion acoustic frequency is indicative of, although not proof of, Brillouin backscattering; such red-shifts have been obtained for solid target interactions with Nd lasers [27-30] and CO_2 lasers [31]. Mitchell et al. [31] find about 5% of the incident laser energy backscattered over a wide range of energy and intensity (2J at 3×10^{13} W/cm^2 to 170J at 7×10^{14} W/cm^2), of which only about 30% is red-shifted, and suggest that the lack of substantial Brillouin backscatter is due to steep gradients in the underdense region. Saturation of the backscattered energy at a small fraction of the incident energy, as laser intensities increase above the instability thresholds, is indeed a commonly - observed phenomenon.

Brillouin backscatter has also been investigated in underdense homogeneous plasmas [32-34], created from a gas either by a discharge [33] or from the irradiation of the laser itself [34, 32]. The three experiments cited all use CO_2 lasers, and intensities ($\sim 10^{11}$ W/cm^2) and electron temper-

atures (∿100eV) well below the corresponding values in solid target experiments. However competing instabilities occurring at the critical density are avoided as are the problems of wave-number mismatching associated with steep gradients. Such studies are also relevant to the possible laser-heating of long magnetically-confined plasma columns [34].

The parametric decay instability is believed to give rise to suprathermal electrons, whose bremsstrahlung will produce high energy x-rays. The presence of this instability was inferred from the observation of x-rays with an apparent temperature of ∿40 keV by Shearer et al. [35] in 1972; their Nd laser (∿70J, 5 nsec) gave a maximum intensity of about 2×10^{14} W/cm^2 and plasma temperatures around 1keV, but because their measurements were integrated in both time and space they did not preclude the existence of a localized hot spot of electron temperature. Nor was the oscillating two stream instability ruled out, although it has a higher threshold intensity than the parametric decay instability.

One of the basic characteristics of non-linear oscillatory processes is the production of sum and difference frequencies from whatever natural frequencies may be present. Thus any non-linear interaction at the critical density between the laser wave and excited plasma oscillations of the same frequency may be expected to give rise

to second, third and higher harmonic emission from the plasma. Or, if the two plasmon instability is present, plasma waves of half the laser frequency are excited and we may expect 1/2, 3/2, 4/2, 5/2 and higher harmonic emission. Observations have been made for Nd lasers of second harmonic [29, 30, 36, 37], 3/2 harmonic [30, 36] and 1/2 harmonic [36] light; and for CO_2 lasers, second [38] and third [39] harmonic light. In general very little energy appears in harmonics; for example Baldis et al [39] found backscattered emissions of 10^{-1}, 4×10^{-7} and 8×10^{-9} for the fundamental, second and third harmonics respectively, expressed as fractions of the incident light, for an incident intensity of $7 \times 10^{12} W/cm^2$.

Eidmann and Sigel [37] examined the spatial distribution of second harmonic light backscattered through the focussing lens of a Nd laser (20J, 5nsec, intensity $\simeq 4 \times 10^{14}$ W/cm^2) to provide strong evidence that the second harmonic generation resulted from resonance absorption. In particular the emission was observed at oblique incidence and for electric fields polarized in the plane of incidence. The optimum angle of incidence θ for resonant absorption is given theoretically in terms of the density lengthscale L in the critical density region by [40]

$$\left(\frac{2\pi L}{\lambda_{las}}\right)^{2/3} \sin^2 \theta \simeq 0.6, \qquad (2.20)$$

Using this formula and the experimental value of $\theta (\geq 25^{\circ}$, the

periphery of the lens), they obtain $L \leq 1\mu m$. While some doubt must be attached to the applicability of (2.20), they consider that this result provides evidence for a steepening of the density gradient at the critical density, as has been obtained from a two-dimensional electromagnetic particle code (ZOHAR) by Estabrook et al.[41]

An interesting application of harmonic production was described by Jackel et al.[42] Four coplanar Nd beams were incident upon a spherical target; by photographing the plasma in emitted light at twice and three-halves the laser frequency, assumed to originate mainly from the critical and quarter critical density regions respectively, an estimate could be made of the density scale-length. Because the photographs were time-integrated, the scale-length measured was that between the maximum excursions of the two emitting layers; it varied linearly from 10μm to 30μm as the absorbed energy increased from 5J to 20J, at laser intensities around 10^{15} W/cm^2.

Some evidence has recently been obtained by Donaldson and Spalding[43] for the existence of density cavitons near the critical layer of a carbon target irradiated by a CO_2 laser (75J, 50 nsec) of intensity $\sim 9 \times 10^{12}$ W/cm^2. These are regions of low density which are believed to arise from filamentation or from large radiation pressures generated during resonant absorption. Using holographic interferometry they inferred a reduction in density by a

factor of about 2.5, at 25 nsec after the initiation of the laser pulse and in a region about the axis of spatial extent about 100μm. In addition they observed filamentary structures in x-ray pinhole photographs.

Time integrated x-ray pinhole photographs were also taken at Livermore by Haas et al.[44] of targets illuminated by Nd and CO_2 light at intensities in the 10^{13}- 10^{14} W/cm^2 range. For CO_2 light but not for Nd light they showed several localized regions ("spots") of high emission, of spatial dimensions (∿40-60μm) less than the spot diameter (∿80μm FWHM). In contrast the spatial distribution of the incident CO_2 beam was much smoother than that of the Nd beam. The observed photographic exposures are consistent with measured fluxes of either 1 keV x-rays or 50 keV suprathermal electrons. Haas et al. too suggest that these spots are indicative of filamentation and/or cavitons ("bubbles"), the conditions for which are not met in the Nd case. They note that the effect of self-generated magnetic fields on the stability of filaments and bubbles is as yet uncertain.

Indeed, we must ask the question whether these spots of emission are associated with hot spots in the electron temperature distribution caused by large magnetic fields. The mean free path of a 50 keV electron in a plasma of ion charge $z = 6$ and $n_e = 10^{19}$ cm^{-3} is about 100cm, whereas its Larmor radius in a mega-Gauss magnetic field is about 7.5μm. Therefore it is possible for such variations of electron temp-

erature to occur over lengthscales of the order of 40-60μm in the presence of large magnetic fields. Even electrons with energies 50 times lower still have long mean free paths (~400μm), so without magnetic fields the small-scale spatial structure must be explained in terms of spatial variations not of the electron temperature but of the plasma density or the laser intensity. It is notable that Donaldson and Spalding [43] infer an isothermal atmosphere above 50 μm from the axis on the basis of the x-ray intensity being proportional to the density squared.

One may also ask whether small-scale variations of density will generate significant magnetic fields; in such circumstances it is probably impossible to separate field generation from the detailed nature of the absorption processes themselves.

2.2.3 Fast ions

A standard diagnostic in laser-target experiments is the measurement of the ion current in a collector placed at some distance from the target as a function of the arrival time. Such arrival times are generally of the order of microseconds, so that time resolution with respect to the laser pulse ($\lesssim$1nsec) is impossible. If just a single ion species is present one obtains velocity or energy distributions of the ablated ions, but if several species are present the interpretation is less certain.

A common feature of these measurements is that at sufficiently high laser intensities fast ion peaks are superimposed upon these arrival time graphs; results from a typical experiment (Ehler[45]) are shown in Fig.2-5 for the interaction of CO_2 laser light with a polyethylene

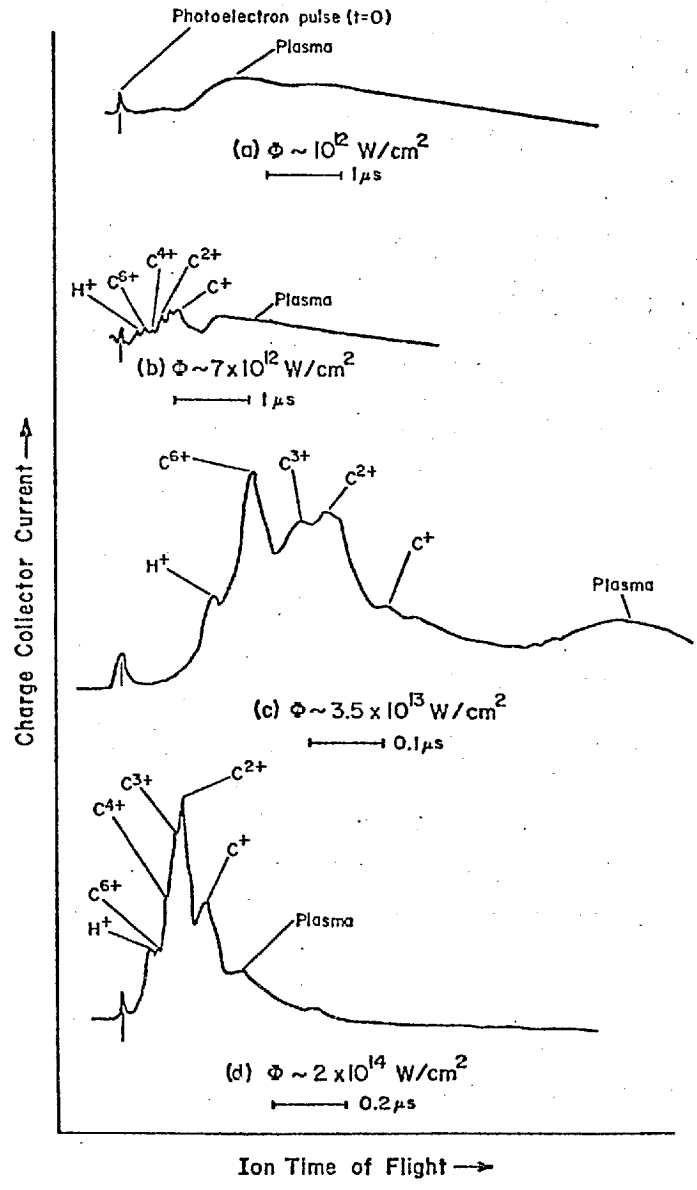

Fig.2-5 Graphs of ion current from a polyethylene (CH_2) target for a 1.5 nsec pulse of CO_2 light at various intensities. Target to collector distance: 26.8cm for (a) and (b) and 32.8cm for (c) and (d). Vertical lines on left indicate time origin.

(CH_2) target. These peaks appear for intensities in excess of 5 x 10^{12} W/cm^2 (Fig.2-5, b-d). The labelling according to charge species is not experimental identi-

fication, but an indication of where the peaks might lie if they were determined relative to one another solely by the various charge to mass ratios. The energy of the H^+ peak in Fig.2-5d is given as 140 keV. Ehler also observed high energy electrons (~500keV) which he attributed to a hot region in the plasma.

The crude model proposed as an explanation for the fast ions may be described as collisionless electrostatic acceleration in the electric fields associated with large temperatures in the absorption region. The rapid loss from the plasma of a few energetic electrons, produced by whatever heating process is present, generates a large electric field directed away from the plasma in which the various ion species gain energies in proportion to their charge. A key parameter is clearly the ion mean free path; if the species undergo collisions with each other during their acceleration they will arrive together, but at sufficiently low densities or high energies they will separate.

The direct measurement of large electric fields in expanding carbon plasmas has been reported by Mendel and Olsen[46], and Olsen and Mendel[22]. Fields of up to 1900V/cm were detected by the deflection of a fast ion beam (H_e^+) at distances a few millimeters from their targets.

The situation is complicated by atomic processes; it may be that finite ionization rates explain the

presence of ions other than H^+ and C^{6+} at temperatures well above the ionization energies of most of the carbon stages - see Table 2-2. This situation is accentuated

Table 2-2 Ionization energies of carbon. (From [47].)

Ionization stage	Ionization energy (eV)	Cumulative energy (eV)
$C - C^+$	11.256	11.256
$C^+ - C^{2+}$	24.376	35.632
$C^{2+} - C^{3+}$	47.871	83.503
$C^{3+} - C^{4+}$	64.476	147.979
$C^{4+} - C^{5+}$	391.986	539.965
$C^{5+} - C^{6+}$	489.84	1029.805

because at equilibrium, according to the collision-radiative (CR) model in which collisional excitation balances radiative recombination and three-body recombination, the temperature required to produce a particular charge state is several times lower than the cumulative ionization energy. The CR equilibrium equations were solved for $n_e = 10^{21}$ cm^{-3} by Colombant and Tonon[48] and Table 2-3 is taken from their results. It gives the temperature range for which each species is more than 10% abundant. In equilibrium above $T_e = 160eV$, negligible amounts of carbon species below C^{6+} should be present.

Table 2-3 Abundance ranges of carbon. (From [48].) Temperature range in which ion abundance exceeds 10%, according to CR equilibrium model at $n_e = 10^{21}$ cm^{-3}.

Ion	Temperature range (eV)
C^{+}	2 - 10
C^{2+}	5 - 14
C^{3+}	8 - 20
C^{4+}	10 - 100
C^{5+}	50 - 160
C^{6+}	80 -

Ehler [45] does not explain the fast ions as arising directly from anomalous absorption mechanisms; rather he suggests, following Malone et al. [49], that high electron temperatures are generated as a result of flux-limiting. However the severe flux-limiting properties of large magnetic fields provide an alternative explanation, and there is also the possibility of $\underline{J} \times \underline{B}$ acceleration.

2.2.4 X-ray emission

Interest in the x-rays produced in laser-target experiments arises for various reasons, including the following [50]:

(a) the x-rays provide diagnostics for the experiments producing them;

(b) any target material may be used, thereby enabling the

compilation of a wide range of spectroscopic data;

(c) the target may be used as an x-ray source, for the diagnostics of other plasmas or for medical applications[51];

(d) the x-rays may be of use in the development of an x-ray laser.

It is primarily (a) above that is of concern to us; we shall illustrate the use of x-ray diagnostics by outlining some work performed in the last two years at the U.S. Naval Research Laboratory[50, 52, 13, 53].

Nagel et al.[50] performed a systematic survey of the spectra (in the 1-2keV region) for a wide range of elements across the periodic table, using 250-900 psec pulses of Nd light focussed at intensities around 10^{14} W/cm^2 on spots of about 50μm diameter. The plasmas were found to contain highly stripped atoms (up to Al^{12+}, Zn^{22+} and Gd^{38+}). Because of the intense spectra found in the 1-2keV region they estimated a plasma temperature of about 0.5keV, as an approximation to the actual situation where the electron temperature varies strongly with space and time.

Young[52] measured the energy-integrated hard x-ray emission (15-100keV) from various targets, transmitted through 1mm aluminium absorbers and detected by Na I scintillators. The total energy, though extremely small (3×10^{-9}J for an incident energy of 10J, equivalent to just 500 20-keV photons), was three orders of magnitude

higher than that calculated assuming a Maxwellian temperature distribution. Also, it was insensitive to atomic number. Young suggested that the x-rays arose from electrons accelerated to high energies while confined by high magnetic fields, as originally proposed by Tidman and Stamper[54].

This work was extended by Ripin et al.[13] who measured hard x-ray energy spectra using a variety of filters to cover the range 1-500 keV. Laser intensities were around $1.2 \times 10^{16} W/cm^2$. They estimated that 75% of the laser energy was absorbed, 5% specularly reflected, 15% Brillouin backscattered through the focussing lens, and 5% scattered elsewhere.

The experimental spectra were compared with the spectra calculated by a two-dimensional Eulerian computer code; their main result was that better agreement was obtained when magnetic fields were included in the code: for energies above about 20 keV the x-ray fluxes observed experimentally were much larger than those predicted by the magnetic field - free model. This arose because the reduction in the thermal conductivity gave rise to larger electron temperatures (6-60 keV) in the target atmosphere.

When they also included suprathermal electrons in their code they obtained x-ray fluxes orders of magnitude higher than the experimental results for energies above 2 keV; they therefore questioned suprathermal electron production. However the distinction between suprathermal electrons, and

thermal electrons of temperatures up to 60 keV, is unclear.

Similar experimental results were obtained at Los Alamos by Kephart et al.[55] for photon energies in the 4-50 keV range, using a crystal spectrometer with one crystal for each energy sampled. Results for both CO_2 and Nd light are shown in Fig.2-6; they were interpreted

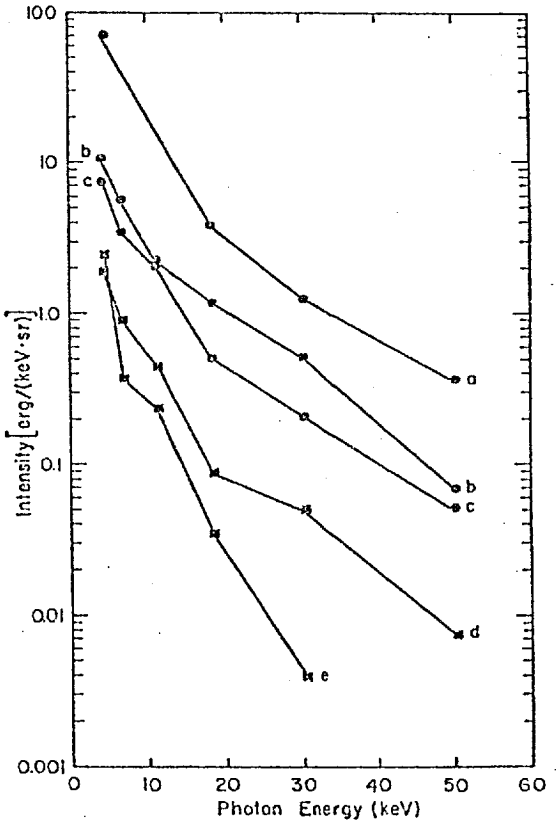

Fig.2-6 X-ray spectra of plasmas produced by 10.6μm pulses (1.3nsec, spot diameter 90μm) of energies 8.5,7.8 and 7.4J (a-c) and 1.06μm pulses (25psec, spot diameter 100μm) of energies 9.2 and 10.4J (d-e). The solid lines are intended only to distinguish the different spectra.[55]

by Malone et al.[49] in terms of flux - limiting to within some fraction of the "free-streaming limit", in contrast

to the N.R.L. work[13].

Images of laser-produced plasmas, not in the x-ray region but in the extreme ultra-violet (XUV), have been obtained by Feldman et al.[53] using a slitless normal incidence spectrograph which covered the 200-550 Å range (20-60 eV). Each line in the spectrum (on the spectroheliograph) was therefore an image of the plasma, rather than the image of a slit; spectral broadening, mainly Döppler broadening arising from the plasma expansion, was less than the dimensions of the image.

Analysing the spectroheliographs with a densitometer they were able to obtain two-dimensional contour plots of the regions of emission of each spectral line. These plots were time-integrated, but they suggested a method of obtaining time resolution: a thin foil ($\sim$ 0.1μm) is placed in the path from the plasma to the spectrograph, and is burnt by a small fraction of the main beam which is diverted with a variable time delay.

One observation was that the plasma expanded back towards the laser in a cylindrical (rather than spherical) plume, almost independently of the angle of incidence. They suggested magnetic fields as an explanation for this. They also performed thin foil experiments, looking for emission on the rear of the foil. A 100 psec Nd pulse of energy 4.1J, with a focal spot of 20μm, was able to penetrate up to about 10μm of iron.

Finally, the x-ray measurements described in this section, like the x-ray pinhole photographs of Section 2.2.2, suffer the drawback of time-integration. Time-streaked x-ray spectrographs promise greatly improved diagnostics.

2.2.5 Compression.

Most, but not all, of the experiments so far described have used single beams. KMS Fusion, Inc., have concentrated on obtaining an approximately uniform irradiation of spherical targets[56-59], in which context it is interesting that none of these papers consider self-generated magnetic fields. They focus two Nd beams using either two f/0.6 lenses or the KMS ellipsoidal mirror system, as described by Downward[56] who measured the intensity variation of reflected light from spherical glass shell targets. For the mirror system the reflected energy increased from 36% to 64% of the incident energy as the average intensity increased from 4.8×10^{13} to 2.7×10^{15} W/cm^2.

Campbell et al.[57] reported volume compressions of these targets of the order of 100, inferred by comparing microdensitometer traces of x-ray pinhole photographs with the predictions of a one-dimensional computer code. For example, with an absorbed energy of a few Joules (4J in slow ions, 2J in fast ions) the inner radius of the shell was compressed from 35.2μm to about 5.2μm. While these are compressions not of solid matter but of DT gas

they do give some indication of the uniformity of the irradiation. Typically 10^6 to 10^7 neutrons were obtained.

Evidence that these neutrons originate from inside a closed shell, rather than from fast fuel ions released into the corona after a break-up of the shell, was obtained by Goforth[58]. He used shells filled with ^3He, chosen because of the unique charge to mass ratio of $^3He^{2+}$ ions, and looked for these ions among the fast ion species using a time-of-flight mass spectrometer. Because only fast ions corresponding to the shell species were detected he deduced that the ^3He had been contained.

One way of estimating the plasma expansion energy is by heating the shells in an atmosphere of helium and monitoring the expansion of the blast-wave front.[59]

Microshell experiments producing similar neutron yields have also been performed at Livermore by Slivinsky et al.[60] By a time-of-flight analysis of the α-particle energy spread they estimated the ion temperature within the shell to have an upper limit of 3-4 keV.

CHAPTER 3

SPECIFICATION OF A FLUID MODEL

Underlying our work is the basic assumption that several processes of interest in laser-plasma interactions may be realistically described by a fluid model. It is the purpose of this chapter to provide a specification of such a model.

In Section 3.1 we outline ways in which a finite two-dimensional cylindrically-symmetric domain may be used to model interactions occurring in regions which are infinite and which may lack strict two-dimensional symmetry. In Section 3.2 we give a complete system of equations for the fluid model, including coefficients for all the transport properties used. As the equations are generally familiar they will be given with a minimum of comment; a discussion of the physics treated by, and omitted from, the model is the subject of the next chapter.

3.1 THE BASIC GEOMETRY

The essential feature of our model, implicit in our equations and common to all our simulations, is a laser beam impinging on a target at normal incidence. This enables us to make the simplifying assumption of azimuthal symmetry about the axis of the beam, so that we may describe all variables as functions of the cylindrical co-ordinates (r,z) and time t.

A typical configuration is shown in Fig.3-1. The laser is incident from the right, parallel to the z-axis, usually with a spatial profile which has a maximum on the axis. An initial cool plasma is assumed with an atmosphere which has been created by blow-off from the target surface, either by a prepulse or more usually during the earliest stage of the laser pulse ($t \leq 0$). An initial density profile which is a function of z only is a reasonable (but

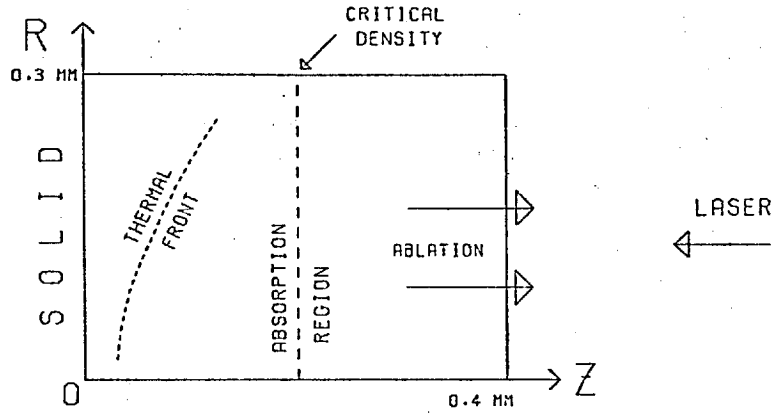

Fig. 3-1 Basic configuration

not necessary) assumption, because at early times the axial lengthscale, determined by the sound speed in a cool plasma, will be less than the radial lengthscale determined by the laser beam. This will also be true at later times in many cases, because density changes generally occur on timescales much longer than heating and conduction times.

The critical density corresponding to the incident laser wavelength occurs at $z = z_c$. In this region absorption from the laser is a maximum; on the right low density plasma is ablated with high velocities, and on the

left a thermal front (and maybe a compression front) propagate towards the solid.

As described in Section 4.2.1 magnetic fields are generated in the absorption region in the negative θ- direction, corresponding to clockwise current loops in the (r, z) plane - see Fig. 2-1. Because all spatial gradients are in this plane, the heat flow is always perpendicular to the magnetic field.

The region of simulation is defined as

$$o \leqslant r \leqslant r_{max}$$

$$o \leqslant z \leqslant z_{max} ,$$

and the four boundaries will be referred to as north, south, east and west.

By suitably specifying the boundary conditions we are able to model various physical situations, with varying degrees of realism. We shall see later that much of the physics described by our model is independent of the boundary conditions chosen. We now consider in turn the three basic geometries that will be of interest.

3.1.1 Single beam on thick target

This is the simplest case - see Fig. 3-2. The boundaries would ideally be as far as possible from the interaction region, so that boundary conditions would not be needed, but in practice this is not feasible. The north

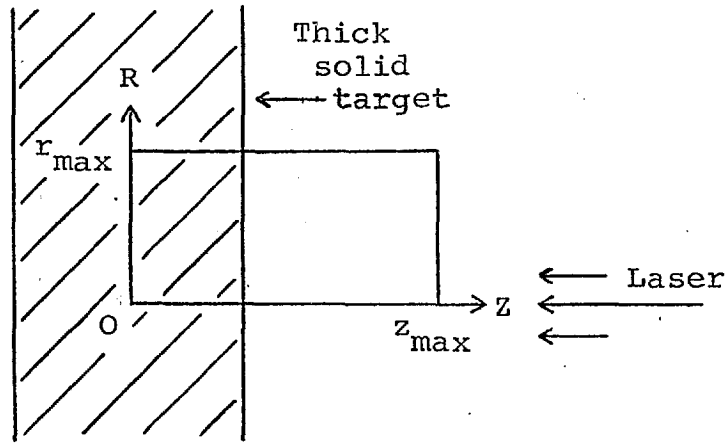

Fig. 3-2 Single beam on thick target

and east boundaries are taken to be "free-flux" boundaries, across which matter may flow freely. The west boundary is fixed, as is approximately true for a sufficiently thick target, and as would be exactly true were another identical laser simultaneously incident from the west; it is therefore characterized as a "no-flux" boundary. The axis is not a physical boundary and therefore no boundary conditions apply there, although of course it forms a computational boundary which has to be treated with care. The radial velocity and magnetic field are zero on the axis because of the assumed axisymmetry.

An example using this configuration is given in Chapter 8.

3.1.2 Multiple beam

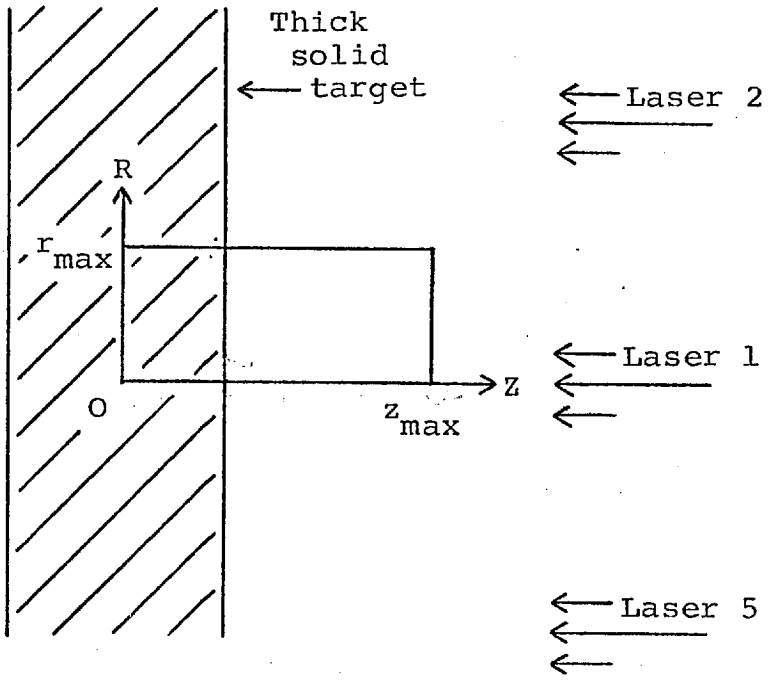

Fig. 3-3 Multiple beam configuration

The multiple beam case, exemplified by Fig.3-3, is similar. The laser beam (1) is surrounded by six other equal parallel beams (2-7); a view looking along the central beam onto the target plane is shown in Fig. 3-4. The beams are drawn separated, but in practice they will overlap. It is seen that there exists a hexagonal "surface of symmetry"

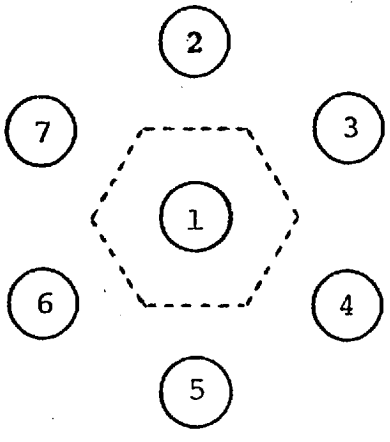

Fig.3-4 Target plane of multiple beam configuration.

around the central beam, whose intersection with the target is shown as a dotted line, across which no fluid will flow and on which the magnetic field will be zero. The word "symmetry" is used loosely because the illumination pattern does not extend to infinity.

A similar pattern with genuine symmetry may arise in compression experiments using multiple beam irradiation. For example, a six-beam irradiation along the Cartesian axes would have right square prisms as surfaces of symmetry. These configurations are strictly three-dimensional, but we may approximate them by treating the dotted lines as circles, thereby regaining cylindrical symmetry.

In the simple case of two-sided illumination no approximation is involved, and the plane $z = 0$ is the surface of symmetry. This case is included in Section 3.1.1 above: by allowing light rays to travel other than parallel to the z-axis we may obtain a configuration appropriate to, for example, the K.M.S. system.

The multiple-beam boundary conditions are the same as in Section 3.1.1 except that the north boundary becomes a "no-flux" boundary with no magnetic field. Such a configuration is used in Chapter 7.

3.1.3 Thin film

The thin film configuration is shown in Fig. 3-5. The film is placed in the centre of the simulation region,

and "free-flux" conditions are applied to all three boundaries. Calculations using this geometry are described in Chapter 9.

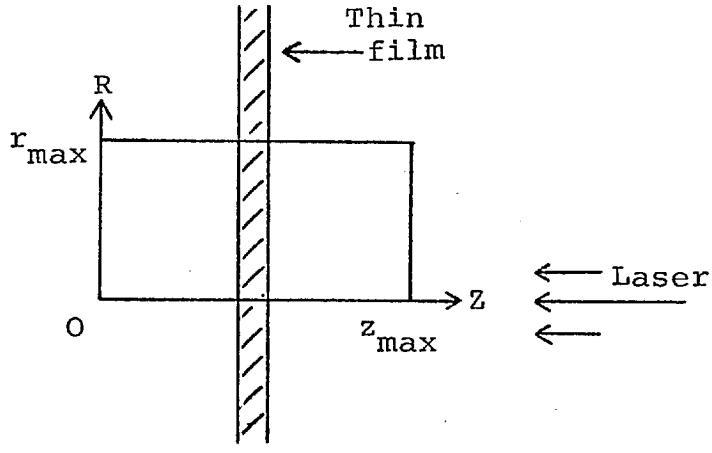

Fig. 3-5 Thin film configuration

3.2 THE FLUID EQUATIONS

Our system is governed by equations for the time evolution of what will be referred to as the six major variables: the density (ρ), the radial and axial velocities (V_r, V_z), the magnetic field (B), and the electron and ion temperatures (T_e, T_i). These equations are

$$\frac{\partial \rho}{\partial t} + \nabla \cdot \rho \underline{V} = 0 \qquad (3.1)$$

$$\frac{\partial}{\partial t} (\rho \underline{V}) + \nabla \cdot (\rho \underline{V}\underline{V}) + \nabla (P_e + P_i) = \underline{J} \times \underline{B} \qquad (3.2)$$

(3.2)

$$\frac{\partial}{\partial t}\frac{P_i}{\gamma-1} + P_i \nabla.\underline{V} + \nabla.\left[\frac{P_i \underline{V}}{\gamma-1} + \underline{Q}_i\right] = \frac{n_e k(T_e-T_i)}{(\gamma-1)\tau_{eq}} \tag{3.3}$$

$$\frac{\partial}{\partial t}\frac{P_e}{\gamma-1} + P_e \nabla.\underline{V}_e + \nabla.\left[\frac{P_e \underline{V}_e}{\gamma-1} + \underline{Q}_e\right] = -\frac{n_e k(T_e-T_i)}{(\gamma-1)\tau_{eq}} + \eta \underline{J}^2 - P_{rad} + P_{las} \tag{3.4}$$

$$\frac{\partial B}{\partial t} = -(\nabla \times \underline{E})_\theta . \tag{3.5}$$

In terms of the cylindrical (r,θ,z) co-ordinate system we have introduced

$$\underline{V} = (V_r, 0, V_z) \tag{3.6}$$

$$\underline{B} = (0, B, 0). \tag{3.7}$$

Because $\underline{B}$ is always azimuthal we write B rather than B_θ.

Minor variables are defined from the six major variables as follows:

ion number density	$n_i = \rho/m_i$	(3.8)
electron number density	$n_e = z n_i$	(3.9)
ion pressure	$P_i = n_i k T_i$	(3.10)
electron pressure	$P_e = n_e k T_e$	(3.11)
current	$\underline{J} = \mu_o^{-1} \nabla \times \underline{B}$	(3.12)
electron velocity	$\underline{V}_e = \underline{V} - \underline{J}/n_e e$	(3.13)

electric field $$\underline{E} = \eta \underline{J} - \underline{V}_e \times \underline{B} - \frac{1}{n_e e} \nabla (n_e k T_e) \quad (3.14)$$

electron heat flux $$\underline{Q}_e = (Q_{er}, 0, Q_{ez}) \quad (3.15)$$

ion heat flux $$\underline{Q}_i = (Q_{ir}, 0, Q_{iz}), \quad (3.16)$$

where

$$Q_{er} = -K_{e\perp} \partial T_e/\partial r - K_{e\wedge} \partial T_e/\partial z \quad (3.17)$$

$$Q_{ez} = K_{e\wedge} \partial T_e/\partial r - K_{e\perp} \partial T_e/\partial z \quad (3.18)$$

and

$$Q_{ir} = -K_{i\perp} \partial T_i/\partial r + K_{i\wedge} \partial T_i/\partial z \quad (3.19)$$

$$Q_{iz} = -K_{i\wedge} \partial T_i/\partial r - K_{i\perp} \partial T_i/\partial z . \quad (3.20)$$

The terms in $K_{e\wedge}$ and $K_{i\wedge}$ are known as the Righi-Leduc fluxes.

To determine the transport coefficients ($K_{e\perp}$, $K_{e\wedge}$, $K_{i\perp}$, $K_{i\wedge}$, η and τ_{eq}) we first define the following quantities:

$$\Lambda = \frac{3 (4\pi\varepsilon_o k T_e)^{3/2}}{2e^3 \sqrt{\pi n_e}\, z} \quad (3.21)$$

$$\tau_{ei} = 6\pi\sqrt{2\pi}\, \frac{\varepsilon_o^2 m_e^{1/2}}{e^4 \ln\Lambda}\, \frac{(kT_e)^{3/2}}{z^2 n_i} \quad (3.22)$$

$$\tau_{ii} = 6\pi\sqrt{2\pi}\, \frac{\varepsilon_o^2 m_i^{1/2}}{e^4 \ln\Lambda}\, \frac{(kT_i)^{3/2}}{z^4 n_i} \quad (3.23)$$

$$\nu_{ei} = \tau_{ei}^{-1} \tag{3.24}$$

$$\nu_{ii} = \tau_{ii}^{-1} \tag{3.25}$$

$$\Omega_e = eB/m_e \tag{3.26}$$

$$\Omega_i = eB/m_i \tag{3.27}$$

$$\tau'_{ei} = \frac{2}{0.654}\,\tau_{ei} \tag{3.28}$$

$$\tau'_{ii} = \frac{2}{0.896}\,\tau_{ii} \tag{3.29}$$

$$K_{eo} = \frac{5n_e k^2 T_e}{2m_e}\,\tau'_{ei} \tag{3.30}$$

$$K_{io} = \frac{5n_i k^2 T_i}{2m_i}\,\tau'_{ii}. \tag{3.31}$$

Then we may define

$$K_{e\perp} = \frac{K_{eo}}{1+(\Omega_e \tau'_{ei})^2} \tag{3.32}$$

$$K_{e\wedge} = K_{e\perp}(\Omega_e \tau'_{ei}) \tag{3.33}$$

$$K_{i\perp} = \frac{K_{io}}{1+(\Omega_i \tau'_{ii})^2} \tag{3.34}$$

$$K_{i\wedge} = K_{i\perp}(\Omega_i \tau'_{ii}) \tag{3.35}$$

$$\eta = \frac{0.5064\ m_e}{n_e e^2 \tau_{ei}} \tag{3.36}$$

$$\tau_{eq} = \frac{m_i}{2m_e}\,\tau_{ei}. \tag{3.37}$$

Note that it is the actual magnetic field B rather than the modulus which is used in the definitions of the Larmor frequencies Ω_e and Ω_i, so that it is the vectors

$$\underline{\Omega}_e = (0, \Omega_e, 0) \tag{3.38}$$

$$-\underline{\Omega}_i = -(0, \Omega_i, 0) \tag{3.39}$$

which describe the directions of gyration of the electrons and ions. This is reflected in the difference of signs between (3.17)-(3.18) and (3.19)-(3.20).

The bremsstrahlung radiation loss rate P_{rad} is taken from Shkarofsky et al.[61]:

$$P_{rad} = \left(\frac{2\pi kT_e}{3m_e}\right)^{\frac{1}{2}} \frac{32\pi}{3hm_e c^3} \left(\frac{e^2}{4\pi\varepsilon_o}\right)^3 z^2 n_e n_i . \tag{3.40}$$

The laser source P_{las} is derived from the incident intensity profile $I(r, z, t)$ at $z = z_{max}$. Light is assumed to travel in straight lines in the negative z-direction subject to

$$\frac{\partial I}{\partial z} = K_{IB} I \qquad (z \geqslant z_c) \tag{3.41}$$

$$I(r,z,t) = I(r,z_c,t)\phi(z_c-z) \quad (z \leqslant z_c), \tag{3.42}$$

where the inverse bremsstrahlung length K_{IB}^{-1} is given by

$$K_{IB} = \frac{\nu_{ei}\ \nu_p^2}{c\nu_{las}^2 (1-\nu_p^2/\nu_{las}^2)^{1/2}} \tag{3.43}$$

$$\nu_p = \omega_p/2\pi \tag{3.44}$$

and

$$\omega_p^2 = \frac{n_e e^2}{\varepsilon_o m_e} \cdot \tag{3.45}$$

$\phi(z_c - z)$ is an ad hoc dumping profile which is used to reduce the intensity to zero over a small region in the overdense plasma. The absorption rate P_{las} is then given everywhere by*

$$P_{las} = \frac{\partial I}{\partial z} \cdot \tag{3.46}$$

Apart from the specification of appropriate initial and boundary conditions, the formulae given above form a complete set on the inclusion of the following material and laser properties

ion mass	m_i
(constant) ion charge number	z
specific heat ratio	γ (always taken to be 5/3)
laser frequency	ν_{las}

and the following fundamental constants (47)

k	=	1.380662×10^{-23}	Joules/^oK
c	=	2.99792458×10^{8}	m/sec
μ_o	=	$4\pi \times 10^{-7}$	Henrys/m
ε_o	=	$1/(c^2\mu_o)$	
e	=	$1.6021892 \times 10^{-19}$	Coulombs
h	=	6.626176×10^{-34}	Joule-sec
m_e	=	$0.9109534 \times 10^{-30}$	kg,

---

*The simple physical origin of inverse bremsstrahlung is immediately apparent from (3,46) expressed in terms of the peak electron velocity V_p in the oscillating electric field:

$$P_{las} = \tfrac{1}{2} n_e m_e V_p^2 / \tau_{ei} \cdot$$

For a deuterium plasma we take z=1 and $m_i=2.014m_A$; for carbon we take z=4 and $m_i=12m_A$, where $m_A=1.6605655\times10^{-27}$kg. The excessive accuracy of these figures is of course unwarranted.

The definitions of the collision times τ_{ei} and τ_{ii}, and the formulae for K_{eo}, K_{io} and η, are taken from Shkarofsky et al.[62], but with the z-dependence included- they consider only z=1. They give more accurate formulae for the conductivities ($K_{e\perp}$,$K_{e\wedge}$,$K_{i\perp}$,$K_{i\wedge}$) than our equations (3.32) - (3.35); for example,

$$K_{e\perp}+iK_{e\wedge}=\frac{K_{eo}}{g/g(o)-i(\Omega_e\tau'_{ei})h/h(\infty)} \qquad (3.47)$$

where the g and h factors are slowly varying functions of $\Omega_e\tau'_{ei}$ which they tabulate for a hydrogen plasma. Our simplified equations preserve the main features of the more accurate form (3.47); for example the dominant terms agree in both the high and low $\Omega_e\tau'_{ei}$ limits.

The equipartition time τ_{eq} is taken from Spitzer[8], the inverse bremsstrahlung length K_{IB}^{-1} from Johnston and Dawson[63], and the formula for Λ from Rosenbluth et al.[64] However in practice, for convenience, $\ln\Lambda$ is always taken to be 10.

The main set of equations (3.1-3.16) may be manipulated to give an equation for T_e (which will be integrated separately from the other variables):

$$\frac{n_e k}{\gamma-1}\frac{\partial T_e}{\partial t} - \frac{n_e k T_e}{(\gamma-1)\rho}\nabla.\rho\underline{V} + P_e\nabla.\underline{V}_e + \nabla.\left[\frac{P_e\underline{V}_e}{\gamma-1} + \underline{Q}_e\right]$$

$$= \eta\underline{J}^2 - \frac{n_e k(T_e-T_i)}{\tau_{eq}} - P_{rad} + P_{las} \tag{3.48}$$

and four integral relations:

$$\frac{\partial}{\partial t}\int_V \rho d\tau + \int_S \rho\underline{V}.d\underline{s} = 0 \tag{3.49}$$

$$\frac{\partial}{\partial t}\int_V \rho V_r d\tau + \int_V \left[\frac{\partial P}{\partial r} + \frac{B}{\mu_o r}\frac{\partial}{\partial r} rB\right] d\tau + \int_S \rho V_r \underline{V}.d\underline{s} = 0 \tag{3.50}$$

$$\frac{\partial}{\partial t}\int_V \rho V_z d\tau + \int_S \left[\rho V_z\underline{V} + (P_e+P_i+\frac{B^2}{2\mu_o})\hat{\underline{z}}\right].\underline{ds} = 0 \tag{3.51}$$

$$\frac{\partial}{\partial t}\int_V \left[\frac{P_e}{\gamma-1} + \frac{P_i}{\gamma-1} + \frac{1}{2}\rho V^2 + \frac{1}{2\mu_o}B^2\right] d\tau$$

$$+ \int_S \left[\frac{\gamma}{\gamma-1}(P_i\underline{V} + P_e\underline{V}_e) + \underline{Q}_i + \underline{Q}_e + \frac{1}{2}\rho V^2\underline{V} + \frac{1}{\mu_o}\underline{E}\times\underline{B}\right].\underline{ds}$$

$$= \int_v P_{las}\, d\tau - \int_v P_{rad}\, d\tau, \tag{3.52}$$

(3.49), (3.51) and (3.52) represent the conservation of mass, axial momentum and total energy. Because the displacement current is neglected the electromagnetic momentum does not appear in (3.51), and nor does the electric field energy in (3.52).

The derivation of the energy equation involves the intermediate results

$$\frac{\partial}{\partial t}\ \frac{B^2}{2\mu_o} + \nabla.\ \frac{\underline{E}\underline{x}\underline{B}}{\mu_o} = -\ \underline{J}.\underline{E}$$

$$= -\ \underline{J}.\left[\eta\underline{J}-\underline{V}_e\underline{x}\underline{B}\ -\nabla P_e/n_e e\right]$$

$$= -\eta\underline{J}^2-\underline{V}.\underline{J}\underline{x}\underline{B}\ -\ (\underline{V}_e-\underline{V})\,.\nabla P_e, \qquad (3.53)$$

The third term on the right hand side represents the transfer of energy to the magnetic field through the source term; the first term is Ohmic heating and the second term is the rate of transfer of magnetic field energy into kinetic energy.

The energy equation will not hold exactly when expressed in difference form; the origin of the errors so incurred is intimately connected with the derivation of (3.52) and will be discussed in detail in Section 5.2.11.

We also give (3.2) and (3.5) in component form:

$$\frac{\partial}{\partial t}(\rho V_r)+ \frac{1}{r}\ \frac{\partial}{\partial r}(r\rho V_r V_r)+\frac{\partial}{\partial z}(\rho V_r V_z)+ \frac{\partial}{\partial r}(P_e+P_i)=-\ \frac{B}{\mu_o r}\ \frac{\partial}{\partial r}(rB) \qquad (3.54)$$

$$\frac{\partial}{\partial t}(\rho V_z)+ \frac{1}{r}\ \frac{\partial}{\partial r}(r\rho V_z V_r)+ \frac{\partial}{\partial z}(\rho V_z V_z)+\frac{\partial}{\partial z}(P_e+P_i)= -\ \frac{1}{\mu_o}\ \frac{\partial}{\partial z}(\tfrac{1}{2}B^2) \qquad (3.55)$$

$$\frac{\partial B}{\partial t} + \frac{\partial}{\partial r}(BV_{er}) + \frac{\partial}{\partial z}(BV_{ez})= \frac{k}{en_e}\left[\frac{\partial T_e}{\partial z}\ \frac{\partial n_e}{\partial r} - \frac{\partial T_e}{\partial r}\ \frac{\partial n_e}{\partial z}\right]$$

$$+ \frac{\partial}{\partial r}\left[\frac{\eta}{\mu_o}\ \ \frac{1}{r}\ \frac{\partial}{\partial r}(rB)\right]+ \frac{\partial}{\partial z}\left[\frac{\eta}{\mu_o}\ \ \frac{\partial B}{\partial z}\right]. \qquad (3.56)$$

CHAPTER 4

DISCUSSION OF THE FLUID MODEL

We proceed to a discussion of the physics implied by, and omitted from, the fluid model specified in the previous chapter. The validity of this model and the relative importance of the various processes described therein are two important considerations, and are addressed in Section 4.1 by means of a comprehensive survey of the pertinent characteristic parameters.

In Section 4.2 we consider in greater detail the theory of magnetic field generation; this involves extra source terms, in addition to the pressure gradient source of (3.56). The rôle of self-generated magnetic fields is summarized in Section 4.3; in Section 4.4 we examine the concept of the "free-streaming limit", and in Section 4.5 we discuss the atomic physics omitted.

4.1 CHARACTERISTIC PARAMETERS

From the fundamental point of view the physics of laser-plasma interactions is determined by Maxwell's Equations and the Lorentz Force (and the rate equations for atomic processes which we are neglecting in this work); indeed these equations form the basis of particle simulations of the absorption processes. However in certain circumstances conditions are such that we may profitably use fluid equations for averaged quantities such as density and

temperature. The fluid may also be a plasma and satisfy plasma transport equations. It is important to ascertain in what respects our model is well-justified, and in what regimes it is invalid or only marginally valid.

In order to examine the applicability of our equations and the relative importance of the various terms therein, we shall make use of the order of magnitude formulae given in Appendix A for characteristic timescales, velocities, lengthscales and other parameters. Some of these formulae, those for Larmor frequencies for example, are exact while others, in particular those involving collision times, are not: the definitions of τ_{ei} used by various authors (e.g. Spitzer [8] and Shkarofsky et al.[62]) differ, although these two sources agree on the value for the magnetic field-free thermal conductivity to three figures. All these formulae are defined in Appendix A, and most of them use conventional symbols and definitions.

We shall illustrate our discussion by means of Tables 4.2 - 4.5 which give these characteristic parameters for the representative quantities selected in Table 4.1. They apply to a deuterium plasma (A=2, Z=1), at the critical density ($n_e=10^{21}$/cc) for Nd laser light (λ_{las} = 1.06μm) of intensity 10^{14}W/cm^2. The electron temperature (1 keV) is an order of magnitude greater than the ion temperature (100 eV), as is typical; the magnetic field is a mega-Gauss; the scale-length has been taken as 50μm,

Table 4.1 Basic plasma parameters required to obtain Tables 4.2-4.5 from Tables A.1-A.4.

Atomic number	A	=	2
Ion charge	Z	=	1
Electron number density	n_e	=	10^{21} /cc
Laser wavelength	λ_{las}	=	1.06 μm
Laser intensity	I	=	10^{14} W/cm^2
Electron temperature	T_e	=	1 keV
Ion temperature	T_i	=	100 eV
Magnetic field	B	=	1 MG
Lengthscale	L	=	50 μm
Ablation velocity	V	=	10^8 cm/sec

the diameter of a typical laser beam; and we have chosen a quite high ablation velocity of 10^8 cm/sec. (The ablation velocity will only be used to calculate the energy of ablating ions).

While all these parameters are realistic, they will probably not all apply to the same place at the same time. The intensity could be two orders of magnitude higher, the temperatures and magnetic field could all be one order of magnitude higher, and L could be much smaller - perhaps as low as 1μm for density variations.

4.1.1 Timescales

The timescales (Table 4.2), all given in picoseconds, should be considered in relation to laser pulses of width as low as 50 psec, simulation times of the order

Table 4.2 Characteristic timescales (psec.)

Electron plasma time	$\omega_p^{-1} = 5.61 \times 10^{-4}$
Ion plasma time	$\omega_{pi}^{-1} = 3.38 \times 10^{-2}$
Electron - ion collision time	$\tau_{ei} = 1.09$
Ion - ion collision time	$\tau_{ii} = 2.08$
Equipartition time	$\tau_{eq} = 1.98 \times 10^{3}$
Electron Larmor time	$\Omega_e^{-1} = 5.69 \times 10^{-2}$
Ion Larmor time	$\Omega_i^{-1} = 2.07 \times 10^{2}$
Thermal diffusion time	$\tau_k = 2.56$
Resistive diffusion time	$\tau_\eta = 1.90 \times 10^{5}$
Viscous diffusion time	$\tau_v = 1.83 \times 10^{5}$
Ion thermal diffusion time	$\tau_{ki} = 6.70 \times 10^{4}$
Brem.radiation loss time	$\tau_{rad} = 4.95 \times 10^{5}$
Light travel time	$\tau_l = 1.67 \times 10^{-1}$
Laser oscillation time	$\omega_{las}^{-1} = 5.63 \times 10^{-4}$

of 100 psec, and simulation timesteps of around 1psec. The shortest timescales are the electron and ion plasma times ω_p^{-1} (5.61×10^{-4} psec) and ω_{pi}^{-1} (3.38×10^{-2} psec) which are well below the picosecond timescales on which fluid variables

will vary; as was noted in Section 2.1.1 particle simulations following a few hundred electron plasma periods will terminate after about 1psec.

The basic requirements for the validity of a fluid model are that the lengthscales and timescales of variation of fluid quantities should be greater than the species mean free paths and collision times respectively; small collision times are also required for the species to be described as approximately Maxwellian. In view of the collision times given (τ_{ei} = 1.09 psec, τ_{ii} = 2.08 psec) these requirements are only marginally satisfied.

In view of the formula (3.22)

$$\tau_{ei} \sim m_e^{1/2} T_e^{3/2} / z^2 n_i, \qquad (4.1)$$

it is clear that at higher temperatures or lower densities τ_{ei} may become very large. In such circumstances the possible existence of a non-Maxwellian electron distribution function imposes limitations, not just upon the validity of our model but also on the feasibility of laser fusion itself. The introduction of a small proportion of high Z ions is a possible remedy.

The situation with regard to the ions is less severe, because of the large equipartition time τ_{eq} (1.98×10^3 psec) at the critical density. The ions are significantly heated only at higher densities, where τ_{ii} will be less than the 2.08 psec given in Table 4.2.

The electron and ion Larmor times (5.69×10^{-2} and 207 psec), separated by the electron-ion mass ratio, are widely different. The electrons, whose gyrations occur more rapidly than collisions, are magnetized and large $\Omega\tau$ effects are expected to be important. However there are certain regions, particularly near the axis where B is zero and in the higher density regions where τ_{ei} is smaller, where this will not be so. The ions are effectively unmagnetized and may be thought of as moving in straight lines between collisions. (Strictly, collisions in a plasma are not instantaneous although it is often useful to think of them as being so).

We note that $\omega_p >> \Omega_e$, so that much larger magnetic fields (or lower densities) would be required for the realization of the theoretically interesting regime where $\omega_p < \Omega_e$.

Of the four diffusion processes only electron thermal diffusion, described alternatively as electron thermal conduction, is important. Gradients in T_e, but not in T_i, $\underline{V}$ or B, may be expected to be smoothed out. From Table A.1,

$$\tau_k \sim \frac{z^2 n_i L^2}{T_e^{5/2}} \qquad (4.2)$$

and

$$\tau_\eta \sim T_e^{3/2} L^2/Z; \qquad (4.3)$$

therefore at larger T_e this situation is accentuated - thermal conduction becomes still stronger, and magnetic field diffusion becomes even weaker. At lower T_e and larger densities this situation could reverse, when we would find the magnetic fields but not the electron temperature diffusing towards the solid.

To consider under what circumstances viscosity and ion thermal diffusion become important, we have (also from Table A.1)

$$\tau_v, \tau_{ki} \sim \frac{A^{\frac{1}{2}} Z^4 n_i L^2}{T_i^{5/2}} . \qquad (4.4)$$

To reduce τ_v from 1.83×10^5 psec by a factor of 10^4 we would have to decrease n_i to 10^{17} cm^{-3}, decrease L to 0.5μm, increase T_i to about 4 keV or perform some combined variation. We omitted viscosity from the equations, and consider that this will not be a source of serious errors, particularly as the low equipartition rate at low densities precludes high ion temperatures there.

The bremsstrahlung radiation time, defined in Table A.1 as

$$\tau_{rad} = \frac{3}{2} n_e k T_e / P_{rad} \qquad (4.5)$$

$$\sim \frac{T_e^{\frac{1}{2}}}{Z^2 n_i} , \qquad (4.6)$$

is so large (4.95×10^5 psec) that omitting it from our model would make very little difference. Even at

$n_i = 10^{23}$ cm^{-3} and T_e = 10 eV, supposing such a situation possible, τ_{rad} would still be several hundred picoseconds.

The light travel time τ_l is, as we might anticipate, too small to concern us. It is of course relevant to two dimensional electromagnetic particle simulations.

4.1.2 Velocities

There are fewer characteristic velocities - see Table 4.3. The electrons are non-relativistic: at 1 keV the thermal velocity is 2.3 x 10^9 cm/sec, and even at 100 keV most electrons have kinetic energies below their rest energy. Characteristic plasma expansions occur at about the sound speed C_s (2.2 x 10^7cm/sec), or perhaps a few times C_s, which is somewhat higher than the ion thermal speed $V_{th,i}$ (1.2 x 10^7 cm/sec). Because C_s depends weakly on T_e and the charge to mass ratio, ablation velocities generally lie in the range 10^7 - 10^8 cm/sec.

Table 4.3 Characteristic velocities (cm/sec.)

Electron	thermal velocity	$V_{th,e} = 2.30 \times 10^9$
Ion	thermal velocity	$V_{th,i} = 1.20 \times 10^7$
Sound	speed	$C_s = 2.20 \times 10^7$
Alfvén	speed	$V_A = 4.89 \times 10^6$
Current	velocity	$V_{rel} = 9.93 \times 10^5$
Quiver	velocity	$V_o = 2.72 \times 10^8$

The Alfvén speed V_A is generally lower, corresponding to a low ratio of magnetic to plasma field energy, or to $\underline{J} \times \underline{B}$ forces being dominated by pressure gradient forces. But locally, particularly in some low density regions, we may find $V_A > C_s$, in which case the acceleration of plasma will be enhanced by $\underline{J} \times \underline{B}$ forces.

We have written the electron energy equation (3.4) in terms of the electron centre of mass velocity $\underline{V}_e$, and an electron heat flux $\underline{Q}_e$ (3.17-3.18) dependent only on the temperature gradient and not on the current. Sometimes the fluid velocity $\underline{V}$ is used instead of $\underline{V}_e$, when $\underline{Q}_e$ includes terms in both ∇T_e and $\underline{J}$. Both approaches allow for convection of heat with the electron velocity $\underline{V}_e$ and thermal diffusion due to temperature gradients, but they are not equivalent. Our transport equations for the heat fluxes (3.17-3.20) and the electric field (3.14) are simplified versions of the equations given in Shkarofsky et al.[62] and Braginskii[70].

In general the distinction between $\underline{V}$ and $\underline{V}_e$ is not important because the relative velocity $\underline{V}_{rel}$ (9.93×10^5 cm/sec) is small, and the use of $\underline{V}$ instead of $\underline{V}_e$ in (3.4) and (3.14) would make little difference. However if large spatial variations of magnetic field are allowed, as may arise at a discontinuity in density gradient (and therefore in the magnetic field source term), we may find a thin "skin" current path where $\underline{V}_e$ is at least as large as $\underline{V}$.

The interaction between the plasma and the incident laser is characterized by the relative magnitudes of the quiver velocity V_o and the thermal velocity $V_{th,e}$. More often this is expressed by the closely related dimensionless parameter η^2, given by

$$\eta^2 = \frac{\varepsilon_o E_o^2}{n_e k T_e} \tag{4.7}$$

evaluated at $n_e = n_c$. From the definitions

$$E_o = \sqrt{2c\mu_o I} \tag{4.8}$$

and

$$V_o = eE_o/m_e\omega_{las} \tag{4.9}$$

we have

$$\eta^2 = 3(V_o/V_{th,e})^2, \tag{4.10}$$

$$= 4.16 \times 10^{-2}$$

for our parameters. η may also be considered to give an indication of the laser-induced anisotropy of the electron distribution function.[17]

We have written out these simple formulae to emphasize that our definitions of V_o and E_o are independent of number density. Very near the critical density the peak electric field becomes greater than E_o, the oscillating electron velocity exceeds V_o and the peak magnetic field becomes less than B_o ($\equiv E_o/c$). This "swelling" phenomenon

increases the local electromagnetic energy density and lowers the thresholds for various instabilities. Ginzburg [66] gives the swelling factor S ($= E^2/E_o^2$) as

$$S \sim 3.6 \left(2\pi \frac{L}{\lambda_{las}}\right)^{1/3} \qquad (4.11)$$

for a density distribution rising linearly to the critical density over a length L. Anticipating Table 4.5, S for our parameters is quite large (= 24). S decreases slowly with L; thus for $L \sim \lambda_{las}$, $S \sim 6.6$.

In our case $V_o \simeq 0.1\ V_{th,e}$, and η^2 is small, although it would be larger near the critical density had its definition included the swelling factor. If I increases to 10^{16} W/cm^2 we have $V_o \simeq V_{th,e}$, and at 10^{18} W/cm^2, which has not yet been experimentally attained, V_o is relativistic. In the relativistic regime ($I \geq 10^{18}$ W/cm^2) the laser beam may propagate into the overdense plasma because the maximum current at the critical density ($n_e$ec) is insufficient to shield the plasma from the wave. [67]

Plasma instabilities will occur at values of η less than unity and we must expect them to be present at the intensities of our simulations. Recognizing that the actual absorption mechanisms are not yet well understood, our scheme of dumping unabsorbed energy at the critical density is not unreasonable; nor indeed is it original.

4.1.3 Lengthscales

The characterization of a plasma requires that

$$b_o << n_e^{-1/3} << \lambda_D << \lambda_e . \qquad (4.12)$$

Because (as is well known) these lengths are in the ratios

$$\frac{z}{12\pi}\alpha^{-2/3} : 1 : \alpha^{1/3} : \frac{6\pi\sqrt{6\pi}}{z\ln\Lambda}\alpha^{4/3} \qquad (4.13)$$

where

$$\alpha = n_e\lambda_D^3 , \qquad (4.14)$$

all these inequalities are satisfied when α is large, or equivalently when n_D and Λ (defined in Table A.4) are large. That this is the case in our example is seen in Table 4.4; α is 410. Because α, n_D and Λ depend on $T_e^{3/2}\, n_e^{-1/2}$, the inequalities (4.12) may not be satisfied in the cooler, denser regions.

Only the electron mean free path λ_e (=25μm) is not a microscopic quantity with respect to our plasma scale-lengths of around 50μm. The requirement that fluid variables change over lengthscales greater than λ_e is at best marginally satisfied. From the formula

$$\lambda_e \sim T_e^2/z^2 n_i \qquad (4.15)$$

it is clear that at lower densities or higher temperatures λ_e may be comparable with or greater than the target dimensions. For this reason isothermal atmospheres are expected.

The same problem does not arise with the ions

(λ_i= 0.25μm) because T_i is lower. If T_i were equal to T_e we would have, from Table A.3,

$$\lambda_i = \lambda_e/z^2, \qquad (4.16)$$

because the mean free path is independent of mass, but this is unlikely to occur on account of slow equipartition at

Table 4.4 Characteristic lengthscales (μm)

Impact parameter	b_o	=	4.80×10^{-7}
Inter-particle distance	$n_e^{-1/3}$	=	1.00×10^{-3}
Debye length	λ_D	=	7.43×10^{-3}
Electron mean free path	λ_e	=	2.50×10^{1}
Ion mean free path	λ_i	=	2.50×10^{-1}
Electron Larmor radius	a_e	=	1.31
Ion Larmor radius	a_i	=	2.49×10^{1}
Collisionless skin depth	δ_s	=	1.68×10^{-1}
Inverse brem. length*	K_{IB}^{-1}	=	3.24×10^{2}
Electron excursion	x_o	=	1.53×10^{-3}

*without square root factor.

low densities. The mean free path for a fast ion, however, is given by the same formula

$$\lambda_i \sim T_i^2/z^4 n_i, \qquad (4.17)$$

but with the ion temperature (in eV) replaced by the energy of the fast ion (in eV). So an ion of energy 10keV would have a mean free path of 2500μm at $n_e = 10^{21}$/cc. This would

be reduced by a factor of 64 to 39μm for a z=4 plasma, indicating the strong dependence on z. These figures are pertinent to the fast ion peaks obtained in experimental arrival time traces: separation of the charge species into peaks (with energy proportional to charge number), such as shown in Fig.2-5, depends on the accelerated ions having long mean free paths. Otherwise the species will ablate together with a single centre of mass velocity.

The electron Larmor radius a_e(1.31μm) is significant because it permits the localization of hot electrons into small regions and allows a substantial reduction in the electron thermal conductivity. Moreover, it will remain small at larger temperatures because

$$a_e \sim T_e^{\frac{1}{2}}/B; \qquad (4.18)$$

the dependence on T_e is weak and is at least partially cancelled by the larger magnetic fields generated at higher temperatures. The ions, as already noted, are effectively unmagnetized (a_i= 24.9μm).

Let us now take an alternative view of the four diffusion processes. The diffusion times for the smoothing-out of variations occurring on the scale-length L may all be written (from Appendix A) in the characteristic "random walk" form:

$$\tau_k = \left(\frac{9}{10}\,0.654\right)\left(\frac{L}{\lambda_e}\right)^2 \tau_{ei} \qquad (4.19)$$

$$\tau_{ki} = \left(\frac{9}{10}\,0.896\right)\left(\frac{L}{\lambda_i}\right)^2 \tau_{ii} \qquad (4.20)$$

$$\tau_v = (3 \times 0.7326)\left(\frac{L}{\lambda_i}\right)^2 \tau_{ii} \qquad (4.21)$$

$$\tau_\eta = \left(\frac{1}{0.5064}\right)\left(\frac{L}{\delta_s}\right)^2 \tau_{ei} \,. \qquad (4.22)$$

For resistive diffusion it is the collisionless skin depth δ_s rather than a mean free path which corresponds to one random step of duration τ_{ei}. τ_k is the most important of these timescales because λ_e is very large. However the formula for τ_k is based on the magnetic field-free conductivity (3.30); in the presence of strong magnetic fields τ_k is increased roughly by a factor $(\Omega_e\tau_{ei})^2$, which we usually refer to simply as $(\Omega\tau)^2$, corresponding to the replacement of λ_e by a_e in (4.19). Apart from drifts, an electron can move only one Larmor radius per collision.

This must represent an upper limit to τ_k, as we have neglected here possibly important electron drifts in the inhomogeneous magnetic fields and the Righi-Leduc heat flow perpendicular to the temperature gradient.

To conclude this subsection, the collisionless skin depth, evaluated at the critical density, will be recognized as the laser wavelength divided by 2π; the inverse bremsstrahlung length K_{IB}^{-1} (3.43) is large (= 324μm) and will be discussed in detail in Chapter 8; and the electron excursion x_o in the wave field, defined in Table

A.3, is very small (1.53×10^{-3} μm) reflecting the microscopic nature of the absorption processes.

4.1.4 Miscellaneous parameters

Table 4.5 Miscellaneous Parameters

Electron Hall parameter	$(\Omega\tau)_e = 19.1$
Ion Hall parameter	$(\Omega\tau)_i = 0.01$
Lambda	$\Lambda = 1.55 \times 10^4$
Coulomb logarithm	$\ln\Lambda = 9.65$
No.of electrons in Debye sphere	$n_D = 1.72 \times 10^3$
Peak em electric field	$E_o = 2.74 \times 10^8$ V/cm
Peak radiation/thermal pressure	$\eta^2 = 4.16 \times 10^{-2}$
Plasma beta	$\beta = 66.4$
Classical heat flux	$Q_c = 4.69 \times 10^{14}$ W/cm^2
Free-streaming heat flux	$Q_{fs} = 5.52 \times 10^{14}$ W/cm^2
Free-streaming transition temperature	$T_{fs} = 1.09$ keV
Faraday rotation*	$\Delta\phi = 1.48$ rad
Quiver energy	$\varepsilon_q = 21$ eV
Peak em magnetic field	$B_o = 9.16 \times 10^5$ Gauss
Fermi energy	$\varepsilon_F = 3.65 \times 10^{-1}$ eV
Fermi pressure	$P_F = 2.26 \times 10^3$ atm
Electron pressure	$P_e = 1.55 \times 10^7$ atm
Photon energy	$\varepsilon_\nu = 1.17$ eV
Critical number density	$n_c = 9.92 \times 10^{20}$ cm^{-3}
Energy of ablating ion	$\varepsilon_v = 10.4$ keV
Swelling factor	$S = 24$

*without square root factor

Referring to Table 4.5, the fact that $(\Omega\tau)_e > 1$ whereas $(\Omega\tau)_i < 1$ is in accordance with our earlier comments, and the significance of Λ, n_D, E_o, η^2 and S has already been discussed. It is reassuring to find that $\ln\Lambda = 9.65$ because we take it throughout to be 10.

The plasma β (=66.4) is sufficiently large to ensure that $\underline{J}\times\underline{B}$ forces are relatively unimportant, which is consistent with the magnetic field energy being derived from electron thermal energy through the $\underline{J}.\nabla P_e$ term. However the appearance of regions with $\beta < 1$ locally is not precluded.

It is interesting that in our regime the classical and "free-streaming" heat fluxes (Q_c, Q_{fs}) are comparable, both slightly greater than the incident laser flux. The classical flux Q_c is a rapidly increasing function of $T_e (\alpha\ T_e^{3.5})$ and at the "transition temperature" T_{fs}(1.09keV), Q_c and Q_{fs} are equal. We note (from Table A.4) the form of T_{fs}:

$$T_{fs} \sim \sqrt{zLn_e}\ , \qquad (4.23)$$

so that at $n_e = 10^{19}$/cc (for a CO_2 laser) the situation is more severe. The ratio of the two heat fluxes is of course related to the electron mean free path:

$$\frac{Q_c}{Q_{fs}} = \frac{10}{9(0.654)} \frac{\lambda_e}{L}\ . \qquad (4.24)$$

We shall discuss the "free-streaming" concept further in Section 4.4.

The Faraday rotation angle $\Delta\phi$ is obtained from

$$\Delta\phi = L\ \Delta k \tag{4.25}$$

where Δk is twice the difference between the wave numbers of left and right circularly polarized waves, giving

$$\Delta\phi = \frac{\Omega_e L}{2c}\ \frac{\omega_p^2/\omega_{las}^2}{\sqrt{1-\omega_p^2/\omega_{las}^2}} \tag{4.26}$$

where ω_{las} is now the angular frequency of the probe beam. For our conditions, neglecting the square-root factor, $\Delta\phi$ is 1.48 rad. This is larger than was obtained by Stamper and Ripin[26], partly because ω_{las} must be expected to exceed ω_p.

The quiver energy ε_q (21 eV) is low compared to thermal energies of 1 keV, and is related to the low η^2. However, as

$$\varepsilon_q \sim \lambda_{las}^2\ I, \tag{4.27}$$

at $I=10^{16}$ W/cm^2 or λ_{las}= 10.6μm we obtain significantly larger quiver energies (about 2keV).

The energy of an ablating ion ε_v (10.4 keV) is generally a little higher than zkT_e. The formula for ε_v is the only one involving the ablation velocity of Table 4.1, which we chose possibly a little high at 10^8 cm/sec.

While the electron motion in the wave field is predominantly along the electric vector, a full treatment of the absorption process, particularly at higher intensities, must include the motion due to the oscillating magnetic field B_o (0.92 MG here for I = 10^{14} W/cm^2). The self-generated magnetic fields are of comparable order and

therefore may influence the absorption process. (See Section 4.2.2).

The electrons at the critical density are certainly not Fermi-degenerate, as the Fermi energy ε_F is less than an eV and the Fermi pressure P_F is much less than the plasma pressure P_e (= 1.55 x 10^7 atm). For comparison, Nuckolls et al.[1] give the minimum (i.e. Fermi) pressure of liquid deuterium compressed by a factor of 10^4 as 10^{12} atm.

The two remaining parameters, ε_ν and n_c, do not require comment.

4.2 THE ORIGIN OF MAGNETIC FIELDS

4.2.1 The thermal source

Because of the importance of magnetic fields to our work we shall examine their origin in greater detail. The time derivative of the electric field $\underline{E}$ (i.e. the displacement current term) has been omitted from Ampère's Law (3.12), as is standard in magnetohydrodynamic (MHD) theory, and $\underline{E}$ is determined instead from the Generalized Ohm's Law (3.14). This is in contrast to the usual transport theory in which this latter equation determines the current $\underline{J}$ of a plasma subject to imposed electric and magnetic fields $\underline{E}$ and $\underline{B}$.

The Ohm's Law merely expresses the fact that, because the electron inertial timescales are very short

compared with fluid timescales, electric fields must be set up to ensure a quasi-equilibrium of the electron fluid. On substituting (3.13) and (3.36) into (3.14) we obtain the simplified electron equation of motion

$$0 = - n_e e(\underline{E} + \underline{V}_e \times \underline{B}) - \nabla(n_e k T_e) - \frac{n_e m_e (\underline{V}_e - \underline{V})}{\tau_{ei}/0.5064} \qquad (4.28)$$

with the inertial term omitted. The frictional term proportional to $(\underline{V}_e - \underline{V})$ is an approximation to the true rate of momentum transfer to the ions. In the absence of magnetic fields $\underline{V}_e = \underline{V}$, so that (4.28) becomes

$$0 = - n_e e\underline{E} - \nabla(n_e k T_e). \qquad (4.29)$$

If n_e is uniform, $\underline{E}$ can be written as $-\nabla\Phi$ where the electrostatic potential $\Phi = kT_e/e$, the plasma temperature expressed in electron-volts. However if n_e varies spatially, it may no longer be possible to express $\underline{E}$ as a gradient, and a magnetic field is generated. In full,

$$\frac{\partial \underline{B}}{\partial t} = - \nabla \times \left[\eta \underline{J} - \underline{V}_e \times \underline{B} - \frac{1}{n_e e} \nabla(n_e k T_e)\right]$$

$$= -\mu_o^{-1} \nabla \times (\eta \nabla \times \underline{B}) + \nabla \times (\underline{V}_e \times \underline{B}) + \nabla(kT_e/e) \times \nabla(\ln n_e) \qquad (4.30)$$

The first two terms on the right hand side of (4.30) represent the well-known diffusion and convection of the magnetic field, while the third term (the source term) does not generally appear in MHD theory because the pressure gradient term of (3.14) is omitted. In our cylindrically-symmetric

configuration only the azimuthal component of (4.30) is non-trivial, giving (3.56) which may be alternatively written as

$$\frac{\partial B}{\partial t} = - \frac{\partial}{\partial r}(kT_e/e) \frac{\partial}{\partial z} (\ln n_e) + \text{other terms;} \qquad (4.31)$$

we have retained explicitly on the right hand side only the dominant source term for the usual situation where the number density is primarily a function of z. In the configuration of Fig.2-1 both $\partial T_e/\partial r$ and $\partial n_e/\partial z$ are negative, and therefore the magnetic field is generated in the negative θ direction; its initial growth rate is a maximum near the radius of maximum spatial variation of the laser beam, but the situation becomes more complicated later when thermal conduction has developed. For example, if a hot spot of T_e forms off-axis, the region of positive $\partial T_e/\partial r$ may give rise to a reversed magnetic field. It should be noted that because the density profile changes on slower hydrodynamic timescales the magnetic field is to lowest order a response to $\partial T_e/\partial r$.

There appear to be four possible limiting mechanisms on the growth of magnetic fields: smoothing out of the density gradient and convection away from the heating region, both occurring on hydrodynamic timescales, smoothing out of $\partial T_e/\partial r$ on thermal diffusion timescales (which are strongly dependent on the electron Hall parameter), and resistivity which is generally ineffective (see Section 4.1.1).

An estimate for the magnitude of the magnetic field generated is easily obtained from (4.31); neglecting diffusion and advection,

$$B \simeq 10 \frac{T_e(\text{keV})\ t\ (\text{psec})}{L_r(\mu\text{m})\ L_z(\mu\text{m})} \text{ mega-Gauss,} \qquad (4.32)$$

where L_r and L_z are the radial and axial lengthscales of T_e and n_e respectively. For example, taking T_e= 1keV, L_r= 50μm and L_z = 20μm, B becomes 1 MG after 100 psec. However this is also the timescale on which advection at the sound speed of 2×10^7 cm/sec is expected to smooth out the density scale-length L_z, so we expect B to saturate at around this level.

A similar result may be obtained for convective limitation using an order of magnitude argument. If we assume the balance:

$$\underline{V} \times \underline{B} \sim \nabla (n_e k T_e) / n_e e \qquad (4.33)$$

and suppose that $\underline{V}$ is predominantly in the z-direction with magnitude C_s, the radial component of (4.33) gives the maximum magnetic field B_{max}:

$$B_{max} \simeq \frac{\sqrt{AT_e/z}}{L_r} \text{ MG} \qquad (4.34)$$

where T_e is in eV and L_r in μm. With T_e = 1keV, A=2, z=1 and L_r = 50μm we find $B_{max} \simeq 0.9$MG. Not without reason are self-generated magnetic fields often referred to as mega-Gauss magnetic fields. (4.34) is more restrictive than

(4.32) because L_z is absent; the requirements on T_e and the beam lengthscale L_r if a field of 10 MG is to be attained are severe.

It would be wrong to attach too much weight to this argument, in which we unjustifiably ignored the axial component of (4.33). In practice the situation is more complicated and larger magnetic fields do result from smaller values of L_z - see Section 8.3.3. However, fields exceeding 10 MG are rarely obtained.

4.2.2 Other sources

Our model is simplified in that we use only the thermal source ($\nabla T_e \times \nabla n_e$) of magnetic field. Further source terms arise from a more complete electron equation of motion, averaged over the timescale of the laser oscillation (Stamper[17], [68], Stamper and Tidman[69]):

$$0 = -n_e e(\underline{E}+\underline{V}_e \times \underline{B}) - \nabla P_e - \nabla . \underline{\underline{\Pi}}_e - \nabla . \underline{\underline{P}}^r_e + \nabla . \underline{\underline{P}}^r + \eta \underline{J} + \underline{\underline{\alpha}} . \nabla T_e . \qquad (4.35)$$

Four extra terms have been introduced in (4.35). They involve

(a) $\underline{\underline{\Pi}}_e$, the anisotropic part of the electron fluid pressure tensor. On fluid timescales longer than the electron collision time, $\nabla . \underline{\underline{\Pi}}_e$ is expected to be small in comparison with ∇P_e (for B=0). When the collision time is long and the electron distribution is strongly anisotropic we may expect this term to be important;

in the presence of magnetic fields the situation is more complicated.[70]

(b) $\underline{\underline{\alpha}}.\nabla T_e$, the thermal force. Braginskii[70] gives (for B=0)

$$\underline{\underline{\alpha}}.\nabla T_e = -0.71\ n_e k \nabla T_e \qquad (4.36)$$

so that

$$\nabla \times \frac{1}{n_e e}(\underline{\underline{\alpha}}.\nabla T_e) = 0. \qquad (4.37)$$

Only the smaller magnetic field-dependent terms of the thermal force contribute. Unless one is specifically referring to these terms, it is erroneous to describe the spontaneously generated magnetic fields as "thermoelectrically generated".

(c) $\underline{\underline{P}}_e^r$, the averaged contribution of quiver motion to the electron pressure tensor. For a linearly polarized wave this has only one component[69]:

$$P_e^r = \tfrac{1}{2} n_e m_e \left(\frac{e\,\underline{\delta E}_o}{m_e \omega_{las}}\right)^2, \qquad (4.38)$$

where $\underline{\delta E}_o$ is the peak electric field of the electromagnetic wave.

(d) $\underline{\underline{P}}^r$, the radiation pressure tensor averaged over oscillation timescales. This is defined as the negative of the time-averaged Maxwell stress tensor:

$$\underline{\underline{P}}^r = -\left\langle \varepsilon_o\, \underline{\delta E}\ \underline{\delta E} + \mu_o^{-1}\, \underline{\delta B}\ \underline{\delta B} - \tfrac{1}{2}\, \underline{\underline{I}}(\varepsilon_o \underline{\delta E}.\underline{\delta E} + \mu_o^{-1} \underline{\delta B}.\underline{\delta B})\right\rangle \qquad (4.39)$$

and satisfies

$$-\nabla.\underline{\underline{P}}^{r} = \langle \delta\rho\ \underline{\delta E} + \underline{\delta J} \times \underline{\delta B} \rangle + \varepsilon_o \frac{\partial}{\partial t} \langle \underline{\delta E} \times \underline{\delta B} \rangle . \qquad (4.40)$$

$\delta\rho$, $\underline{\delta J}$, $\underline{\delta E}$ and $\underline{\delta B}$ are the oscillating charge density, current, electric field and magnetic field respectively. Applying simple ordering to (4.40) we may neglect the last term on the right hand side, with respect to $\nabla.\underline{\underline{P}}^{r}$, for pulses with timescales exceeding the light transit time over a characteristic plasma lengthscale[68]; (4.40) then allows the total time-averaged Lorentz force to be expressed as the sum of the fluid part

$$- n_e e\ (\underline{E} + \underline{V}_e \times \underline{B})$$

and the radiation pressure force $-\nabla.\underline{\underline{P}}^{r}$.

Sometimes $\underline{\underline{P}}_e^{r}$ and $\underline{\underline{P}}^{r}$ are combined into a "total radiation pressure" : from (4.38)

$$\underline{\underline{P}}_e^{r} = \frac{\omega_p^2}{\omega_{las}^2}\ \varepsilon_o \langle\ \underline{\delta E}\ \underline{\delta E}\ \rangle , \qquad (4.41)$$

so that

$$\underline{\underline{P}}_e^{r} + \underline{\underline{P}}^{r} = -\langle \varepsilon_o \varepsilon\ \underline{\delta E}\ \underline{\delta E} + \mu_o^{-1} \underline{\delta B}\ \underline{\delta B} - \tfrac{1}{2}\ \underline{\underline{I}} (\varepsilon_o \underline{\delta E}.\underline{\delta E} + \mu_o^{-1} \underline{\delta B}.\underline{\delta B}) \rangle \qquad (4.42)$$

where

$$\varepsilon = 1 - \frac{\omega_p^2}{\omega_{las}^2} . \qquad (4.43)$$

This result may be obtained by treating the plasma as a medium with a dielectric constant of ε, but such an approach is not recommended: ε should be thought of as a useful parameter but not as a constitutive relation.[68]

At this point we digress to consider the "ponderomotive force" F_{pm}, defined as [5], [68]

$$F_{pm} = \frac{-\omega_p^2}{\omega^2} \nabla < \tfrac{1}{2}\varepsilon_o E^2 > . \qquad (4.44)$$

It arises[5] from the motion of a single particle (centred on the origin) in a spatially varying electromagnetic field $\underline{E}_s(r)$ cos ωt:

$$m\ddot{\underline{r}} = -e\left[\underline{E}_s(\underline{r}) \cos \omega t - \dot{\underline{r}} \times \{\frac{1}{\omega} \nabla \times \underline{E}_s \sin \omega t\}\right] . \qquad (4.45)$$

An expansion in $\dot{r}/c$ is reasonable for the lasers currently available (see Section 4.1.2); to lowest order $\underline{r}$ is given by $\underline{r}_1$ where

$$\underline{r}_1 = \frac{e\underline{E}_s(o)}{m\omega^2} \cos \omega t; \qquad (4.46)$$

to next order

$$\underline{r} = \underline{r}_1 + \underline{r}_2 \qquad (4.47)$$

where

$$m\ddot{\underline{r}}_2 = -e\left[\underline{r}_1 . \nabla \underline{E}_s(o) \cos \omega t - \dot{\underline{r}}_1 \times \{\frac{1}{\omega} \nabla \times \underline{E}_s(o) \sin \omega t\}\right]. \qquad (4.48)$$

Using (4.46), the time-averaged part of (4.48) is

$$\langle m\ddot{\underline{r}}_2 \rangle = - \frac{e^2}{2m\omega^2} \nabla (\tfrac{1}{2} E_s^2) \qquad (4.49)$$

which when multiplied by n_e gives (4.44).

We note in passing that the oscillatory parts of the right hand side of (4.48) are at twice the laser frequency. Also, if a uniform magnetic field is imposed parallel to the magnetic vector of the (plane-polarized) incident wave, $\underline{r}_2$ gains a component oscillating at the plasma frequency and in the direction of propagation; for this reason resonant absorption is possible even at normal incidence in the presence of spontaneously-generated magnetic fields.[71]

The ponderomotive force (4.44) has been calculated on a simplified single-particle model. It differs from the more general total radiation pressure force

$$- \nabla . (\underline{\underline{P}}_e^r + \underline{\underline{P}}^r)$$

which is preferred by Stamper[68]. For example, the ponderomotive force does not contribute to magnetic field generation because $\langle m\ddot{\underline{r}}_2 \rangle$ is irrotational.

Returning to (4.42), $\underline{\underline{P}}_e^r$ and $\underline{\underline{P}}^r$ may be expected to be important for magnetic field generation when they are comparable to the thermal pressure P_e, thus requiring $\eta^2 \gtrsim O(1)$. Stamper and Tidman[69] point out that at times

when thermal conduction has smoothed out gradients of T_e a lower value of η^2 may suffice, corresponding to laser intensities of the order of 10^{14} W/cm^2 for example. The fields generated in such circumstances could, however, be lower than those generated earlier by the pressure gradient source.

At first sight it might appear from (4.38) that our azimuthal symmetry is destroyed if the incident wave is plane polarized. But the combined radiation pressure retains its symmetry for any polarization, when, as shown by Stamper[17] for a wave travelling in the z direction,

$$\underline{\underline{p}}^r_e + \underline{\underline{p}}^r = \frac{I}{2\mu c}\,\mathrm{diag}\left\{\frac{\omega_p^2}{\omega^2}, \frac{\omega_p^2}{\omega^2}, 2 - \frac{\omega_p^2}{\omega^2}\right\} \qquad (4.50)$$

where

$$\mu^2 = 1 - \frac{\omega_p^2}{\omega^2} . \qquad (4.51)$$

(4.50) breaks down at the critical density where the square of the electric field does not become infinity but increases by the swelling factor (4.11). Nevertheless the radiation pressure source of magnetic fields occurs primarily near the critical density - in the low density limit the vacuum pressure tensor is regained.

It is also apparent that the radiation pressure source of d-c magnetic fields is intimately tied up with the absorption process itself. These magnetic fields have been observed in two dimensional relativistic electromagnetic

computer simulations: their occurrence during resonant absorption is described by Thomson et al.[6], who apply an expansion technique to the Vlasov equation in which the d-c magnetic field is small compared with the oscillating magnetic field. They obtain (4.42) for the total radiation pressure, but with ε corrected by an effective collision frequency $\nu(\nu >> \tau_{ei}^{-1})$ due to resonant absorption:

$$\varepsilon = \mathrm{Re}\left\{1 - \frac{\omega_p^2}{\omega(\omega - i\nu)}\right\}. \qquad (4.52)$$

From a simulation they find a large spatially oscillating d-c magnetic field, concentrated near the critical density in a small region of spatial extent about one wavelength (λ_{las}). This field grows rapidly and within 0.1 psec saturates at 1.5 MG, due to the expulsion of energetic electrons towards the lower density region. The laser intensity was 2.2×10^{16} W/cm^2 (B_o = 13.6 MG).

The extent of the errors incurred by the omission of these processes from the fluid model is unclear. The "resonant source" is highly localized, but the fields generated may diffuse or be convected into wider regions. Possibly a turbulent field is set up. For the present, however, such questions remain unanswered.

Finally we should mention two other sources for magnetic fields, which depend on the familiar pressure gradient term. They are:-

(a) The field-generating thermal instability, the linear theory of which was considered by Tidman and Shanny[72]. A perturbation of T_e near the critical density, with wave vector at right angles to the density gradient, gives rise to a perturbation of B through the source term, which in turn increases the perturbation of T_e through the Righi-Leduc heat flux (the $K_{e\wedge}$ terms of (3.17) and (3.18)). The optimum scale-length depends on the two diffusion processes (of B and T_e). The non-linear development of this instability (i.e. for $\Omega\tau \geq 1$) is unclear; one may speculate that it saturates at a low level because $K_{e\wedge}$ reduces with $\Omega\tau$ above $\Omega\tau = 1$.

(b) Seeded mega-Gauss turbulence. As described by Tidman [73, 74], turbulent magnetic fields may arise from the use of a target containing small-scale fluctuations of a high z impurity seed; the induced electron density variations cause magnetic fields to grow until the impurity ions have mixed with the host ions. As one possible application he suggests a hybrid laser - electron beam fusion scheme, in which a relativistic electron beam fired after the laser couples with the turbulent fields.

4.3 THE ROLE OF MAGNETIC FIELDS

We summarize here the main consequences of magnetic field generation, the first five of which have already been discussed:

(a) hot spots in the electron temperature distribution may be created as a result of the reduction in thermal conductivity, causing the acceleration of fast ions and the emission of energetic x-rays;

(b) $\underline{J} \times \underline{B}$ forces may accelerate the plasma;

(c) the absorption processes may be affected;

(d) stochastic acceleration of electrons "tied" to field lines may give rise to suprathermal electrons;

(e) mega-Gauss turbulence from a seeded target may be used to couple a relativistic electron beam to the plasma;

(f) the fields may be greatly magnified during the compression process and the subsequent thermonuclear burn.[75]

4.4 THE FREE-STREAMING LIMIT

We have already remarked (in Section 4.1.4) that at sufficiently high temperatures, depending on n_e, z and L but typically above about 1keV, the Spitzer heat flux Q_c exceeds the "free-streaming limit" Q_{fs}, defined as the product of the electron energy density and thermal velocity:

$$Q_{fs} = \frac{3}{2} n_e k T_e \sqrt{3kT_e/m_e} \quad . \tag{4.53}$$

In this regime ($\lambda_e > L$ from (4.24)) the derivation of the Spitzer flux breaks down, and it is reasonable to suppose that the actual heat flux Q will be limited to Q_{fs}, or more

precisely to some multiple α of Q_{fs}. α is known as the "flux-limit parameter", and in numerical calculations a smooth transition between regimes is made by taking

$$Q = \frac{\alpha Q_{fs} \; Q_c}{\alpha Q_{fs} + Q_c} \; . \qquad (4.54)$$

For example, Ashby and Christiansen[76] using a one-dimensional compression code find degraded fusion yields for values of α of order 0.1, due to a decreased heat flux towards the compression front. Bickerton[77] considers the perturbed electron distribution function and suggests that at lower heat fluxes the ion acoustic instability may be excited, in which case α should be of the order of the square root of the electron-ion mass ratio: in effect the electron thermal energy is transported at the sound speed rather than at the electron thermal speed. Malone et al.[49] compare numerical predictions for x-ray spectra and thin film transmissivities with experimental observations and infer a value for α of around 0.01 (their f = 0.03) - see Chapter 9.

The purpose of this section is simply to point out that this model is not necessarily valid, because there is no limit in principle to the heat flux that may be carried by an electrostatically stable distribution function with a given temperature.

We consider the following one-dimensional electron distribution function, described by Morse and Nielson[7] and

illustrated in Fig.4-1:

$$f(v) = \begin{cases} n_h/V_h & 0 \leqslant v \leqslant V_h \\ n_c/V_c & -V_c \leqslant v < 0 \\ 0 & \text{otherwise.} \end{cases} \tag{4.55}$$

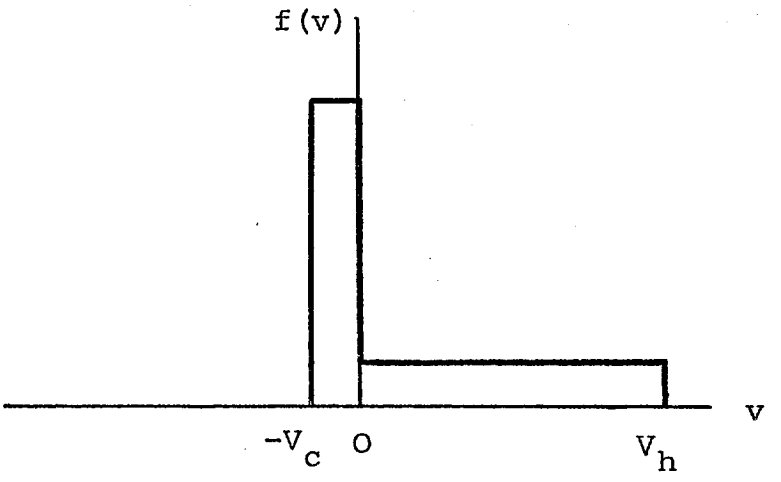

Fig.4-1 Electron distribution function.

We shall consider only current - free cases; therefore

$$n_c V_c = n_h V_h \tag{4.56}$$

and only three free parameters remain. We then have

$$N = n_h\left(1 + \frac{V_h}{V_c}\right) \tag{4.57}$$

$$E = \frac{n_h m V_h^2}{6}\left(1 + \frac{V_c}{V_h}\right) \tag{4.58}$$

$$Q = \frac{n_h m V_h^3}{8}\left(1 - \frac{V_c^2}{V_h^2}\right) \tag{4.59}$$

where N, E and Q are the total particle number, energy and heat flux, and m is the electron mass.

Morse and Nielson find that for given N and V_h, Q has a maximum (= $Nm\ V_h^3/32$) when $V_c = V_h/2$. However it is more appropriate to consider N and E as given, in which case Q may be made as large as required.

To express this in terms of the "flux limit" model, we may define the "limiting" flux Q_{lim} to be Ec, where c is the mean thermal velocity defined by

$$E = \tfrac{1}{2} Nmc^2 \qquad (4.60)$$

and therefore given by

$$c^2 = \tfrac{1}{3} V_h V_c . \qquad (4.61)$$

Then

$$\frac{Q}{Q_{lim}} = \frac{3}{4}\sqrt{\frac{3\ V_h}{V_c}}\left(1 - \frac{V_c}{V_h}\right), \qquad (4.62)$$

so that by taking V_h/V_c sufficiently large we may exceed the free streaming limit by any desired amount.

We note that f has no double hump and is therefore electrostatically stable, a feature which is unaltered by the addition of an ion Maxwellian or δ- function about the origin. Also f could be smoothed somewhat, for example by replacing the top-hats of Fig.4-1 by half-Maxwellians, without the qualitative results being altered. What distribution functions actually occur in practice is another

question; the effect of collisions on f has not been considered here.

We do not include the free-streaming limit in our work because we are interested in investigating the generally more severe flux-limitations imposed by the presence of large magnetic fields.

4.5 ATOMIC PHYSICS

We have omitted from our model the atomic physics associated with ionization, line radiation and radiative transfer because at high (keV) temperatures we expect low z elements such as deuterium to be fully ionized. This simplification is less satisfactory when the model is applied to current experiments with targets such as polystyrene (CH), polyethylene (CH_2) or aluminium, because a mixture of charge species is generally found[45], probably due to finite ionization rates.

Our simulations with carbon use an average z of 4, when the neglect of the various ionization stages will introduce errors on at least five grounds:

(i) the position of the critical density should change as ionization takes place;

(ii) as the thermal front propagates into the solid, thermal energy should be absorbed by ionization;

(iii) transport coefficients depend on the ionic charge z - for example the electron-ion collision frequency is

proportional to z^2;

(iv) some of the fluid equations will be affected - for example the magnetic field source term contains a term in $\nabla \ln(n_e)$, which unlike $\nabla \ln(n_i)$ will not remain predominantly in the axial direction during the laser pulse.

(v) we preclude the separation of the different charge species into peaks on the arrival time graphs.

While we shall not attempt to justify the omission of a variable z, we consider that most of the errors incurred will not be of major importance for the following reasons:

(i) Generally the exact position where the laser energy is absorbed is unimportant because the electron thermal conductivity is large (except at hot spots). Moreover, if the ion density profile exhibits a rapid cut-off from solid density, a factor of 4 in the density will not correspond to a large spatial distance.

(ii) For most of the runs described later in this work the thermal front makes little impact on the solid.

(iii) The variations in transport coefficients as z changes between 4 and 6, say, are less than an order of magnitude,whereas magnetic fields can affect transport coefficients by several orders of magnitude.

(iv) The magnetic field source term is proportional to

$$\nabla T_e \times \nabla \ln(n_e) = \nabla T_e \times \nabla \ln (n_i z)$$

$$= \nabla T_e \times \left[\nabla \ln (n_i) + \nabla \ln z\right]. \qquad (4.63)$$

If to lowest order z is a function of T_e, the z-dependence of the source term disappears.

(v) While the ion mean free path is small the various species will be accelerated together with a common centre of mass velocity.

These considerations should be regarded not as a justification for our model, but rather as an indication of its range of validity. For example, if we wish to predict the arrival time curves of the separate charge states we have no option but to add to our model separate equations for these species.

CHAPTER 5

THE COMPUTATIONAL MODEL

This chapter describes in detail the numerical implementation of the system of fluid equations given in Chapter 3 and discussed in Chapter 4. Section 5.1, which summarizes the overall operation of the code, contains the only material in this chapter necessary for an understanding of the code as a "black box" integrator of the fluid equations; the detailed operation of the "black box" is the subject of the extensive Section 5.2, which forms the heart of this chapter. It is intended that Section 5.2 should provide a complete description of the numerical method. Apart from what is described here, no "adjustments" are required to ensure the working of the code. In Section 5.3 we briefly note some other codes which include magnetic fields.

5.1 INTRODUCTION TO LASERB

The code LASERB originated from the code FOCUS of Potter [78], of which it retains the staggered mesh configuration and the Lax-Wendroff hydrodynamics of interior points. However, whereas FOCUS was dominated by advective processes (the run-down and pinching of a plasma focus), the laser-plasma interactions under investigation are dominated by laser heating and electron thermal conduction. Indeed, on picosecond timescales the plasma often moves very little. This has necessitated the introduction of an implicit technique for the integration of the electron energy equation separately from the hydrodynamics. (3,48) instead of (3,4) is therefore used for the integration of T_e.

5.1.1 The computational mesh

The rectangular simulation region is split into a uniform rectangular mesh as shown in Fig. 5-1, with an odd number of

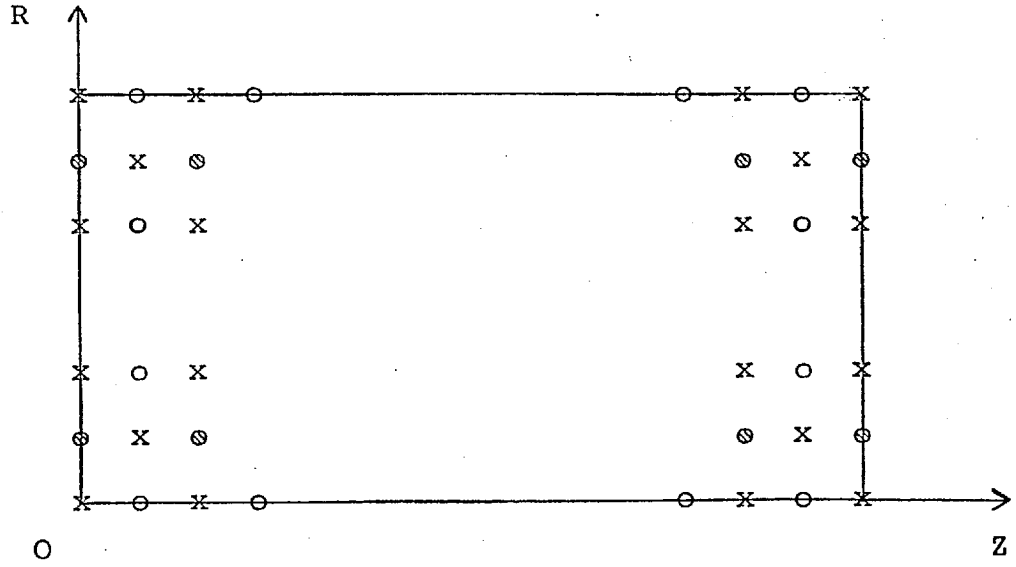

Fig. 5-1 Staggered mesh. Submeshes "1" (⊗) and "2" (O) are decoupled. X denotes auxiliary mesh used by Lax-Wendroff scheme.

points in each direction. The "overall mesh" (all points) is divided into a "main" mesh (circles) and an "auxiliary" mesh (crosses). The main mesh may be seen to comprise two meshes: submesh "1" (⊗) and submesh "2" (O) which are only weakly coupled with respect to the hydrodynamic difference scheme used. Typical mesh sizes range from 15 x 21 to 29 x 41 points in R x Z.

The mesh is Eulerian and is therefore not used to investigate compression phenomena.

Given the six major variables at time t on the main mesh, the code calculates their values on that mesh at time t + dt. The auxiliary mesh is used to hold intermediate values calculated during the Lax-Wendroff stage, which are then forgotten at the end of the step; for display purposes values on the auxiliary mesh are calculated as averages of the surrounding points on the main mesh.

The decoupling of submeshes "1" and "2" causes the major variables defined on each submesh to evolve more or less independently of each other: for example conventional differencing of the thermal diffusion terms results in the heat absorbed on submesh "1" being unable to transfer to submesh "2". To avoid this the heat diffusion equation is solved once every ten steps on the diagonal mesh of Fig. 5-2, thereby allowing the temperature distributions on the two submeshes to couple.

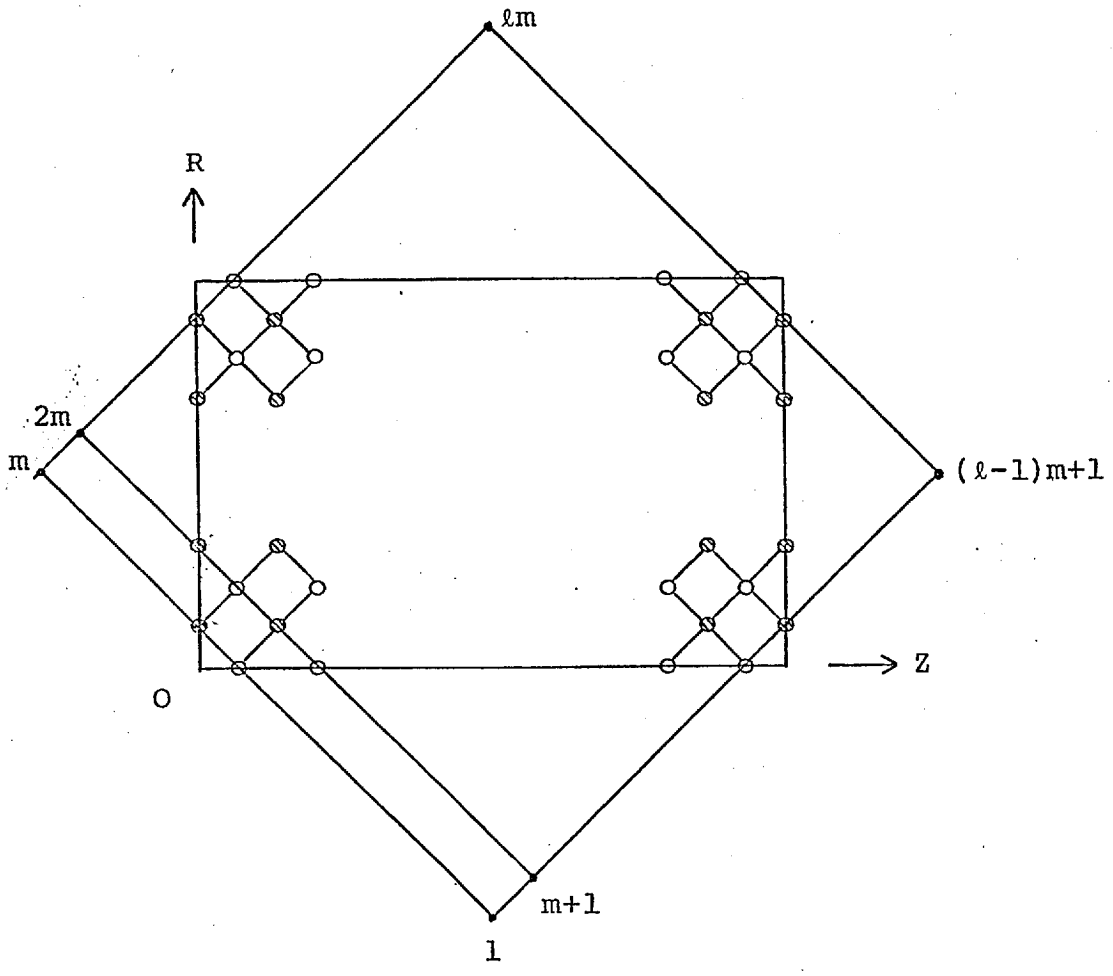

Fig. 5-2 Diagonal mesh. By differencing the diffusion equation for T_e in the diagonal directions heat may be transferred between submeshes "1" and "2".

5.1.2 Input

To run the code it is necessary to specify such physical quantities as

(a) mesh dimensions r_{max}, z_{max};

(b) ion mass and charge numbers A, z ;

(c) initial distributions of the 6 major variables on the main mesh, and in particular the density: usually $\underline{V} = B = 0$ and $T_e = T_i$ = a few eV ;

(d) boundary conditions ;

(e) the laser wavelength (λ_{las}), time history and spatial profile ;

(f) the form assumed for the energy dump at the critical density ;

and such computational variables as

(a) mesh size ($n_r \times n_z$) ;

(b) timestep control ;

(c) output control ;

(d) logical variables to omit selected terms from the equations ;

(e) variables selecting minor variants of the difference scheme.

5.1.3 Output

Graphical output may include

(a) perspective plots of the major variables, and diagnostic variables such as B^2/P or $\Omega\tau$;

(b) flow fields such as $\underline{V}$, $\underline{J}$ and $\underline{Q}$;

(c) graphs of the maximum T_e, B, $\Omega\tau$ and V_z against time, and of the ion flux at a collector against arrival time.

Line printer output may include

(d) tables of (a) - (c) above ;

(e) details of the energy, mass and momentum balance ;

(f) characteristic timescales associated with the computational mesh;

(g) warnings and error diagnostics if applicable.

Binary output from LASERB always comprises restarting information extracted at specified stages in the simulation and data for the graphical post-processing program.

5.2 DETAILS OF LASERB

This section describes in detail the code LASERB. We aim to provide a specification sufficiently complete to enable regeneration of the code.

We commence in Section 5.2.1 by assigning elemental volumes and surface areas to every main point on the mesh; using these definitions we show in Section 5.2.2 how careful differencing of divergence terms ensures that the divergence theorem holds exactly in discrete form. In Section 5.2.3 we see how our boundary conditions may be included in a manner which allows boundary points to be conveniently integrated together with interior points.

We proceed in Section 5.2.4 to outline the five main stages required to advance the major variables from time t to time t + dt. The most important stage is considered to be the implicit solution of the electron thermal diffusion equation; in Section 5.2.5 the steps leading to a quindiagonal matrix equation are given in detail, and the significance of the terms in the quindiagonal matrix is discussed as a background to Chapter 6 which describes the solution of such matrix equations. In Section 5.2.6 we digress to consider some aspects of the theory of the

numerical solution of diffusion equations which relate to our choice in Section 5.2.7 of fully implicit diffusion.

The Lax-Wendroff stages are not discussed in such detail; however some limitations of this method are mentioned in Section 5.2.8 and the averaging that forms part of the auxiliary step is given in Section 5.2.9.

The following three sections describe the simple algorithm used for laser heating (Section 5.2.10), the extent to which the code conserves energy (Section 5.2.11) and the basis of our predictions of ion arrival time graphs (Section 5.2.12).

We complete the specification of the integration scheme in Section 5.2.13 by listing a few minor modifications that are made for numerical reasons but which do not significantly modify the physics.

Finally in Section 5.2.14 we consider an unresolved problem associated with the numerical implementation of the Righi-Leduc heat fluxes. As these terms are omitted from most runs (despite being included in Section 5.2.4) we have left their discussion to the end of Section 5.2.

5.2.1 Volume and surface elements

The purpose of the definitions of this section is simply to allow us to define exact conservation laws in terms of volume and surface integrals without the boundaries needlessly introducing errors.

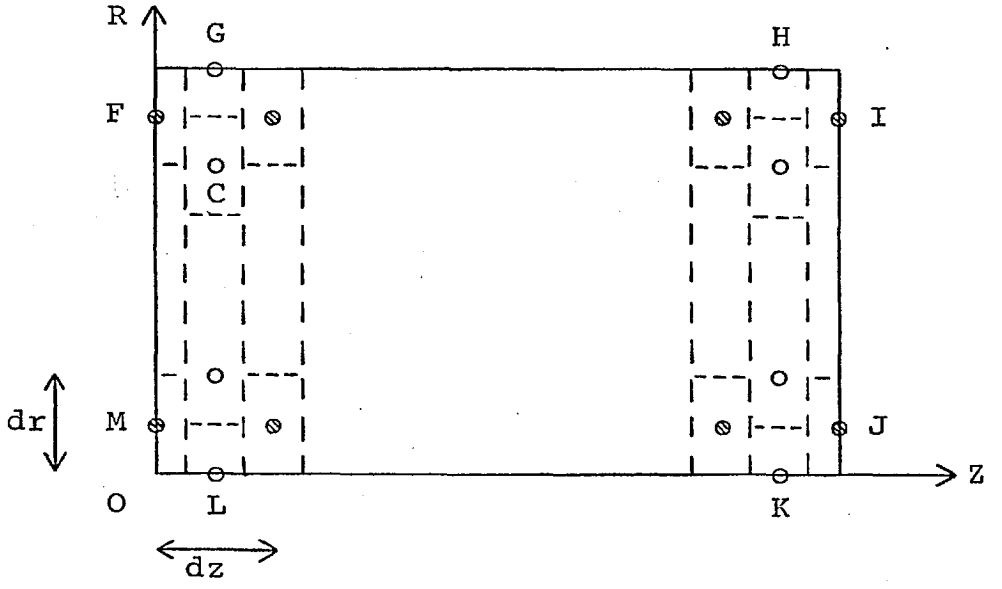

Fig. 5-3 Partition of the simulation region.

Volumes ΔV_c are associated with points C on the main mesh and correspond to the partition of the (r,z) plane shown in Fig. 5-3. Using the elementary result that the area of any disc of central radius r and width dr is $2\pi r dr$, we have

$$\Delta V_c = \frac{\pi r_c \, dr \, dz}{1 + \delta_b} , \tag{5.1}$$

where

$$\delta_b = \begin{cases} 1 & \text{boundary points} \\ 0 & \text{otherwise} \end{cases} \tag{5.2}$$

and

$$r_c = \begin{cases} r_{max} - dr/4 & \text{north boundary} \\ dr/4 & \text{south boundary} \\ \text{radius of point C} & \text{otherwise.} \end{cases} \quad (5.3)$$

Note that boundary points are to be understood as those lying strictly on the rectangular boundary, so that for example the point F of Fig, 5-3 is a west but not a north boundary point. Points situated at distances dr/2 or dz/2 from a boundary will be referred to as "pseudo-boundary points". We shall adhere rigidly to this distinction.

Our definition (5.1) ensures that the total volume ($\pi r_{max}^2 z_{max}$) is independent of the mesh spacings. Quantities such as the total mass are defined in the obvious way as summations over points on the main mesh.

Correspondingly, surface areas $\Delta S_{n,s,e,w}$ may be assigned to boundary and pseudo-boundary points. The latter are included because fluxes of conserved quantities such as energy can leave the region from these points. For example, all points on the north have "north" areas,

$$\Delta S_n = \pi r_{max}\, dz, \quad (5.4)$$

except points F and I where

$$\Delta S_n = \pi r_{max}\, dz/2 . \quad (5.5)$$

All areas on the south are zero. On the east and west we ensure that the total area does not amount to $2\pi r_{max}^2$ by assigning areas

$$\Delta S_w = \Delta S_e = \pi r_c dr \qquad (5.6)$$

(rather than the $2\pi r_c dr$ suggested by Fig. 5-3). Points G,L,H and K have

$$\Delta S_w = \Delta S_e = \pi r_c dr/2. \qquad (5.7)$$

Our total surface areas are again independent of the number of mesh-points.

In the obvious manner areas $\Delta S_{n,s,e,w}$ may be assigned to all other main points of the mesh.

The vertical bias of Fig. 5-3 is unimportant; if the partition were made horizontally almost all of the areas and volumes would remain unaffected.

5.2.2 Basic differencing concepts

The basic differencing technique is very simple, and conventional. For any quantity f at a central point C, we replace the partial derivatives $\partial/\partial r$ and $\partial/\partial z$ by $\delta/\delta r$

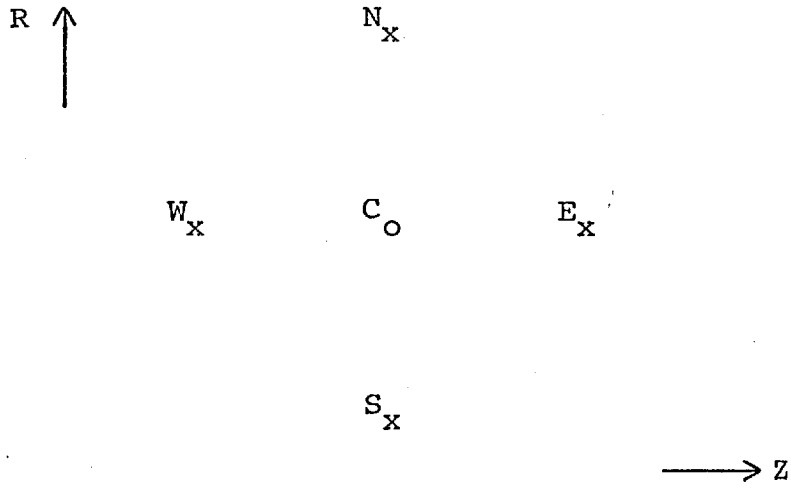

Fig. 5-4 Points required for simple differences

and $\delta/\delta z$ where

$$\frac{\delta f}{\delta r} = \frac{f_n - f_s}{dr} \tag{5.8}$$

and

$$\frac{\delta f}{\delta z} = \frac{f_e - f_w}{dz} \; . \tag{5.9}$$

We have shown C as a main point in Fig. 5-4, but the same formulae apply on the auxiliary mesh.

Where it is required to evaluate such quantities on boundaries, one-sided differencing is used - i.e. if the point C is on the north boundary,

$$\frac{\delta f}{\delta r} = \frac{f_c - f_s}{dr/2} \; . \tag{5.10}$$

Such differencing is not spatially centred, and also connects an auxiliary point with a main point, instead of connecting two auxiliary points. An alternative method is to use, instead of (5.10),

$$\frac{\delta f}{\delta r} = \frac{(f_e + f_w)/2 - f_s}{dr/2} \; . \tag{5.11}$$

As we remarked earlier, the boundaries should ideally be taken sufficiently far from the regions of interest for such inaccuracies not to be of significance.

Straightforward gradients treated in this way occur in the following terms:

$\nabla(P_e + P_i)$	in the momentum equation (3.2)
$\nabla T_e \times \nabla\rho$ and $\nabla \times (\underline{V}_e \times \underline{B})$	in the magnetic field equation (3.56)
$\nabla \times \underline{B}$	in the definition of $\underline{J}$ (3.12).

Most of the derivatives are however divergences, and it is desired to difference them in such a way that the divergence theorem holds exactly in difference form, according to our definitions of surface and volume elements. For a vector $\underline{F}$, $\nabla.\underline{F}$ is conveniently expressed at an interior point as

$$\nabla.\underline{F} \rightarrow \frac{F_e - F_w}{dz} + \frac{1}{r_c\, dr}(r_n F_n - r_s F_s). \qquad (5.12)$$

For a boundary point the same formula will be used, with the following modifications:

(i) When the central point C is on the west boundary, F_w is replaced by F_c and dz by dz/2:

$$\nabla.\underline{F} \rightarrow \frac{F_e - F_c}{dz/2} + \frac{1}{r_c dr}(r_n F_n - r_s F_s). \qquad (5.13)$$

The east boundary is similarly treated.

(ii) When the central point C is on the north boundary, $r_n F_n$ is replaced by $r_{max} F_c$ and dr by dr/2. Also, r_c is as defined in (5.3) and is not taken as r_{max}:

$$\nabla.\underline{F} \rightarrow \frac{F_e - F_w}{dz} + \frac{r_{max} F_c - r_s F_s}{(r_{max} - dr/4)(dr/2)} . \qquad (5.14)$$

The south boundary is similarly treated, but the formula simplifies because both r and F are zero on the axis:

$$\nabla.\underline{F} \rightarrow \frac{F_e - F_w}{dz} + \frac{r_n F_n}{(dr/4)(dr/2)} . \qquad (5.15)$$

With our definitions of r_c, ΔV_c and $\Delta S_{n,s,e,w}$ we have the discrete divergence theorem:

$$\sum_C \nabla.\underline{F} \; \Delta V_c = \sum_E F_e \Delta S_e - \sum_W F_w \Delta S_w + \sum_N F_n \Delta S_n - \sum_S F_s \Delta S_s \qquad (5.16)$$

where the summation over C is over all main mesh points (including boundary points), and the summations on the right hand side are over all boundary and pseudo-boundary main mesh points. The last term on the right hand side of (5.16) is of course zero in our geometry. (5.16) holds because we have effectively defined $\nabla.\underline{F}$ as

$$\nabla.\underline{F} = (F_n \Delta S_n - F_s \Delta S_s + F_e \Delta S_e - F_w \Delta S_w)/\Delta V_c . \qquad (5.17)$$

5.2.3 Boundary conditions

The F that may occur on the right hand side of (5.16) are, from the main equations (3.1) - (3,4), either quantities times a normal velocity or normal heat fluxes. We see at once how easily we may incorporate all our boundary conditions: on a no-flux boundary we set the normal velocity and magnetic field to be zero at all times, on a free flux boundary no special action is required, and on all boundaries we set the normal heat flux to be zero. Boundary points are then treated almost identically to interior points, within the same scan, and whichever variable is being integrated.

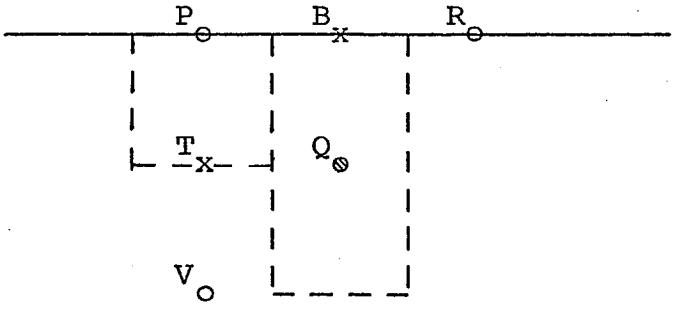

Fig. 5-5 Boundary and pseudo-boundary points on the north.

For example, referring to Fig. 5-5, the mass flow out of the region from the cell centred on the pseudo-boundary point Q is calculated as

$$(\rho V_r)_n \, \Delta S_n$$

where n refers to the auxiliary point B. The flow from the cell associated with P is the same except that n now refers to the main point P itself. If V_r has been set to zero at P and B, no mass will leave the region (no-flux); if not, the

mass lost will depend on the values of V_r at P and B (free-flux). The axial flow from P to R is unaffected and depends on V_z evaluated at B.

Note that pseudo-boundary points do not enter the specification of boundary conditions. The radial velocity at the point T in Fig. 5-5 will in general be non-zero for both types of boundary and determine the mass flow from V to P.

The magnetic field is set to zero on a no-flux boundary for reasons of symmetry - see Section 3.1.2. This will ensure no normal current flow. The axis is always a no-flux boundary.

The imposition of zero heat flux ($\underline{Q}_e = \underline{Q}_i = 0$) across a free-flux boundary may appear inconsistent: we are allowing thermal energy to escape through convection but not conduction. The question is how to specify Q_n when the central point C is a boundary point (Fig. 5-6a) or a pseudo-boundary point (Fig. 5-6b); it is a physical question which cannot be resolved using extrapolations from the interior, whatever their order, to determine the boundary temperature.

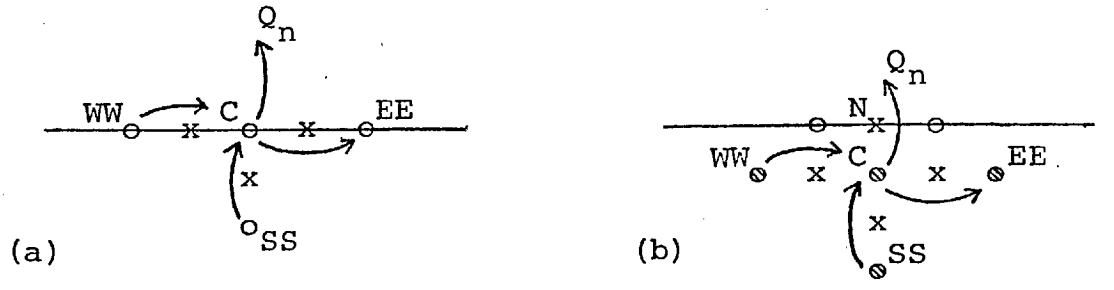

Fig. 5-6 Points involved in heat conduction. (a) boundary point C, (b) pseudo-boundary point C.

If the region beyond the mesh were a heat bath of fixed temperature T_o, either Q_n would be the necessary flux to ensure that T_e at the point C remains equal to T_o (Fig. 5-6a), or Q_n would be calculated from $T_c - T_o$ (Fig. 5-6b). But this is not the case in any of our configurations.

Another important consideration is that we should allow fluxes out of, but not into, our region. A scheme which allows information to enter the region is intuitively unsatisfactory, and possibly unstable numerically. Generally there is no cause for concern because matter flows out through expansion, but in two cases this principle may be violated:

(a) If the magnetic field is allowed to reach the boundaries some current will flow in from outside the region. This could give rise to negative normal electron velocities.
(b) The Righi-Leduc flow across a boundary is proportional to the tangential temperature gradient, and may therefore be directed inwards. This also depends on there being a non-zero magnetic field on the boundary.

In those runs which define $\underline{V}_e$ as $\underline{V}$ instead of using (3.13),(a) does not arise, and when the Righi-Leduc terms are omitted (b) does not arise. If the Righi-Leduc terms are included (b) is not normally a problem, because if $\partial T_e/\partial r$ is negative on the east boundary (the one most likely to be affected) the Righi-Leduc flux will be out of the region.

5.2.4 The main integration stages

The six major variables can be integrated in various ways; the scheme we use requires five main stages, summarized below:

(a) Integrate T_e explicitly but without the diffusion terms, to obtain an intermediate temperature T_e^*.

(b) Correct T_e^* using implicit diffusion to obtain T_e', the temperature at time t + dt.

(c) Integrate B to time t + dt using the average of T_e and T_e' in the source term.

(d) Use the Lax-Wendroff auxiliary step to obtain $\hat{\rho}$, $\hat{\underline{V}}$ and $\hat{T}_i$ on the auxiliary mesh at time t + ½dt.

(e) Use the Lax-Wendroff main step to obtain ρ', $\underline{V}'$ and T_i' at time t + dt.

We are consistently using the following notation:

T_e $\underline{V}$ ρ B T_i	values at the old time t
T_e^*	intermediate temperature
$\hat{\underline{V}}$ $\hat{\rho}$ $\hat{T}_i$	values at the auxiliary time t + ½dt
T_e' $\underline{V}'$ ρ' B' T_i'	values at the new time t + dt.

An alternative method might be to integrate all the variables together using the Lax-Wendroff steps, but without the diffusion of T_e, and then perform the implicit diffusion. This would be less satisfactory because the temperature gradients used to drive $\underline{V}$ and B would be distorted by an undiffused heating increment. The B

integration (c) could be included within the Lax-Wendroff scheme, but it is largely determined by time-centred temperature gradients which are available after stage (b). Also an implicit scheme for the magnetic diffusion could more easily be incorporated (if desired) in a subroutine integrating B alone.

We shall now describe the five stages (a) to (e) in greater detail.

We start the loop with all six major variables defined on the main mesh at time t. As a preliminary we define them on the auxiliary mesh as averages of their values at surrounding main points (Section 5.2.9), define minor variables ($\underline{J}$,$\underline{V}_e$, $K_{e\perp}$, $K_{e\wedge}$ and Ω_τ), and calculate the heat source (Section 5.2.10).

(a) (3.48) may be written as

$$\frac{n_e k}{\gamma - 1}\,\frac{T_e' - T_e}{dt} = f(\rho,\underline{V},T_e,T_i,B) - \nabla.\underline{Q}_e(K_{e\perp},K_{e\wedge},T_e,T_e') \qquad (5.18)$$

where f is a known function at time t. In this stage we calculate the intermediate temperature T_e^* which satisfies

$$\frac{n_e k}{\gamma-1}\,\frac{T_e^* - T_e}{dt} = f(\rho,\underline{V},T_e,T_i,B). \qquad (5.19)$$

(b) We find the temperature T_e' which satisfies

$$\frac{n_e k}{\gamma-1}\,\frac{T_e' - T_e^*}{dt} = -\nabla.\underline{Q}_e(K_{e\perp},K_{e\wedge},T_e,T_e'), \qquad (5.20)$$

and which is therefore a solution of (5.18). The procedure is simplified in the majority of runs which omit the $K_{e\wedge}$ terms, but we consider the general case first.

$\underline{Q}_e$ is the sum of two parts $\{\underline{Q}_{e\perp}, \underline{Q}_{e\wedge}\}$ defined from (3.17) and (3.18) as

$$\underline{Q}_{e\perp}(T) = (-K_{e\perp}\,\partial T/\partial r, -K_{e\perp}\partial T/\partial z) \qquad (5.21)$$

$$\underline{Q}_{e\wedge}(T) = (-K_{e\wedge}\,\partial T/\partial z, K_{e\wedge}\partial T/\partial r). \qquad (5.22)$$

$K_{e\perp}$ and $K_{e\wedge}$ are evaluated at the old time t. Iteration could be performed to time centre these coefficients, but this is omitted because the fully-implicit scheme used in practice (Section 5.2.7) is only of first order accuracy in time.

Our scheme involves a degree of implicitness θ for $\underline{Q}_{e\perp}$ and N partial timesteps for $\underline{Q}_{e\wedge}$. We define

$$T^o \equiv T_e^* ; \qquad (5.23)$$

for $1 \leqslant n \leqslant N$ we solve

$$\frac{n_e k}{\gamma-1}\,\frac{T^n - T^{n-1}}{(dt/N)} = -\nabla\cdot\underline{Q}_{e\perp}(\theta\,T^n + (1-\theta)T^{n-1}) - \nabla\cdot\underline{Q}_{e\wedge}(T^{n-1}); \qquad (5.24)$$

and finally we set

$$T_e' \equiv T^N. \qquad (5.25)$$

If $K_{e\wedge}$ is omitted, N = 1 and we merely solve

$$\frac{n_e k}{\gamma-1}\,\frac{T_e' - T_e^*}{dt} = -\nabla.\,\underline{Q}_{e\perp}(\theta T_e' + (1-\theta)T_e)\,. \qquad (5.26)$$

There is an inconsistency between (5.24) and (5.26) with regard to the explicit heat terms. This may be resolved by modifying the right hand side of (5.24) on the first partial timestep so as to calculate the explicit fluxes from T_e rather than T_e^*.

Details of the solution of (5.24) are given in Section 5.2.5.

(c) B' on the main mesh is calculated explicitly from (3.56). The average of T_e and T_e' is used, so that the generally dominant source term is time centred with respect to temperature. B' on the auxiliary mesh is calculated as the average of B' on the main mesh, and B' overwrites B.

(d) $\hat{\rho}$, $\underline{\hat{V}}$ and $\hat{T}_i$ are calculated on the auxiliary mesh from (3.1) - (3.3), with $\underline{Q}_i$ omitted, as functions of ρ, $\underline{V}$, T_i, T_e and B'.

(e) ρ', $\underline{V}'$ and T_i' are calculated on the main mesh from (3.1)-(3.3) using $\hat{\rho}$, $\underline{\hat{V}}$, $\hat{T}_i$, B' and $\frac{1}{2}(T_e + T_e')$ on the auxiliary mesh. The equipartition term uses the uncentred T_e to ensure that the ions gain the exact amount of energy that the electrons lost in (a).

5.2.5 The implicit diffusion scheme

(5.24) is implicit in T^n and may be differenced as (see Fig. 5-6)

$$Z_w(T^n_{ww} - T^n_c) + Z_s\,(T^n_{ss} - T^n_c) + Z_c(T^n_c - T^{n-1}_c) + Z_n(T^n_{nn} - T^n_c) + Z_e(T^n_{ee} - T^n_c) = \bar{W}^{n-1}, \tag{5.27}$$

where

$$\bar{W}^{n-1} = -(1-\theta)\nabla\cdot \underline{Q}_{e\perp}(T^{n-1}) - \nabla\cdot\underline{Q}_{e\wedge}(T^{n-1}), \tag{5.28}$$

$$Z_w = -\frac{K_w\theta}{dz^2}(1+\delta_b) \qquad Z_n = -\frac{r_n K_n \theta}{r_c dr^2}(1+\delta_b)$$

$$Z_e = -\frac{K_e\theta}{dz^2}(1+\delta_b) \qquad Z_s = -\frac{r_s K_s \theta}{r_c dr^2}(1+\delta_b) \tag{5.29}$$

and

$$Z_c = \frac{n_e k}{(\gamma-1)(dt/N)}. \tag{5.30}$$

In (5.27) all the unknown quantities are on the left hand side; in (5.29) K stands for $K_{e\perp}$ which is always positive.

δ_b was defined in (5.2). Using this, (5.29) may also be written in terms of volume and surface elements; for example,

$$Z_w = -\frac{K_w dS_w \theta}{dz\ \Delta V_c}. \tag{5.31}$$

To ensure no heat fluxes out of the region, Z_w is set to zero when the west-west point WW lies off the mesh, as is the corresponding flux of $\underline{Q}_{e\perp}$ on the right hand side of (5.28) and as may be the corresponding flux of $\underline{Q}_{e\wedge}$ if so desired. The other compass points are treated similarly. Otherwise the boundary and pseudo-boundary points are again treated together with the interior points.

(5.27) may be written in a normalized form as

$$A_q T^n_{q-m} + B_q T^n_{q-1} + T^n_q + C_q T^n_{q+1} + D_q T^n_{q+m} = W_q \qquad (5.32)$$

where

$$\begin{aligned} A_q &= Z_w/Z_a \\ B_q &= Z_s/Z_a \\ C_q &= Z_n/Z_a \\ D_q &= Z_e/Z_a \ , \end{aligned} \qquad (5.33)$$

$$W_q = (\bar{W}^{n-1} + Z_c T^{n-1}_c)/Z_a \ , \qquad (5.34)$$

and

$$Z_a = Z_c - (Z_w + Z_s + Z_n + Z_e). \qquad (5.35)$$

(5.32) is a quindiagonal matrix equation for T^n which is now treated as a column vector of ℓm elements, indexed as shown in Fig. 5-7. The undefined quantities

in (5.32), namely

$$T^n_{q-m} \qquad 1 \leqslant q \leqslant m$$

$$T^n_{q+m} \qquad (\ell-1)m+1 \leqslant q \leqslant \ell m$$

are understood to be zero.

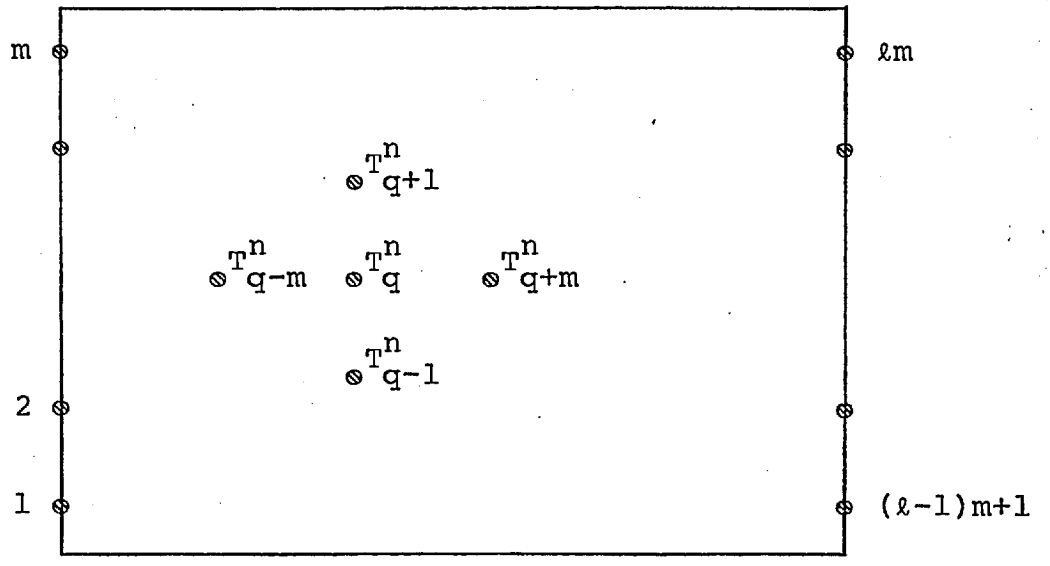

Fig. 5-7 5-point difference scheme for diffusion on submesh "1"

We make a number of observations, which are pertinent to the solution of this matrix equation to be described in Chapter 6:

(i) The two submeshes decouple and are solved separately.

(ii) All those coefficients corresponding to points outside the region are zero. For example $C_m = A_m = 0$, because T^n_m couples only to T^n_{m-1} and T^n_{2m}.

(iii) It may be seen from (5.29), (5.30), (5.33) and (5.35) that A_q, B_q, C_q and D_q are all negative and that

$$|A_q| + |B_q| + |C_q| + |D_q| < 1 \qquad (1 \leqslant q \leqslant \ell m). \quad (5.36)$$

Therefore the quindiagonal matrix M (Fig. 5-8) is diagonally dominant. One consequence of this (see the result (5.51) proved later) is that all of its eigenvalues have real parts greater than zero.

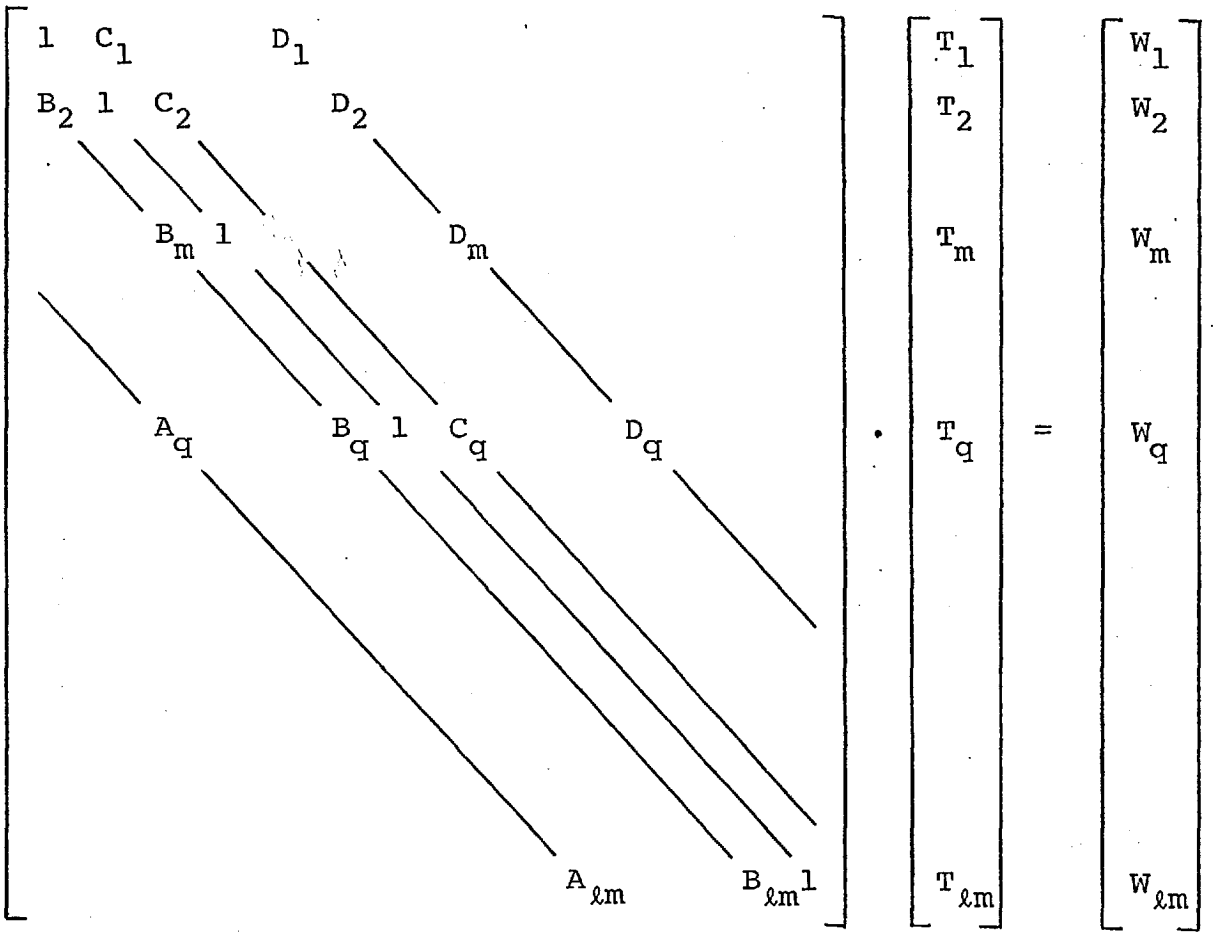

Fig. 5-8 Quindiagonal matrix equation MT = W.

(iv) At each main point C define the "mesh diffusion time" τ_c as follows:

$$\tau_c^{-1} = \frac{(\gamma-1)(1+\delta_b)}{n_e k}\left\{\frac{K_w}{dz^2} + \frac{K_e}{dz^2} + \frac{r_n K_n}{r_c dr^2} + \frac{r_s K_s}{r_c dr^2}\right\} . \qquad (5.37)$$

An alternative and more familiar definition is based on the conductivity K_a at an auxiliary point A:

$$\tau_a = \frac{n_e k}{4(\gamma-1)K_a} \min\{dz^2, dr^2\} . \qquad (5.38)$$

With respect to the form of τ_a, τ_c is reduced by a factor of about 2 on east, west and north boundaries, and a factor of up to 4 on the south (where $r_c = dr/4$, $r_n = dr/2$ and $\delta_b = 1$). This reflects the increased sensitivity of points representing small volumes - see Fig. 5-9. The corresponding coefficients in the quindiagonal matrix are enhanced.

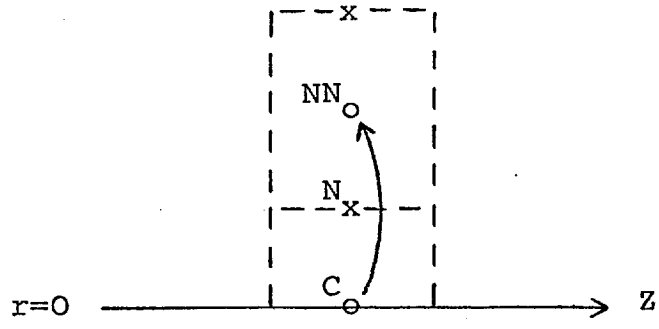

Fig. 5-9 A flow of heat from C to NN causes T_c to change 8 times as much as T_{nn}.

An intimately related effect is that the stability criterion for explicit diffusion ($dt < \tau_c$, which is simply the requirement that temperature differences between neighbouring points are no more than reversed on a timestep) is more severe on the axis. See Section 5.2.6.

(v) In the case of weak conductivity or a small timestep,

characterized by

$$dt << \tau_c \qquad (5,39)$$

everywhere, the magnitudes of the off-diagonal terms of the matrix are all much less than unity.

(vi) In the case of strong conductivity everywhere, the matrix is only just diagonally dominant and the problem becomes ill-conditioned. When $\theta=1$ and $K_{e\wedge}=0$, the only information about the temperature at the previous timestep is contained in the small quantity $Z_c T_c^{n-1}$. In the limit, Z_c and W_q are zero and the matrix is singular; we are then solving the elliptic equation

$$\nabla.(K_{e\perp} \nabla T) = 0 \qquad (5,40)$$

subject to zero gradient boundary conditions, to which any constant T is a solution.

(vii) In general we may expect that (v) will apply in some regions and (vi) in others.

(viii) The rate of convergence of the iterative solution to (5,32) depends on the degree of diagonal dominance of M. See Chapter 6.

(ix) The normalization of the main diagonal of M (Fig.5-8) destroys the symmetry that the matrix might otherwise have had. A symmetric matrix could be constructed directly from (5.27) multiplied by ΔV_c, as may be seen from (5,31) or (5,29): the coefficients Z_w, Z_s, Z_n and Z_e multiplied by ΔV_c, which

would become the off-diagonal elements of M, lose their dependence on the point C. The main diagonal elements of M would however vary by as many orders of magnitude as $K_{e\perp}$. We have not pursued this approach.

To ensure coupling between submeshes 1 and 2 the diffusion equation is sometimes differenced on the large diagonal mesh of Fig.5-2, usually every ten steps. An analogous equation to (5.32) is obtained, except that for points outside the simulation region we set

$$A_q = B_q = C_q = D_q = 0$$
$$W_q = 1. \qquad (5.41)$$

Just under half of the T_q of the solution will then be fictitious (=1), but the computational redundancy introduced is compensated for by the convenience of using the same inversion subroutines.

(5.26) rather than (5.24) is used because the Righi-Leduc terms may be added explicitly just prior to this coupling stage if required.

The difference formulae are established just as before, but with respect to the elemental areas indicated by the dotted lines in Fig.5-10 and the elemental volumes defined in (5.1); the latter are the same as indicated in Fig.5-10, except for points on the north and south boundaries. The conductivity at D is taken as the average

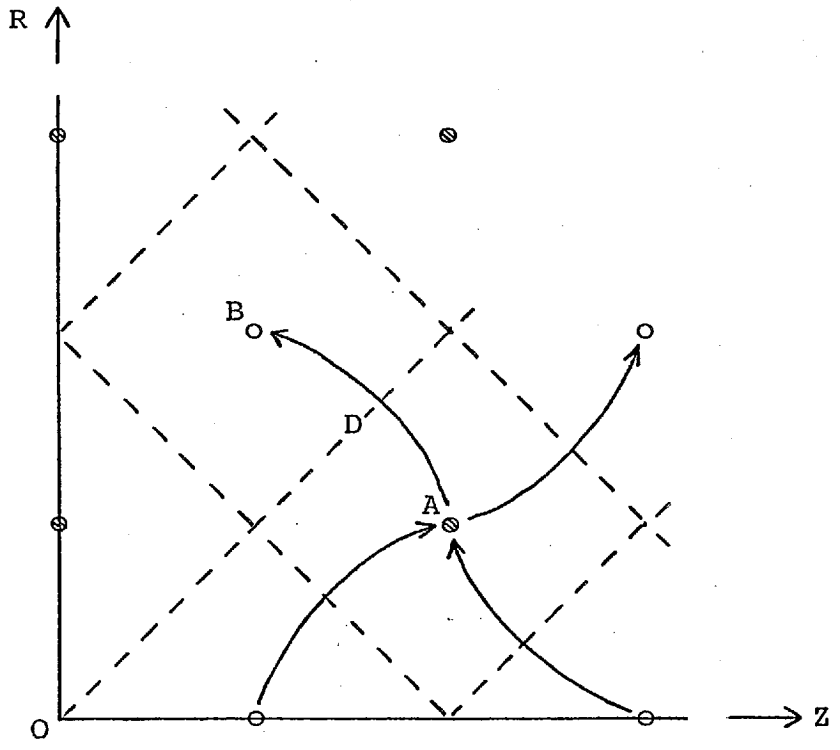

Fig.5-10 Coupling on the large diagonal mesh.

of the conductivities at A and B; however allowance is not made for the fact that the heat flux calculated at the point D is not in general normal to the elemental surface between A and B. Therefore the formulae will be correct only if the mesh is square.

The origin of this inconsistency is that it is impossible to difference the Laplacian of a field f to second order accuracy using a 5- point scheme on a non-orthogonal mesh, because when expanding the values at the four corner points (±dx, ±dy, see Fig.5-11) in a Taylor series about the centre point (0, 0) the required second derivatives occur only in the combination

$$\frac{\partial^2 f}{\partial x^2}\, dx^2 + \frac{\partial^2 f}{\partial y^2}\, dy^2 .$$

However no energy is lost in the process; an example indicating that this error is not serious is given in Section 9.3.2 with reference to Fig. 9-12b : the diffusion of absorbed energy is temporarily delayed.

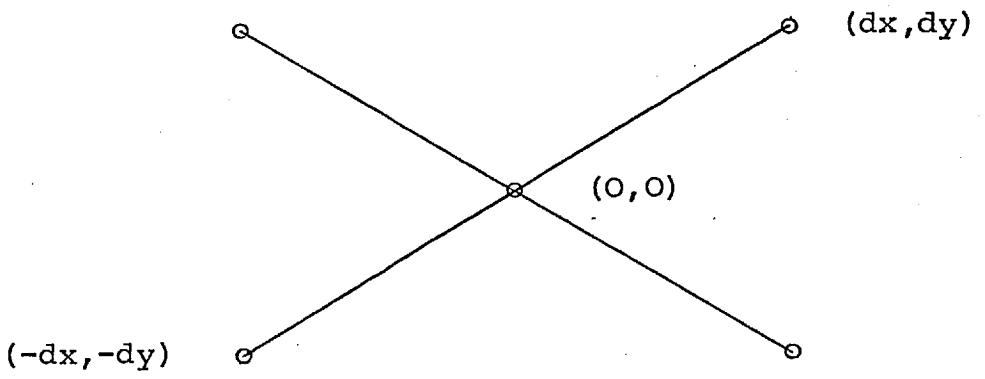

Fig.5-11 Points on a non-orthogonal mesh.

5.2.6 The stability of simple diffusion schemes

Because of the importance to our work of thermal diffusion we consider it worthwhile to digress somewhat to consider the main features of some diffusion schemes. We commence with the simplest, the one-dimensional diffusion equation with constant conductivity

$$\frac{\partial T}{\partial t} = \frac{\partial}{\partial x} K \frac{\partial T}{\partial x} \quad . \qquad (5.42)$$

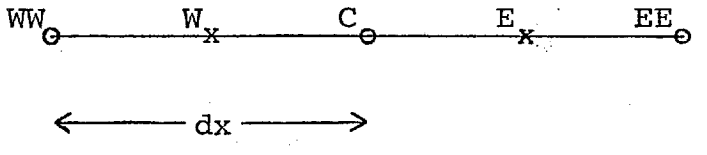

Fig.5-12 Points for one-dimensional diffusion

The explicit scheme (Fig.5-12)

$$\frac{T_c' - T_c}{dt} = \frac{K}{dx^2} (T_{ee} + T_{ww} - 2T_c) \qquad (5.43)$$

is well-known to be stable for

$$s < \tfrac{1}{2} \qquad (5.44)$$

where

$$s = Kdt/dx^2, \qquad (5.45)$$

the exact stability boundary depending on the number of mesh points and the boundary conditions. Because of linearity the error vector obeys the same equation as the true solution, and so the problem of stability reduces to finding growing solutions of (5.43). This is solved by considering the amplification factor g_a of a Fourier perturbation $\alpha\ e^{iax}$, or more rigorously from the eigenvalues λ_a of the amplification matrix. The first method is valid because the eigenvectors of the amplification matrix are precisely those Fourier perturbations which satisfy the boundary conditions. The eigenvalues are given by

$$g_a = \lambda_a = 1 - \frac{4Kdt}{dx^2} \sin^2 \frac{a\ dx}{2} \qquad (5.46)$$

and (5.44) is obtained from the worst case ($adx \simeq \pi$).

A trivial extension for the general implicit case, when T is replaced by

$$\theta T' + (1-\theta)T$$

on the right hand side of (5.43), gives

$$g_a = \lambda_a = \frac{1-4s\ (1-\theta)\ \sin^2\ (adx/2)}{1+4s\ \ (\theta)\ \ \sin^2\ (adx/2)} \qquad (5.47)$$

and the sufficient criterion for stability that

$$\begin{array}{ll} \text{either} & \theta \geqslant \tfrac{1}{2} \\ \text{or} & s(1-2\theta) < \tfrac{1}{2}\ . \end{array} \qquad (5.48)$$

When K varies with x Fourier analysis is inappropriate, and a formal stability analysis involves the harder problem of finding eigenvalues of a general tridiagonal matrix. In the general case when K also depends on T, the amplification matrix (and therefore the eigenvectors) are different on each timestep: linearity has been destroyed and the perturbation is no longer independent of the true solution. The obvious sufficient condition for stability is however that on each step the maximum eigenvalue of the amplification matrix has a modulus not greater than unity.

The case of constant K is easily generalized to two dimensions because the (quindiagonal) amplification matrix has product eigenvectors $e^{iax}\ e^{iby}$. Extra terms in y are included in (5.46) and (5.47), causing the right hand side of the requirement (5.44) to be halved. However when K is variable this does not apply because the x- and y- operators

$$\frac{\partial}{\partial x}\ K_x\ \frac{\partial}{\partial x} \quad \text{and} \quad \frac{\partial}{\partial y}\ K_y\ \frac{\partial}{\partial y}$$

no longer commute.

The general situation of variable K is in fact less intractable than might appear, because (5.44) remains a sufficient criterion for stability where s is taken from the largest $(K_e + K_w)/2$ on the mesh. To see this, consider the amplification matrix L for the explicit scheme

$$T'_c - T_c = s_e T_{ee} + s_w T_{ww} - (s_e + s_w) T_c \qquad (5.49)$$

where

$$s_{e,w} = \frac{dt}{dx^2} K_{e,w}. \qquad (5.50)$$

L is sketched in Fig. 5-13, where we have ignored the boundary conditions which do not affect our argument. Using the result (Gerschgorin's Circle Theorem[79]) that for any matrix A with an eigenvector u with eigenvalue λ,

$$L = \begin{bmatrix} & & & & \\ & s_w & 1-s_e-s_w & s_e & \\ & & & & \end{bmatrix}$$

Fig.5-13 Tridiagonal amplification matrix L

there exists at least one i such that

$$|\lambda - a_{ii}| \leq \sum_{j \neq i} |a_{ij}| , \tag{5.51}$$

(obtained from

$$(\lambda - a_{ii})\, u_i = \sum_{j \neq i} a_{ij} u_j \tag{5.52}$$

for the i corresponding to the largest component of u), it follows that all eigenvalues λ of L satisfy

$$\min \{ 1 - 2(s_e + s_w) \} \leq \lambda \leq 1, \tag{5.53}$$

giving the desired result. The eigenvalues λ are real since the matrices L of interest are symmetric; otherwise λ would be replaced by $\mathrm{Re}(\lambda)$ in (5.53). It is interesting that (5.53) is just satisfied by the λ_a of (5.46) for the case of constant K. The extent to which the λ_a can approach their bounds depends on the range of a allowed by the boundary conditions. The lower bound corresponds to short wavelength modes ("wiggles"), which are most likely to be unstable, and the upper bound to long wavelength modes.

Now consider the fully implicit problem

$$T'_c - T_c = s_e T'_{ee} + s_w T'_{ww} - (s_e + s_w) T'_c, \tag{5.54}$$

or

$$MT' = T \tag{5.55}$$

where M is sketched in Fig. 5-14. The amplification matrix

$$M = \begin{bmatrix} & & & & \\ & -s_w & 1+s_e+s_w & -s_e & \\ & & & & \end{bmatrix}$$

Fig. 5-14 Implicit tridiagonal matrix M

M^{-1} has eigenvalues μ^{-1} where, again from (5.51),

$$1 \leq \mu \leq \max\{1 + 2(s_e + s_w)\}, \tag{5.56}$$

so that the fully implicit scheme is unconditionally stable.

The general implicit problem $(0 < \theta < 1)$ is

$$\hat{M}T' = \hat{L}T \tag{5.57}$$

where $\hat{M}$ is M with the s replaced by θs and $\hat{L}$ is L with the s replaced by $(1-\theta)$s. Because

$$\hat{M} = (I - \theta\hat{L})/(1-\theta), \tag{5.58}$$

where I is the identity matrix, $\hat{M}$ and $\hat{L}$ share common eigenvectors, with eigenvalues $\hat{\mu}$ and $\hat{\lambda}$ related by

$$\hat{\mu} = (1 - \theta\hat{\lambda})/(1-\theta). \tag{5.59}$$

The corresponding eigenvalue g of $\hat{M}^{-1}\hat{L}$ is given by

$$g = \frac{\hat{\lambda}}{\hat{\mu}} = \frac{\hat{\lambda}(1-\theta)}{1-\theta\hat{\lambda}} \tag{5.60}$$

$$= \frac{1-\theta}{\theta}\left[\frac{1}{1-\theta\hat{\lambda}} - 1\right] ; \tag{5.61}$$

g is an increasing function of $\hat{\lambda}$ (for the $\hat{\lambda} \leqslant 1$ of interest); using (5.61), and the appropriate version of (5.53) which is

$$\min\{1-2(s_e+ s_w)(1-\theta)\} \leqslant \hat{\lambda} \leqslant 1, \tag{5.62}$$

it follows that

$$\min\left\{\frac{1-2(s_e+ s_w)(1-\theta)}{1+2(s_e+ s_w)\theta}\right\} \leqslant g \leqslant 1. \tag{5.63}$$

(5.63) compares closely with (5.47), and (5.48) is again sufficient for stability with s replaced by the maximum on the mesh of $(s_e+ s_w)/2$. It is useful to think of the timestep dt as being split into two steps, $(1-\theta)dt$ and θdt, in which the explicit destabilizing L and the implicit stabilizing M^{-1} operate in succession.

The extension to two dimensions is obvious, $\hat{M}$ and $\hat{L}$ are quindiagonal, but still satisfy (5.58); (5.63) becomes

$$\min\left\{\frac{1-2(s_e+ s_w+ s_n+ s_s)(1-\theta)}{1+2(s_e+ s_w+ s_n+ s_s)\theta}\right\} \leqslant g \leqslant 1, \tag{5.64}$$

and the sufficient criterion is (5.48) with s replaced by the maximum of $(s_e+s_w+s_n+s_s)/2$. The generalization of (5.64) to a situation such as (5.26) where the left hand side of the two-dimensional version of (5.42) is multiplied by a density function is straightforward*, yielding, for $\theta < \frac{1}{2}$,

$$dt < \tau_c / (1-2\theta) \qquad (5.65)$$

where τ_c is as defined in (5.37).

The difficult problem is that of finding the necessary criterion for stability, but as this is unlikely to differ greatly from the sufficient criterion this problem may remain unsolved.

The qualitative results we have obtained are intuitively obvious - decreasing the conductivity K at various points from a state of uniform K should make and does make instability less likely. This raises the question of whether an alternative approach is possible; the answer is that there is indeed a simple intuitive method for obtaining all of the above results together with an understanding of the numerics of the diffusion process.

Commencing again with the one-dimensional equation with constant conductivity (5.42), the diffusion scheme (5.43) damps local fluctuations such as shown in Fig.5-15: T_c is reduced by an amount proportional to the excess

$$T_c - \tfrac{1}{2}(T_{ee} + T_{ww}) \qquad (5.66)$$

---

*$\hat{M}$ and $\hat{L}$ lose their symmetry but (5.58) and (5.60) still hold.

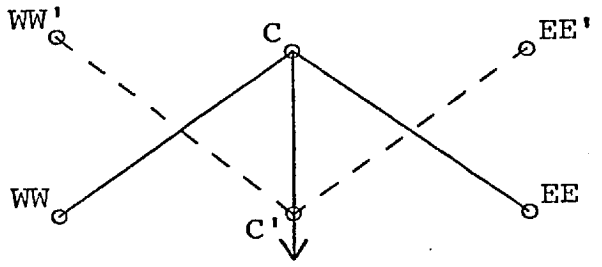

Fig.5-15 Effect of diffusion scheme on local fluctuations.

of T_c over the average of T_{ww} and T_{ee}, the constant of proportionality being 2s; T_{ww} and T_{ee} may be correspondingly increased. If the timestep dt is too large, overshooting will take place. The marginal case for stability occurs when 2s = 1; as shown by the dotted line in Fig.5-15 the perturbation is reversed in sign but retains its magnitude. For good accuracy the timestep should be small enough to only slightly reduce the magnitude of the perturbation; on physical grounds we may argue that the sign should not be reversed, thereby requiring, instead of (5.44),

$$2s \leqslant \tfrac{1}{2}. \qquad (5.67)$$

In the implicit case part of the excess of T_c (5.66) is calculated from the final T'. Because instability is always a result of overshooting, the contribution to the excess in an unstable case from the final T' is of opposite sign to the contribution from T and therefore stabilizing.

The equation (5.48) expressing the balance between the two contributions may be easily obtained along these lines.

For $\theta \geq \frac{1}{2}$ instability is impossible, whatever the timestep, because the implicit contribution is greater. The marginal (Crank-Nicholson) case $\theta = \frac{1}{2}$ reverses perturbations for large timesteps, yielding (almost) the dotted line of Fig.5-15. For large timesteps the fully implicit method ensures strong damping of the perturbations, as any final perturbation implies a large heat flow. Also, this is the only method which ensures no sign reversal for arbitrarily large timesteps.

The two-dimensional case differs only in that four rather than two points surround the central point, so that the permissible timestep for stability is halved. The case of general conductivity treats the point having in some sense the largest conductivity, but is otherwise similar: in the marginal explicit case the point C goes to C' in Fig.5-15 but the points WW and EE may not quite reach WW' and EE'.

The formulae (5.63) and (5.64) for the case of general θ may be obtained along these lines: the explicit step (5.49), applied over a time $(1-\theta)dt$, amplifies a perturbation of the form

$$T_c - T_{ee} = \Delta = T_c - T_{ww} \qquad (5.68)$$

by a factor of, at the worst,

$$\tilde{\lambda} = 1 - 2(s_e + s_w)\ (1-\theta), \qquad (5.69)$$

because

$$T'_c = T_c - (s_e + s_w)(1-\theta)\Delta \tag{5.70}$$

and

$$T'_{ee} \leq T_{ee} + (s_e + s_w)(1-\theta)\Delta \tag{5.71}$$

imply that

$$\Delta' \equiv T'_c - T'_{ee} \geq \Delta(1-2(s_e+s_w)(1-\theta)). \tag{5.72}$$

(5.71) follows because it is assumed that C was chosen as the point which changes the most.

The fully implicit step, (5.54) applied over a time θdt, may be thought of as explicit diffusion acting backwards in time: perturbations are damped rather than amplified, by the same factor as (5.69) except with $(1-\theta)dt$ replaced by $-\theta dt$. Specifically, the factor is

$$\tilde{\mu} = 1+2(s_e+s_w)\theta, \tag{5.73}$$

and (5.63) is recovered.

The reader will have noticed the equivalence of this simple approach with the more rigorous matrix approach. In particular the choice of C as the point which changes the most parallels the choice of i in the proof of Gerschgorin's Theorem (5.51), and the argument about time reversal is contained in (5.58) which expresses the similarity in form of the matrices $\hat{M}$ and $\hat{L}$. The simple argu-

ment is loose because the perturbation (5,68) is not necessarily an eigenvector.

5.2.7 Fully implicit diffusion

We are now in a position to return to the main problem and appreciate why in practice we always choose the fully implicit scheme $\theta=1$. If we evaluate the mesh diffusion time τ_c of (5,37), which is approximately the same as the τ_k of Table A.1 (but with the minimum of dr and dz used instead of L), we find that τ_c may be as low as 10^{-3} psec. The requirement for explicit diffusion that $dt < \tau_c$ at every point on the mesh is excessively restrictive and an implicit method is necessary. We might expect approximately the same criterion to apply to diffusion perpendicular to the temperature gradients (the Righi-Leduc fluxes), which is one reason why the explicit partial timestep scheme described above (Section 5.2.4) is not always satisfactory; this is considered further in Section 5.2.14.

When the timestep dt exceeds the mesh diffusion time τ_c but is less than the physical diffusion time τ_k, the time-centred Crank-Nicholson scheme is the most accurate and is unconditionally stable, although only just stable when $dt >> \tau_c$. However, in practice dt is likely to exceed τ_k, in which case the fully-implicit scheme is more appropriate. This occurs particularly in the low density ablating atmosphere, where we are not interested in following the diffusion

process itself; rather we follow a series of quasi-equilibria where it is the gradients of T_e' rather than T_e which are important, and where the old temperature T_e serves primarily to determine the overall level of T_e'. Heat is added to T_e to obtain T_e^*, and in the one timestep may diffuse throughout the region, around localized barriers of effectively zero conductivity if need be, to yield T_e'.

The timestep must be such that we can follow the overall growth of temperature, so that $(T_e'-T_e)$ should never be too large; however we do not need to follow the more restrictive heating timescale associated with $(T_e^*-T_e)$, and in practice, where the timestep is generally determined by advection, T_e^* exceeds T_e by typically up to 50%. T_e^* is an intermediate value never used to calculate coefficients or drive other variables; it is primarily an indication of the heat absorbed, and may be very sharply peaked.

At the same time we do follow thermal diffusion into regions where the conductivity is lower, in particular the high density region. The errors arising from the use of $\theta=1$ are similar to those which would have arisen had we used the explicit scheme $\theta=0$, but they may not be large at the advancing heat front where characteristically $dt \ll \tau_c$.

We have therefore a numerical scheme which is of first order accuracy only in time for the electron temperature, but which is conveniently applicable to a mesh containing regions of widely varying thermal conductivity,

and whose qualitative features are physically plausible.

5.2.8 Limitations of the Lax-Wendroff scheme

The Lax-Wendroff scheme is well-known to be of second order accuracy in time, and stable for timesteps smaller than the characteristic timescales on the mesh associated with the fluid, sound and Alfvén speeds. In our simulations these conditions are always satisfied, with the fluid speed usually the most important. For reasonable accuracy we should take the timestep to be appreciably smaller than the stability limit; generally we ensure that a maximum of 10% of the mass, momentum or energy of a cell is allowed to flow across each cell boundary in a timestep.

However the Lax-Wendroff scheme has an important drawback - in the presence of strong gradients it exhibits spatially oscillatory behaviour leading eventually to negative density and temperature.[80] Artificial viscosity[81] is often added to prevent this. An alternative technique (Flux-Corrected Transport) has been shown to be more satisfactory in certain test cases.[80],[82]

LASERB contains neither corrective procedure, and therefore cannot correctly describe the long term hydrodynamic behaviour. However, over the timescales of interest in most cases the velocity distributions are driven by a smooth electron density distribution and this problem does not arise. For example, in Fig.9-6b the distribution of

V_r is smooth: there is no decoupling between the values of V_r on the two main submeshes even though the equations for V_r are decoupled and steep gradients are present in certain regions (due in fact to $\underline{J} \times \underline{B}$ forces). The ripples on the distribution of ρ are not "computational wiggles" but are also due to gradients in the velocity distributions. Only at later times, when the laser pulse is over and the plasma has cooled, do "computational wiggles" appear.

We do however make use of one slight ad hoc hydrodynamic adjustment, which while not solving the above problem has proved to be a useful feature. Consider Fig.5-16 and suppose that the central point C is a point of expansion with for example (though not necessarily) $V_{zw} < 0$

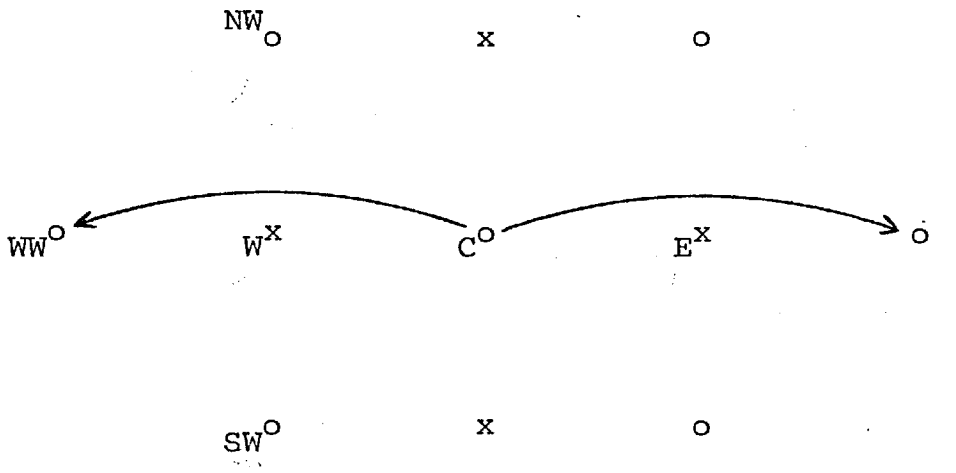

Fig. 5-16 Dependence of mass flux from C on densities at W and E

and $V_{ze} > 0$. If there are large pressure gradients in the plasma, in the vicinity of a hot spot for example, neither V_{zw} nor V_{ze} will be negligibly small. The mass flux out of

the cell centred on C will be proportional to

$$\rho_e V_{ze} - \rho_w V_{zw}, \tag{5.74}$$

and will cause ρ_c to decrease. The quantity (5.74) is not adequately responsive to decreases in ρ_c, because ρ_w is determined basically as some average of the ρ at the surrounding points { NW, SW, WW, and C} and ρ_e likewise. (Where ρ is essentially a function of z the best average for ρ_w is $(\rho_{nw} + \rho_{sw})/2$.) The mass flux out of the cell centred on C will be overestimated, and ρ_c will decrease faster and eventually become negative. A similar argument applies also to T_e and T_i.

Our adjustment is simply to limit the amount of mass, ion energy or electron energy that can flow from a cell in a timestep to a tenth of the mass or energy within the cell. This is applied to the net flux across the four boundaries rather than to the four individual fluxes and is therefore likely to occur only in regions of strong expansion. In practice it is rare that more than a few ($\sim$ 1%) of the mesh points are affected, and often this adjustment does not apply at all. Generally the errors so incurred in the overall mass and energy conservation equations are negligible.

It is worth noting that two distinct features of the code give rise to hydrodynamic problems - the staggered decoupled submeshes and the dispersive properties of the Lax-Wendroff scheme itself. It appears that the long term hydro-

dynamics could be improved by the application of Flux-Corrected Transport techniques to a straightforward rectangular mesh; the quindiagonal diffusion stage would remain unaltered, except that solution on the large diagonal mesh every ten timesteps would no longer be necessary.

5.2.9 Averages on the auxiliary mesh

To commence the auxiliary step of the Lax-Wendroff scheme we need to obtain values of quantities Q at a point C on the auxiliary mesh as averages of values on the main mesh. We have restricted ourselves to averages over the surrounding points only and have not considered higher order schemes.

For an interior point C the conventional average is

$$Q_c = (Q_n + Q_s + Q_e + Q_w)/4 \qquad (5.75)$$

although there are alternatives:

$$Q_c = (Q_n + Q_s)/2 \qquad (5.76)$$

$$Q_c^{-1} = (Q_n^{-1} + Q_s^{-1} + Q_e^{-1} + Q_w^{-1})/4 \qquad (5.77)$$

$$\log Q_c = (\log Q_n + \log Q_s + \log Q_e + \log Q_w)/4 \qquad (5.78)$$

or any weighted average of any of (5.75)-(5.78).

The obvious formula (5.75) attaches equal weights to the two main submeshes and to the two orthogonal directions and is normally used for all quantities except the density. The error is

$$\varepsilon \simeq \frac{1}{4}\left[Q_{rr}\left(\frac{dr}{2}\right)^2 + Q_{zz}\left(\frac{dz}{2}\right)^2\right], \tag{5.79}$$

where the suffices indicate second derivatives.

The other formulae have the same formal accuracy; which is the most accurate depends on the circumstances. For a quantity which varies most strongly in the z-direction (5.76) is preferable; it is used for the density. Alternatively, for density variations exponential in z, (5.78) could be used.

For boundary points we may choose between four schemes exemplified by their application to a point on the north (Fig.5-17):

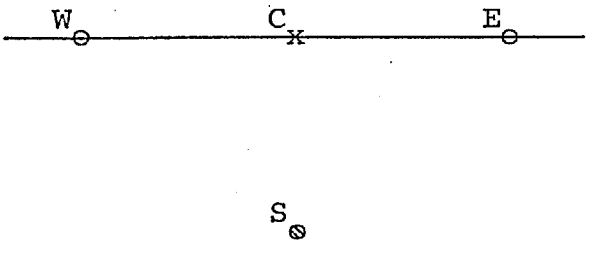

Fig.5-17 Configuration on the north boundary.

$$Q_c = (Q_e + Q_w)/2 \tag{5.80}$$

$$Q_c = (Q_e + Q_w + Q_s)/3 \tag{5.81}$$

$$Q_c = (Q_e + Q_w + 2Q_s)/4 \tag{5.82}$$

$$Q_c = Q_s . \tag{5.83}$$

Only (5.80) has the same formal accuracy as (5.75), unless the normal derivative of Q is zero when the other formulae have the same accuracy; this is the case on the axis for all quantities except B and V_r which are set to zero there as on all no-flux boundaries. Only (5.82) is equally weighted between the two main submeshes. Generally we employ (5.81), although for ρ we use the form (5.83) on the north and south and the form (5.80) on the east and west. Similar considerations apply to corner points.

The averaging implicit in (5.75) only weakly couples the two main submeshes: the fluxes of mass, momentum and energy are coupled, but the conserved quantities themselves cannot flow from one submesh to the other.

5.2.10 The heat source

We have already discussed (in Sections 2.1.1 and 4.1.2) the problems associated with the incorporation of a realistic heat source into a fluid model, in particular in relation to suprathermal electrons. In this section we describe our simple heating algorithm.

Light travels in straight lines in the negative z direction; it suffices to consider one such line, a row distant r from the axis on the main submesh "2" (Fig.5-18). In a timestep dt a total energy of

$$\left[I(r, z_{max}, t+\tfrac{1}{2}dt) - I(r, 0, t+\tfrac{1}{2}dt)\right] \, dS_r \, dt \qquad (5.84)$$

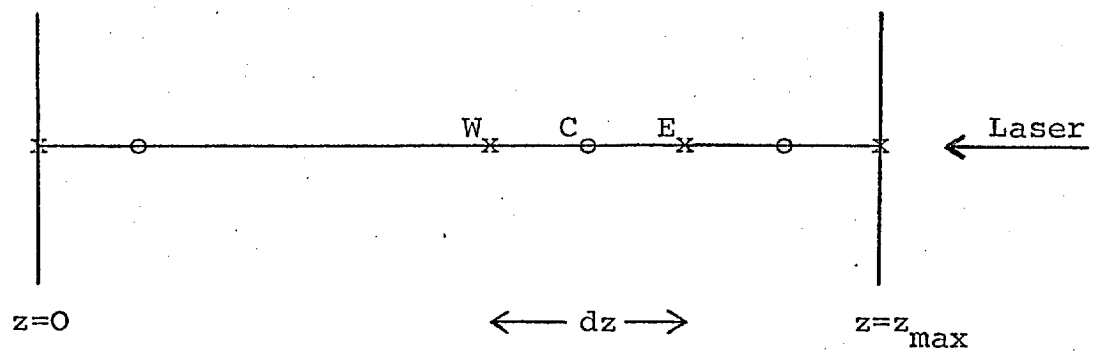

Fig.5-18 Row on main submesh "2" at radius r.

will be absorbed on this row, where dS_r is the surface element perpendicular to the z axis of points at radius r. All rows including the north and south boundaries absorb energy.

For the right - most auxiliary point on the row we set I_e to be the incident intensity, and scanning over main points C from right to left we calculate I_w from I_e as follows:

(a) if $\rho < 0.95\ \rho_{crit}$,

$$I_w = I_e\ (1 - K_{IB}\ dz) \tag{5.85}$$

where ρ and K_{IB} are evaluated at the point C and ρ_{crit} is the critical density. If this gives a negative I_w we set I_w to be zero.

(b) if $\rho \geq 0.95\ \rho_{crit}$,

$$I_w = I_{crit}\ \ d_i \tag{5.86}$$

where I_{crit} was the value of I_e corresponding to the first overdense point and i is one plus the number of overdense points encountered. For example, if the point C of Fig.5-18 is the first overdense point,

$$I_w = I_e \, d_2. \tag{5.87}$$

The d_i are ad hoc dumping factors which will be specified for each run. They are usually zero beyond about i=4.

If points along the row vary between overdense and underdense, which is possible in principle although it has not been observed in our simulations, the count i may start more than once.

Having calculated I_w, the absorption rate P_{las} is determined as

$$P_{las} = (I_e - I_w)/dz. \tag{5.88}$$

The other main submesh ("1") is treated similarly, except that in (5.85) and (5.88) dz is replaced by dz/2 for the end-points.

We use the density cut-off of 0.95 ρ_{crit} to avoid the singularity in the formula (3.43) for K_{IB}. Otherwise there is always a finite chance that some point on our mesh will have a density so close to critical that K_{IB}^{-1} is less than dz, however high the temperature, in which case all the remaining energy will be absorbed at this point. This would be unrealistic because this density is unlikely to be

maintained over more than a fraction of the axial mesh-length. We prefer to control the behaviour at the critical density using the energy dump.

We emphasize the ad hoc nature of the assumed energy dump. There is genuine uncertainty about the correct treatment. It may be a mistake to spread the absorption over several overdense points; when the thermal conductivity is strong it may be satisfactory to dump completely on the first overdense point, but in the presence of large magnetic fields the spatial extent of a hot spot and its subsequent evolution depends somewhat on the spatial extent of the dump.

This heating scheme could be improved: it would be interesting to consider the rôle refraction might play in thin film interactions, and we might also consider focussed rather than parallel light.

5.2.11 Conservation relations

In Section 3.2 we gave integral equations (3.49)-(3.52) for the conservation of mass, (ρV_r), axial momentum and total energy. These should hold also in difference form, with time derivatives replaced by finite differences and integrations replaced by summations. An important feature of the code is that it calculates on each timestep and cumulatively, for each of the two main submeshes and for the main mesh as a whole, all the volume and surface terms appear-

ing in these and another 19 equations. Surface integrals are separated into the contributions from the various boundaries.

The details of the other 19 equations are given in Appendix B. Each equation defines a numerically created energy ε_i corresponding to one stage of the calculation of the (overall) energy equation in difference form; when these equations are added the energy equation obtained includes the sum of the ε_i (ε_{tot}) as the total energy created.

Some of the ε_i are zero to within machine accuracy and provide a check on the coding. Others indicate the errors incurred through spatial and temporal truncation, and one (ε_2) gives the error due to the iterative inversion of the quindiagonal matrices. All of the ε_i provide useful information about which physical processes are dominant.

Omission of terms from the equations, such as the use of $\underline{V}$ rather than $\underline{V}_e$ in the electron energy equation, may generate further errors. However this is not necessarily so because, for example, the incorrect calculation of fluxes such as $\underline{Q}_e$ will clearly not affect any of the ε_i.

Energy is not conserved on either of the main submeshes because of the diffusion equation being differenced on the large diagonal mesh, but on the main mesh as a whole it is conserved to a reasonable accuracy. Total errors ε_{tot} of less than 5% of the absorbed energy are considered satisfactory. Which error terms dominate in

practice depends on the situation; this will be discussed in later chapters - see for example Sections 7.2.4 and 9.3.5.

5.2.12 Arrival times

A standard diagnostic in laser target experiments is the measurement of the ion current at a collector as a function of arrival time. To calculate this we have to assume that the behaviour of the expanding plasma long after the pulse has ended, on timescales typically of the order of microseconds, can be determined from a simulation following no more than a few laser pulse-widths. This assumption may not be unreasonable, because after the end of the pulse, when the plasma is cooled and expanding, a time comes when insufficient thermal energy remains to alter significantly the motion of the accelerated plasma. We therefore calculate at various stages during the simulation arrival time graphs based on the following two assumptions:

(a) every ion in the simulation region moving with a velocity $\underline{V}$ will continue to do so, and

(b) no ion which has left the simulation region undergoes a further change in velocity.

If these graphs converge as the simulation time increases we consider them to provide a reasonable basis for comparison with experiment. Examples of such convergence

are given in Fig.8-6 and Fig.9-10.

Our calculation is simple and unsophisticated, although it could be extended. We consider only the axial velocity V_z, which generally dominates the radial velocity. We consider 96 time intervals, the i^{th} defined as

$$(i-1)\ \Delta t \leqslant t \leqslant i\ \Delta t \qquad (1 \leqslant i \leqslant 96) \tag{5.89}$$

and centred on

$$t_i = (i-\tfrac{1}{2})\ \Delta t, \tag{5.90}$$

where the choice of Δt determines the range and resolution of our arrival time graph. For each fluid element on the main mesh of volume $d\tau$ we add to the i^{th} velocity group $(\rho d\tau/m_i)$ ions, where i is the integer part of

$$1 + L/V_z \Delta t,$$

provided that $i \leqslant 96$. L is the distance to the collector which we take to be 66 cms for comparison with the thin film experiment of Pearlman and Anthes[83]. The ion losses from the boundary and pseudo-boundary cells are similarly accounted.

Smoother arrival time graphs may be obtained by merging the groups into any smaller number of groups which is a factor of 96. The statistics depend on the number of main mesh-points (300-600), the number of fluid elements having left the region (20-30 times the number of timesteps), and the proportions of these with sufficient velocities to

contribute. Resolution of the fast ion peak improves when a significant number of fast ions has been lost.

5.2.13 Miscellaneous considerations

There remain a few minor numerical details whose inclusion is nonetheless important for the satisfactory functioning of the code. Apart from what is described in this and other sections, no adjustments are performed in order to "make the code work". None of the features of this section adversely affects the physics of interest.

(a) Axial heat conductivity. In regions of large $\Omega\tau$ it is possible that the conductivity $K_\perp$, given by

$$K_\perp = \frac{K_o}{1+(\Omega\tau)^2} \quad , \tag{5.91}$$

may vary strongly over the surface of an axial cell, such as is shown in Fig.5-19: $\Omega\tau$ is less than unity only in a very narrow cylinder of radius much less than dr. To avoid an incorrectly high heat flux along the axis between points C and EE we must define $K_\perp$ at the point E to be the average

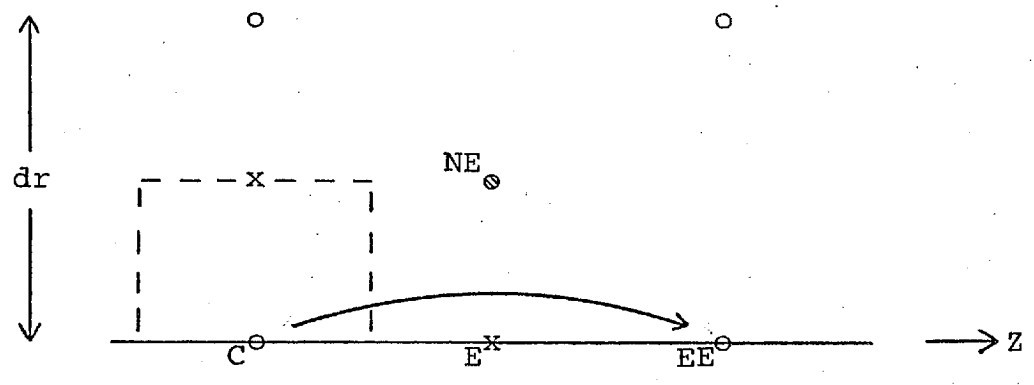

Fig. 5-19 Axial heat flow

of $K_\perp$ over the surface element $r \leq \frac{1}{2}dr$:

$$\bar{K}_\perp = K_o \frac{\log (1+(\Omega\tau)^2)}{(\Omega\tau)^2} , \qquad (5.92)$$

where $\Omega\tau$ is evaluated at the point NE and we are assuming a linear variation of Ω with radius.

A similar technique, which has not been implemented, could be applied to interior points in regions of reversing magnetic field where isolated points sometimes arise with very high conductivities.

(b) Equipartition at high densities. The equipartition time τ_{eq} may vary widely over our simulation region. From Table 4.2, $\tau_{eq} \simeq$ 2nsec in a typical region of interest (T_e = 1keV and $n_i = 10^{21}cm^{-3}$). However, in a region of high number density ($\sim 5x10^{22}cm^{-3}$) and low temperature ($\sim$10eV) τ_{eq} may become very small ($\sim$ 0.04 psec). If τ_{eq} becomes less than the timestep dt, the two temperatures will clearly over-adjust and the explicit equipartition scheme will become unstable. We are not interested in choosing dt small enough to follow equipartition explicitly any more than we are interested in following thermal diffusion explicitly. We simply add to τ_{eq} a small multiple of dt chosen so as to ensure that (T_e-T_i) never reverses sign due to equipartition.

The regions of greatest interest, where equipartition is slow ($\tau_{eq} >> dt$), are not significantly affected. Nor

are regions with $\tau_{eq} << dt$, where our scheme ensures effectively equal temperatures.

(c) Magnetic diffusion at low temperatures. The formula (from Table A.1) for the resistive diffusion time,

$$\tau_\eta = 2.41 \times 10^{-7} L^2 T_e^{3/2}/z, \qquad (5.93)$$

gives a value for τ_η of 1.9×10^5 psec when L = 50μm, T_e = 1keV and z = 1. Over a large range of T_e and L resistivity is unimportant, particularly as large magnetic fields are generally associated with large temperatures. Also, the stability criterion for explicit magnetic diffusion, which requires dt to be smaller than the τ_η obtained by replacing L in (5.93) with the mesh-length, is usually easily satisfied with dt ≈ 1psec. There is one exception, however: on the rear (unheated) side of the thin film described in Chapter 9, T_e is initially low (∿10eV) and the mesh-length dz is very small (2μm). To prevent an instability a maximum resistivity is imposed corresponding to a temperature of 250eV, although a smaller temperature would suffice. This is not a limitation on our physics because significant magnetic fields are only generated in regions where the temperature is well in excess of 250eV. (If the code were to be extended to treat regimes where resistivity is more important, the magnetic field diffusion could be treated by means of the same quindiagonal inversion routines used by the electron temperature.)

It is only in the thin film runs that this restriction on resistivity is necessary.

(d) Radiation loss at low temperatures. Another effect which only occurs at low temperatures is an excessive loss of energy through bremsstrahlung radiation. Bremsstrahlung is another process which is generally unimportant in our model, a typical loss time being 5×10^5 psec. (Table 4.2). However, using the formula for τ_{rad} of Table A.1 and neglecting other effects, we may solve

$$dT_e/dt = - T_e/\tau_{rad} \qquad (5.94)$$

to obtain zero temperature after a time $2\tau_{rad}$; for $n_i = 5 \times 10^{22} cm^{-3}$, $z = 4$ and $T_e = 10eV$, $2\tau_{rad}$ is 124 psec. To avoid this unphysical consequence of using a formula that is in any case inapplicable to such low temperatures we cut out radiation losses at points whose temperatures have fallen to below 20% of the initial (low) temperature.

(c) A slow edge instability. It is well known that the one-sided differencing of the advective equation

$$\frac{\partial f}{\partial t} + V \frac{\partial f}{\partial x} = 0, \qquad (5.95)$$

i.e.

$$\frac{\Delta f}{\Delta t} = - V \frac{(f_c - f_w)}{\Delta x} \qquad (5.96)$$

(which is very similar to the differencing we apply at boundaries - see Fig. 5-20 and Section 5.2.2) is stable

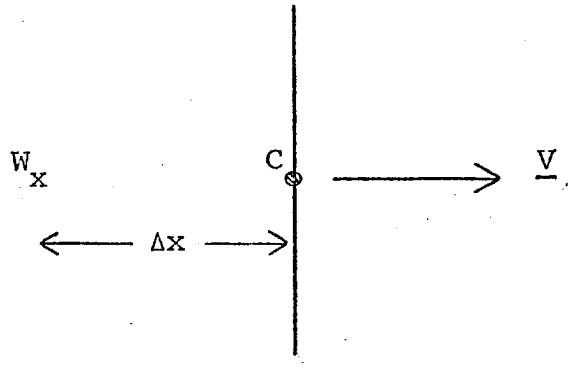

Fig. 5-20 Backwards differencing on the edge.

only if $V \geq 0$. This is usually treated via the amplification factor of Fourier eigenmodes, and may also be seen by considering the (potentially most unstable) mode in which alternate points have perturbations of alternate signs.

If we think in terms of fluxes Vf_W into and Vf_C out of the elementary cell C when $V>0$, or Vf_W out of and Vf_C into the cell when $V<0$, the necessary condition for stability is simply that the flux of f into the cell should not be made proportional to the amount of f already there.

Our boundary difference scheme (Section 5.2.2) is slightly different from that of (5.96), but the same principle applies. If $V_z < 0$ at a point C on (for sake of example) the east boundary as in Fig.5-20, conserved quantities will enter the region in proportion to their values at C. In particular negative axial momentum ρV_z may enter causing a build-up of negative V_z.

Some negative perturbation of normal velocity is needed to commence this process; the instability grows very slowly and might only cross two or three mesh-cells during the whole simulation. In keeping with our earlier remarks (Section 5.2.3) about the physical undesirability of allowing fluxes into our region we avoid this edge instability by disallowing negative normal velocities. When the expanding plasma reaches the boundaries, positive normal velocities are of course ensured.

5.2.14 The Righi-Leduc terms

We described in Section 5.2.4 an explicit scheme for the Righi-Leduc heat flows $\underline{Q}_{e\wedge}$ perpendicular to the temperature gradient. In practice these terms are usually omitted because of their adverse effect on numerical stability, even when they are treated using partial timesteps.

The origin of this problem may be seen by consider-

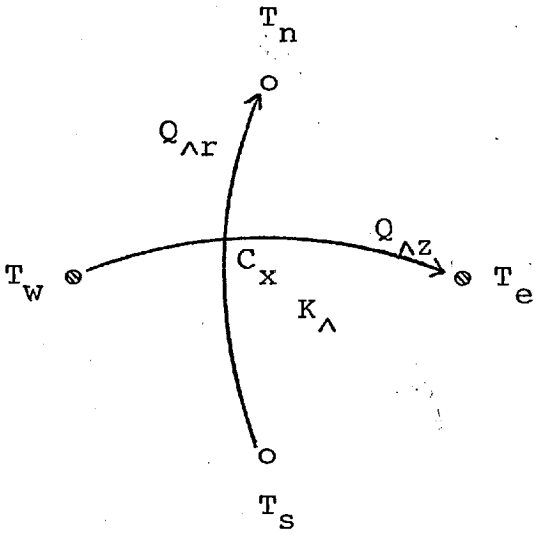

Fig.5-21 Configuration for Righi-Leduc flows.

ing a single point C on the auxiliary mesh, as in Fig. 5-21, with a large $K_{e\wedge}$ dominating the $K_{e\wedge}$ at adjacent points. The general analysis is more involved, but the instability is in fact observed to be associated with configurations similar to Fig.5-21.

The heat flow $Q_{\wedge z}$ between cells W and E is proportional to the temperature difference between T_s and T_n; thus temperature differences on one main submesh will cause large flows of heat on the other submesh, resulting in larger temperature differences there. On the following step still larger differences will arise on the first submesh.

Unlike the implicit difference scheme for diffusion parallel to temperature gradients described in Section 5.2.6, no feedback mechanism operates to damp the perturbations. Stabilization may take place through the $K_{e\perp}$ terms at modest values of $\Omega\tau$, but at large $\Omega\tau$ the $K_{e\wedge}$ terms dominate. At larger $\Omega\tau$ still, $K_{e\wedge}$ and therefore $\underline{Q}_{e\wedge}$ become too low to be important, so that this problem occurs only in an intermediate range of $\Omega\tau$.

To examine this instability in greater detail we consider the effect of neglecting all terms on the right hand side of the diffusion equation (5.24) except those dependent on $K_{e\wedge}$ at the centre point of Fig.5-21. With a slight change of notation (' referring to the new time), the four temperatures shown change as follows:

$$S_n^{-1}(T_n' - T_n) = T_e - T_w = - S_s^{-1} (T_s' - T_s) \qquad (5.97)$$

$$S_e^{-1} (T_e' - T_e) = T_s - T_n = - S_w^{-1} (T_w' - T_w) \qquad (5.98)$$

where

$$S_n = \frac{r_c(\gamma-1)\ K_\wedge\ (dt/N)}{r_n\ n_e k\ dr\ dz} \qquad (5.99)$$

and S_s, S_e and S_w are similarly defined. n_e and $K_{e\wedge}$ are evaluated at C and $K_\wedge$ is understood to be positive here. (For the standard configuration of Fig.2-1 $K_{e\wedge}$ is negative and $K_\wedge = -K_{e\wedge}$). The "stability factors" S_i are to be thought of as ratios of the timestep to the mesh "diffusion" times associated with $K_\wedge$ - compare (5.99) with (5.37) and (5.38).

We define (adjusted) temperature differences

$$\alpha = (T_e - T_w) \qquad (5.100)$$

$$\beta = (T_n - T_s) \sqrt{\frac{S_e + S_w}{S_n + S_s}}\ ; \qquad (5.101)$$

then (5.97) and (5.98) become

$$\alpha' - \alpha = - 2\omega\beta \qquad (5.102)$$

$$\beta' - \beta = 2\omega\alpha \qquad (5.103)$$

where

$$2\omega = \sqrt{(S_e + S_w)(S_n + S_s)}. \qquad (5.104)$$

(5.101) and (5.104) simplify if the four cells surrounding C contain the same mass because all the S_i are then equal. In general ω may be thought of as the average stability factor.

The difference equations (5.102)-(5.103) are the familiar Euler equations for circular motion, and may be generalized to

$$\alpha' - \alpha = - 2\omega \ (\theta\beta' + (1-\theta)\beta) \tag{5.105}$$

$$\beta' - \beta = \ 2\omega \ (\theta\alpha' + (1-\theta)\alpha) \tag{5.106}$$

for a degree of implicitness θ in $\underline{Q}_{e\Lambda}$. They are most conveniently solved by writing

$$z = \alpha + i\beta \tag{5.107}$$

when (5.105) -(5.106) become

$$z' - z = \ 2i\omega \ (\theta z' + (1-\theta)z), \tag{5.108}$$

giving

$$z' = \frac{1 + 2i\omega(1-\theta)}{1 - 2i\omega\theta} \ z. \tag{5.109}$$

For θ=0, as in our partial timestep scheme, $|z'|>|z|$ and the temperature differences α and β grow in time. While this is somewhat mitigated by the choice of a small timestep, growth is inevitable. If a large timestep is chosen (ω large), the amplification factor in (5.109) is large and imaginary and α and β become rapidly bigger on

alternate steps as described earlier.

It is not surprising that the equations of circular motion have been obtained because $\underline{Q}_{e\wedge}$ is associated with the gyrational motion of electrons. On the grounds that these motions are reversible rather than diffusive, we may argue that the Crank-Nicholson scheme ($\theta = \frac{1}{2}$) should be used for $\underline{Q}_{e\wedge}$ in order to ensure that $|z'| = |z|$ in (5.109). However, as we have not implemented such a scheme, we shall not pursue this further.

An example of an attempt to "flux-limit" $\underline{Q}_{e\wedge}$ is given in Section 7.2.1.

5.3 OTHER MAGNETIC FIELD MODELS

We briefly note some of the other numerical work which has been performed on magnetic field generation. The computations described in this section all share the same cylindrical geometry and use similar equations for the six hydrodynamic variables $\{\rho, V_r, V_z, T_e, T_i$ and $B\}$.

Widner [84] calculated magnetic fields in the range 100 kG - 1 MG for laser intensities up to $10^{16} W/cm^2$, and found that early in the simulations $\Omega\tau$ became greater than unity. He used an alternating - direction - implicit method [85], similar to that of Lindemuth [86], in which all fluid variables are simultaneously treated implicitly along rows or columns on alternate timesteps.

Chase et al. [87] simulated anomalous absorption

through enhancing the electron-ion collision frequency near the critical density in proportion to the amount by which the laser intensity exceeded a threshold intensity. They used a non-uniform mesh and investigated various ad hoc prescriptions for reflection and/or focussing. They obtained a long cylindrical cavity in the target when magnetic fields and focussing towards the axis were included, as a result of the reduction of thermal conductivity.

Winsor and Tidman [88] used a split - timestep scheme incorporating the flux-corrected transport technique of Boris and Book[80]. They too found a less rapid penetration of energy into the solid when magnetic fields were omitted. Colombant et al.[89] described an extension to this code which contains an atomic physics model - while principally concerned with x-ray emission, they obtained an off - axis peak of electron temperature due to the reduction in thermal conductivity by large $\Omega\tau$ effects. The enhanced x-ray emission predicted by this code as a result of magnetic fields has already been discussed in Section 2.2.4.

Last but not least, the Livermore Lagrangian code LASNEX[9] includes magnetic field effects.

CHAPTER 6

THE INVERSION OF QUINDIAGONAL MATRICES

We have seen how implicit differencing of the thermal diffusion equation leads to quindiagonal matrix equations such as illustrated in Fig.5-8, and we have already outlined some of the properties of these matrices (Section 5.2.5). It would be futile to attempt their exact inversion; rather we require an iterative method which takes advantage of their sparseness.

In this chapter we describe two such methods: the Alternating Direction Implicit (A.D.I.) method due to Peachman and Rachford [79,90] in Section 6.1, and the Strongly Implicit method due to Stone[91] in Section 6.2. In Section 6.3 we compare the performances of the two methods and compare the A.D.I. results with theory.

6.1 THE ALTERNATING DIRECTION IMPLICIT METHOD

A.D.I. methods for the inversion of matrices arising from elliptic and parabolic problems are familiar, are well documented in the literature (see for example Birkhoff et al.[90] and Varga[79]), and indeed constitute an area of research in their own right. Our treatment is intended to be neither complete nor rigorous; rather, we aim simply to outline the algorithm and gain some insight into why it works and when it works well.

6.1.1 Algorithm

The matrix equation

$$MT = W \tag{6.1}$$

indicated in Fig.5-8 may be written as (5,32)

$$A_q T_{q-m} + B_q T_{q-1} + T_q + C_q T_{q+1} + D_q T_{q+m} = W_q, \tag{6.2}$$

$$(q = 1,2,\ldots,\ell m).$$

We split the matrix M into two matrices V and H:

$$M = V + H \tag{6.3}$$

where

$$(VT)_q = B_q T_{q-1} + \lambda_q T_q + C_q T_{q+1} \tag{6.4}$$

$$(HT)_q = A_q T_{q-m} + \mu_q T_q + D_q T_{q+m} \tag{6.5}$$

and

$$\lambda_q + \mu_q = 1. \tag{6.6}$$

It is clear from Fig.5-7 that V and H operate vertically and horizontally on, respectively, the columns and rows of the matrix form of T. V(or H) may be easily inverted by tridiagonal inversion applied to each of the ℓ(or m) columns (or rows) of T.

Several splittings of the main diagonal are possible, corresponding to different pairs (λ_q, μ_q). One possibility is the "natural" splitting whereby λ_q and μ_q are obtained from

sharing the $(Z_c T_c^n)$ term of the difference equation (5.27) equally between the horizontal and vertical operators; i.e. from (5.32) - (5.35), splitting Z_a as

$$Z_a = \tfrac{1}{2}Z_c - (Z_w + Z_e) \quad + \quad \tfrac{1}{2}Z_c - (Z_s + Z_n), \tag{6.7}$$

we have

$$\lambda_q = \tfrac{1}{2}(1 + A_q + B_q + C_q + D_q) - (B_q + C_q) \tag{6.8}$$

$$\mu_q = \tfrac{1}{2}(1 + A_q + B_q + C_q + D_q) - (A_q + D_q). \tag{6.9}$$

Recalling that A_q, B_q, C_q and D_q are all negative and that the sum of their moduli is less than unity (5.36), but only just so in the case of high conductivity, we see that all the λ_q and μ_q are positive and that both V and H are diagonally dominant, although maybe only just so. Diagonal dominance of V and H ensures the success of the method; sharing the main diagonal of M equally between V and H would risk failure.

An alternative splitting, which we describe as "ratio" splitting, is given by

$$\lambda_q = (B_q + C_q) \;/\; (A_q + B_q + C_q + D_q) \tag{6.10}$$

$$\mu_q = (A_q + D_q) \;/\; (A_q + B_q + C_q + D_q) \tag{6.11}$$

and satisfies the same diagonal dominance requirement. (Our algorithm overrides (6.10)-(6.11) in the strongly diagonal

dominant case by setting $\lambda_q = \mu_q = 0.5$ when $|A_q+B_q+C_q+D_q| < 0.2$.)

Returning to (6.1) and (6.3), the algorithm is defined as the successive solution by tridiagonal inversion of

$$(\omega I + V)\ T^{m+\frac{1}{2}} = (\omega I - H)\ T^{m} + W \qquad (6.12)$$

$$(\omega I + H)\ T^{m+1} = (\omega I - V)\ T^{m+\frac{1}{2}} + W, \qquad (6.13)$$

where T^{o}, the initial guess to the true solution T, is taken as the temperature at the old timestep. ω is an optimization parameter which must be chosen suitably to ensure an acceptable rate of convergence, and I is the identity matrix. (Note that ω=0 would imply that $T^{m+1} = T^{m}$.)

The index m should not be confused with the timestep n, although there is a parallel. Similar equations to (6.12)-(6.13) may occur when the diffusion equation (as distinct from our matrix equation) is solved by an alternating direction (A.D.) technique in which the timestep is split into two halves: m is then the timestep number, ω is proportional to the reciprocal of the timestep dt, W disappears, and V and H are purely spatial operators independent of dt. During the first half timestep the horizontal diffusion is performed explicitly and the vertical diffusion implicitly, and in the second half the directions alternate. Clearly much of the theory of the A.D.I. method carries over into this A.D. method; another parallel is that the optimization parameter ω may be thought of as a pseudo-timestep of relaxation.

Our method of solution may appear to be a partial timestep diffusion scheme and it may be argued that an alternating direction diffusion method involving only one scan (rather than 30 or so iterations) would be more efficient. However the iterations proceed quickly in relation to the overall timestep and a gain in computer time of a factor of only two or three is envisaged. We have not compared solutions from the A.D. method with solutions from our quindiagonal inversion method and will not pursue this point further.

6.1.2 Discussion

We first note that the (ℓm x ℓm) tridiagonal matrix V reduces into ℓ (m x m) tridiagonal submatrices V_ℓ, one for each column of Fig.5-7; all elements adjacent to the main diagonals of these V_ℓ are strictly negative, and the V_ℓ are therefore similar to symmetric matrices and have only real eigenvalues as is shown by Wilkinson [92] (page 336). Because of the diagonal dominance of the V_ℓ, Gerschgorin's theorem (5.51) implies that all of their eigenvalues are strictly positive. Similar arguments apply to H. We therefore have the result, which is important to the following analysis, that V and H have only positive real eigenvalues and a complete set of linearly independent eigenvectors.

The scheme (6.12)-(6.13) is analysed by supposing that the error in the r^{th} iterate T^r is ε^r, where

$$T^r = T + \varepsilon^r. \tag{6.14}$$

ε^{r+1} will then be given by

$$\varepsilon^{r+1} = X\ \varepsilon^r \tag{6.15}$$

where

$$X = (\omega I + H)^{-1}(\omega I - V)(\omega I + V)^{-1}(\omega I - H). \tag{6.16}$$

Successive application of X involves successive multiplication by the factors

$$\frac{\omega I - V}{\omega I + V} \quad \text{and} \quad \frac{\omega I - H}{\omega I + H}, \tag{6.17}$$

each of which is error-reducing. To see this, any error vector may be expressed as a linear combination of eigenvectors e_i of V with eigenvalues v_i and is reduced by the first factor of (6.17) as follows:

$$\sum_i a_i e_i \quad \rightarrow \quad \sum_i a_i \frac{\omega - v_i}{\omega + v_i} e_i. \tag{6.18}$$

The v_i are all positive, and therefore if ω is chosen to be greater than zero all the factors

$$\frac{\omega - v_i}{\omega + v_i} \tag{6.19}$$

will have modulus less than unity. Similarly the second factor of (6.17) is also reducing.

If ω happened to equal a particular one of the v_i, the corresponding eigenvector e_i would disappear from the error vector in one step of (6.18); it is theoretically

tempting to vary ω between iteration steps to equal the different eigenvalues v_i in turn so that after m steps (m being the mesh column length) the error becomes zero. In practice the eigenvalues are unknown and numerous, and schemes exist which use a cycle of values of ω, ranging between estimates for the lowest and highest eigenvalues v_i. This applies when H and V commute, but in the general case, such as is of interest to us, H and V do not share common eigenvectors and the H-factor of (6.17) may reintroduce any eigenvectors e_i removed in (6.18).

Suppose that V has minimum and maximum eigenvalues a and b respectively. Then, for $\omega>0$,

$$-1 < \frac{\omega-b}{\omega+b} \leqslant \frac{\omega-v_i}{\omega+v_i} \leqslant \frac{\omega-a}{\omega+a} < 1, \qquad (6.20)$$

The rate of convergence will clearly depend on either $(\omega-b)/(\omega+b)$ or $(\omega-a)/(\omega+a)$, whichever is larger in magnitude. The optimum ω, namely ω_o, lies between a and b and satisfies

$$-\frac{\omega_o-b}{\omega_o+b} = \frac{\omega_o-a}{\omega_o+a}, \qquad (6.21)$$

giving

$$\omega_o = \sqrt{ab} \; ; \qquad (6.22)$$

for larger values of ω, $(\omega-a)/(\omega+a)$ is closer to 1, and for smaller values of ω, $(\omega-b)/(\omega+b)$ is nearer -1. The optimum ω for the H - factor of (6.17) is in general different - see Section 6.3.2.

To see the physical connection, we know from (6.4) and (6.6), using (5.51), that

$$0 < \min\{ \lambda_q+B_q+C_q \} \leqslant a < b \leqslant \max\{ \lambda_q-B_q-C_q \} < \max \{ 2\lambda_q \} < 2. \quad (6.23)$$

In the case of high conductivity V is only just diagonally dominant and we may expect the minimum eigenvalue a to be very close to zero (and b to be close to $\max\{2\lambda_q\}$). We shall refer to such a matrix V as a "weak" matrix. From (6.21) and (6.22) the optimum rate of convergence is very slow. If however the conductivity is low, or the timestep small, all the eigenvalues of V lie close to the diagonal elements λ_q and an ω of (say) 0.5 would give very rapid convergence. In this case V will be classed as a "strong" matrix. An obvious consequence is that more computer time is required for runs with hotter plasmas.

The same argument applies to H, but the overall situation is complicated because we must expect the total error damping to depend on, at worst, the product of the worst v-factor (6.19) and the worst h-factor. It is only necessary for one of V and H to be a "strong" matrix for good convergence to be possible: supposing V to be "strong", and choosing ω from (6.22), the V-factor of (6.17) will provide good damping despite the H-factor providing virtually no damping at all. In practice however H and V are comparable in "strength".

We remarked that V splits into tridiagonal submat-

rices V_ℓ; in general some of these will be "strong" (e.g. in the high density, low temperature region) and some "weak" (e.g. in the low density hot atmosphere).

As an example of such a "weak" matrix consider the (m x m) matrix A^m of Fig.6-1, which could arise as any of the submatrices of V in the case of Laplace's equation solved

$$A^m = \frac{1}{4}\begin{bmatrix} 2 & -1 & & & & & \\ -1 & 2 & -1 & & & & \\ & -1 & 2 & -1 & & & \\ & & -1 & 2 & -1 & & \\ & & & & & & \\ & & & & & & \\ & & & & & -1 & 2 & -1 \\ & & & & & & -1 & 2 & -1 \\ & & & & & & & -1 & 2 \end{bmatrix}$$

Fig. 6-1 Matrix A^m for Laplace's equation with specified boundary temperatures.

subject to specified temperature boundary conditions. The eigenvectors $X^{(s)}$ and the corresponding eigenvalues $\lambda^{(s)}$ are given by

$$X_j^{(s)} = \sin\{s\pi j/(m+1)\} \qquad (1 \leq j \leq m) \qquad (6.24)$$

and

$$\lambda^{(s)} = \sin^2 \{ \pi s/2(m+1) \}. \tag{6.25}$$

The lowest eigenvalue is

$$a_m = \lambda^{(1)} \simeq \{ \pi/2(m+1) \}^2 \tag{6.26}$$

corresponding to the longest wavelength Fourier mode, and the largest eigenvalue is

$$b_m = \lambda^{(m)} \simeq 1 - \lambda^{(1)} \tag{6.27}$$

corresponding to the most rapidly oscillating Fourier mode. Note how close a_m is to zero; if ω is taken too large it is the longest wavelength mode with eigenvalue a_m which is damped the slowest.

There is one important difference between A^m and the submatrices V_ℓ and H_m: convergence of the A.D.I. method for A^m relies on the boundary conditions. Gerschgorin's theorem (5.51) for A^m tells us only that

$$0 \leqslant a_m < b_m \leqslant 1; \tag{6.28}$$

the reason why a_m does not attain its lower bound is that the top left and bottom right entries in A^m are $\frac{1}{2}$. If these entries were $\frac{1}{4}$, corresponding to no-flux boundary conditions, A^m would be singular with respect to the eigenvector $(1,1,\ldots,1)$.

We see that the A.D.I. method for A^m converges because of the fixed temperature boundary conditions, the rate of convergence deteriorating as the influence of the boundaries decreases (i.e. as m increases, from (6.26)). The

A.D.I. method for our quindiagonal matrix M (which incorporates no-flux boundary conditions) converges because of strict diagonal dominance on the interior, the rate of convergence deteriorating with increasing conductivity or timestep. In the limit of very large conductivity M becomes only marginally diagonally dominant and almost singular, and the computer time required to invert it to a specified degree of accuracy becomes an important consideration.

6.2 THE STRONGLY IMPLICIT METHOD

An alternative and less well-known method for solving equations of the type (6.2) was given by Stone[91]. We shall specify the algorithm below and refer the reader to the original source for a more detailed discussion.

To conform closer to Stone's notation we rewrite (6.2) as

$$B_{jk}T_{j,k-1}+D_{jk}T_{j-1,k}+E_{jk}T_{jk}+F_{jk}T_{j+1,k}+H_{jk}T_{j,k+1} = Q_{jk}, \quad (6.29)$$

$$1 \leqslant j \leqslant J,$$
$$1 \leqslant k \leqslant K,$$

or in matrix notation

$$MT = Q \quad (6.30)$$

as indicated in Fig.6-2. The coefficients $\{B_{j1}, D_{1k}, F_{Jk}, H_{jK}\}$ multiplying out of range temperatures are zero.

The essence of Stone's method is the calculation of a matrix N, in some sense small, such that M+N is easily invertible. Specifically, N is required to satisfy

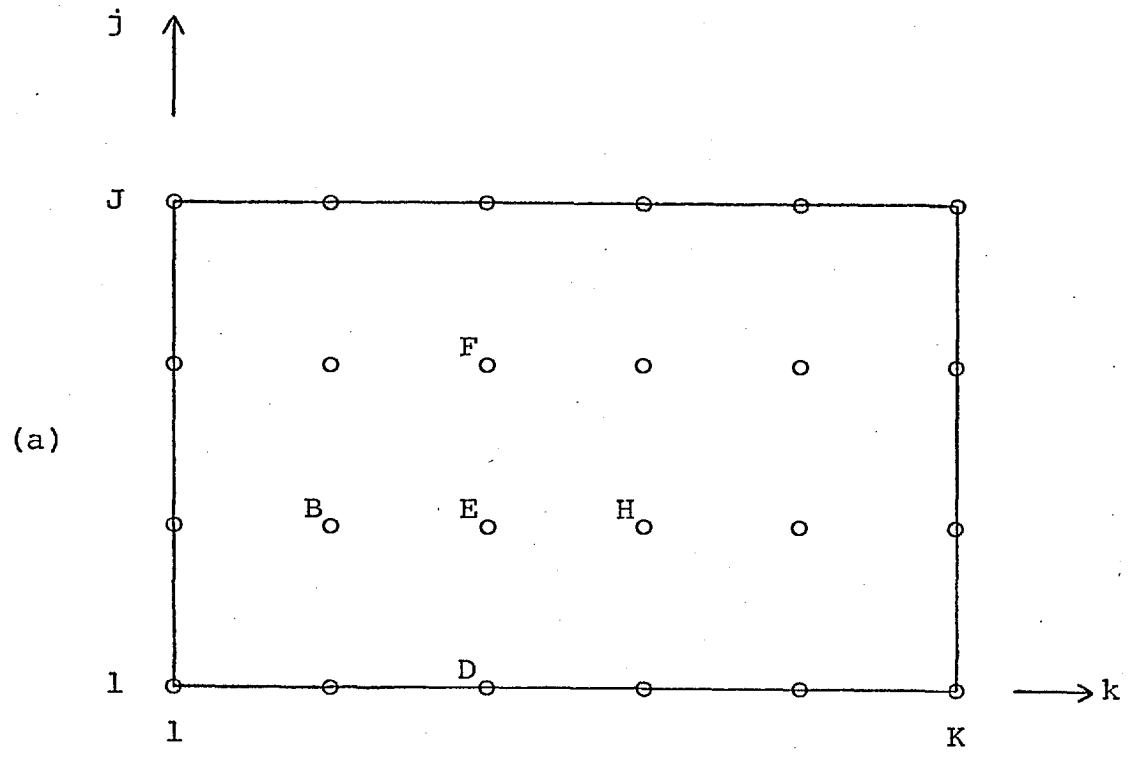

(b) $M =$

$$\begin{bmatrix}
E & F & & H & & & & & & & & \\
D & E & F & & H & & & & & & & \\
 & D & E & F & & H & & & & & & \\
 & & D & E & & & H & & & & & \\
B & & & E & F & & & H & & & & \\
 & B & & & D & E & F & & H & & & \\
 & & B & & & D & E & F & & H & & \\
 & & & B & & & D & E & & & H & \\
 & & & & B & & & E & F & & & \\
 & & & & & B & & & D & E & F & \\
 & & & & & & B & & & D & E & F \\
 & & & & & & & B & & & D & E
\end{bmatrix}$$

Fig. 6-2 (a) Grid configuration for Stone's method;
(b) Stone's matrix M.
In (a) we have taken J=4 and K=6; in (b) J=4 and K=3.

$$M+N = LU, \tag{6.31}$$

where L and U are sparse lower and upper triangular matrices, each containing only three non-zero diagonals, determined by the coefficients $\{b_{jk}, c_{jk}, d_{jk}, e_{jk}, f_{jk}\}$ as shown in Fig.6-3; the diagonals b and f lie in the same positions as the diagonals B and H of Fig. 6-2.

$$L = \begin{bmatrix}
d & & & & & & & & \\
c & d & & & & & & & \\
 & c & d & & & & & & \\
 & & c & d & & & & & \\
b & & & d & & & & & \\
 & b & & c & d & & & & \\
 & & b & & c & d & & & \\
 & & & b & & c & d & & \\
 & & & & b & & c & d & \\
 & & & & & b & & c & d
\end{bmatrix}$$

$$U = \begin{bmatrix}
1 & e & & f & & & & & \\
 & 1 & e & & f & & & & \\
 & & 1 & e & & f & & & \\
 & & & 1 & & & f & & \\
 & & & & 1 & e & & f & \\
 & & & & & 1 & e & & f \\
 & & & & & & 1 & e & \\
 & & & & & & & 1 & e \\
 & & & & & & & & 1
\end{bmatrix}$$

Fig.6-3 Lower and upper triangular matrices.

The coefficients {b, c, d, e, f} are found by scanning through the mesh ($1 \leqslant j \leqslant J$, $1 \leqslant k \leqslant K$) and setting

$$
\begin{aligned}
b_{jk} &= B_{jk}/(1 + \alpha e_{j,k-1}) \\
C_{jk} &= b_{jk}\, e_{j,k-1} \\
c_{jk} &= D_{jk}/(1 + \bar{\alpha} f_{j-1,k}) \\
G_{jk} &= c_{jk}\, f_{j-1,k} \\
d_{jk} &= E_{jk} + \alpha\, C_{jk} + \bar{\alpha}\, G_{jk} - b_{jk} f_{j,k-1} - c_{jk} e_{j-1,k} \\
e_{jk} &= (F_{jk} - \alpha\, C_{jk})/\, d_{jk} \\
f_{jk} &= (H_{jk} - \bar{\alpha}\, G_{jk})/d_{jk}.
\end{aligned}
\qquad (6.32)
$$

If computational space is assigned for the out of range quantities e_{jo} and f_{jo} and these are set to zero, (6.32) may be applied identically to each mesh point without regard to boundaries. Quantities such as f_{ok} and e_{ok} do not cause trouble in the evaluation of c_{1k} and d_{1k} because D_{1k} is zero.

α and $\bar{\alpha}$ are iteration parameters chosen in an attempt to minimise NT; from (6.31)-(6.32),

$$
\begin{aligned}
(NT)_{jk} = {} & C_{jk}\{T_{j+1,k-1} - \alpha(-T_{jk} + T_{j+1,k} + T_{j,k-1})\} \\
& + G_{jk}\{T_{j-1,k+1} - \bar{\alpha}(-T_{jk} + T_{j,k+1} + T_{j-1,k})\}.
\end{aligned}
\qquad (6.33)
$$

If $\alpha = \bar{\alpha} = 1$ and the second derivatives of T vanish, NT is equal to zero. In practice α and $\bar{\alpha}$ should be less than unity, and

are always taken to be equal. It was the formula (6.33) which led Stone to the equations (6.32).

The iterative method is defined by

$$(N+M)\ T^{n+1} = NT^n + Q. \tag{6.34}$$

(6.34) may be solved directly; alternatively and equivalently we may work with residuals R^n, in which case we calculate successively

$$R^n = Q - MT^n \tag{6.35}$$

$$\delta^{n+1} = (M+N)^{-1} R^n \tag{6.36}$$

$$T^{n+1} = T^n + \delta^{n+1}. \tag{6.37}$$

(6.36) is solved in two sweeps: dropping suffices, we define an intermediate vector V,

$$V_{jk} = (R_{jk} - c_{jk} V_{j-1,k} - b_{jk} V_{j,k-1})/ d_{jk}, \tag{6.38}$$

$$(j,k) = (1,1), \ldots, (J,K),$$

and calculate δ:

$$\delta_{jk} = V_{jk} - e_{jk} \delta_{j+1,k} - f_{jk} \delta_{j,k+1}, \tag{6.39}$$

$$(j,k) = (J,K), \ldots, (1,1).$$

No complications arise with (6.38) and (6.39) if we assign dummy storage locations (set zero) for V_{jo} and $\delta_{j,K+1}$. Note also that R,V and δ may share the same locations in core.

Variants on the method include varying α and $\bar{\alpha}$ between iterations (and therefore necessitating the recalcul-

ation of L and U), and altering the direction of scan of one of the indices j and k.

Convergence of the method depends on $(N+M)^{-1} N$ having no eigenvalues of modulus greater than or equal to unity, which should be so if N is in some sense small. This motivated the introduction of α and $\bar{\alpha}$ in (6.33). It is clear that for a strongly diagonally dominant matrix M (e.g. $E_{jk} \equiv 1$ and all the other elements of M much less than one, as is appropriate to our problems when the conductivity is low), all the off-diagonal elements of L and U are small (from (6.32)),and all the elements of N are very small (from (6.33)). Indeed the method converges very rapidly in such circumstances.

In marked contrast to the A.D.I. method, little work has been done on the Strongly Implicit method, although some progress has been made by Bracha-Barak and Saylor[93], Bracha-Barak[94] and Saylor[95]. The main obstacle to analysis is that N is in general a nonsymmetric matrix. In such circumstances trial and error is the easiest means of investigation, and Stone [91] compared his method with the A.D.I. method for various test problems. The A.D.I. method converged somewhat faster (30%) for a simple problem (constant conductivity) but three to four times slower for a difficult problem (widely varying conductivity).

It is interesting to note one similarity between the two methods - they both involve factorization. The inversion of the matrices (ωI+V) and (ωI+H) involves their factorization into upper and lower triangular matrices, similar to the matrices of Fig.6-3 but with the b and f diagonals missing. Stone's factorization appears to be closer to the exact factorization of M and for this reason he describes his method as "Strongly Implicit".

6.3 NUMERICAL TESTS

6.3.1 Comparison of the two methods

We shall compare the A.D.I. and Strongly Implicit methods in two test cases, namely the solutions of the diffusion equation on submesh "1" at two times (36 and 76 psec) during the illustrative run 7A to be described in the next chapter. This run has been chosen because of the complexity of the matrices of coefficients A-D of (6.2) that form the quindiagonal matrix M. At 36 psec a hot spot has just formed and at 76 psec the hot spot and reversed magnetic field structure is well-developed.

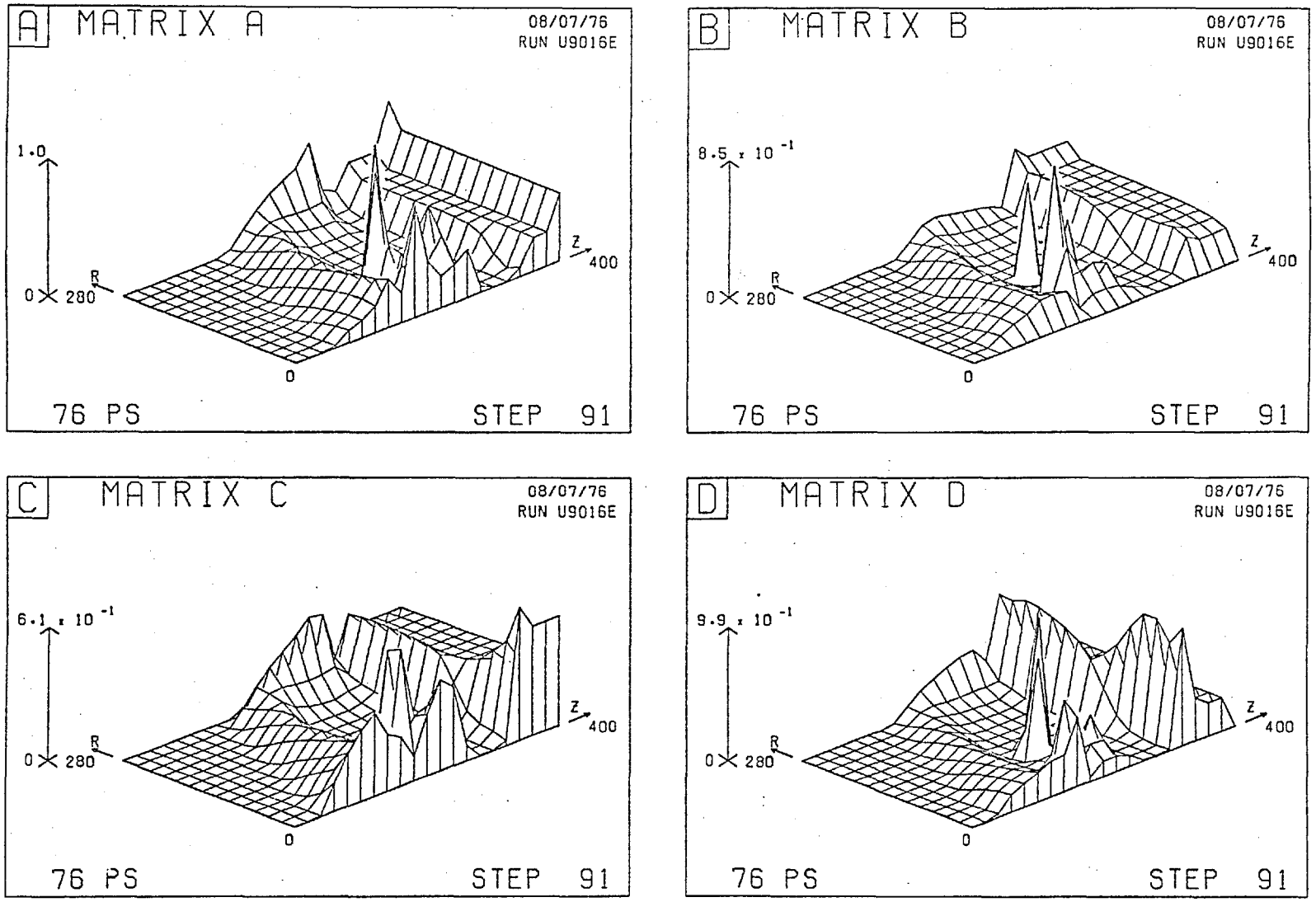

Fig.6-4 Matrices A - D for the test problem at 76 psec.

These matrices (actually their negatives) are plotted in Fig.6-4 on submesh "1" at the later time. The extreme variations of conductivity over the mesh are reflected in the variations of the coefficients A-D, although our normalization ensures that they can only vary in the range -1 to 0. We list below details of the origin of these matrices although doing so presupposes an understanding of the results of Run 7A. The plots all show the following main features:

(i) In the cool solid region near the west boundary all of A-D are approximately zero.

(ii) In the zero initial density gradient region near the east, magnetic field growth is minimal and the conductivity is very large; thus

$$|A+B+C+D| \simeq 1; \qquad (6.40)$$

in fact, at a representative point, the sum is 0.995.

(iii) In the region of large $\Omega\tau$ all of A-D are reduced to nearly zero.

(iv) There are a few odd points on the auxiliary mesh where $\Omega\tau$ reverses sign and happens to take a value very close to zero. These are readily identifiable by the spikes they produce in the plots of A-D: at one point A is -0.998 and B-D are all effectively zero. The result will be temperature equalization between the mesh points on either side of these auxiliary points. These spikes are only present

in the 76 psec case.

(v) On each edge the elements of one matrix become identically zero, and the other matrices are correspondingly affected. For example, D is zero on the east and A is enhanced there.

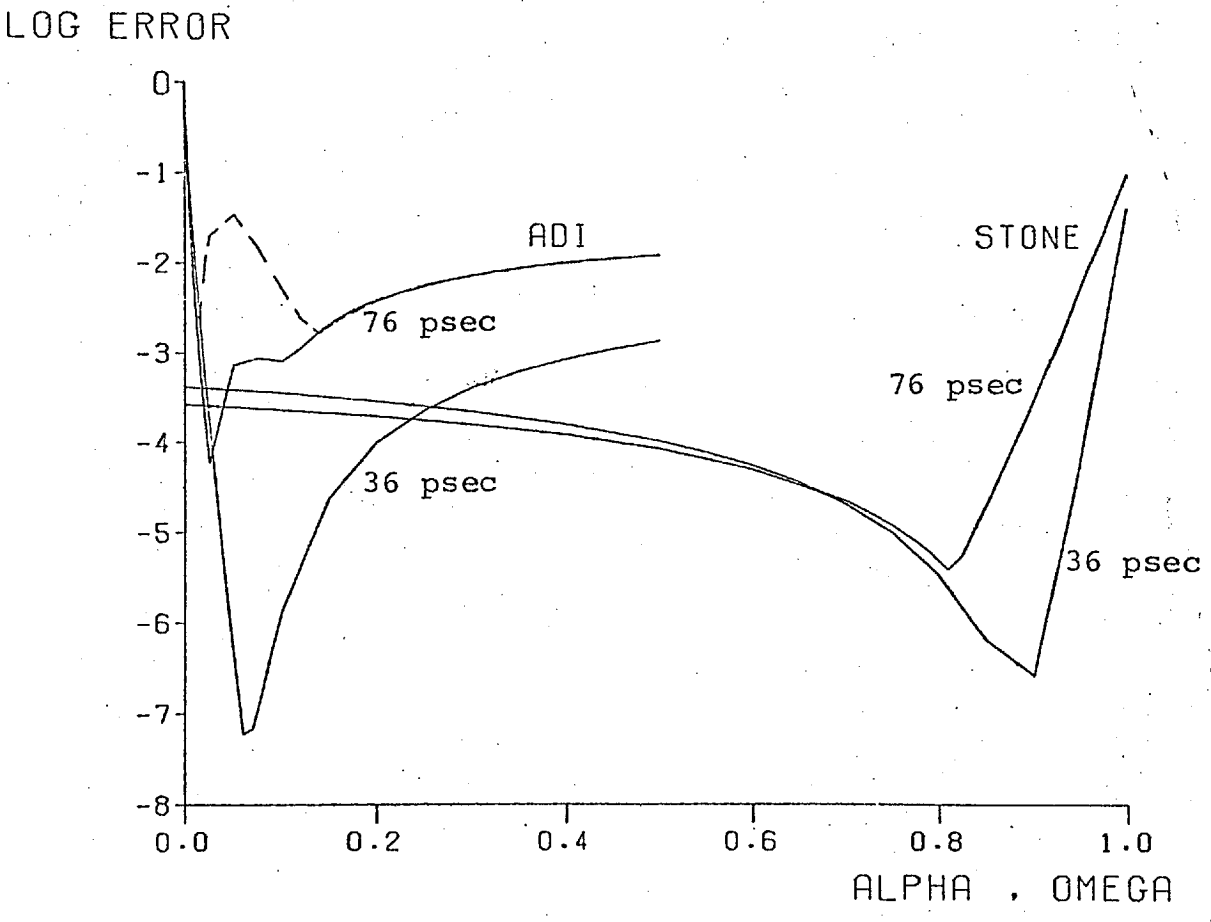

Fig.6-5 Error after 50 iterations from the A,D,I method and Stone's method.

Proceeding to the comparison, our results are summarized in Fig.6-5. We plot the logarithm (to base 10) of the modulus of the maximum fractional error ε remaining after 50 iterations, for each method and at each of the two times. Along the x-axis are the iteration parameters, α of Stone's Strongly Implicit method and ω of the A.D.I. method. The dotted A.D.I. line for the "harder" matrix at 76 psec corresponds to the "ratio" splitting (6.10)-(6.11) and the solid A.D.I. lines to the "natural" splitting (6.8)-(6.9). For the "easier" matrix at 36 psec the choice of splitting makes no difference to the convergence rate (to within about 1%).

Both methods have an optimum rate of convergence for a suitably chosen optimization parameter, converge somewhat slower if the parameter is varied in one direction, and dramatically slower if it is varied in the other direction. The similarity in form is remarkable and may be indicative of a relationship between the two methods, but we have not pursued this point further.

The optimum iteration parameter is difficult if not impossible to determine. It varies between runs, and as we see in Fig.6-5 within runs; in practice it is chosen according to intuition and experience. While at 36 psec the A.D.I. method compares well with Stone's method for both optimal and non-optimal choices of α or ω, at 76 psec its rate of convergence is markedly lower and the best choice

of iteration parameter is unlikely to be made.

While satisfactory results may be obtained from the A.D.I. method, we prefer Stone's method on the following grounds:

(a) The rate of convergence is insensitive to a non-optimum choice of α. In fact we have always taken α to be 0.5.

(b) Stone's method is less sensitive than the A.D.I. method to "difficult" matrices. (Stone found this too for his model problems, as we remarked earlier).

(c) As coded, Stone's method requires slightly less core storage and computer time per iteration.

6.3.2 Comparison of A.D.I. results with theory

We conclude this chapter with an attempt to understand the A.D.I. curves in terms of the theory of Section 6.1.2. The eigenvalues of the V and H matrices are the eigenvalues of the tridiagonal submatrices V_ℓ and H_m; they have been calculated by Wright [96] by means of an efficient generalized root solver, for the matrices at 36 and 76 psec and for each splitting of the main diagonal. They are represented in Fig.6-6, for the "natural" splitting at 76 psec, as follows. Each column on the mesh contains m (=14 here) points and is operated on by the corresponding V_ℓ which has m eigenvalues; these eigenvalues are plotted on this column in ascending order (Fig.6-6a). Similarly the eigenvalues of H (Fig.6-6b) are plotted in ascending order on the corresponding rows.

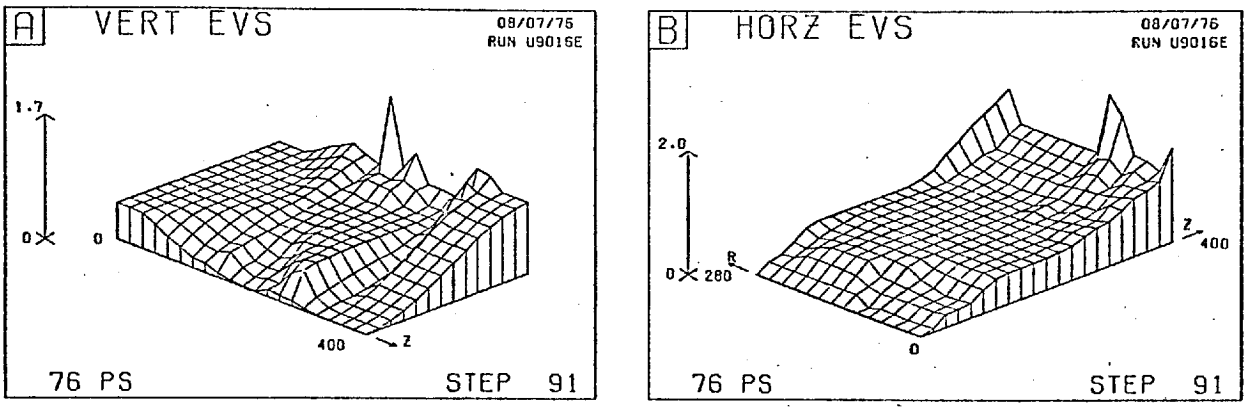

Fig.6-6 Eigenvalues of the matrices V and H.

Both H and V have several eigenvalues of about 0.5, corresponding to the region near the solid with very small conductivity. For example, the submatrices V_1 and V_2 are 0.5 times the unit (m x m) matrix to within one part in 10^4. The minimum eigenvalues of H and V occur on row 6 and column 12 respectively; it is no coincidence that it is at (6, 12) that A has its largest value (-0.998). It appears to be this single point of high conductivity which causes the slow convergence.

The minimum and maximum eigenvalues a and b of V and H for the four cases are given in Table 6-1. According to (6.22) the optimum iteration parameter ω_o for the A.D.I.

Table 6.1 Minimum and maximum eigenvalues a and b for vertical and horizontal matrices V and H.

Time	Matrix	Splitting	a	b	$\sqrt{ab}$
36 psec	V	Natural	0.0031	1.7064	0.073
		Ratio	0.0029	1.7080	0.070
	H	Natural	0.0032	1.4274	0.068
		Ratio	0.0032	1.4450	0.068
76 psec	V	Natural	0.0011	1.7200	0.043
		Ratio	0.0002	1.7376	0.017
	H	Natural	0.0018	1.9903	0.060
		Ratio	0.0031	1.9916	0.079

method is $\sqrt{ab}$; this is given in the right hand column. For the "easier" matrices at 36 psec, V and H (and therefore their eigenvalues) depend only weakly on the choice of splitting, which is consistent with the convergence rate being effectively independent of the splitting. Moreover, ω_o is about the same for V and H ($\simeq$ 0.07), consistent with the A.D.I. curve of Fig. 6-5 at 36 psec having a single minimum at $\omega \simeq 0.065$.

The situation for the "harder" matrix at 76 psec is distinctly different. For the "ratio" splitting the matrix V has a very small minimum eigenvalue of 0.0002 and therefore a lower ω_o than H. For the "natural" splitting the values of

ω_o still differ but by a smaller margin.

This suggests an explanation for the form of the A,D,I. curves of Fig.6-5 at 76 psec. For the "ratio" splitting (the dotted curve) there are two minima: one at $\omega \simeq 0.015$ due to optimum damping by the V-factors (6,19) predicted in Table 6.1 for $\omega_o = 0.017$, and the other at $\omega \simeq 0.14$ due to optimum damping by the H-factors predicted for $\omega_o = 0.079$. For the "natural" splitting there is a definite minimum at $\omega \simeq 0.025$ corresponding to $\sqrt{ab}$ for V being 0.043, and another less marked minimum at $\omega \simeq 0.1$ corresponding to $\sqrt{ab}$ for H being 0.060. On either side of the range of ω described in this paragraph the two curves merge.

This explanation provides only reasonable agreement between theory and practice. We should not expect more as the V and H operators of (6.17) do not commute and may therefore regenerate each others' eigenvectors. (Also we cannot be sure that the asymptotic rate of convergence will be the same as the rate after 50 steps.) However this line of argument affords some insight into the A,D,I. method.

The "natural" splitting is believed to be superior because it ensures that the lower bound for the minimum eigenvalue $a_{,,}$ as obtained from Gerschgorin's theorem (5,51), is the same for V and H; the "ratio" splitting is derived from a different requirement, that the proportional diagonal dominance as measured by the ratio of the diagonal element

to the sum of the off-diagonal elements should be the same for V and H. It is clear from (6.22) that the minimum eigenvalue is the most significant in determining convergence.

We conclude by indicating how the best value of ω might be estimated in practice, using the "natural" splitting scheme. We may obtain the lower bound $\tilde{a}$ for the minimum eigenvalue of either V or H from (6.8):

$$\tilde{a} = \min \{ \tfrac{1}{2} (1+A_q + B_q + C_q + D_q) \}, \qquad (6.41)$$

estimate the maximum eigenvalue as 2, and use $\omega=\tilde{\omega}$ where

$$\tilde{\omega} = \sqrt{2\tilde{a}} \ . \qquad (6.42)$$

Using (5.33), (5.35), (5.29)-(5.30) with N=1, and (5.37), we find that

$$\tilde{a} = \min \{ \tfrac{1}{2} \frac{\tau_c}{\tau_c + \theta dt} \}. \qquad (6.43)$$

For the fully implicit scheme (θ=1) and with the timestep dt much greater than τ_{min}, the minimum τ_c on the mesh,

$$\tilde{a} = \tau_{min} \ / \ 2dt, \qquad (6.44)$$

so that (6.42) gives

$$\tilde{\omega} = \sqrt{\tau_{min} \ /dt}. \qquad (6.45)$$

Using (6.21) and assuming that the damping factors due to V and H are similar, the error decreases as

$$e^{-2\tilde{\omega}n}$$

where n is the number of iterations. The computational work required to reach a specified degree of accuracy is proportional to the square root of the number of steps that would be required by an explicit partial timestep scheme.

CHAPTER 7

HOT SPOTS

The major result that hot spots in the electron temperature distribution may arise from the reduction in thermal conductivity caused by large magnetic fields has already been reported (Appendix C). In this chapter we describe this phenomenon in greater detail.

We commence (Section 7.1) with an extensive account of a basic run (7A) which exhibits distinctive hot spot behaviour and whose parameters are very similar to those of the illustrative run of Appendix C. The features of this run are in marked contrast to those of three other runs (7B, 7C, 7D) described in Section 7.2 in which, respectively, the laser power is reduced, the beam is less sharply focussed, and magnetic field effects are switched off. It is evident that sufficient laser intensities together with sufficient non-uniformities in the irradiation are necessary for hot spot formation.

The first of the comparative runs (7B) was performed with the Hall terms and the Righi-Leduc terms (which are usually omitted from the calculations) included, and the difficulties associated with the latter terms are noted.

7.1 AN ILLUSTRATIVE RUN

7.1.1 Specification of Run 7A

We consider a deuterium plasma occupying the simulation region

$$\begin{aligned} 0 \leqslant r \leqslant r_{max} &= 280\ \mu m \\ 0 \leqslant z \leqslant z_{max} &= 400\ \mu m\ , \end{aligned} \tag{7.1}$$

which is covered by 29 mesh points radially and 41 axially.

We assume an initial plasma with a small arbitrary temperature ($T_e = T_i = 50$ eV), and with an electron number density (Fig. 7-1) which is a uniform $n_e = 40 n_c$ for $0 \leqslant z \leqslant 100\ \mu m$, drops exponentially through the critical density n_c at $z = 200\ \mu m$ to $n_c/40$ at $z = 300\ \mu m$, and is uniform for $300 \leqslant z \leqslant 400\ \mu m$. This gives a modest density lengthscale, the distance between critical and quarter critical densities being 38 μm; smaller density lengthscales will be considered in Chapters 8 and 9.

We consider the multiple beam configuration described in Section 3.1.2, so that the north boundary ($r = r_{max}$) is a "no-flux" boundary of zero B and V_r.

The incident Nd-glass laser profile at $z = z_{max}$ is Gaussian:

$$I(r,t) = P(t) \frac{e^{-r^2/r_b^2}}{\pi r_b^2 \left(1 - e^{-r_{max}^2/r_b^2}\right)}\ , \tag{7.2}$$

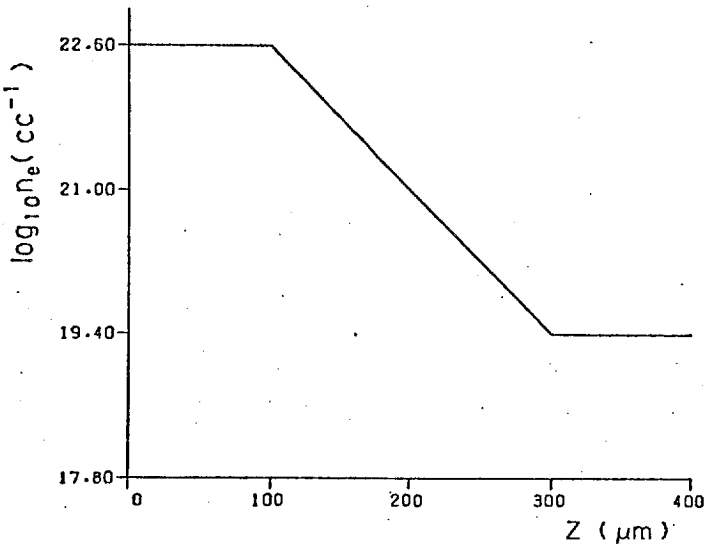

Fig.7-1 Initial electron number density distribution n_e (electrons/cc).

with the beam radius r_b = 100μm and the laser power rising linearly with time to 1.83×10^{12}W at 40 psec and thereafter remaining constant. The peak intensity is then 5.8×10^{15} W/cm^2. Current experiments may achieve this intensity, but with smaller focal spots and lower laser energies than the 100 J that we are depositing in the first 75 psec. Comparison with figures quoted for experimental intensities should take into account that we absorb 100% of the incident energy.

The dumping factors (5.86) at the critical density are taken as

$$d_i = 1.0, 0.6, 0.2, 0.1, 0.0 \quad \text{for} \quad i = 1,2,3,4,5. \qquad (7.3)$$

The equations listed in Chapter 3 are implemented in full, except that the electron Righi-Leduc terms (those involving $K_{e\wedge}$ in (3.17) and (3.18)) are omitted and $\underline{V}$ is used in place of $\underline{V}_e$ in (3.48) and (3.56). $\underline{J}$ is retained

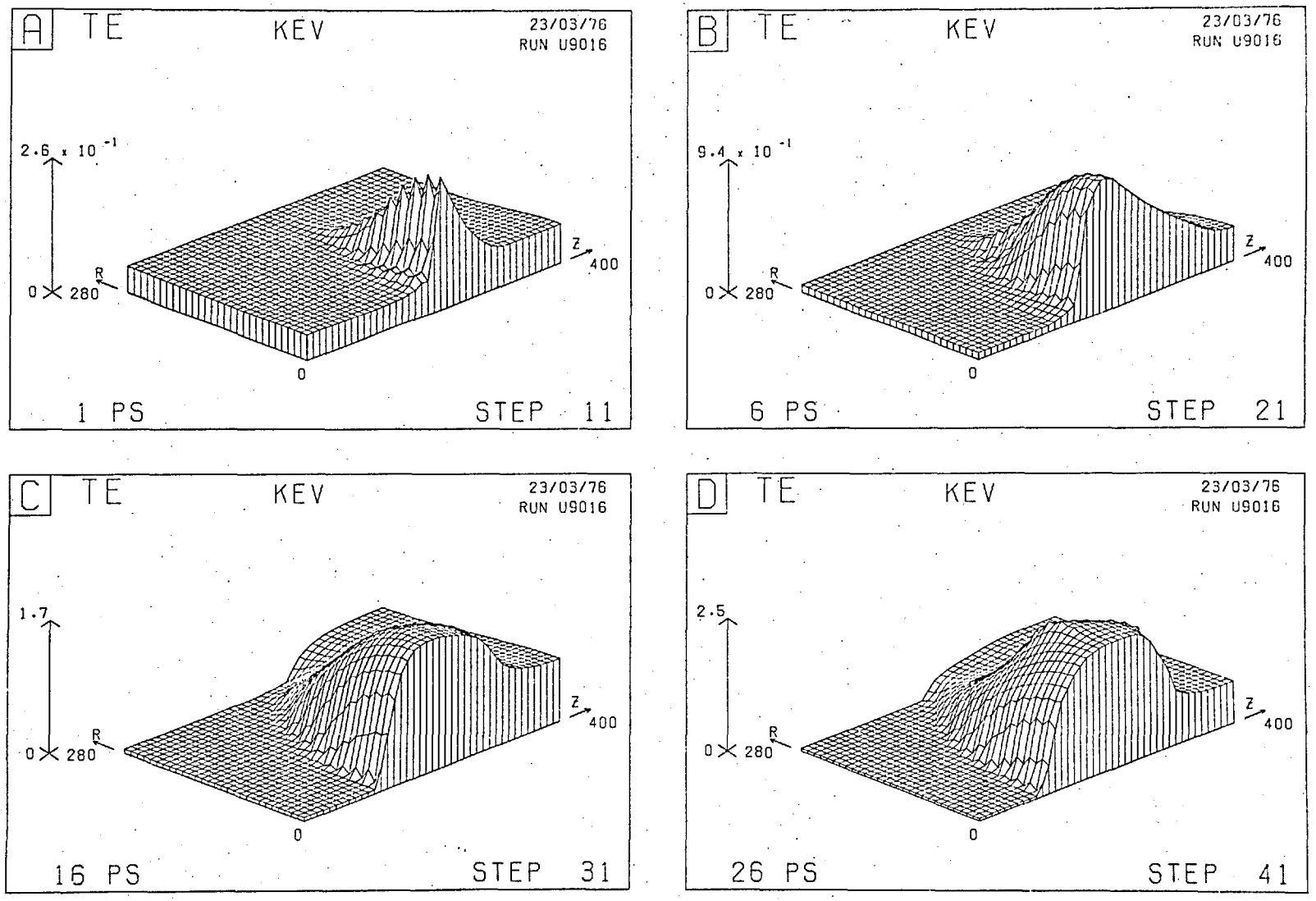

Fig.7-2 Run 7A, T_e at (a) 1 psec (b) 6 psec (c) 16 psec (d) 26 psec

where it appears explicitly, i.e. in the JxB force and in resistivity.

The timestep* dt starts with the small value of 0.1 psec so as to follow the inverse bremsstrahlung heating, is increased to 1 psec to follow the growth of the fluid variables, and is later decreased to follow the large ablation velocities.

Having specified the pertinent parameters required by Section 5.1.2, we proceed to a consideration of the results.

7.1.2 Results

Without doubt the most important of the six major variables is the electron temperature, as it is this which drives ablation, compression, equipartition and magnetic field generation. We therefore commence by describing its development.

The early heating stages are shown in Fig.7-2. In these perspective plots the mesh may be viewed from any of the four corners, although the origin is usually chosen to be the nearest point. Here the laser is incident along the z-axis from the right and the solid is on the left. The axis lengths are given in microns, and all plots are normalized to the maximum value on the mesh which is indicated by the arrow on the left.

---

*The term "timestep" is used variously to denote a point in time when all variables are defined, the period of time between two such points, and the value of dt. This is unlikely to cause confusion.

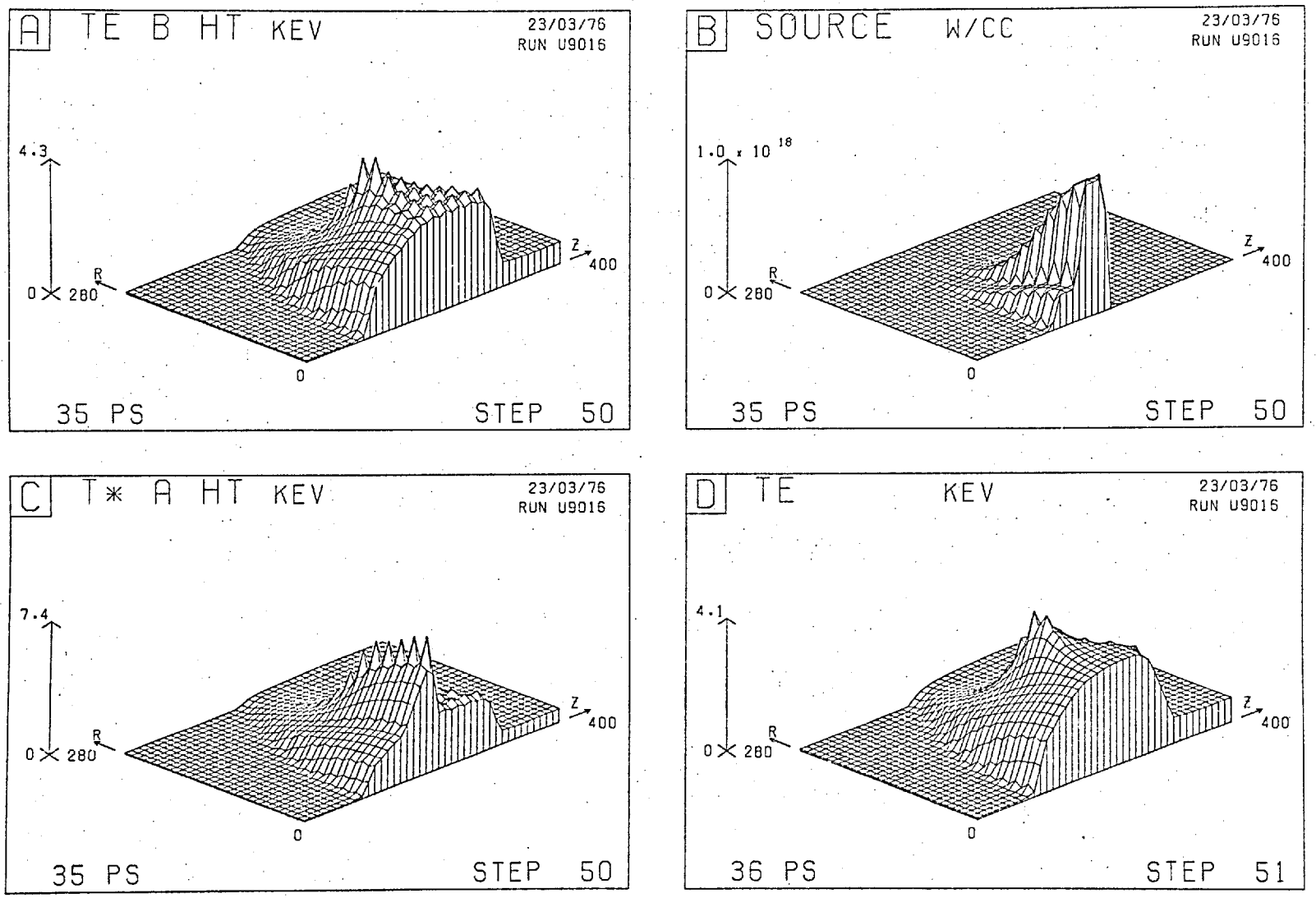

Fig.7-3 Run 7A. Details of the absorption process at 35 psec,

(a) T_e before heating (b) Heat source

(c) T_e after heating (d) T_e after diffusion

Very early (1 psec, Fig.7-2a) heating is by inverse bremsstrahlung, mostly on the underdense half of the density ramp. Soon (6 psec, Fig.7-2b) most of the laser energy is dumped and thermal diffusion towards the east boundary (z = 400μm) developes; as $\Omega\tau$ grows it first restricts the diffusion in the low density region giving rise to the hump on the axis at 16 psec (Fig.7-2c), and then restricts the diffusion in the heating region (26 psec, Fig.7-2d) where the beginnings of a hot spot can just be perceived with a peak temperature of 2.5 keV. We also note a thermal front advancing slowly towards the solid.

The details of the assumed absorption process are illustrated in Fig.7-3. During the 9 steps between steps 41 and 50 the distributions of T_e on the two main submeshes have decoupled somewhat, as is seen in Fig.7-3a. The heat source (Fig.7-3b) may be seen to correspond to (7.3) with heat deposited in a 4:4:1:1 ratio on the first four overdense points on each main submesh. No heat is actually deposited on the auxiliary mesh,but averaged values are assigned to the auxiliary points for display purposes. It is apparent that the heating increment from inverse bremsstrahlung is negligible.

After the heating stage (Section 5.2.4, stage (a)) the intermediate temperature T_e^* is as shown in Fig.7-3c. Hydrodynamics, equipartition and radiation are also included in this stage but the heating is dominant. The peak T_e^*

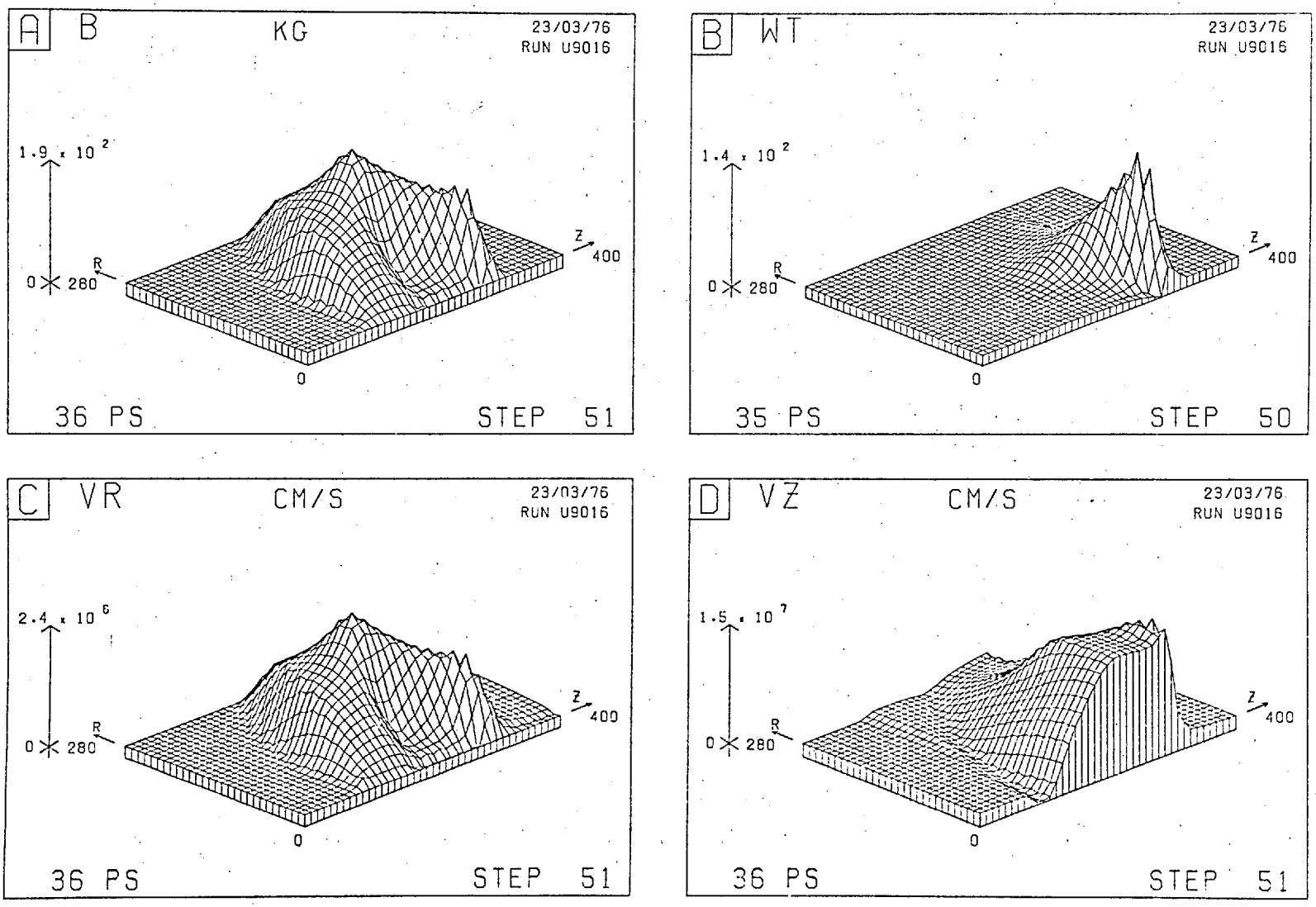

Fig.7-4 Run 7A. At 36 psec: (a) B (b) $\Omega\tau$ (c) V_r (d) V_z

(7.4 keV) is substantially larger than the previous T_e (4.3 keV), but because T_e^* is never used to calculate coefficients or drive other variables this does not matter. The quin-diagonal diffusion stage is then applied to the diagonal mesh (Fig.5-2), yielding the new T_e at the next timestep (Fig.7-3d) with a peak of 4.1 keV.

Over this timestep the peak values of T_e on the south rows of submeshes "1" and "2" (Fig.5-1) changed from 3.389 and 2.987 keV to 3.167 and 3.160 keV respectively, the decoupling therefore being decreased from $\pm$6% to effectively zero. The decoupling at the incipient hot spot (i.e. the difference between the peaks on each submesh) decreased from $\pm$13% to $\pm$6%, thereby causing a slight decrease in the peak temperature.

In addition we would expect there to be some difference between the diagonal and normal solutions because of the different coefficients of conductivity in the two cases, particularly at the advancing heat front.

Fig.7-3d is similar to Fig.1b of Appendix C. There the absorption region is larger and the peak temperature is less (3.1keV).

In Fig.7-4 we show some of the other variables at the same time, 36 psec. The magnetic field, with a peak of 190 kG (Fig.7-4a), and the radial velocity, with a peak of 2.4×10^6 cm/sec (Fig.7-4c), have virtually identical distributions because in our configuration they are both responses

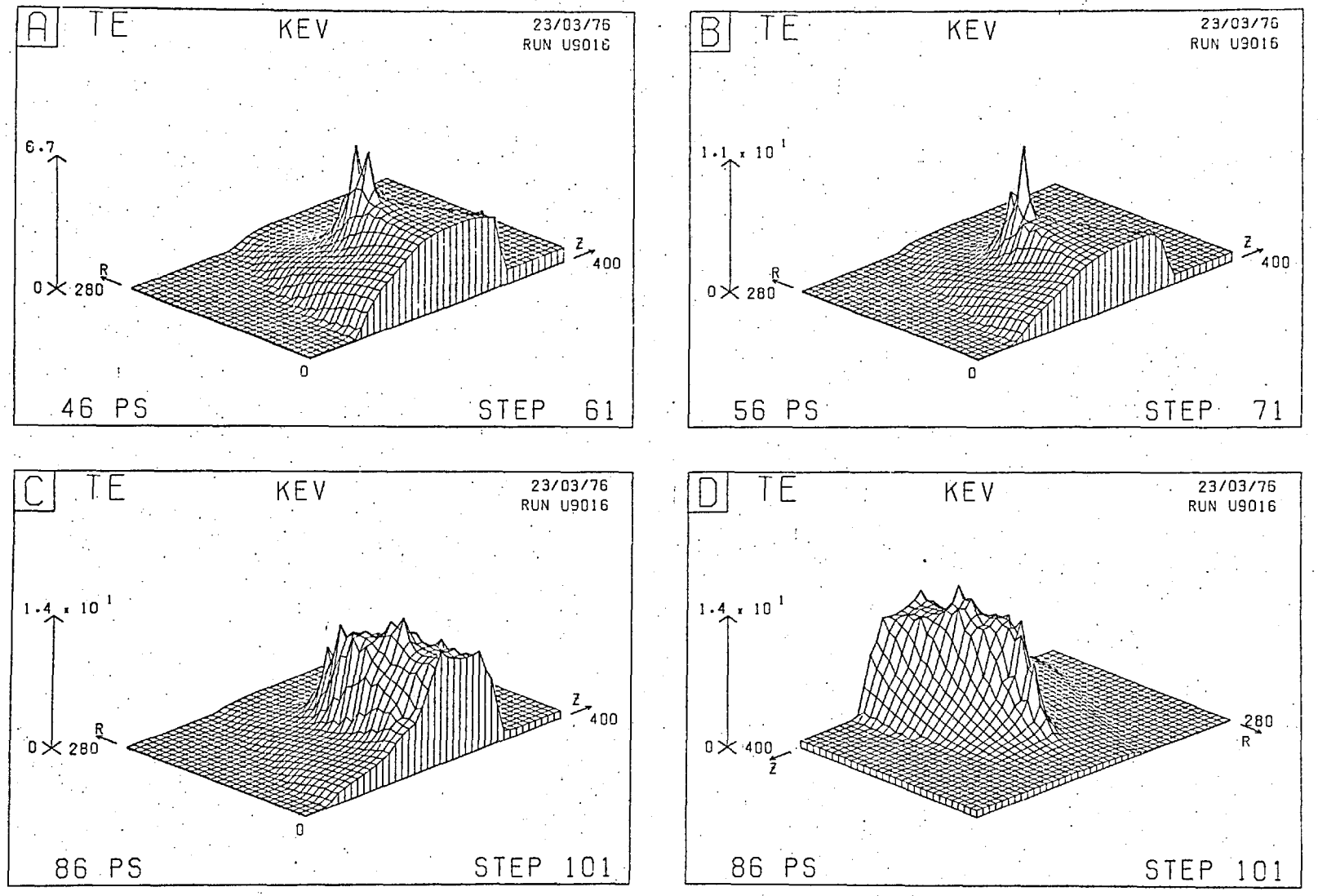

Fig.7-5 Run 7A. T_e at (a) 46 psec (b) 56 psec (c), (d) 86 psec

to $\partial T_e/\partial r$. (We have plotted the negative of B.) Only later, on the longer timescales of density changes, do their driving terms differ.

A notable feature is the dip of B beginning to form on the south side of the hot spot, as a result of a reversed $\partial T_e/\partial r$. A reversed magnetic field configuration will be set up, although the generation of large reversed fields is hindered by small values of $\Omega\tau$ and therefore good conductivity in the region of reversal. At the same time the enhanced $\partial T_e/\partial r$ north of a hot spot enhances magnetic field generation there.

$\Omega\tau$(Fig.7-4b)*, varying inversely with n_e, is greatest at the low density end of the density ramp, and cuts off sharply for $z \geqslant 300\mu m$ where there is effectively no density gradient and no magnetic field. The hot spot does not form in the region of largest $\Omega\tau$ because there is no heat source there.

The distribution of V_z (Fig.7-4d) shows two main features - ablation from the region where T_e and $\partial n_e/\partial z$ are large, and a weak compression near the solid. The plasma acceleration is in its early stages as velocities ten times greater than the 1.5×10^7 cm/sec here will be reached later. The product of the present velocity with the simulation time is 5.4μm, indicating why the density distribution has so far hardly been affected.

---

*As is the case with the magnetic field, we always plot the negative of $\Omega\tau$.

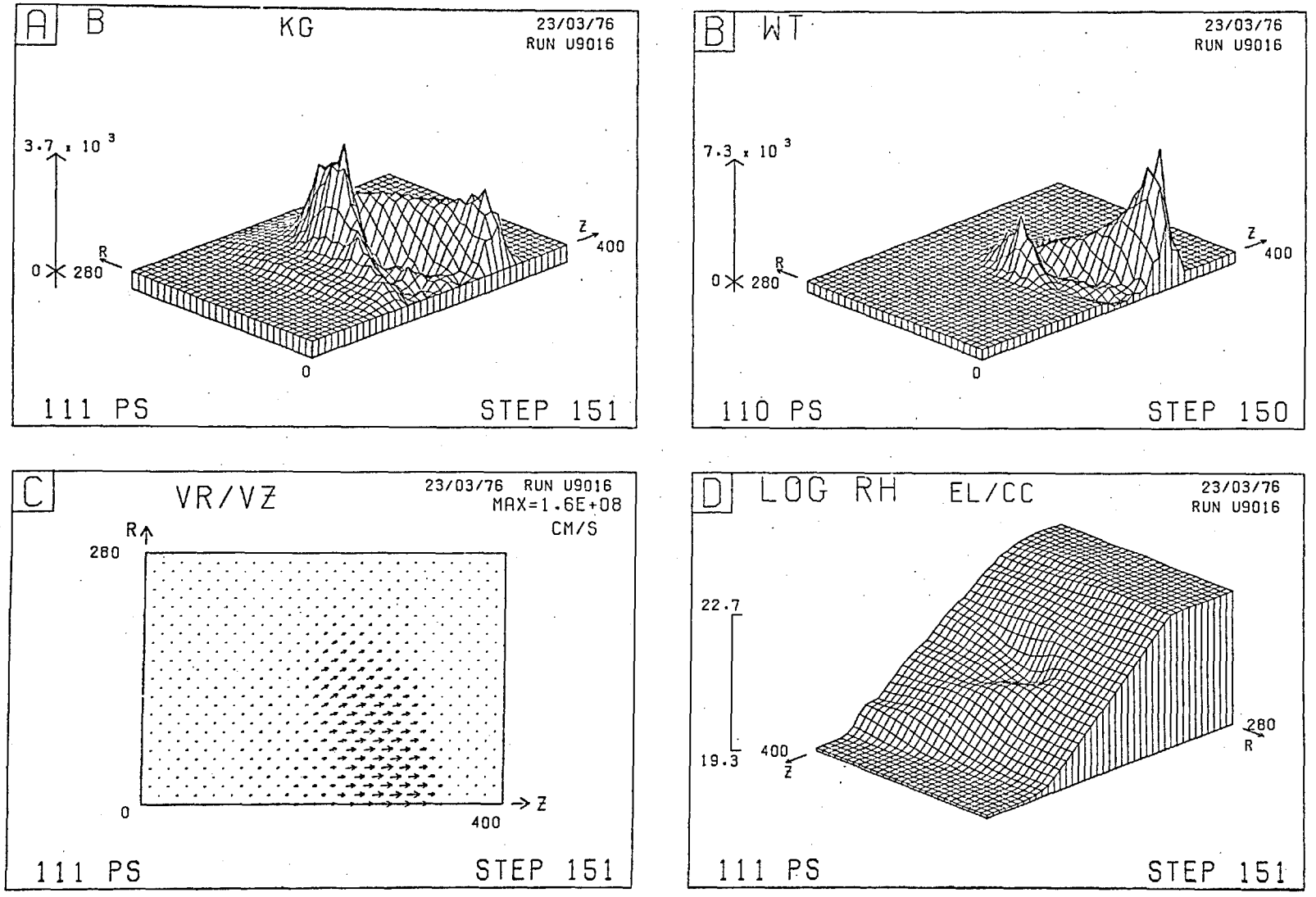

Fig.7-6 Run 7A. At 111 psec: (a) B (b) $\Omega\tau$ (c) $\underline{V}$ (d) $\log_{10} n_e$

The hot spot is shown in Fig.7-5, the peak temperature increasing to 6.7 keV at 46 psec, 11 keV at 56 psec and 14 keV at 86 psec. The point of maximum temperature tends to move away from the axis (compare with Fig.7-3d), because the region of largest magnetic field always occurs just north of the hot spot as indicated above. This tendency is limited by the radial extent of the heat source.

By 86 psec the reversed field south of the hot spot is large enough to inhibit the conductivity there, and the hot spot increases in spatial dimensions as shown in Fig.7-5c, or in Fig.7-5d where it is viewed from a different angle. There must be a conduction path bordering the region of reversed $\Omega\tau$, but this may be too narrow to be of significance: in this case $\Omega\tau$ varies from being large and positive to large and negative at adjacent mesh points (50 $\rightarrow$ -70 for example). There is a finite chance numerically of obtaining an $\Omega\tau$ of order unity, in which case adjacent points couple. (This was the case with the second of the quindiagonal matrices discussed in Section 6.3.)

Two other effects increase the spatial extent of the hot spot: ablation and the slowly changing critical density surface.

The reversal of B and $\Omega\tau$ is shown at a later time (111 psec) in Fig.7-6(a-b). The peak B is substantial (3.7 MG), and the values of reversed $\Omega\tau$ are greater than might-

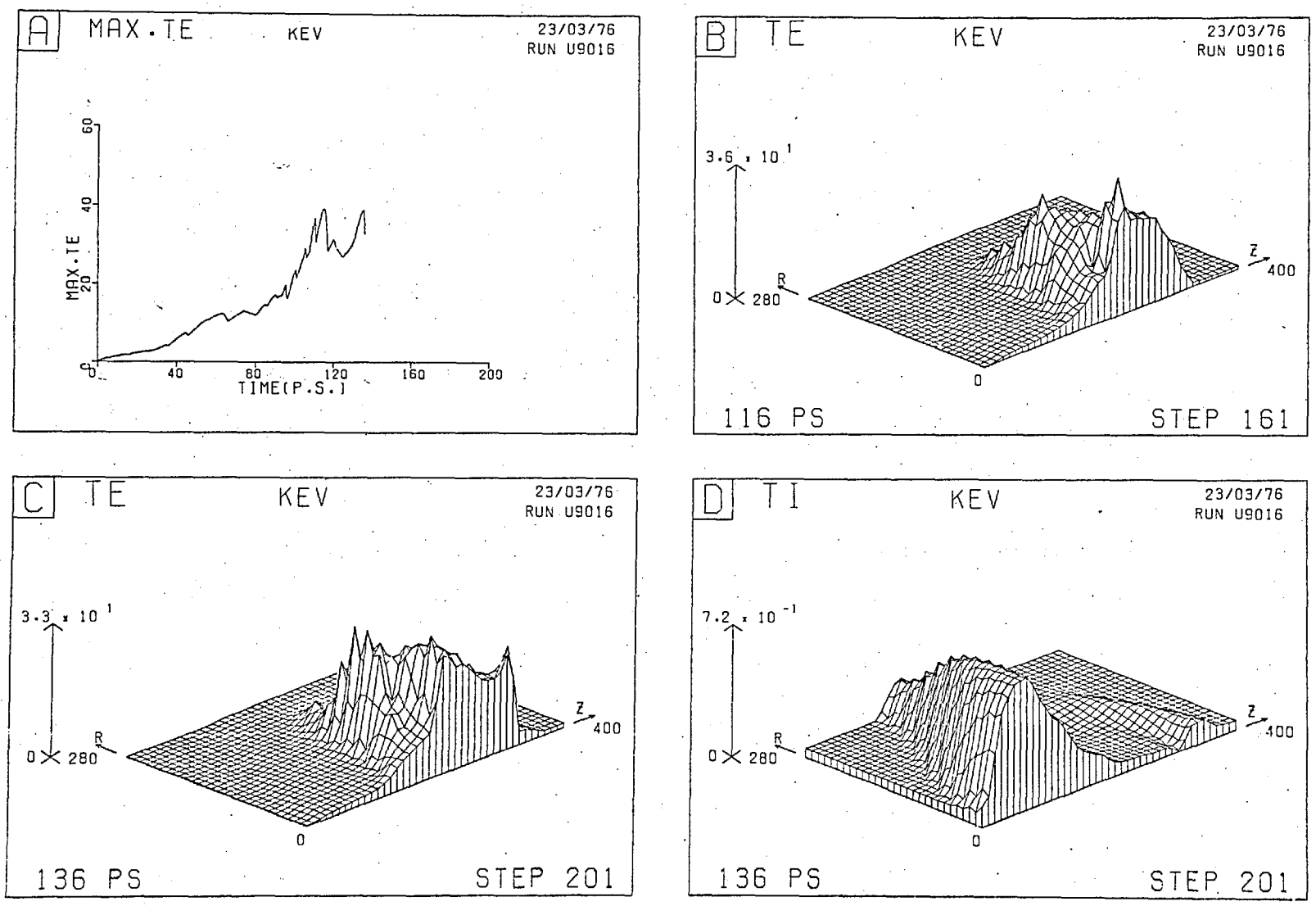

Fig.7-7 Run 7A, (a) Time history of maximum T_e on mesh (b) T_e at 116 psec (c) T_e at 136 psec (d) T_i at 136 psec

appear because of the scaling. Fig.7-6c shows large ablation velocities away from the hot region - up to 1.6×10^8 cm/sec, or 27 keV for deuterium.

An effect due to the pressure gradient towards the solid appears in the density distribution of Fig.7-6d, viewed from the opposite corner - although it is not very marked on the logarithmic plot, a dip in density occurs beneath the hot spot. Density "cavitons" or "bubbles" have been inferred experimentally (see Section 2.2.2), and have been ascribed to radiation pressure or "ponderomotive pressure" effects. It is also possible that thermal pressure forces at hot spots may cause localized plasma expansion.

The time evolution of the maximum temperature on the mesh is shown in Fig.7-7a and is notable for the fluctuations at later times. This is a consequence of the fragmentary nature of hot spots, which is apparent at these times (Fig.7-7b,c) and is associated with further magnetic field reversals and the occurrence of points having a fortuitously high conductivity. Thus a spike of T_e appears at 116 psec (Fig.7-7b) which does not persist to 136 psec (Fig.7-7c) because at some stage it is able to share its energy with a neighbouring point. (The spike on the far right of Fig.7-7c is believed to be a spurious numerical effect associated with the hydrodynamics of the small very high temperature gradient region at the expanding plasma front.)

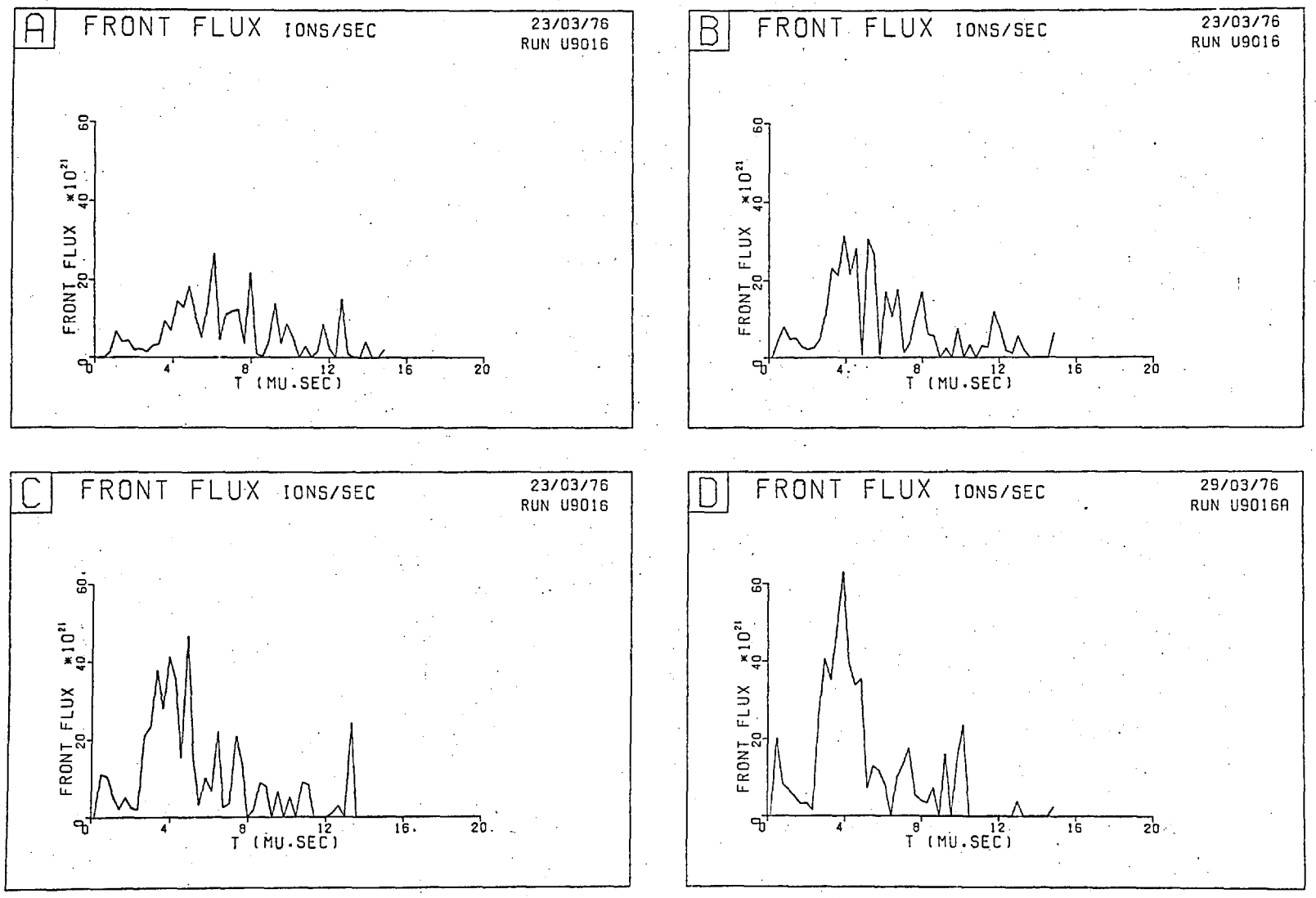

Fig.7-8 Run 7A. Ion arrival time graphs at collector 66 cms from target based on axial velocity distributions at:

(a) 86 psec (b) 111 psec (c) 136 psec (d) 161 psec

It is worth noting at this point that because of the assumed cylindrical symmetry "hot spots" are really hot rings. Our two-dimensional code has precluded investigation of their stability in the azimuthal direction.

The distribution of ion temperature (Fig.7-7d) exhibits two main features - equipartition in the denser region yielding a peak T_i of 720 eV, and cooling by expansion from the hot spot region. The ions however gain large directed energies through ablation.

Predictions of the graph of ion flux at a collector (66 cms from the target) against arrival time are shown in Fig.7-8, based on the velocity distributions at 86, 111, 136, and 161 psec. The algorithm used was described in Section 5.2,12; in this case 48 velocity groups cover the arrival time range 0 - 15 μsec. The contributions to these graphs from ions which have left the mesh are negligible. Convergence is not expected because the laser pulse has not been switched off and the plasma is continually being accelerated. However one feature persists - the fast peak on the high energy end of the distribution. It is apparent that peaks in arrival time traces do not require the existence of more than one charge species.

7.1.3 / Energetics.

Table 7.1 Energy gains for Run 7A (as percentages of the total energy absorbed.)

	at 36 psec	at 86 psec	at 136 psec
Electron internal energy	93.0	78.4	61.6
Ion internal energy	5.8	15.2	18.2
Kinetic energy	0.5	5.3	15.3
Magnetic field energy	0.004	0.04	0.2
Radiation loss	0.7	0.5	0.5
Numerically created energy ε_{tot}	0.1	-0.9	-4.0
Total energy absorbed (J)	30	120	211

Table 7.1 analyses how the laser energy is shared at various times during the simulation. Near the beginning of the pulse most of the absorbed energy is in the electrons, but this is transferred later to thermal ions in the high density region and to ablating ions in the atmosphere. The radiation loss is unimportant.

Globally very little energy goes into the magnetic field; locally the plasma β (Table A.4) never decreases below 10. For this reason $\underline{J}\times\underline{B}$ forces are never important in this run, although the situation is different in the next chapter where similar magnetic fields but smaller electron temperatures are generated from a less intense laser pulse.

due to a larger assumed initial density gradient and a smaller beam diameter.

The "numerically created energy" can occur in a number of ways, as discussed in Section 5.2.11 and Appendix B. Here the dominant cause of error was a program "bug" (affecting the radial component of the $T_e \nabla.(\rho \underline{V})$ term of (3.48)), which when corrected made no noticeable difference to any of the results except the total created energy. Other sources of error are at least a factor of 10 lower. Generally errors of a few per cent are considered tolerable.

More discussion of numerical errors will be given in Sections 7.2.4 and 9.3.5.

7.2 COMPARATIVE RUNS

Three runs were performed for comparison with the run just described. They differed from Run 7A as follows:

Run 7B: The laser power was reduced by a factor of 10.

Run 7C: The laser spatial profile was smoothed; specifically it was taken to be proportional to

$$f(r) = e^{-r^2/r_b^2} + e^{-(2r_{max}-r)^2/r_b^2}, \qquad (7.4)$$

with $r_b = 240\mu m$ and $r_{max} = 280\mu m$, the second term included to ensure a zero gradient on the north "symmetry" boundary. As a result the beam intensity varied by a factor of two across the simulation region.

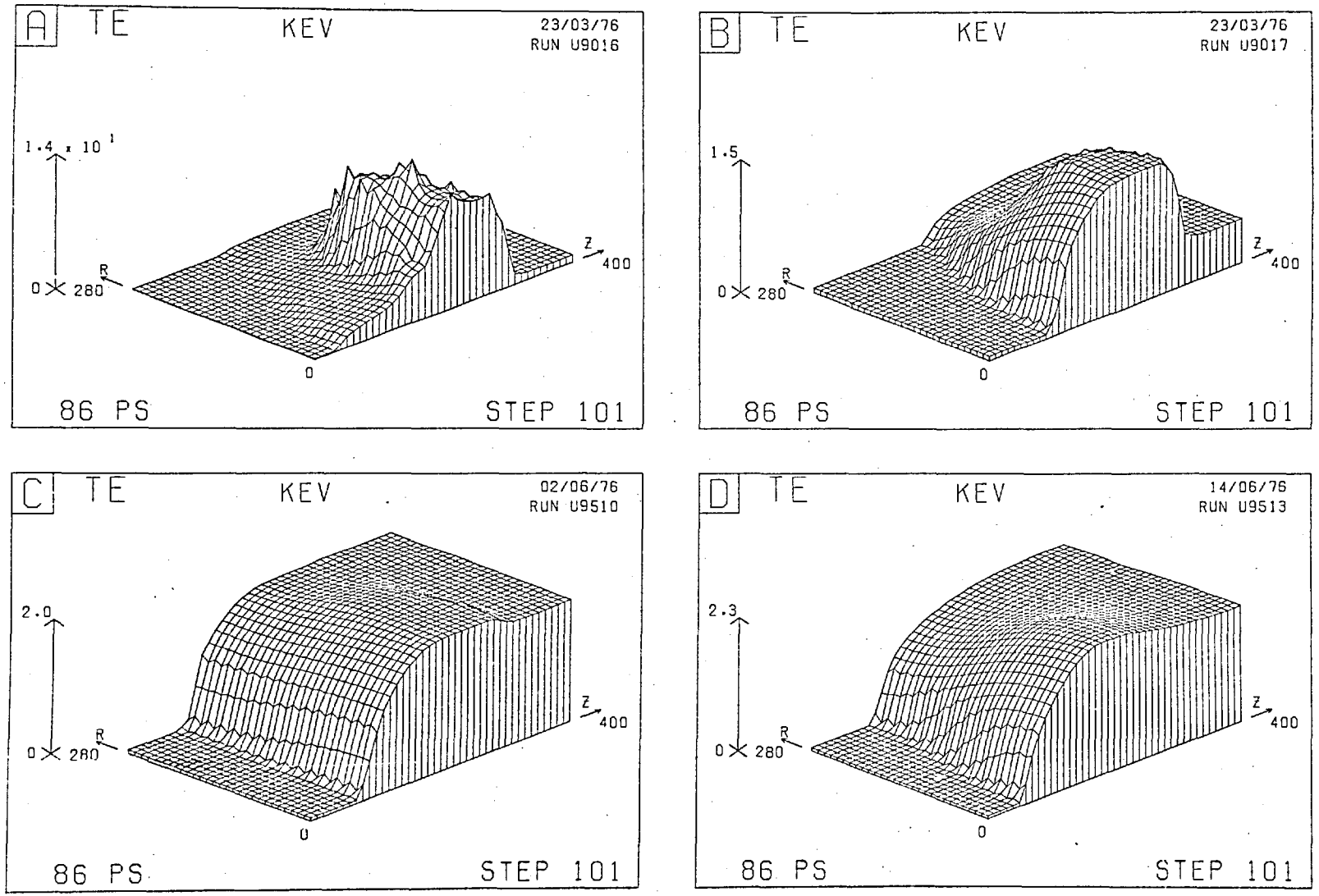

Fig.7-9 T_e at 86 psec. (a) Run 9A - basic (b) Run 9B - cooler
(c) Run 9C - wider beam (d) Run 9D - no B effects

Run 7D: Magnetic field effects (i.e. $\Omega\tau$ and $\underline{J}x\underline{B}$) were switched off. (But the magnetic fields were still calculated.)

Before describing each run in turn we shall briefly consider Fig.7-9 which shows the distribution of T_e at 86 psec for each run, and Table 7.2 which provides comparative data. Run 7A is the only run to exhibit distinctive hot spot behaviour; temperatures in the other runs fall within the 1-2 keV range. It is clear that significantly higher ablation velocities, and indeed magnetic fields, are generated in Run 7A; for example, at 86 psec the presence of a hot spot has caused an enhancement of the peak magnetic field by a factor of 10.

Comparing Runs 7B and 7C, Run 7C has a slightly higher intensity and therefore slightly higher T_e and V_z; Run 7B has a smaller beam lengthscale and therefore higher magnetic fields. It appears that the laser intensity and beam diameter are two key parameters in determining whether or not hot spot behaviour will occur. Run 7D shows how, in the absence of magnetic field effects, classical thermal conduction can be remarkably efficient at smoothing out illumination non-uniformities.

Table 7.2 Comparative parameters for Runs 7A-7D.

		7A Basic	7B Cooler	7C Wider Beam	7D No B effects
Peak I_A on axis	W/cm^2	5.8×10^{15}	5.8×10^{14}	1.1×10^{15}	5.8×10^{15}
Peak laser power	W	1.8×10^{12}	1.8×10^{11}	1.8×10^{12}	1.8×10^{12}
Simulation time	psec	186	426	213	86
No.of timesteps		301	301	238	101
Hot spot ?		Yes	Later	No	No
At 36 psec:					
Max. T_e	keV	4.06	1.07	1.63	2.05
Max. $\Omega\tau$		157	5.91	6.75	–
Max. B	MG	0.191	0.055	0.016	0.10
Max. V_z	10^7cm/s	1.45	0.485	0.71	1.11
At 86 psec:					
Max. T_e	keV	14.4	1.48	1.98	2.31
Max. $\Omega\tau$		2610	52.8	23.5	–
Max. B	MG	2.09	0.194	0.044	0.20
Max. V_z	10^7cm/s	8.02	1.92	2.48	3.29
At 136 psec:					
Max. T_e	keV	32.7	1.84	2.32	
Max. $\Omega\tau$		16900	112	41.6	
Max. B	MG	7.51	0.42	0.105	
Max. V_z	10^7cm/s	24.7	3.56	4.43	

7.2.1 Run 7B: Lower laser power

Run 7B, in contrast to Run 7A, does not exhibit a hot spot on the same timescale. Towards the end of the simulation, however, hot spot formation is commencing, which explains the uncertainty of the "Hot spot?" entry in Table 7.2. Otherwise the distributions of fluid variables are similar, except that they have lower maxima and are spatially more smooth. We have not thought it necessary to include diagrams to illustrate this.

The main purpose of this section is to describe an attempt to include the electron Righi-Leduc terms ($\underline{Q}_{e\wedge}$), and also the Hall terms. In this run all of the equations of Chapter 3 are implemented fully, except that we "flux-limit" $\underline{Q}_{e\wedge}$ by not allowing it to exceed

$$f \cdot n_e k T_e \sqrt{kT_e/m_e} \ . \qquad (7.5)$$

In this case f was chosen to be $\sqrt{m_e/m_i}$, so that the advective velocity associated with $\underline{Q}_{e\wedge}$ is the sound speed. We make no attempt to justify physically this choice of f; (7.5) represents severe flux-limitation.

We show the distribution of T_e at 36 psec in Fig.7-10a, together with the heat flows parallel to the temperature gradient ($Q_{e\perp}$, Fig.7-10b) and perpendicular to the temperature gradient ($Q_{e\wedge}$, Fig.7-10c). The former is directed mainly towards the cool solid, as we would expect, and the latter involves a circulation of heat around the

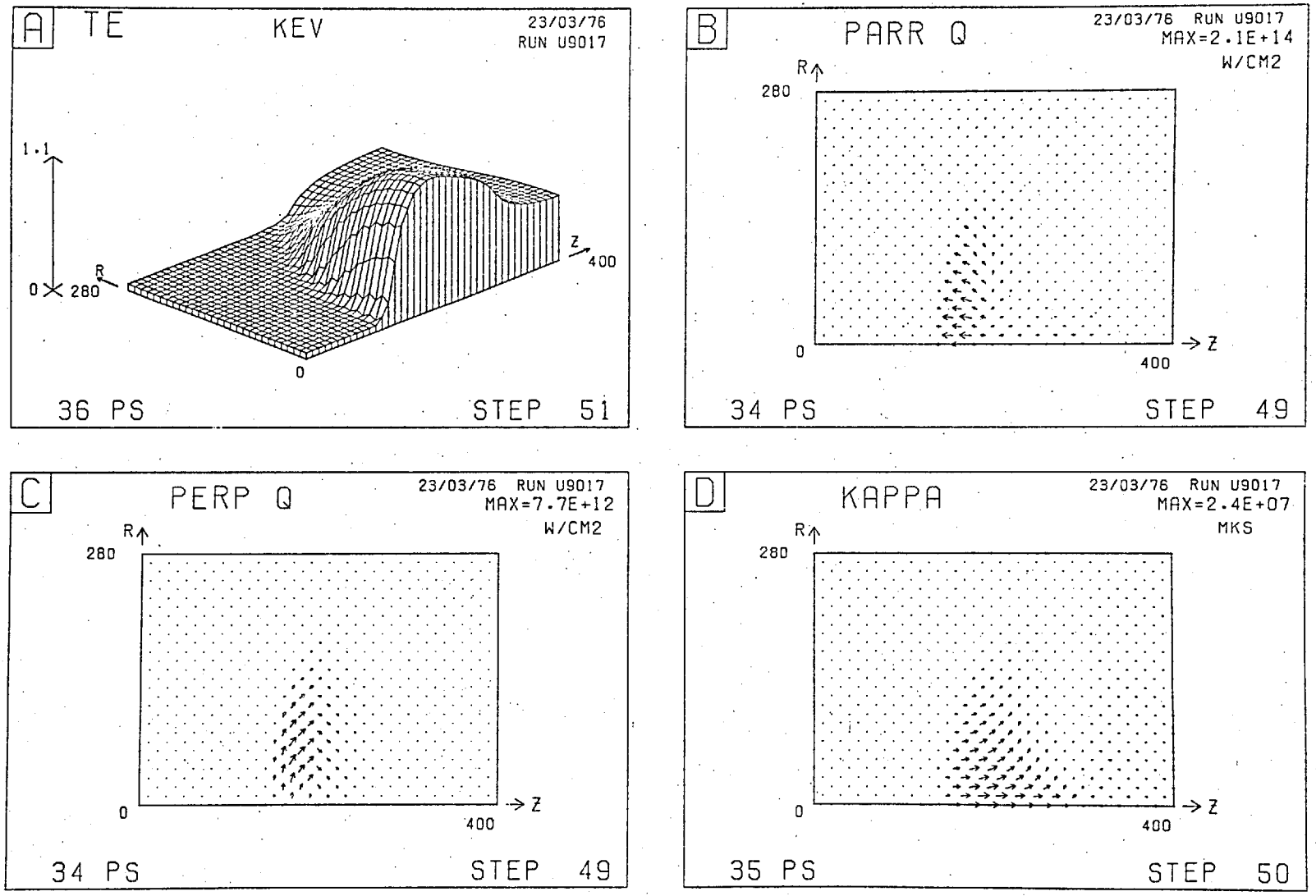

Fig.7-10 Run 7B. Around 35 psec: (a) T_e (b) $\underline{Q}_\perp$
(c) $\underline{Q}_\wedge$ (d) $(-K_{e\wedge}, K_{e\perp})$ plotted as velocities

temperature contours. In Fig.7-10d the coefficients $(-K_{e\wedge}, K_{e\perp})$ are plotted as though they were radial and axial velocities - thus when $\Omega\tau \ll 1$ the arrows are parallel to the z-axis and of magnitude proportional to $K_{e\perp}$, and when $\Omega\tau \simeq 1$ they are at 45^{o} (see (3.33)). When $\Omega\tau > 1$, as is indeed the case near the low density end of the density ramp, $K_{e\wedge}$ dominates $K_{e\perp}$ but both are small.

Because we have severely restricted $Q_{e\wedge}$ in this calculation, the Righi-Leduc terms do not have much effect and we see at 225 psec a temperature distribution (Fig.7-11a) with an incipient hot spot, not very dissimilar from T_e in Run 7A at 36 psec (Fig.7-3d). The distribution of T_e is flat near the axis because B is reduced there (Fig.7-11d). The corresponding heat fluxes are shown in Fig.7-11(b-c); $Q_{e\perp}$ is again directed towards the solid, but this time it is more localized near the axis. $Q_{e\wedge}$ appears rather unphysical, and has arisen as follows: $\partial T_e/\partial z > 0$, and so the radial component of $Q_{e\wedge}$ is positive. $\partial T_e/\partial r$ reverses sign between z = 190 and 200μm, and so the axial component of $Q_{e\wedge}$ reverses too. We made the mistake of applying the restriction (7.5) separately to each component of $Q_{e\wedge}$, and therefore $Q_{e\wedge}$ is always at 45^{o} to the mesh. Clearly we should have applied this restriction to $Q_{e\wedge}$ as a whole, but the question still arises as to whether (7.5) is the correct functional form for $Q_{e\wedge}$ or just an upper limit.

We see in Fig.7-11a a spike of electron temperature

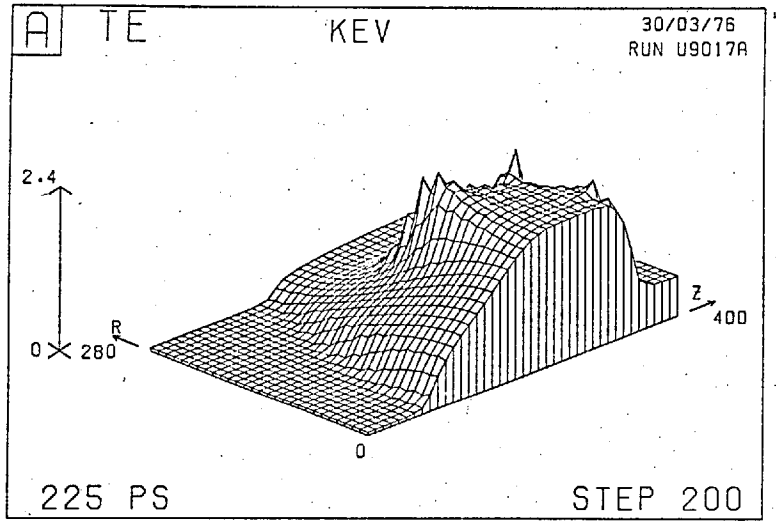

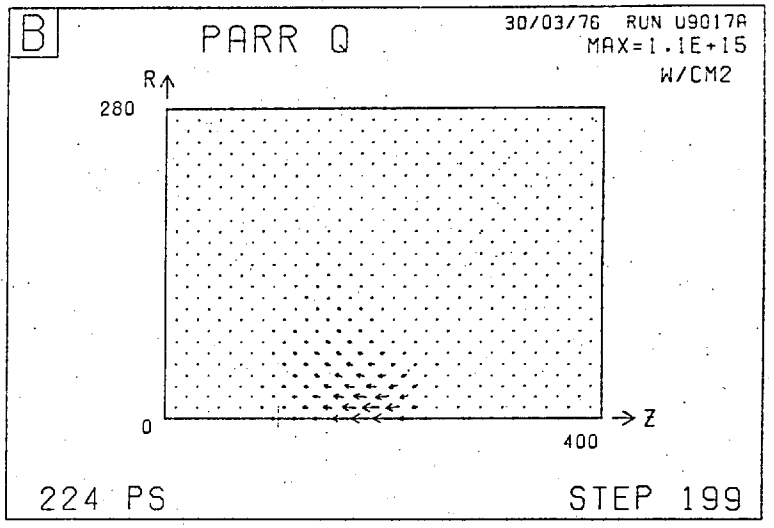

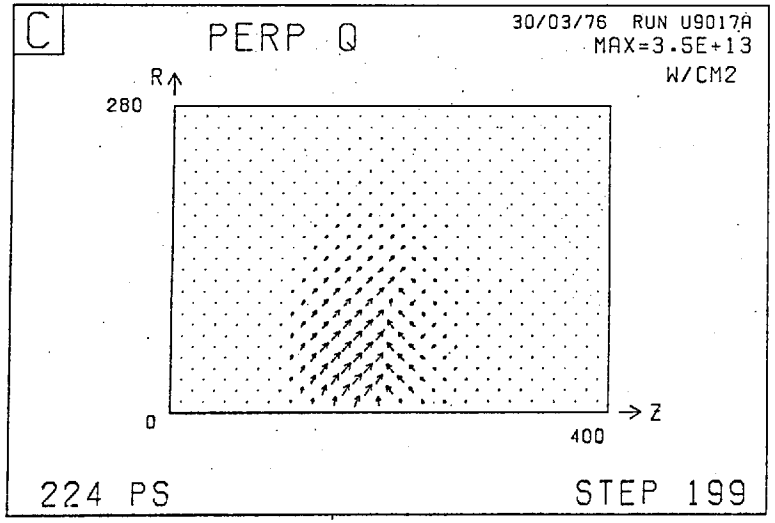

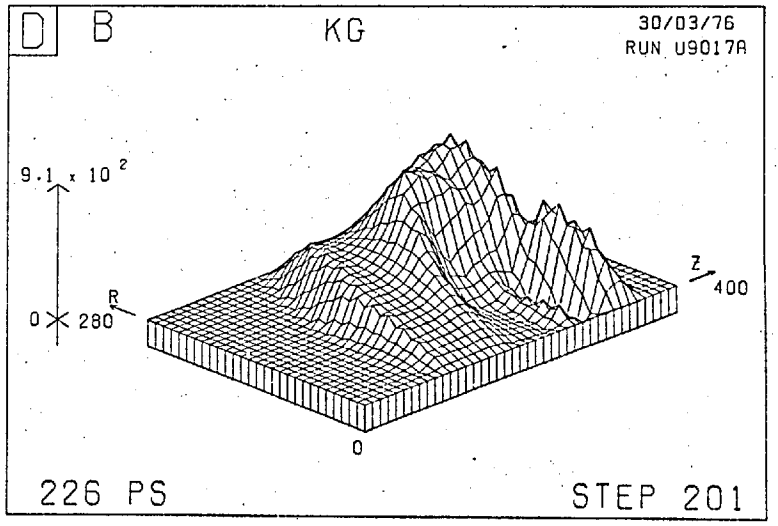

Fig.7-11 Run 7B. Around 225 psec:

(a) T_e (b) $\underline{Q}_\perp$

(c) $\underline{Q}_\wedge$ (d) B

near the far corner. The two possible causes are

(a) $\underline{Q}_{e\wedge}$ dominating $\underline{Q}_{e\perp}$ in that region, where $\Omega\tau >> 1$ (Fig.7-12a); and

(b) the Hall terms associated with the current $\underline{J}$ in that region (Fig.7-12b). (Note also in this diagram the characteristic distortion of the current paths in the presence of a reversed field configuration.)

The run was continued 50 steps with and without the Righi-Leduc terms, to give the temperature distributions at 326 psec in Fig.7-12c and Fig.7-12d respectively. It is clear that the poor numerical features of Fig.7-11a are caused by the Righi-Leduc terms rather than the Hall terms. In fact the relative velocities $\underline{J}/n_e e$ are always small here, with a peak of 10^7 cm/sec compared with the fluid velocity peak of 6×10^7 cm/sec. Indeed the relative velocities in Run 7A were also small enough not to cause numerical problems and we consider that their omission from that run was unnecessary.

We note that the rough temperature distribution in Fig.7-11a was produced by very strongly flux-limited Righi-Leduc terms. If they were limited by $V_{th,e}$ rather than C_s the effect would have been greater; in runs where they have not been flux-limited, but treated by partial timesteps as outlined in Section 5.2.4, similar temperature distributions arise, only sooner, and become strongly unstable leading ultimately to negative electron temperatures. This was

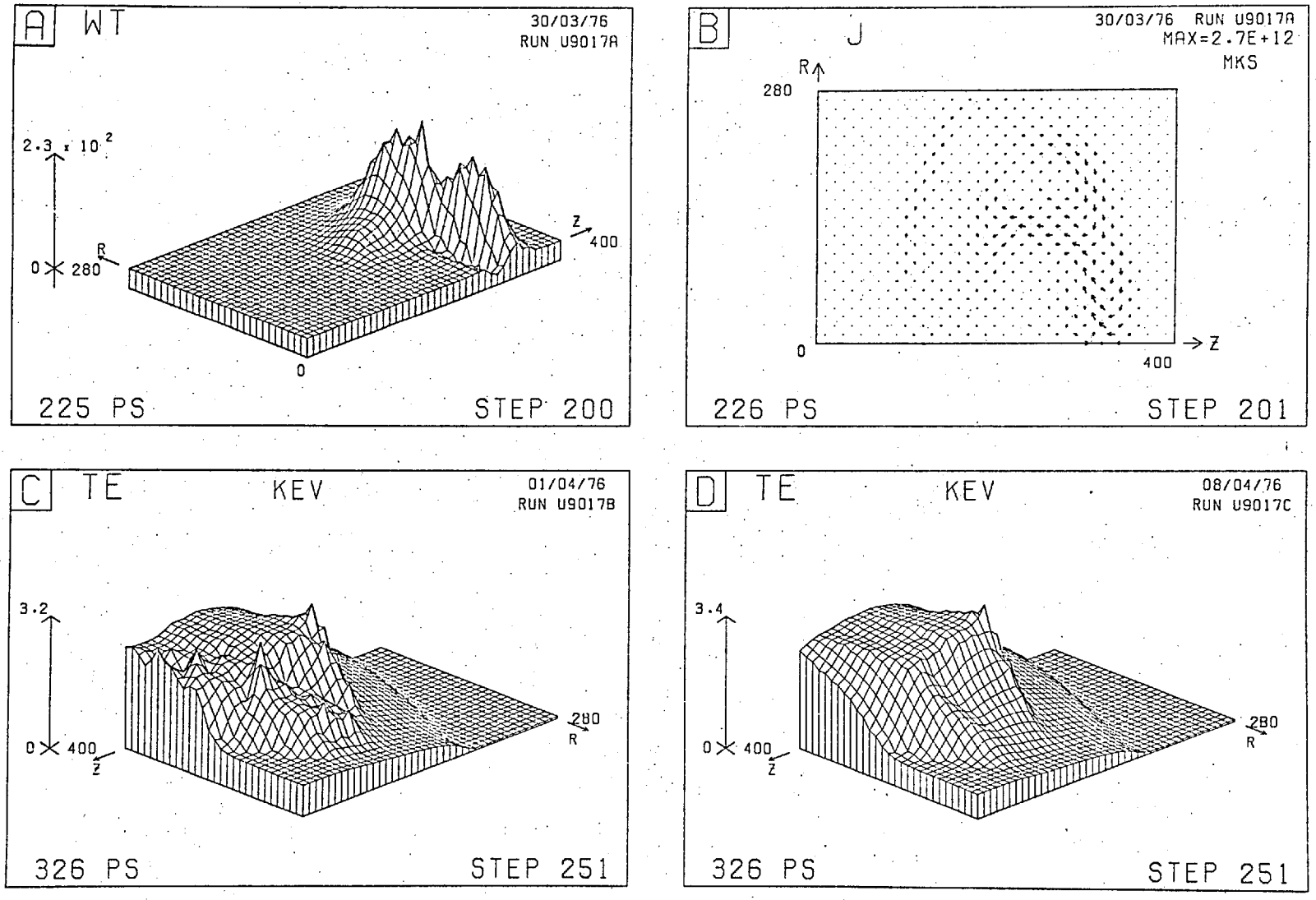

Fig.7-12 Run 7B. (a) $\Omega\tau$ at 225 psec (b) $\underline{J}$ at 226 psec
(c) T_e at 326 psec (d) T_e at 326 psec (without Righi-Leduc terms)

discussed in Section 5.2.14. Run 7B does not become as unstable as this because of the limit imposed on the allowed fluxes of electron energy from cell to cell.

The problem of the Righi-Leduc terms is physical as well as computational. $K_{e\wedge}$ is greatest when $|\Omega\tau| = 1$ (3.32, 3.33), and is then of the same magnitude as $K_{e\perp}$. The corresponding fluxes $Q_{e\wedge}$ are very large because of the keV temperatures present. But in this regime the electron mean free path and Larmor radius are of the order of the pellet dimensions (see Table 4.4) and the correct transport equations to use are uncertain.

7.2.2 Run 7C: Less focussed beam

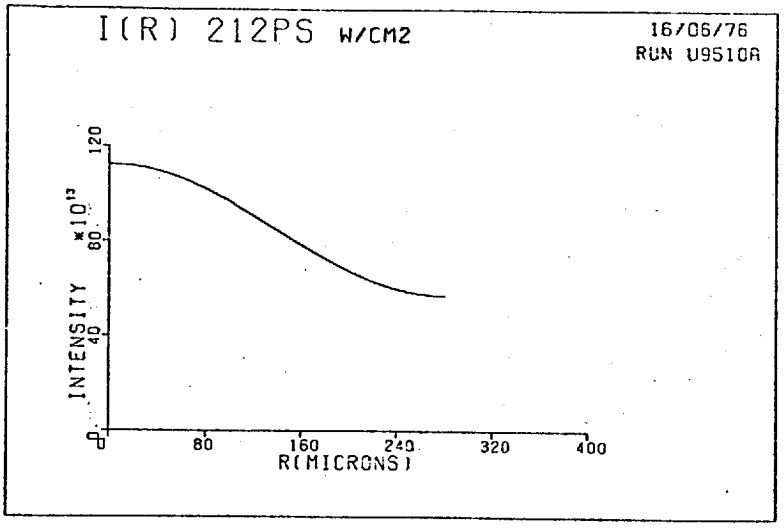

Fig.7-13 Radial intensity profile of Run 7C.

The beam profile (7.4) used for Run 7C is shown in Fig.7-13; the laser power is the same as in the illustrative Run 7A. The main feature of Run 7C is that because

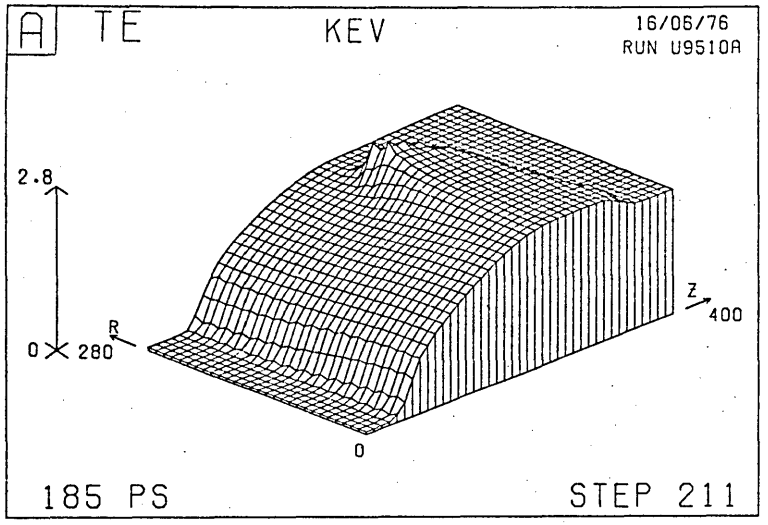

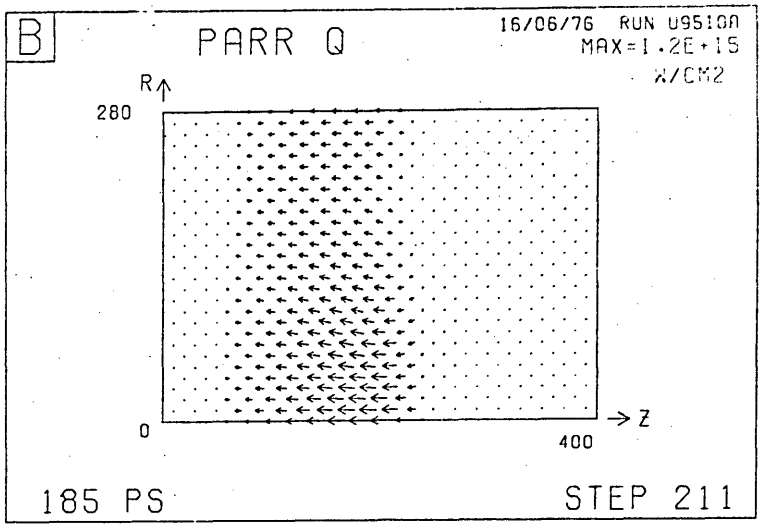

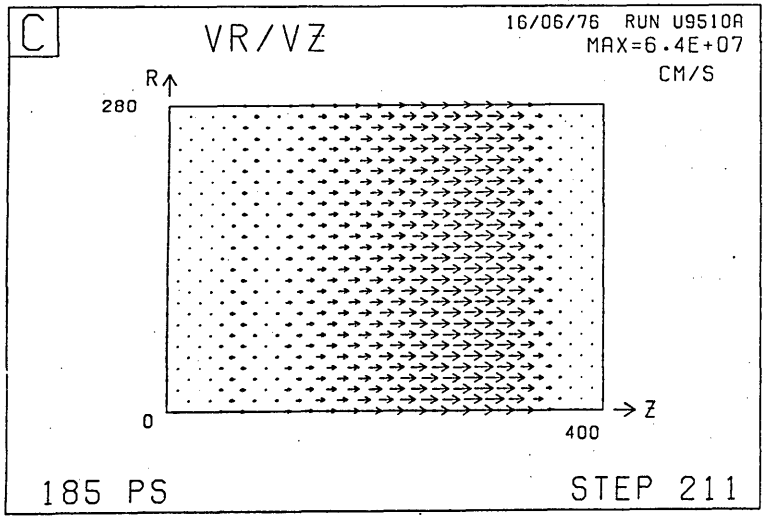

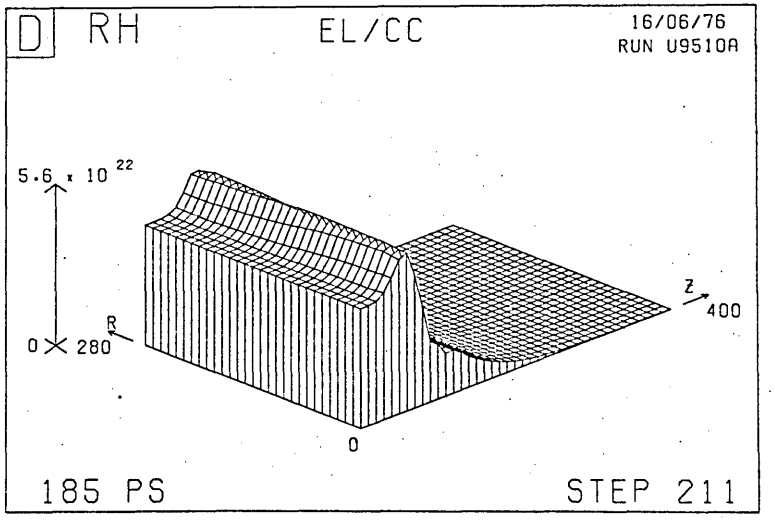

Fig.7-14 Run 7C, At 185 psec: (a) T_e (b) $\underline{Q}_\perp$
(c) $\underline{V}$ (d) n_e

magnetic fields grow at a reduced rate further symmetrization is able to take place. This is seen qualitatively at 185 psec in Fig.7-14, where the temperature distribution (Fig.7-14a) is flattened, although a hot spot is beginning to form near the radius of minimum laser intensity. The heat flux (Fig.7-14b) is primarily towards the solid, approximately balancing the incident flux of 1.1×10^{15} W/cm^2, and ablation (Fig.7-14c) and compression (Fig.7-14d) are uniform.

Table 7.3 The extent of non-uniformity in Run 7C at 185 psec.

	$\frac{\text{at } (0,200)\,\mu m}{\text{at } (280,200)\,\mu m}$	$\frac{\text{max. on mesh}}{\text{max. on r=280}\mu m}$
Incident laser profile		1.96
T_e	1.19	1.32
V_z	1.11	1.14
T_i	1.04	1.14
ρ	1.12	1.05

A quantitative assessment of this effect appears in Table 7.3, which refers to the same time in the simulation. The first column compares values of various quantities at two specified points (the north and south boundaries at $z = 200\mu m$, the initial position of the critical density), and the second column compares the maximum on the whole mesh with the maximum on the north. These figures should be compared with the variation by a factor of 1.96 in the incident laser profile from $r = 0$ to $r = r_{max}$.

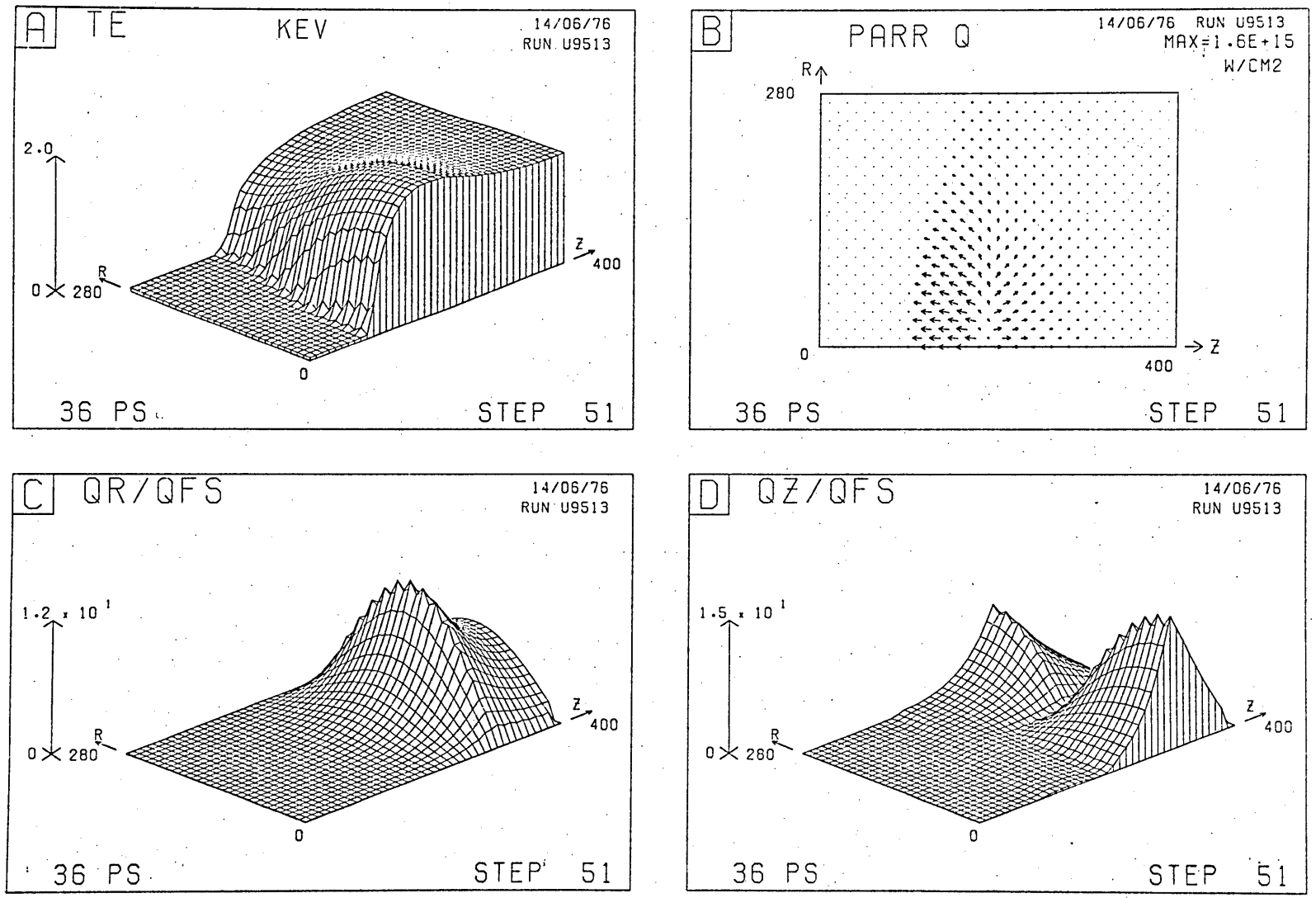

Fig.7-15 Run 7D. At 36 psec: (a) T_e (b) $Q_\perp$
(c) $Q_{\perp r}/Q_{fs}$ (d) $Q_{\perp z}/Q_{fs}$

7.2.3 Run 7D: Magnetic field effects excluded

This run may appear artificial because of the exclusion of important terms in the equations, but it serves to highlight the magnetic field effects.

The heat flows in the absence of $\Omega\tau$ effects are considerably different as is seen in Fig.7-15. This figure refers to an early time (36 psec) and shows the distribution of T_e (Fig.7-15a), the heat flux $\underline{Q}$ (Fig.7-15b), and the ratios of the radial and axial heat fluxes to the "free-streaming" limiting flux Q_{fs} defined as in (4.53) but with the $3\sqrt{3}/2$ factor omitted (Fig.7-15c,d). The free-streaming limit is violated by an order of magnitude in the low density atmosphere, but not in the heat front advancing towards the high density solid which accounts for about 30% of the laser flux of 5×10^{15} W/cm^2. The remaining 70% is heating the plasma.

The distribution of Q_r/Q_{fs} is straightforward - Q_r is always positive and must be zero on the north and south boundaries. The distribution of Q_z/Q_{fs} is perhaps less easy to understand: Q_z is generally negative because the only effective sink of heat is the solid. However Q_z is positive near the axis to the right of the absorption region because $\partial T_e/\partial z$ is negative there. When Q_z changes sign, at around r = 140μm, the free streaming limit is not violated.

We have observed that the growth of magnetic fields

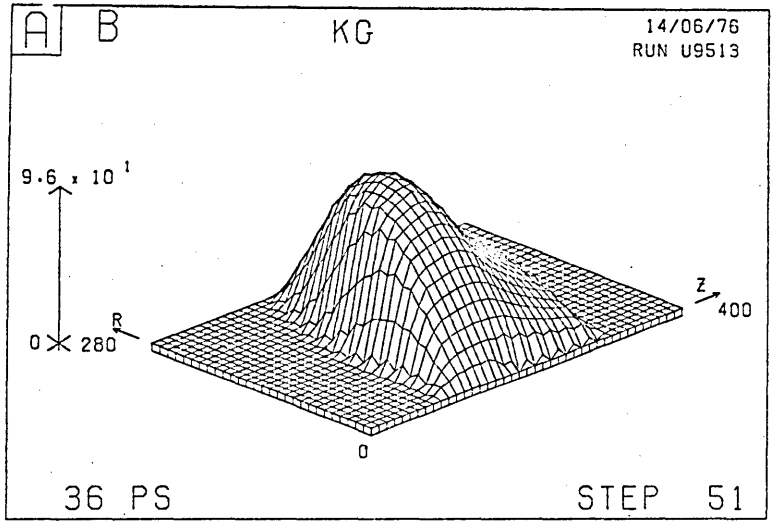

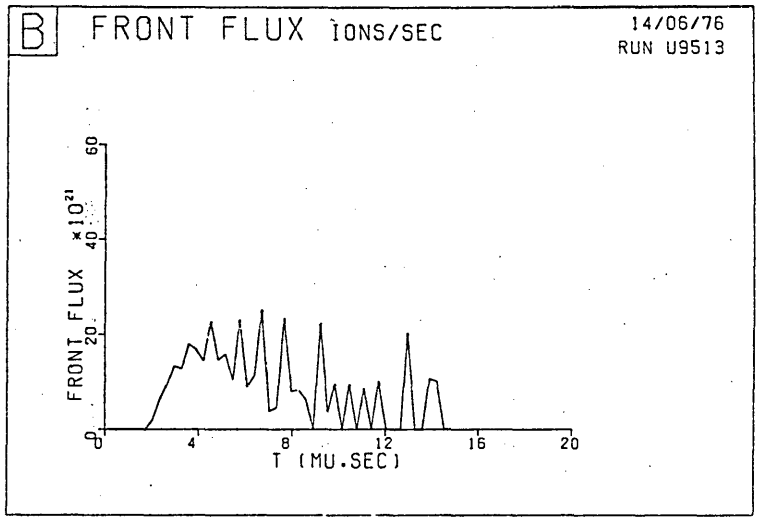

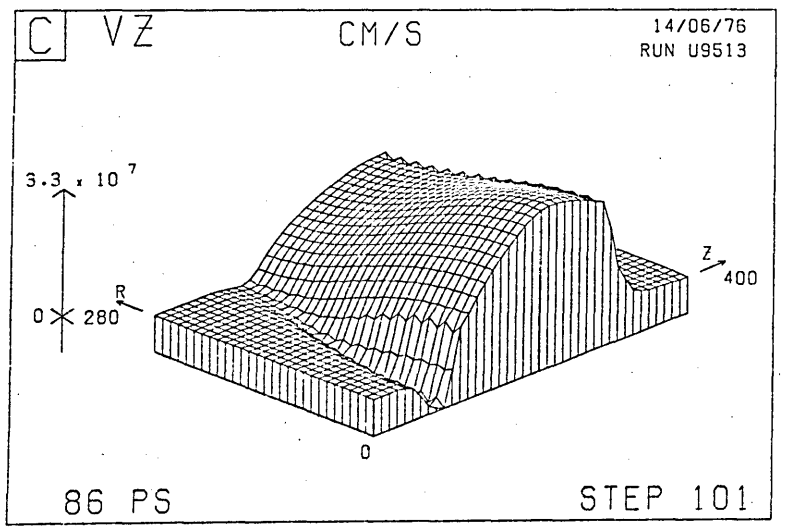

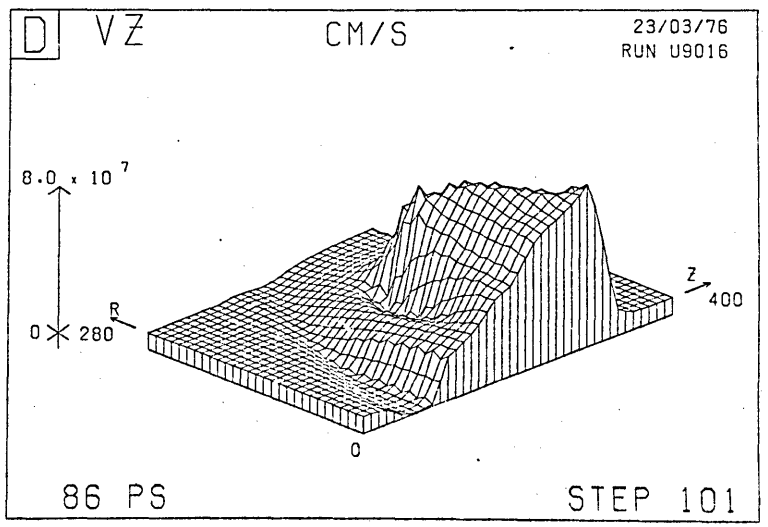

Fig.7-16 (a) Run 7D: B at 36 psec (b) Run 7D: arrival time prediction at 86 psec
(c) Run 7D: V_z at 86 psec (d) Run 7A: V_z at 86 psec

is enhanced in the presence of hot spots. This may be seen by comparing Fig.7-16a for the magnetic field at 36 psec (peak 96 kG) with the corresponding plot (Fig.7-4a) from Run 7A (peak 190 kG).

Run 7D was not continued sufficiently far to provide a good prediction of the arrival time graph; however a comparison of predictions based on the velocity distributions at 86 psec (Fig.7-16b and Fig.7-8a) shows that the fast peak present in Run 7A is absent from Run 7D. A comparison of the velocity distributions at this time (Figs.7-16c and 7-16d for Runs 7D and 7A respectively) shows clearly how a fast ion peak may arise from a hot spot. The peak ablation velocity of Run 7A is over twice that of Run 7D.

It is also apparent that plasma distant from the axis is accelerated more in Run 7D, where the peak V_z on $r = r_{max}$ is twice that of Run 7A. This compensates for the fast peak of Run 7A as far as the total area beneath the arrival time graph is concerned; in fact 10% more ions are accounted in Run 7D.

7.2.4 Energetics

We conclude this chapter by indicating the magnitudes of the overall numerical errors incurred in the four runs 7A-7D. These are given in Table 7.4 for three times in the simulations and are expressed as percentages of the laser energy absorbed. We give also the main sources of error; the ε_i are as defined in Appendix B.

Table 7.4 Numerically created energies for Runs 7A-7D as percentages of the total energy absorbed. The main source of error is given in parentheses.

	at 36 psec		at 86 psec		at 136 psec	
Run 7A	0.1	(ε_6)	-0.9	(ε_6)	-4.0	(ε_6)
Run 7B	0.02	(ε_6)	-0.4	(ε_6)	-1.1	(ε_6)
Run 7C	-0.1	(ε_2)	0.2	**	0.33	(ε_{12})
Run 7D	0.05	(ε_2)	1.0	(ε_2)		

** $\varepsilon_{2,6,12,14,15}$

In Runs 7A and 7B the error (ε_6) led to the discovery of a small coding error, as we remarked earlier. In Run 7C at 86 psec several errors contributed in almost equal amounts. In Run 7D the error (ε_2) resulting from the quindiagonal inversion stage was dominant.

In all cases the errors were sufficiently small so as not to undermine our confidence in our conclusions. The true errors in our results arise from the inadequacies of our physical equations rather than from the numerical model.

CHAPTER 8

A SHORT PULSE INTERACTION

In this chapter we consider an interaction different in many respects from that of the previous chapter; the parameters were suggested by Hall.[97] We consider a short pulse, Gaussian rather than uniform in time, containing about one Joule rather than 100 Joules and incident upon a carbon target. The target mass in the simulation region (0.1-0.2 μg compared with 4.4 μg) and the intensity are both an order of magnitude lower. However the radial and axial length-scales are less, so that magnetic field growth is enhanced.

Section 8.1 gives the parameters of the problem and Section 8.2 describes the results obtained from four comparative runs (8A-8D). An important effect is the enhanced acceleration of ablating plasma through $\underline{J} \times \underline{B}$ forces.

In Section 8.3 we analyse the results in greater detail, comparing the different runs with particular attention to the dependence of the results on the initial density gradient and the laser power.

8.1 SPECIFICATION OF THE PROBLEM

A 1.06 μm laser pulse, Gaussian in space and time with spot diameter (d_{FW}) and pulse time (t_{FW}) both measured at half amplitude, is defined by the intensity profile $I(r,t)$:

(8.1)

$$I(r,t) = J \cdot \frac{e^{-(t-t_p)^2/t_o^2}}{t_o\sqrt{\pi}} \cdot \frac{e^{-r^2/r_b^2}}{\pi r_b^2(1-e^{-r_{max}^2/r_b^2})}$$

where

J is the total energy delivered,

$t_o = t_{FW} / 2\sqrt{\ln 2}$

$r_b = d_{FW} / 2\sqrt{\ln 2}$

$t_p = 2t_o$

and r_{max} ($>2r_b$) is the simulation radius. (8.1)

The proportion of laser energy lost due to starting the simulation at t=0 is clearly negligible.

In the four cases to be described we choose the following parameters:

pulse full width	t_{FW}	= 30 psec
spot diameter	d_{FW}	= 50 μm
simulation radius	r_{max}	= 67 μm

which imply the subsidiary parameters:

Gaussian parameter	t_o	≈ 18 psec
time of peak power	t_p	≈ 36 psec
beam radius	r_b	≈ 30 μm.

With these parameters a pulse of J Joules gives a peak intensity I_A on the axis of 1.11×10^{15} J Watts/cm^2; in particular, pulses of 300 mJ and 1.2 J give peak intensities of 3.34×10^{14} W/cm^2 and 1.34×10^{15} W/cm^2 respectively.

We consider the single beam configuration described

in Section 3.1.1, so that both north and east boundaries are "free-flux" boundaries.

The target is assumed to comprise carbon atoms four times ionized with an initial arbitrarily chosen temperature of 10 eV. The omission of ionization processes was discussed in Section 4.5.

We consider two alternative initial density profiles, given in terms of the electron number density n_e, similar to the profile of Fig.7-1 and illustrated in Fig.8-1.

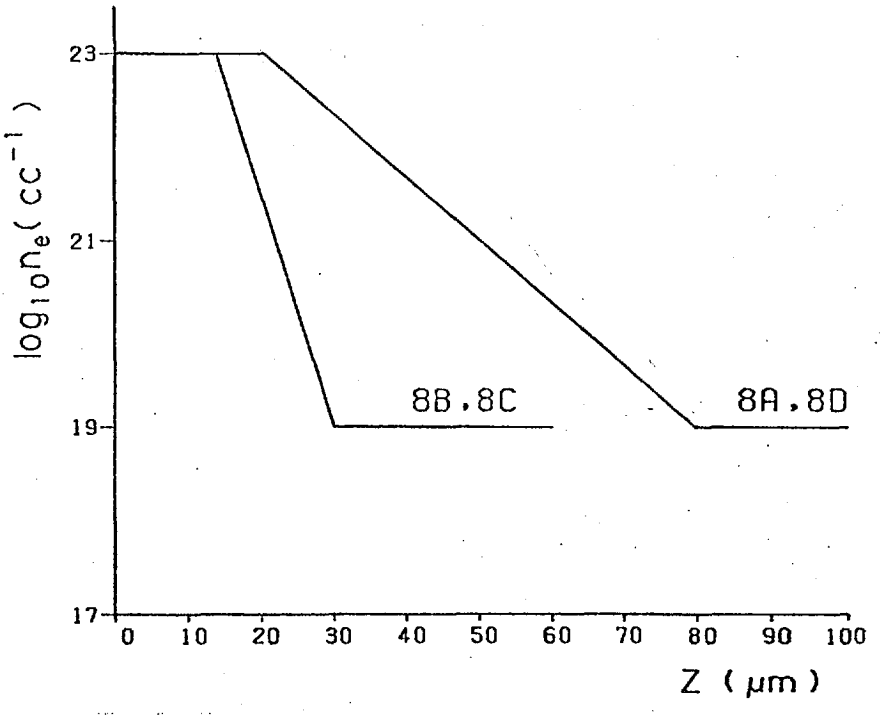

Fig.8-1 "Standard" and "Steep" initial density profiles of Runs 8A-8D.

In the first ("Standard") case the distance z_{c4} between the critical and quarter critical density surfaces is 9μm, while in the second ("Steep") case it is 2.4μm. z_{max} is 100μm in

the first case and 60μm in the second, and the mesh is 21 points by 31.

The four cases to be described correspond to a standard or steep initial density gradient and a laser energy of 300 mJ or 1.2 J. (See Table 8.1.) The timestep,

Table 8.1 Characterization of Runs 8A-8D.

	Standard $\nabla\rho$	Steep $\nabla\rho$
Low Energy	Run 8A	Run 8B
High Energy	Run 8D	Run 8C

chosen to follow advection and heating, varies from 0.5 psec to 2.0 psec, except for the first ten steps when a timestep of 0.1 psec is required to follow the early inverse bremsstrahlung heating. Details of comparative parameters of Runs 8A-8D will be given in Table 8.2 in Section 8.3.1.

The dumping factors (5.86) at the critical density are given by

$$d_i = 1.0,0.6,0.3,0.1,0.0 \quad \text{for} \quad i = 1,...,5. \qquad (8.2)$$

This is considered to be a broad dump, probably less realistic in the steep density gradient cases 8B and 8C as will be discussed in Section 8.2.4.

As in Chapter 7, the equations are fully implemented, except that the Righi-Leduc terms are omitted and $\underline{V}_e$ is set to equal $\underline{V}$. The $\underline{J}x\underline{B}$ force and resistivity are unaffected.

8.2 GENERAL FEATURES OF THE RESULTS

In all cases the laser pulse has its peak at 36 psec, and the plasma is followed until at least twice this time. Features common to all four runs include

(a) the creation of a hot region (not necessarily a hot spot) near the critical density, with temperatures of just over a keV, and the formation of a thermal front which propagates only slowly towards the solid;

(b) a slight shift of the critical density region towards the laser, due to ablation;

(c) the generation of magnetic fields of the order of a few mega-Gauss, which contribute significantly to the acceleration of the low density plasma. However only in the higher power runs (8C and 8D) is the electron thermal conductivity sufficiently reduced so as to give rise to hot spots.

In this section we shall give a qualitative description of the results. The main features of Runs 8A and 8B are discussed in Section 8.2.1 with particular but not exclusive reference to plasma acceleration by $\underline{J}\times\underline{B}$ forces. We then note the time history of Run 8A (Section 8.2.2), an edge effect in Run 8B (Section 8.2.3), and the occurrence of hot spots in Runs 8C and 8D (Section 8.2.4).

8.2.1 Runs 8A and 8B: $\underline{J}\times\underline{B}$ acceleration

We compare here the two lower power runs 8A and 8B, differing in that Run 8B has the steeper density gradient.

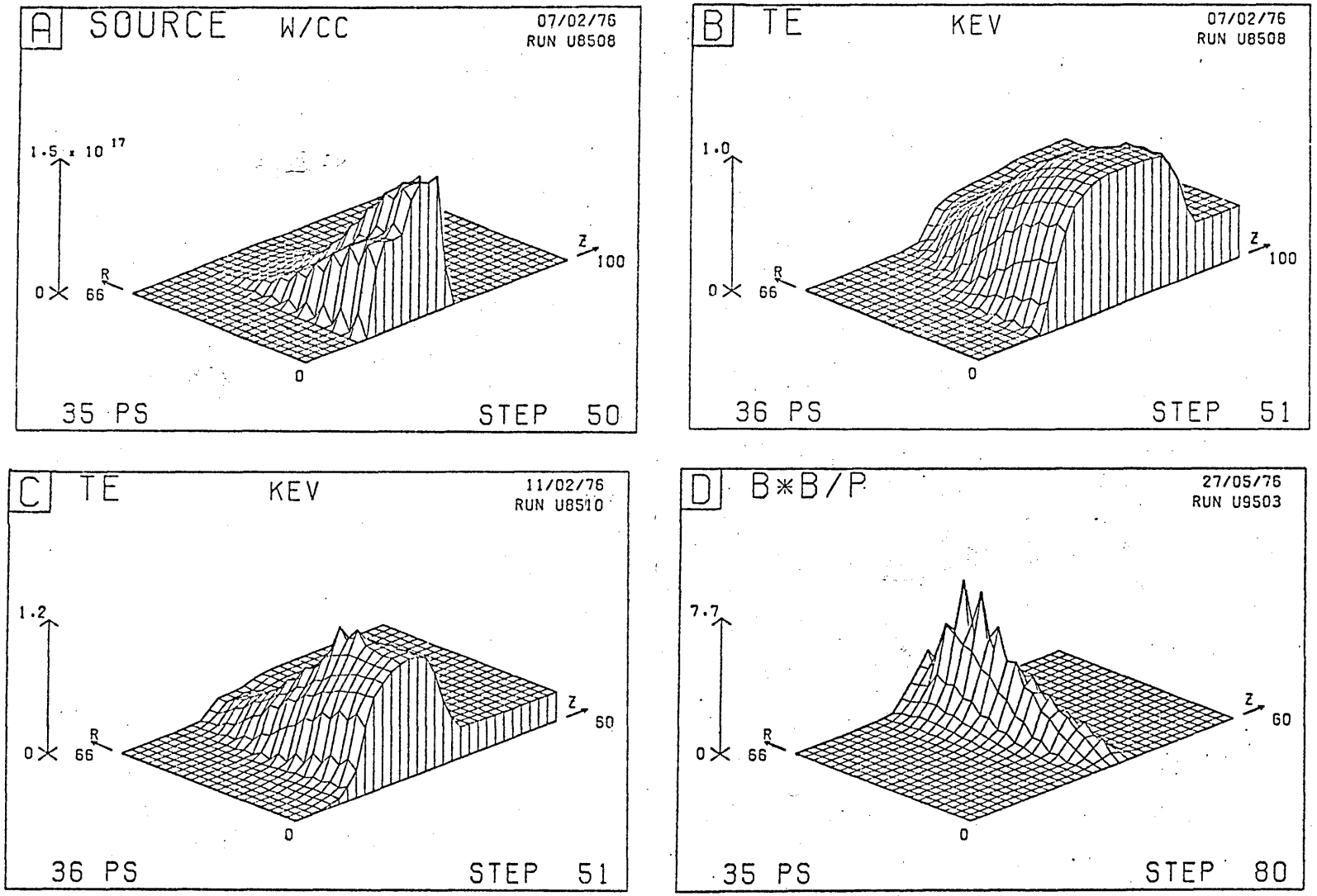

Fig.8-2 (a) Run 8A: Laser source at 35 psec (b) Run 8A: T_e at 36 psec
(c) Run 8B: T_e at 36 psec (d) Run 8B: B^2/P at 35 psec

We commence with Figs.8-2 and 8-3 which correspond to 36 psec, the time at which the laser power is a maximum. Fig.8-2a shows the laser source of Run 8A, the energy being almost totally dumped over a broad overdense region with a peak deposition rate of 1.5×10^{17} W/cc. Fig.8-2(b-c) shows the distributions of T_e in Runs 8A and 8B respectively; in both cases some axial diffusion is possible until a low density region with high $\Omega\tau$ is encountered. Run 8B has a larger magnetic field, exhibits less diffusion, and a hot spot is almost formed.

The ratio of magnetic to plasma pressure in Run 8B is shown in Fig.8-2d*, with a peak of 7.7 located near the low density end of the density ramp. The corresponding peak in Run 8A is only 0.55. More precisely we have plotted $B^2/\mu_o P \equiv 3/\beta$ where

$$\beta = \frac{3}{2}k(n_e T_e + n_i T_i) \; / \; (B^2/2\mu_o). \qquad (8.3)$$

This ratio $(3/\beta)$ provides an indication of the importance of $\underline{J}\times\underline{B}$ forces. Recalling the configuration of Fig.2-1, $\underline{J}\times\underline{B}$ is always directed outwards from the current loops. Alternatively the $\underline{J}\times\underline{B}$ force may be thought of as a magnetic pressure $B^2/2\mu_o$, directed away from regions of large B, together with a curvature force $B^2/\mu_o r$ which is always radially inwards. Thus, when the $\underline{J}\times\underline{B}$ force domin-

---

*The labelling of the dates and timestep numbers in Figs. 8-2, 8-3 and 8-4 may appear inconsistent. Runs 8A-8B were rerun after the discovery of a coding error which affected the radial component of $\underline{J}\times\underline{B}$. The only significant difference appeared in the plots of V_r where the corrected versions have been substituted.

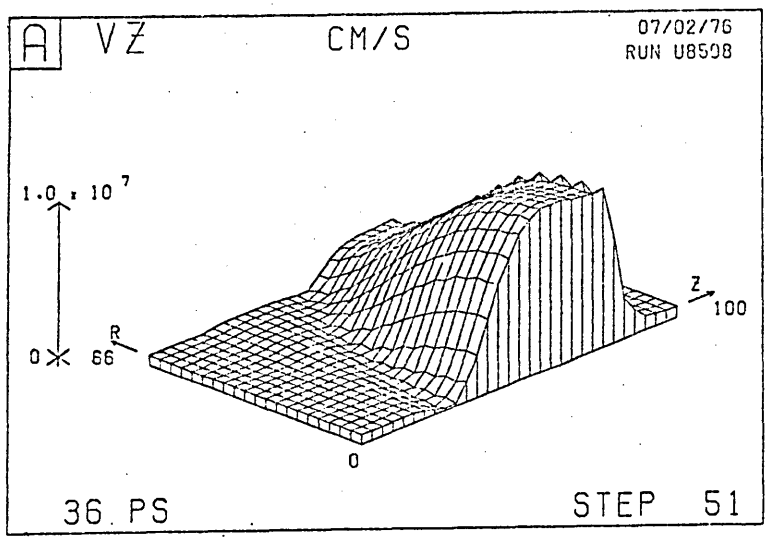

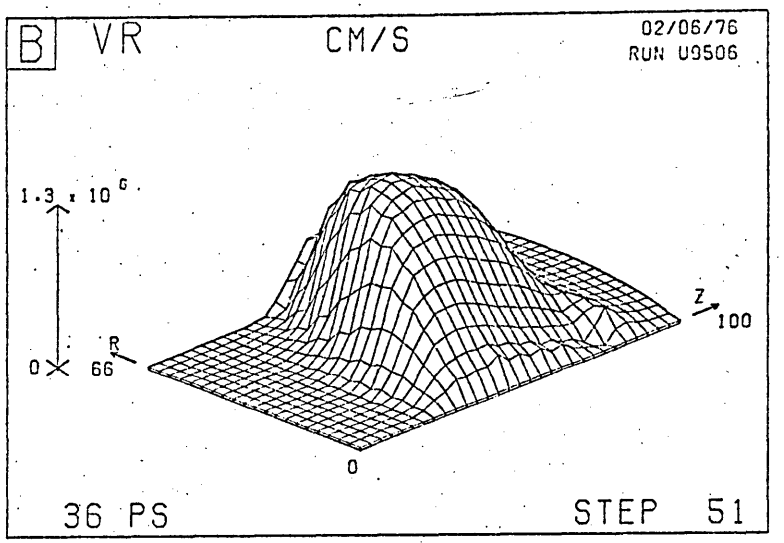

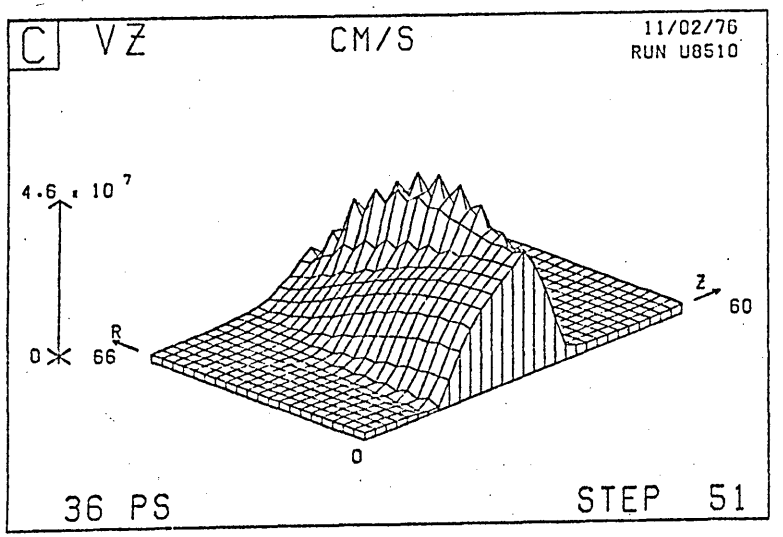

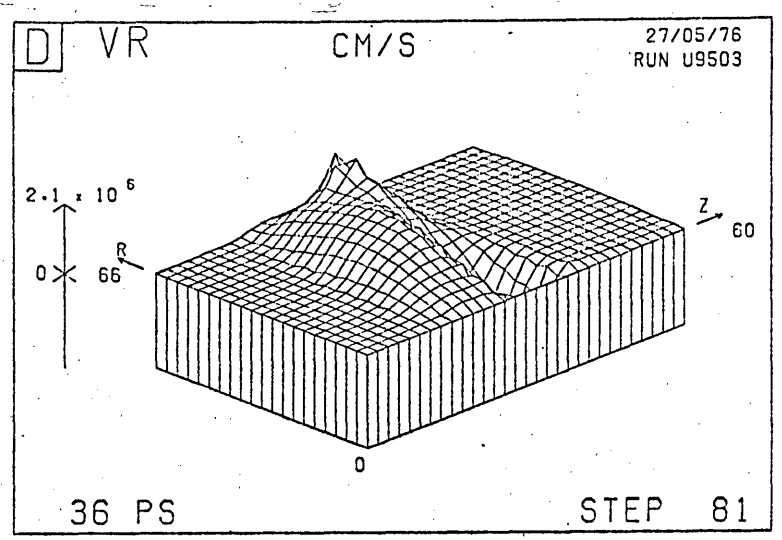

Fig.8-3 At 36 psec. Run 8A: (a) V_z (b) V_r
Run 8B: (c) V_z (d) V_r

ates the plasma pressure gradient, we expect to find enhanced acceleration away from the interaction region and pinching towards the axis.

The velocity distributions V_z and V_r of Run 8A are shown in Fig.8-3(a-b), and those of Run 8B in Fig.8-3(c-d). The region of significant V_z is further to the left in Run 8B because the half of the simulation region given by $z \geq 30\mu m$ has no initial density gradient (see Fig.8-1). The significant feature demonstrating $\underline{J}x\underline{B}$ acceleration is that in Run 8A V_z peaks on the axis, where the electron temperature is maximum, whereas in Run 8B V_z peaks off-axis, in the region where the magnetic field is maximum.

We also note in Run 8B (Fig.8-3d) the generation of negative radial velocities ($\sim 3 \times 10^6$ cm/sec) near the axis and enhanced radial velocities away from the axis. The pinch velocity is small in comparison with the axial velocity ($\sim 5 \times 10^7$ cm/sec).

At this time pinching has not occurred in Run 8A; however $\underline{J}x\underline{B}$ forces do become important later for this run too, as may be seen in Fig.8-4 which refers to 86 psec. Fig.8-4a shows the distribution of B, and Fig.8-4(b-c) shows V_z and V_r respectively. Again the pinch velocity ($\sim 7 \times 10^6$ cm/sec) is small compared with the axial velocity ($\sim 5 \times 10^7$ cm/sec).

Fig.8-4d shows T_e, with a peak now of 680 eV. As the laser pulse is effectively over the temperature is

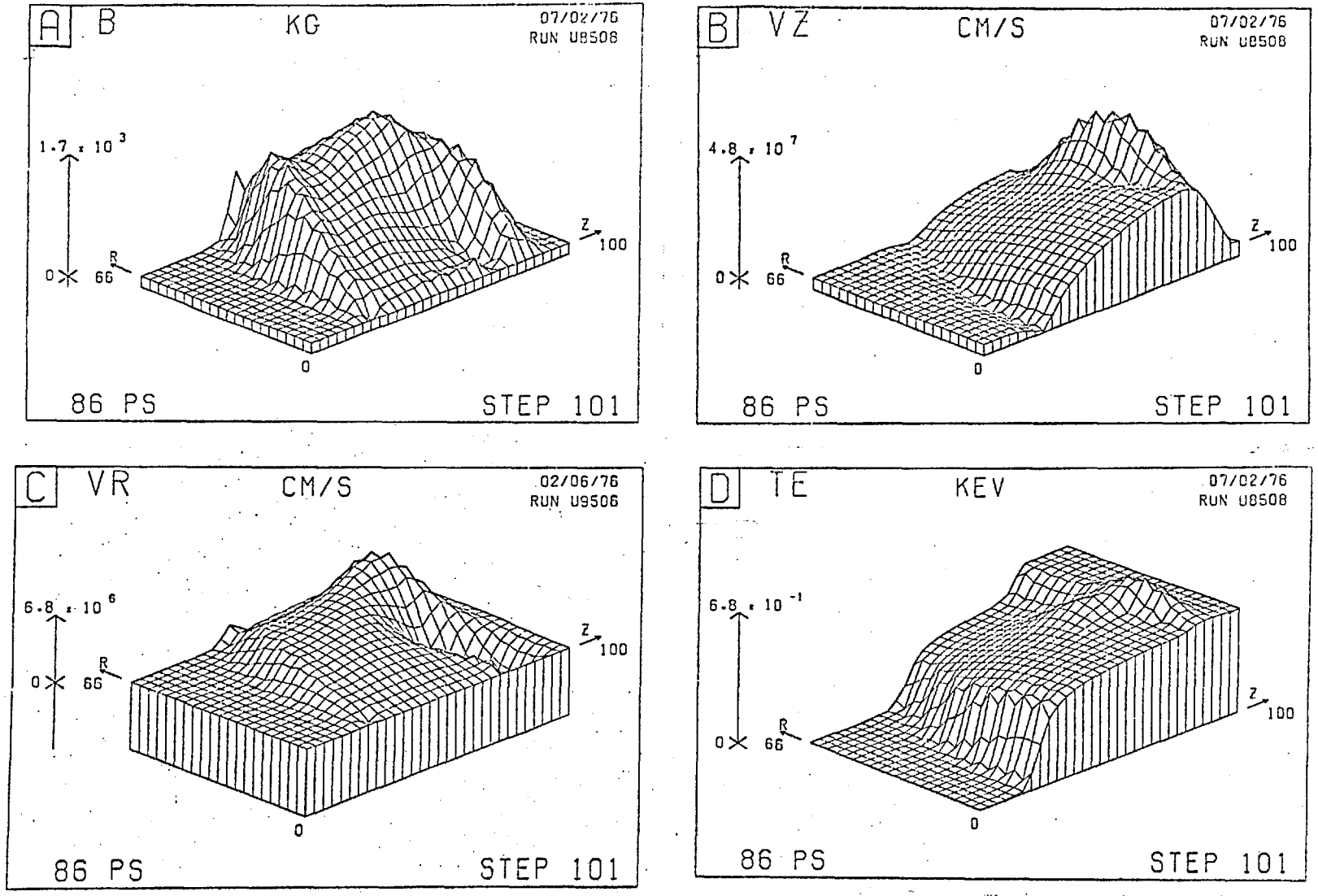

Fig.8-4 Run 8A. At 86 psec: (a) B (b) V_z (c) V_r (d) T_e

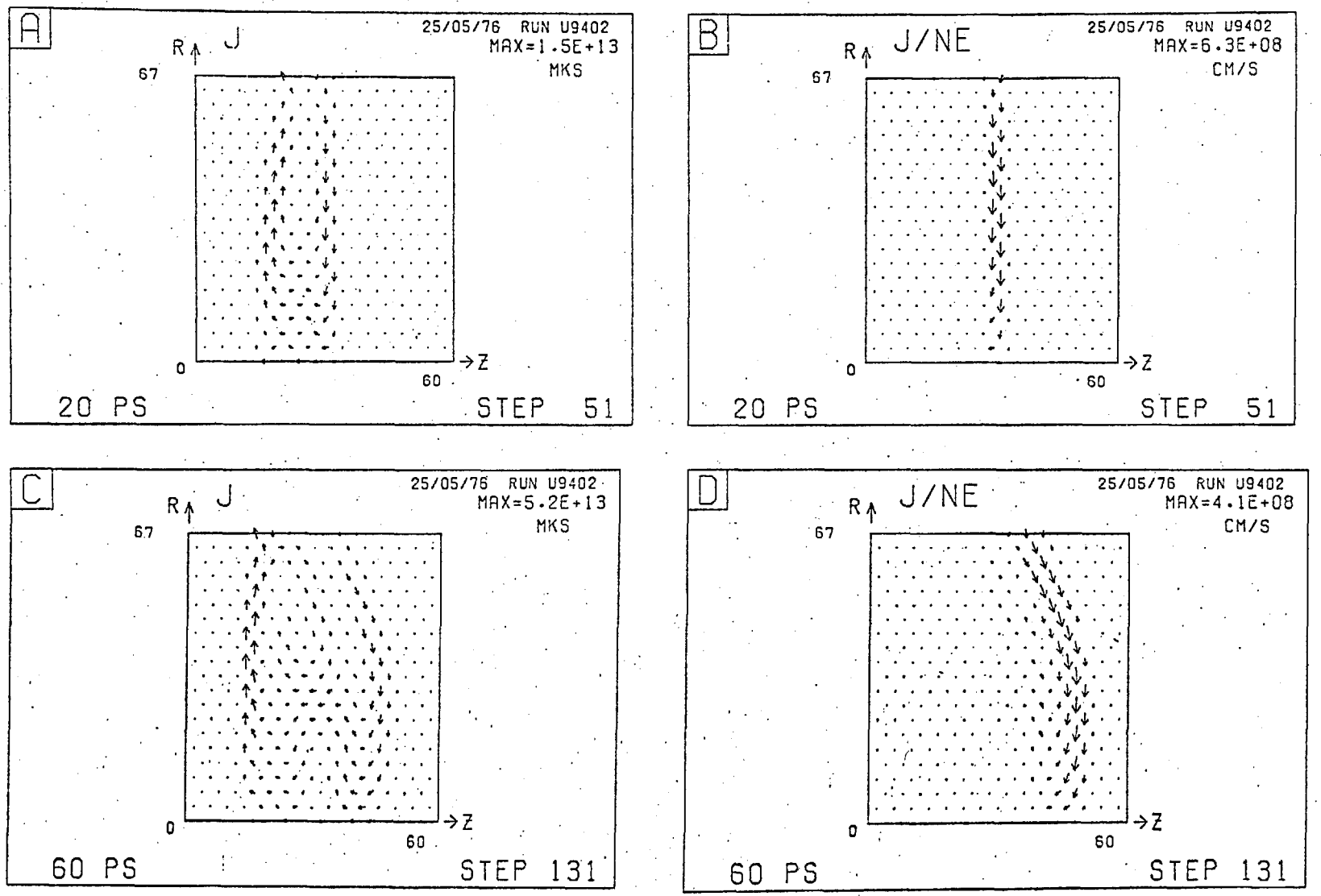

Fig.8-5 Run 8B. (a) $\underline{J}$ at 20 psec (b) $\underline{J}/n_e e$ at 20 psec
(c) $\underline{J}$ at 60 psec (d) $\underline{J}/n_e e$ at 60 psec

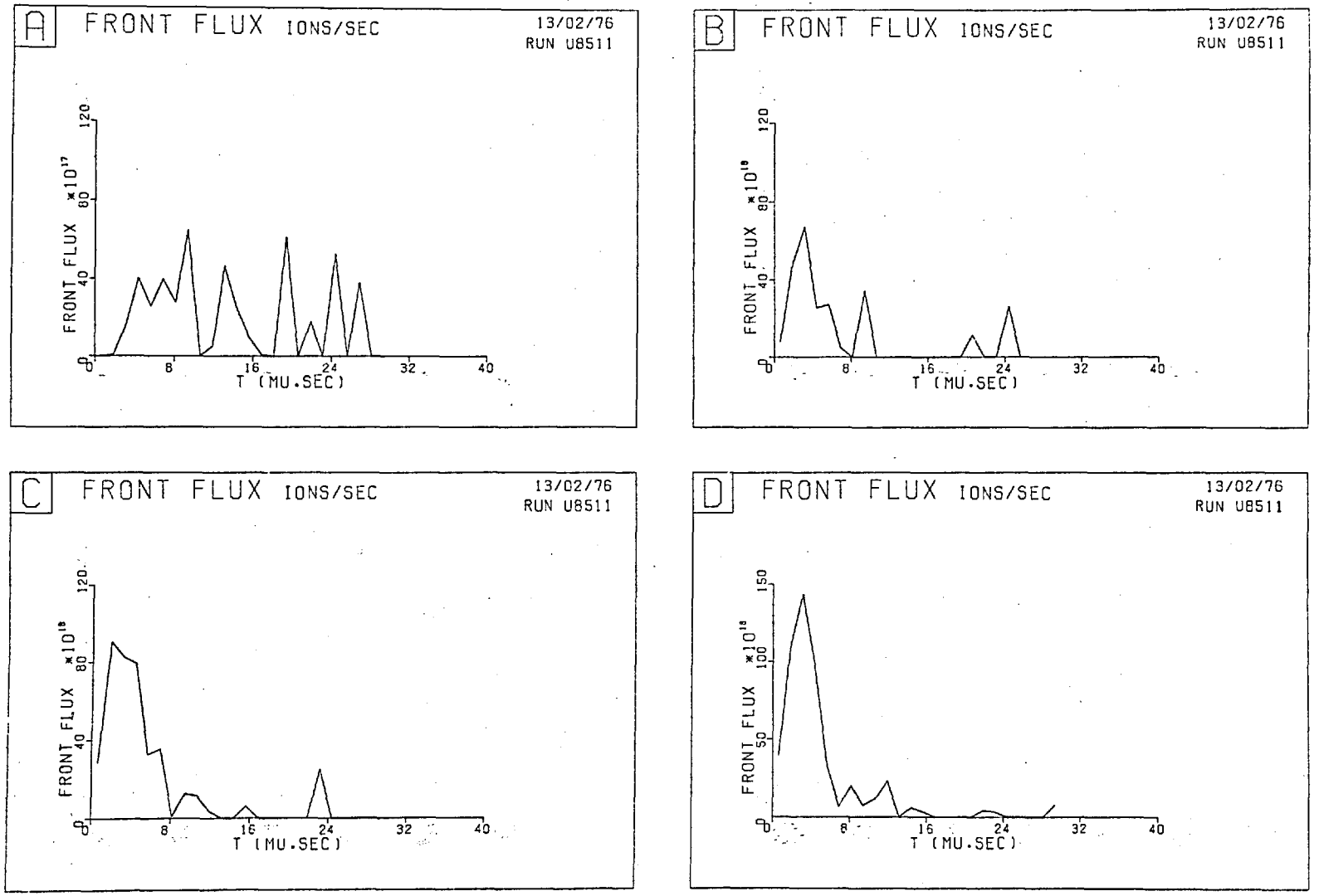

Fig.8-6 Run 8C. Ion flux at collector based on axial velocity distributions at: (a) 21 psec (b) 46 psec (c) 71 psec (d) 96 psec.

decreasing, by conduction towards the solid and by the blow-off of hot plasma. T_e is largest at large z due to the ablation of the former heating region, and has a peak off-axis because of the reduced thermal conductivity there - the region of large $\Omega\tau$ has almost reached the east boundary. This peak is not what we have termed a hot spot because there is no associated laser source; it should perhaps be known as a "warm spot".

We include Fig.8-5 to show for Run 8B the distribution of the current ($\underline{J}$) and the relative velocity between electrons and ions ($\underline{V}_{rel} = \underline{J}/n_e e$) at 20 psec and 60 psec. Early in the simulation (20 psec, Fig.8-5a) the current is largest at either end of the density ramp because the source term for B (4.31) is discontinuous there. Later (60 psec, Fig.8-5c) the current loop is more extended axially due to ablation in the low density atmosphere. This figure also exhibits the characteristic distortion due to a small magnetic field reversal near the axis. The positions of the current loops in Fig.8-5 are consistent with the region of operation of $\underline{J}\times\underline{B}$ forces evidenced in Figs.8-2d,8-3c and 8-3d.

In Fig.8-5b $\underline{V}_{rel}$ is very large (6×10^8 cm/sec) in a small skin on the low density edge of the current loop; it spreads out later and reduces to 4×10^8 cm/sec in Fig.8-5d, although the peak current has by then increased threefold. It is because of the extra computer time required to follow these large velocities that the Hall terms were omitted from

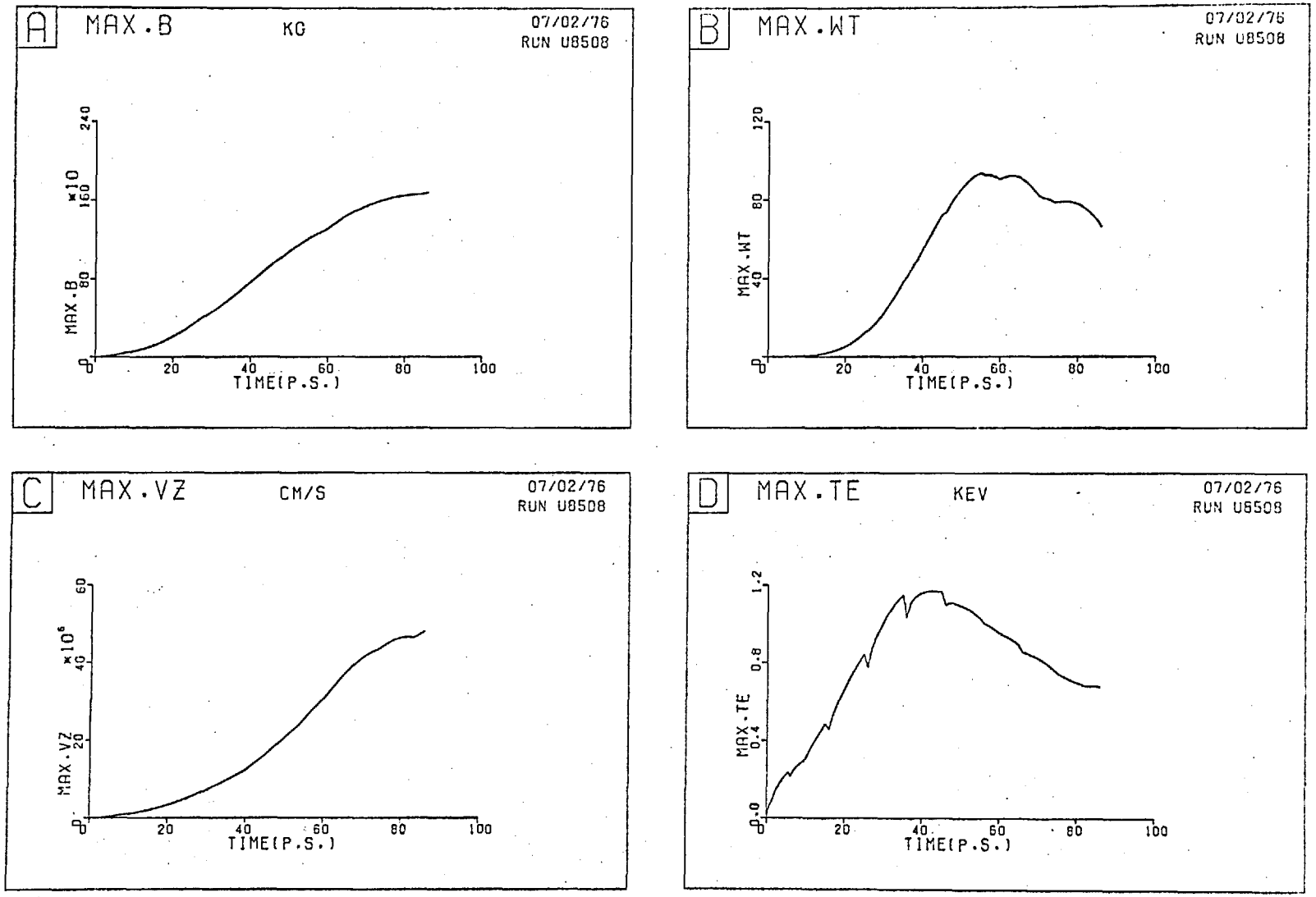

Fig.8-7 Run 8A. Time histories of the maximum on the mesh of (a) B (b) $\Omega\tau$ (c) V_z (d) T_e

these runs. A smoother initial density profile would mitigate this somewhat,but not dramatically. Probably the main physical effect omitted as a consequence of suppressing the Hall terms is the convection of heat by the current.

Returning to the question of plasma acceleration, predictions of the graph of the ion flux at a collector (66 cms from the target) against arrival time are shown for Run 8C in Fig.8-6, based on the axial velocity fields at 21, 46, 71 and 96 psec*. Some convergence is seen with concentration into the first peak, which occurs at around 3 μsec, but a plot at a later time would be desirable as the peak has increased from 8×10^{19} to 1.5×10^{20} ions/sec between 71 and 96 psec.

The corresponding velocities (in this case 2.1×10^{7} cm/sec or 2.8 keV) are substantially lower than the peak velocities (to be given later in Table 8.2), which correspond to energies from 10 to 100 keV. It is doubtful whether such energies can arise from values of T_e of the order of 1 keV, despite the enhancement of 4 from the ion charge and the further enhancement from the initially large $\nabla\ln(\rho)$. The explanation inferred is that small quantities of low density plasma are accelerated by the magnetic forces; this is consistent with the ratio $B^2/\mu_o P$ having a peak of order 5-10. It should be noted, however, that because the energy in the magnetic field derives from the electron thermal energy we do not expect $\underline{J}\times\underline{B}$ forces to shift the peak

---

*Similar graphs were obtained for Runs 8A and 8B.

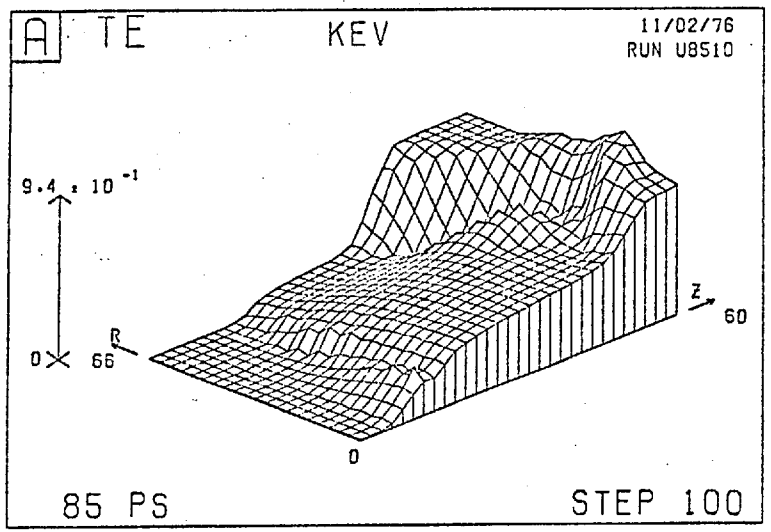

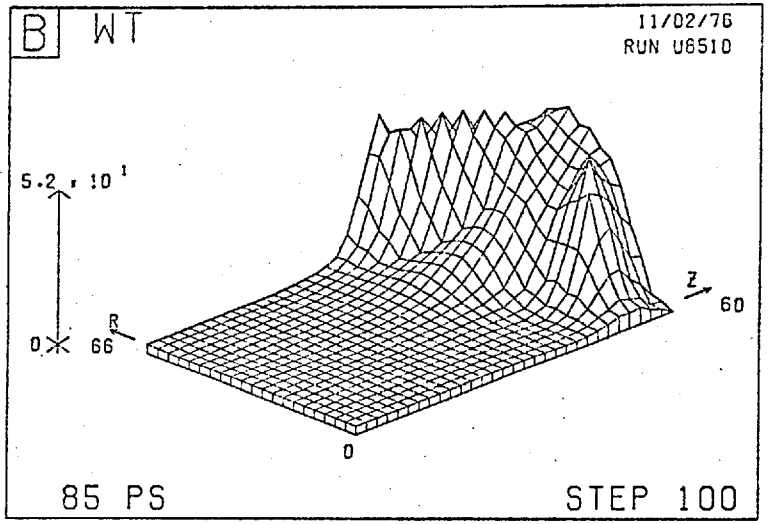

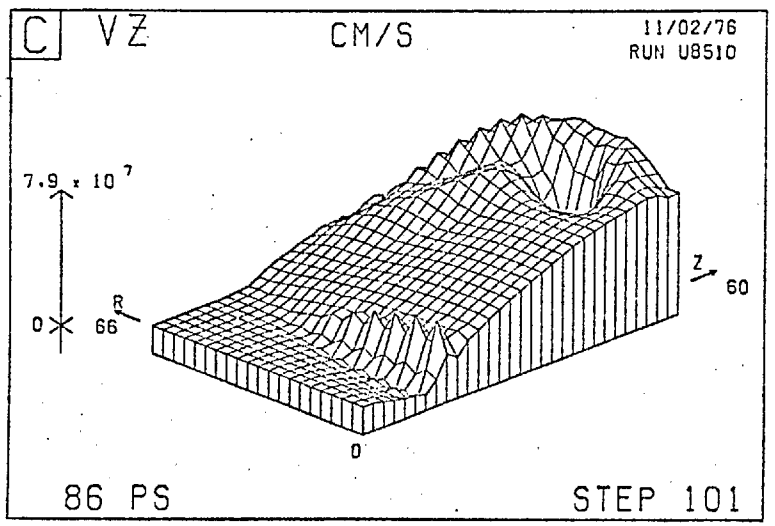

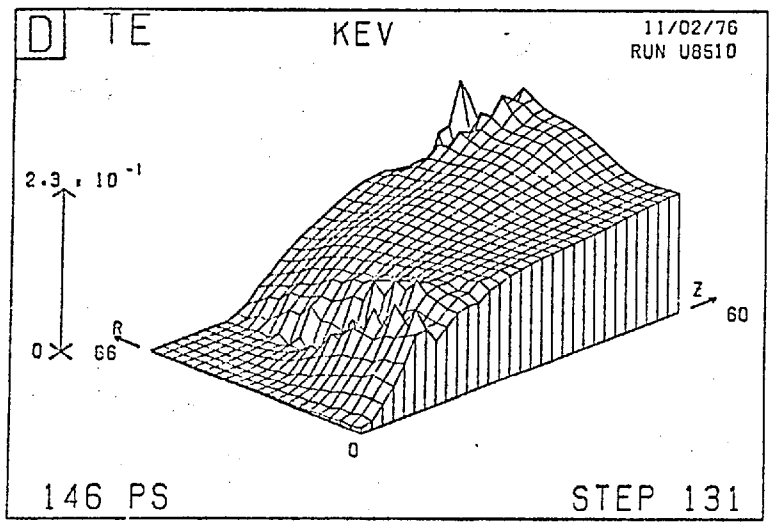

Fig.8-8 Run 8B. (a) T_e at 85 psec (b) $\Omega\tau$ at 85 psec
(c) V_z at 86 psec (d) T_e at 146 psec

in the arrival time curve, the peak being understood to arise from the bulk of the hot plasma.

8.2.2 Run 8A: Overall behaviour

The overall behaviour of Run 8A is indicated in Fig.8-7 which shows the maximum B, $\Omega\tau$, V_z and T_e on the mesh as a function of time. Recalling that the laser pulse peaks at 36 psec and has a half-width of 15 psec, the maximum T_e and $\Omega\tau$ begin to decrease as soon as the pulse is over. The maximum B and V_z continue to grow, and only decay through advection out of the simulation region.* The slight dips in the graph of maximun T_e occur when the diffusion equation is solved on the large diagonal mesh in order to couple the two staggered main submeshes.

8.2.3 Run 8B: An edge effect

Problems often arise with finite difference schemes at or near boundaries, for the computational reason that not all points are treated alike and for the physical reason that information should only travel out of the region. It is more satisfactory numerically though more wasteful of computer time to use a mesh large enough so that all the interesting physics takes place before boundary effects become important, while on the other hand it may be desired to continue the run until the hot plasma has left the simulation region. In our present series of four runs the laser pulse has finished before a significant mass of plasma crosses the

*This occurs later than is shown in Fig.8-7.

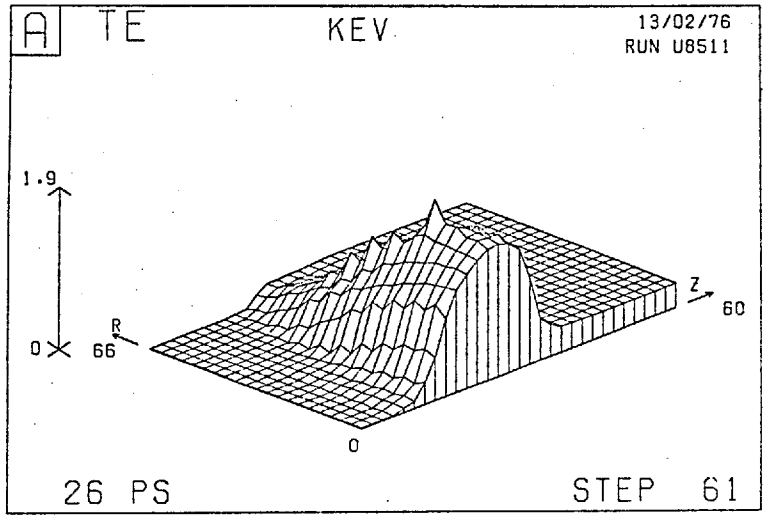

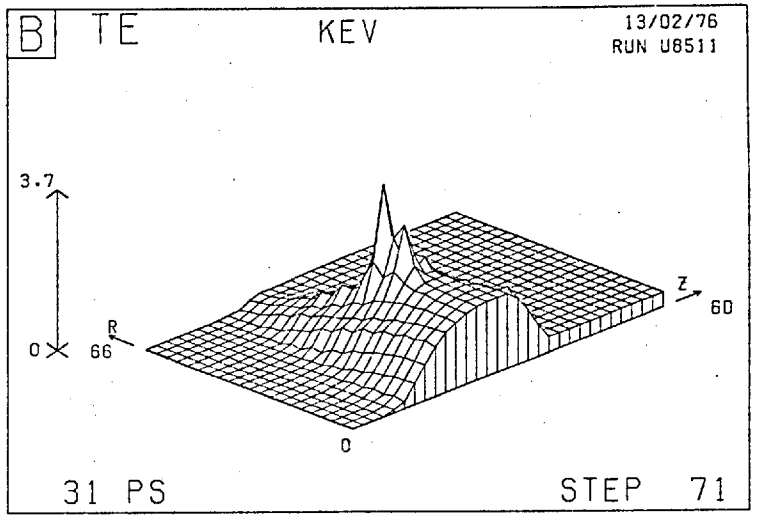

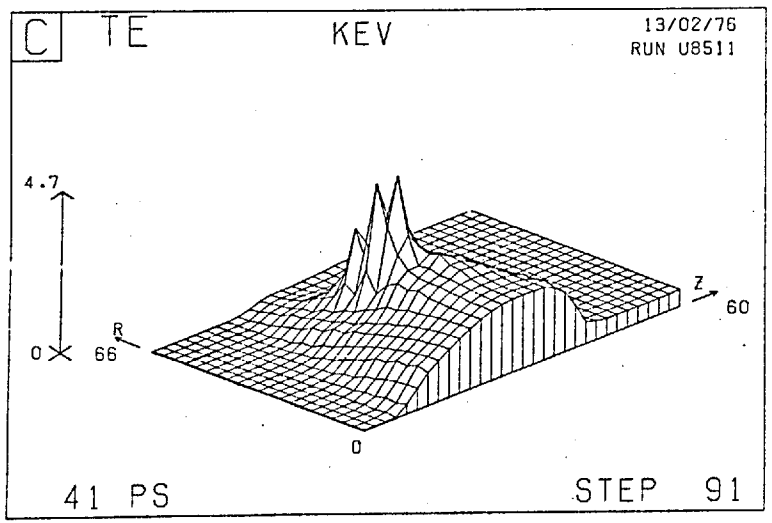

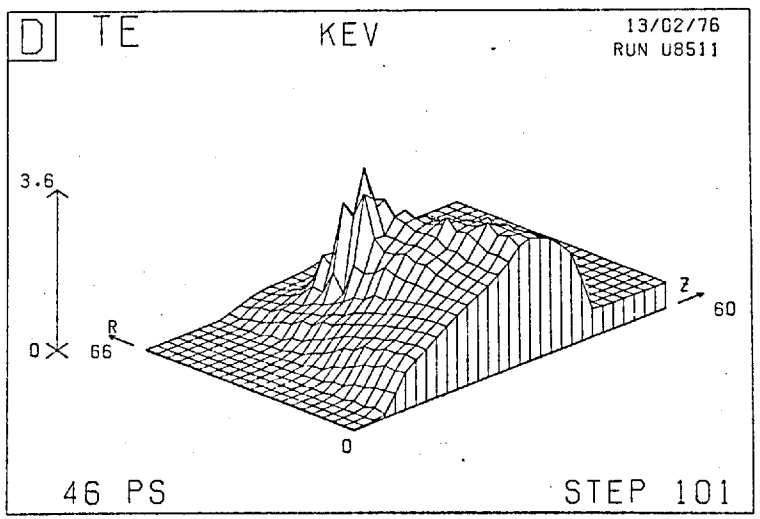

Fig.8-9 Run 8C, T_e at (a) 26 psec (b) 31 psec (c) 41 psec (d) 46 psec

boundaries, but later in these runs this is no longer the case. We consider that while we may validly attempt to understand and learn from phenomena occurring near a boundary, we should always treat such results with caution.

With this important proviso in mind we shall examine the later development of Run 8B shown in Fig.8-8. The distribution of T_e at 85 psec (Fig.8-8a) is similar to that of Run 8A (Fig.8-4d) and exhibits a "warm spot" on the east boundary. The magnetic field at 85 psec is generally large, but $\Omega\tau$ (Fig.8-8b), which depends inversely on density, is only large near the east boundary. Therefore the plasma near this edge cannot cool and a positive $\partial T_e/\partial z$ is set up, causing a localized dip in the distribution of V_z (Fig.8-8c). Eventually this hot plasma is ablated out of the region leaving a cooled plasma with the electron temperature not exceeding 230 eV at 146 psec (Fig.8-8d).

8.2.4 Runs 8C and 8D: Hot spots

Because in many respects these runs are similar to the lower power runs 8A and 8B it would be unnecessarily repetitive to describe them in detail.

There is an important difference, however - these runs exhibit hot spots, while in the previous runs the magnetic fields generated never gave rise to a value of $\Omega\tau$ exceeding unity in the crucial absorption region. Here the conditions for hot spots are just satisfied at a few mesh-points, as may be seen in Fig.8-9 which shows the development

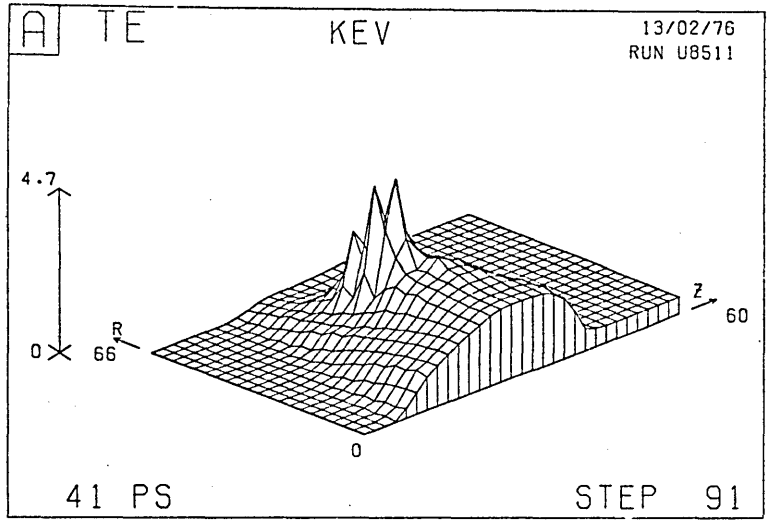

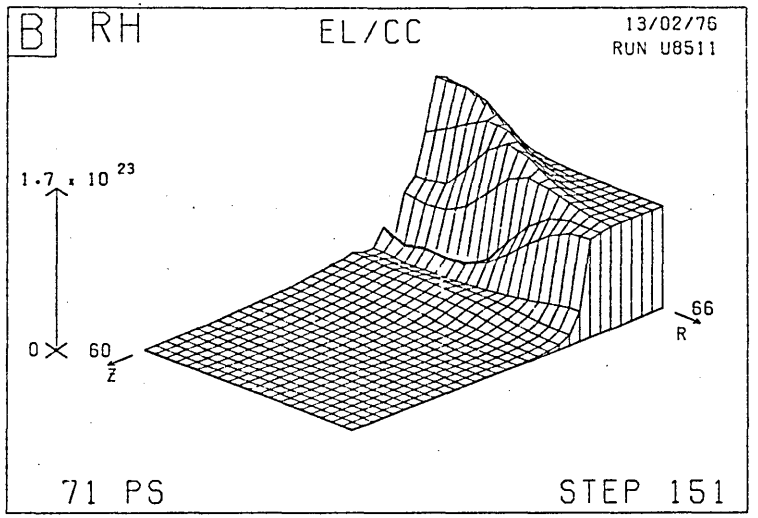

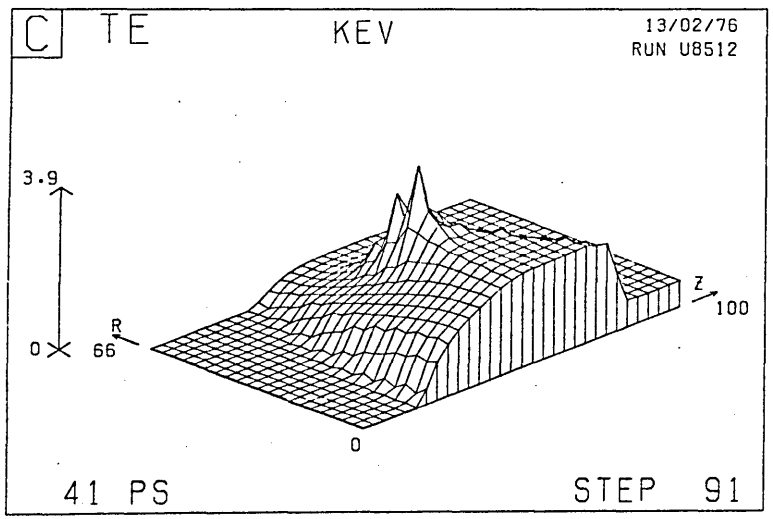

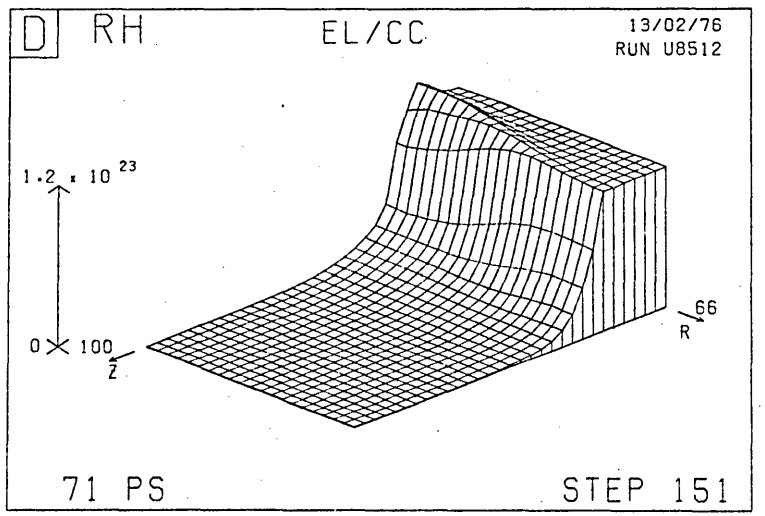

Fig.8-10 (a) Run 8C: T_e at 41 psec (b) Run 8C: n_e at 71 psec

(c) Run 8D: T_e at 41 psec (d) Run 8D: n_e at 71 psec

of a hot spot in Run 8C. At 41 psec, just after the time of peak power, the hot spot has almost attained its peak (Fig.8-9c). It later decays through a combination of thermal diffusion and advection, a process which has just begun at 46 psec (Fig.8-9d).

Fig.8-10 provides a comparison between Runs 8C and 8D, showing for each run T_e at 41 psec and n_e at 71 psec. The hot spots are compared at the time of their peaks; that of the lower density gradient Run 8D is slightly less pronounced. Greater though insubstantial compression is seen in Run 8C; it is surprising that runs with a similar electron temperature distribution (which drives the compression) should differ so markedly. This is due to the assumed form for the energy dump, which in these runs spreads the unabsorbed energy in the ratios 4:3:2:1 over the four mesh points counting from the first overdense point (see (8.2)), thereby allowing regions of higher density to be heated in Run 8C. This effect dominates the slow propagation of the thermal front into the high density region. Clearly a better comparison would be obtained by dumping either over equal lengths or over equal density ranges.

8.3 ANALYSIS OF THE RESULTS

We now proceed to a more detailed consideration of the runs whose qualitative features we have just described. In Section 8.3.1 we provide a table of comparative param-

Table 8.2 Comparative parameters of Runs 8A-8D.

	Units	Run 8A	Run 8B	Run 8C	Run 8D
Initial $\nabla\rho$		Standard	Steep	Steep	Standard
Lengthscale z_{c4}	μm	9.0	2.4	2.4	9.0
Laser energy	Joules	0.3	0.3	1.2	1.2
Peak I_A on axis	W/cm^2	3.3×10^{14}	3.3×10^{14}	1.3×10^{15}	1.3×10^{15}
Simulation time	psec	176	91	96	80
No.of timesteps		146	191	201	168
Hot spot ?		No	No	Yes	Yes
At 36 psec (a)					
Max.T_e on axis	keV	1.04	1.07	1.99	2.20
Max.T_e	keV	1.04	1.22	4.10	3.14
Max.B	MG	0.64	2.15	6.25	1.74
Max.V_z	10^7cm/s	1.02	4.58	7.42	2.42
Max.$\Omega\tau$		41	63	178	256
At 76 psec					
Max.T_e	keV	0.74	0.97	1.54	(22.3) (b)
Max.B	MG	1.62	2.98	6.63	(28.1) (b)
Max.V_z	10^7cm/s	4.47	8.17	12.1	(16.6) (b)
Max.$\Omega\tau$		78	70	208	(9230) (b)
Peak values (c)					
Peak T_e	keV	1.2 (43)	1.3 (48)	5.0 (42)	
Peak B	MG	1.7 (95)	3.6 (57)	9.6 (56)	
Peak V_z	10^7cm/s	5.2 (113)	8.2 (73)	13 (64)	
Peak $\Omega\tau$		93 (55)	89 (57)	551 (62)	
Arrival time of ion peak (d)	μsec	5.4	3.0	3.1	5.0
Corresponding velocities	10^7cm/s	1.2	2.2	2.1	1.3
Corresponding energies	keV	0.9	3.0	2.8	1.1
Energy of first ions to arrive	keV	17	41	109	

(a) Time of peak power; (b) Unreliable - see text;
(c) Corresponding times in psec in parentheses;
(d) Approximate figures: ±0.5 μsec.

eters; in Section 8.3.2 we examine the rôle of inverse bremsstrahlung at early times in the simulation with reference to Run 8C; in Section 8.3.3 we assess the dependence of the results on the initial density gradient by comparing Runs 8A and 8B; and in Section 8.3.4 we compare Runs 8B and 8C to investigate how various quantities scale with the laser power.

8.3.1 Comparison of Runs 8A-8D

Some comparative parameters of the four runs are given in Table 8.2. They include the maximum values on the mesh of T_e, B, V_z and $\Omega\tau$ at 36 psec (the time of peak power) and at 76 psec (when the pulse is effectively over). For each run the peak values of these quantities are given with the corresponding times in parentheses. Comparing Runs 8A and 8B we see that the stronger density gradient has little impact on T_e, whose distribution is affected more by the thermal conductivity, while B and V_z which depend on $\nabla\ln(\rho)$ for their generation are significantly larger in Run 8B.

Because of the strong temperature dependence of the thermal conductivity, quadrupling the laser input results in the peak temperatures on the axis at 36 psec being only approximately doubled. Off-axis the increase is greater due to the occurrence of hot spots at the higher intensity.

In Run 8D an instability occurred on the axis at the low density end of the plasma, commencing at around 50 psec. While not affecting the bulk of the plasma, this caused the misleading bracketed figures in Table 8.2 at 76 psec.

8.3.2 The rôle of inverse bremsstrahlung

The inverse bremsstrahlung (I,B,) length is given from (3.43) or Table A,3 by K_{IB}^{-1} where

$$K_{IB} \simeq 98\left(\frac{n_e}{10^{21}/cc}\right)^2 \frac{z}{T_{eV}^{3/2}} \left(\frac{\lambda_{las}}{1.06\mu m}\right)^2 \frac{1}{\sqrt{1-n_e/n_c}} \ \mu m^{-1}, \qquad (8,4)$$

and the associated heating (in the absence of other processes) is determined from

$$\frac{3}{2} n_e k \frac{dT}{dt}e = K_{IB} I. \qquad (8.5)$$

At constant laser power and constant (sub-critical) density, (8,5) may be written as

$$\frac{dT}{dt}e = \sigma T_e^{-3/2}, \qquad (8.6)$$

where T_e and t are now measured in eV and psec, and σ is a constant. (8,6) is trivially integrated to give

$$\frac{2}{5}\left(T_e^{5/2} - T_{eo}^{5/2}\right) = \sigma t, \qquad (8.7)$$

where T_{eo} is the initial temperature.

The basic result that I,B, is relatively ineffective at high temperatures and low densities is well known; we quantify this for our situation in Table 8,3 where we give for three electron number densities:

(a) K_{IB}^{-1} for various T_e, calculated from (8,4) with z = 4;

(b) the temperatures at which K_{IB}^{-1} becomes 100μm, the length-

Table 8.3 Inverse bremsstrahlung lengths and heating rates, calculated for z=4, λ_{las}=1.06μm, and I=1.34x10^{15} e^{-4} W/cm^2.

	Electron number density (cm^{-3})		
	10^{19}	10^{20}	0.94x10^{21}
K_{IB}^{-1} for T_e = 10 eV	802 μm	7.6 μm	0.02 μm
100 eV	2.54 cm	242 μm	0.65 μm
1000 eV	80.2 cm	7650 μm	20.7 μm
T_e at which K_{IB}^{-1} = 100μm	2.5 eV	55.7 eV	2.9 keV
Coefficient σ of (8.6)	4.03 x 10^3	4.41 x 10^4	1.72 x 10^6
Time in psec to increase T_e to: 100 eV	9.9	0.9	0.02
300 eV	155	14	0.36
1000 eV	3140	287	7.35

scale of our simulation region;

(c) the heating coefficient σ of (8.6);

(d) the time required for heating to various temperatures by a laser of constant intensity I(0,0), given by (8.1) for Runs 8C and 8D as

$$I(0,0) = 1.34 \times 10^{15}\ e^{-4}\ \text{W/cm}^2\ , \qquad (8.8)$$

other processes assumed constant.

Initially, in Run 8C, T_e = 10 eV and n_e = 10^{19} cm^{-3} on the half of the mesh with z > 30μm. We see from Table 8.3 that K_{IB}^{-1} = 802μm, so that almost uniform heating occurs throughout this region, at a rate which is initially

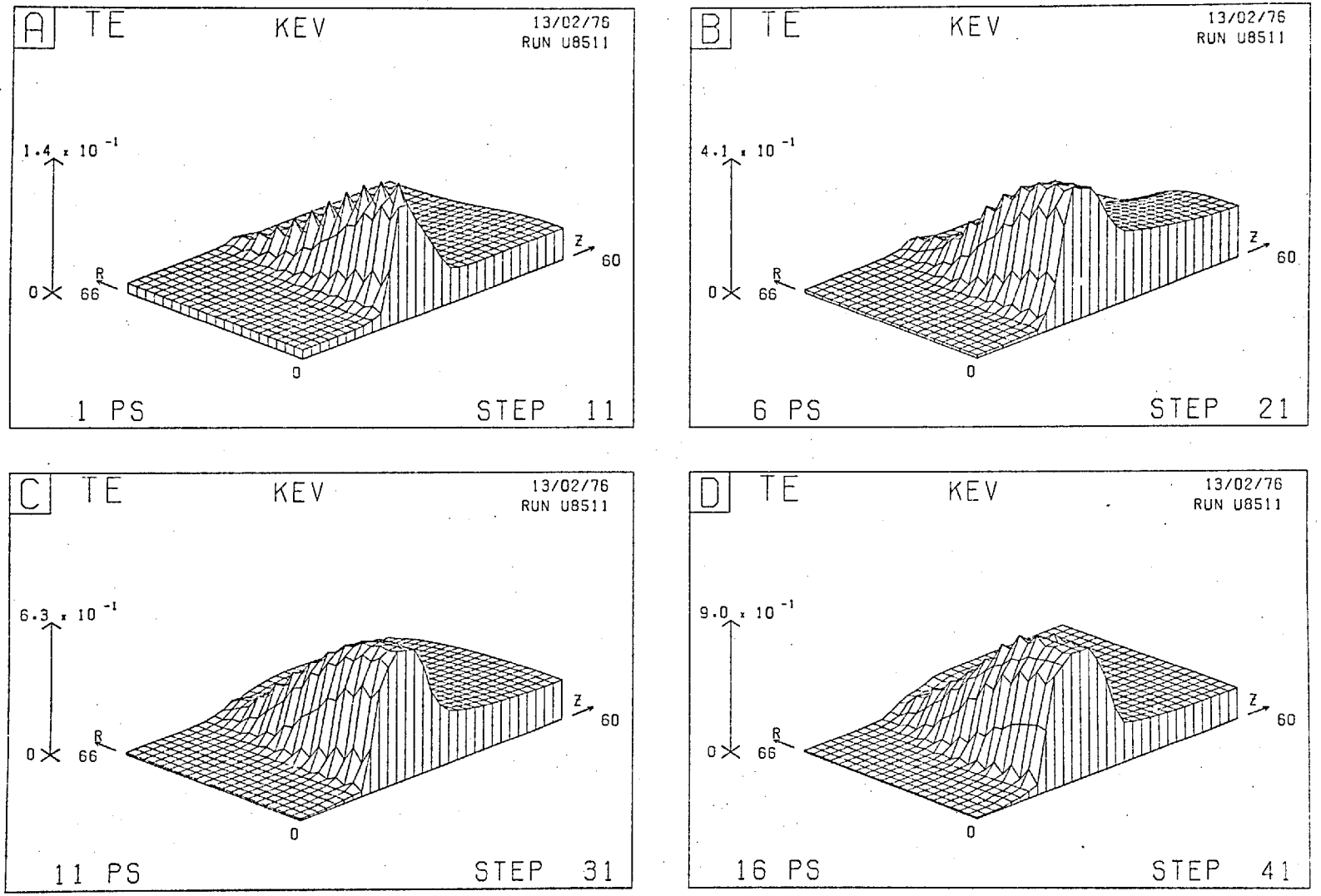

Fig.8-11 Run 8C. T_e at (a) 1 psec (b) 6 psec (c) 11 psec (d) 16 psec

$4030/10^{3/2}$ = 127 eV/psec, but which rapidly drops off with time; on the timescale of the pulse I.B. does not heat this region to much more than 100 eV. It is for this reason that the first few timesteps are chosen to be 0.1 psec.

Heating is more significant on the density ramp, but very rapidly T_e exceeds 100 eV, the absorption length exceeds the length of the ramp, and dumping commences.

We noted in Section 5.2.10 that a small problem arises in the numerical treatment of I.B. absorption very near to the critical density on account of the square root factor in (8.4). To avoid this we consider the plasma to be overdense when

$$n_e > 0.95 n_c \simeq 0.94 \times 10^{21} \text{ cm}^{-3} , \qquad (8.9)$$

and then commence the ad hoc dump. For this reason the last column of Table 8.3 corresponds to the maximum I.B. permissible; the maximum enhancement due to the square root factor is then a factor of about 4.

These features are illustrated in Fig.8-11 which shows the early development of T_e in Run 8C. At 1 psec (Fig.8-11a) we note the uniform low heating in the low density region and the increased heating near the critical density. At 11 psec (Fig.8-11c), $T_e \simeq 600$ eV at half the critical density, giving $K_{IB}^{-1} \simeq 106 \mu m$, so that the bulk of the energy is dumped. As early as 6 psec (Fig.8-11b) thermal diffusion is becoming effective, as is also seen at 11 psec by which time the distribution of T_e has flattened

Table 8.4 Comparison of high and low density gradient runs 8B and 8A.

Quantity	Units	Time (psec)	Run 8B	Run 8A	B ÷ A
$\nabla \ln(\rho)$ (a)	μm^{-1}	0	0,578	0,154	3,75
		36	0,359	0,144	2,49
		86	0,098	0,107	0,92
max. B	kG	0.1	0,145	0,036	4.05
		1.0	5.48	1.41	3.89
		36.0	2150	640	3.36
max. V_z	cm/sec	0.1	4.64×10^3	1.17×10^3	3,97
		1.0	1.06×10^5	2.71×10^4	3,91
		36,0	4.58×10^7	1.02×10^7	4.49
max. T_e	eV	0,1	29,7	29,0	1,02
		1,0	77,0	74,5	1,03
		36.0	1220	1040	1,17
max. $B^2/\mu_o P$		36,0	7,7	0,55	14,0
Axial change of critical density position at r=0	μm	36,0	2,9	0,5	5.8

(a) At the critical density at r = 0.

in the low density region. The axial gradient of T_e to the right of the heating region in Fig.8-11 is sustained throughout most of the run by large $\Omega\tau$ effects - the maximum $\Omega\tau$ becomes unity as early as 3 psec.

8.3.3 Dependence on the initial density gradient

The dependence on the initial density gradient is illustrated in greater detail in Table 8.4, which compares Runs 8A and 8B at early times. In the early stages the correspondence is almost exact: after the first timestep (at 0.1 psec) the ratios of the peak values of B and V_z are approximately equal to 3.75, the ratio of the initial density gradients. That they are not exactly equal arises because:

(a) finite differences are taken over different length-steps;

(b) the profiles of T_e will be different because inverse bremsstrahlung is more effective over shallower density gradients;

(c) the peak B occurs off-axis unlike the peak V_z;

(d) the driving terms, $\partial(\rho T)/\partial z$ for V_z and $(\partial\rho/\partial z)(\partial T_e/\partial r)$ for B, involve finite differences of variables on the auxiliary mesh whose calculation involves averages on the main mesh.

As time increases the density gradient flattens out, more rapidly in the high $\nabla\rho$ case, and the corresponding ratio decreases from 3.75 to 2.49 at 36 psec. Consistently

the rate of growth of magnetic field decreases faster in Run 8B, so that the magnetic field ratio decreases from 4.05 to 3.36 in the same time; this is not a logical consequence, however, because of other competing effects, particularly thermal conductivity. That the ratio of peak V_z increases is ascribed to the fact that the $\underline{J}x\underline{B}$ acceleration, which depends on B^2, is much greater in Run 8B.

It appears that beyond a certain point a further steepening of the density gradient will have a diminishing effect. We may estimate that an expansion velocity of $\sim 10^7$ cm/sec will smooth out density lengthscales of less than 1μm within timescales of the order of 10 psec.

8.3.4 Dependence on the laser power

Of interest is the scaling of various important quantities with the laser power (or the laser intensity), already alluded to in the discussion of Table 8.2.

Experimentally, quantities Q are often plotted against the laser intensity and scaling relationships of the form

$$Q \quad \alpha \quad I^s$$

are obtained, where s is chosen to give the best fit. Theoretically, such scaling laws may be obtained from simplified models.

The purpose of this section is twofold: to calculate the values of s applicable to various quantities at

various times assuming such scaling laws, and to demonstrate the difficulty of obtaining our results using scaling laws such as might be predicted by simple analytical models.

Recalling that the intensities of Runs 8B and 8C are in the ratio 1:4 , the scaling index s for any quantity Q is calculable from

$$Q_C = Q_B \, 4^s \, . \tag{8.10}$$

In Table 8.5 we give the s obtained from taking Q as the peak T_e , $\Omega\tau$, B or V_z on the mesh at eight different times in the simulations.

It is important to note that the positions of the peaks on the mesh vary according to both quantity and run, and that hot spots do not necessarily originate where $\Omega\tau$ is greatest. The peak $\Omega\tau$ will generally be found at lower densities. For these reasons the maximum $\Omega\tau$ does not scale as

$$\max\,(\Omega\tau) \quad \alpha \quad \max\,(B) \; . \; \max\,(T_e^{3/2}) \tag{8.11}$$

at constant density, and nor is the conductivity $K_\perp$ at a hot spot given by

$$K_\perp = \frac{K_o}{1+\max(\Omega\tau)^2} \tag{8.12}$$

with K_o scaling as

$$K_o \quad \alpha \quad \max\,(T_e^{5/2}) \; . \tag{8.13}$$

It is apparent from Table 8.5 that the sensitivity

Table 8.5 Scaling index s for Runs 8B and 8C.

Time (psec)	T_e	$\Omega\tau$	B	V_z
0.1	0.79	1.86	1.00	0.54
1	0.42	1.83	0.62	0.52
5	0.61	1.73	0.76	0.62
10	0.26	0.88	0.52	0.49
15	0.54	0.75	0.38	0.48
20	0.41	0.78	0.36	0.49
25	0.39	0.67	0.37	0.37
30	0.95	0.85	0.43	0.37

to laser power is greater in the early stages of a run, before thermal diffusion and other effects become important. It is instructive to examine all quantities after the first timestep, at 0.1 psec.

The increases of temperature in the two cases must be in the ratio 1:4 at every point on the mesh, but because of the initial temperature of 10 eV the index for T_e (0.79) is less than unity. The peak increases of T_e (19.7 and 78.9 eV) are in the ratio 1:4 . Because there are no initial temperature gradients, B scales exactly with laser power and has an index s=1.00. If $\Omega\tau$ were to scale according to (8.11) its index would be 2.2; this is an overestimate because the point of peak $\Omega\tau$ occurs at a lower density than the point of peak T_e , i.e, at a point where the initial temperature is relatively more important. In

the absence of initial density gradients, V_z , depending like B on the increases of T_e , would have an index of 1.0; however the equation

$$\frac{1}{\rho} \nabla(\rho T_e) = T_e \nabla \ln(\rho) + \nabla T_e \qquad (8.14)$$

is dominated by the first term on the right hand side which depends on the scaling of T_e in the region of greatest density gradient, and so the index of V_z is less than unity. Also, the averaging implicit in the auxiliary part of the Lax-Wendroff scheme causes the temperature used in (8.14) to be underestimated on the first few steps when T_e has large spatial gradients, thereby causing a further reduction in the sensitivity of V_z; alternatively stated, the index of V_z (0.54) is less than the index of T_e (0.79) because the peak T_e on the auxiliary mesh, which is what counts in (8.14), is less than the peak T_e on the main mesh.

We note large fluctuations in the index of T_e in Table 8.5, but lesser fluctuations in the indices of B and V_z which depend on the time integral of the temperature. The fluctuations in the index of T_e would be very difficult to predict on the basis of an analytical model. They may however be understood in terms of the various processes present in the computational model as we shall now indicate.

On the first step, as already explained, the increase of temperature is proportional to the input laser power and the index s is 0.79. In the inverse bremsstrahlung

phase (8.7) predicts s = 0.4, because the constant σ is proportional to the laser power. Thus at 1 psec, s = 0.42. The input from the energy dump however is proportional to the laser power and the index rises to 0.61 at 5 psec. At 10 psec thermal conduction has developed in Run 8C but not in Run 8B causing a temporary decrease in s to 0.26. At 15 psec thermal conduction has developed in Run 8B while in Run 8C $\Omega\tau$ has become large enough to inhibit thermal conduction towards the lower density atmosphere, and s increases to 0.54. It would be unreasonable to attempt to explain why s changes from 0.41 at 20 psec to 0.39 at 25 psec. s jumps to 0.95 at 30 psec because of the onset of a hot spot in Run 8C.

It should be clear why we are reluctant to infer scaling laws from our results.

CHAPTER 9

A THIN FILM INTERACTION

The work of this chapter is motivated by a desire to compare our numerical predictions with the experimental results obtained by Pearlman and Anthes[83] for the interaction of a short neodymium pulse with a thin polystyrene film.

In Section 9.1 we summarize these experimental results and discuss the inferences made concerning flux-limited electron thermal conductivity. The one-dimensional numerical results of Malone et al.[49] are also pertinent to this question.

In Section 9.2 we discuss at some length the approximations inherent in our numerical model, especially the extent to which a smoothed-out density profile can reasonably resemble a thin film of thickness 0.1μm.

In Section 9.3 we present some numerical results. We describe the time history of a typical run and compare it with two other runs of slightly different parameters. We also discuss the energy balance.

In Section 9.4 we compare the numerical and experimental results for the dependence of the ion arrival time peaks and the thin film transmissivity on the laser intensity. We also outline some modifications to the code which would be required to obtain better agreement.

(a)

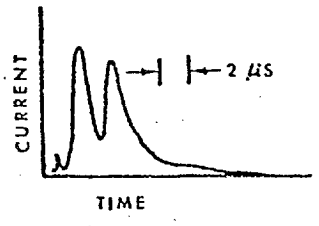

(b)

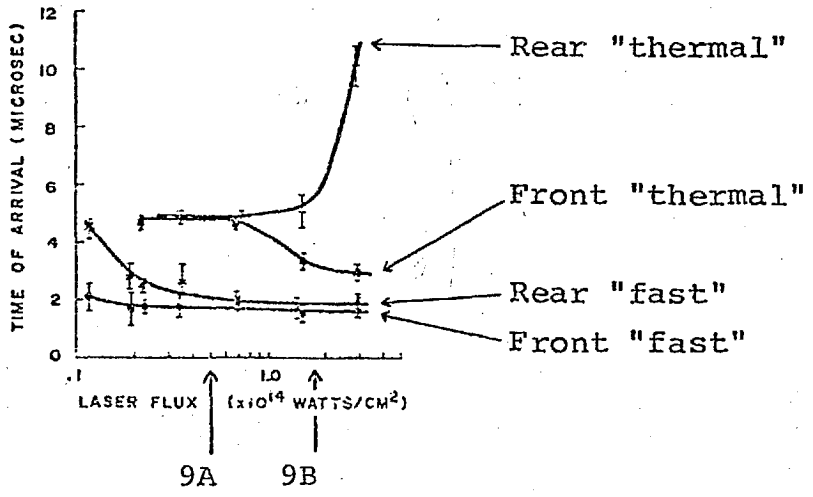

(c)

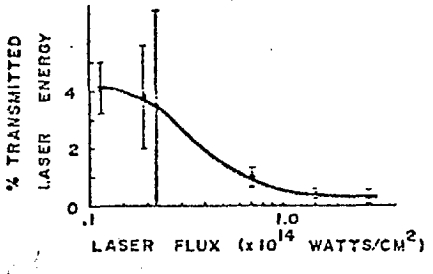

Fig. 9-1 Experimental results of Pearlman and Anthes[83].

(a) Typical double-peaked current output of Faraday cup detector.

(b) Ion arrival time as a function of laser flux for front and rear "fast" and "thermal" peaks. Vertical arrows indicate intensities of our runs 9A and 9B.

(c) Percentage of laser energy transmitted through the film as a function of incident laser flux.

9.1 THE EXPERIMENTAL RESULTS

9.1.1 Summary of the main results

A laser pulse of 50 psec FWHM and about 100μm diameter was focussed onto a polystyrene (CH) film of thickness 0.1 μm, with the peak intensity varying from 10^{13} to 3×10^{14} W/cm^2. Two Faraday cups were positioned on each side of the target, at angles of 0° and 17° to the normal and at 66 cms from the target, and were used to measure ion arrival times. The time-resolved ion charge states were determined using Thomson parabolae[98]. The incident and back-reflected light, and the core of the transmitted light, were monitored.

The Faraday cup traces, exemplified by Fig.9-1a, showed two peaks, occurring at around 2 and 4 μsec. The first peak was found to be more pronounced in the collectors normal to the target, and for this reason this peak was interpreted as "fast" and the second peak as "thermal": the "fast" peak was understood to originate from the early quasi-one-dimensional plasma and the "thermal" peak from a later expansion of the hot plasma. The arrival times of these peaks, front and rear, rear meaning opposite to the laser, were plotted in Fig.9-1b as a function of laser intensity.

It was observed that at the higher intensities the front and rear "fast" peaks arrived at the same times while

the front and rear "thermal" peaks arrived respectively earlier and later. Also the percentage of laser energy transmitted through the film decreased as shown in Fig. 9-1c, while the percentage scattered back towards the laser was approximately the same (∿2%) in all cases.

In contrast to the results of Ehler (Section 2.2.3) the peaks were not identified by charge species. All peaks contained a mixture of species; the "thermal" peak was predominantly C^{3+} and C^{4+}, while the "fast" peak contained all carbon ionic species without any type of quasi-equilibrium number balance.[99]

9.1.2 Discussion of the results

The changes in behaviour of the "thermal" peaks and the transmissivity at intensities above about 10^{14} W/cm^2 were interpreted in terms of a reduction in the classical thermal conductivity. This would increase the time taken for thermal penetration through the film, so that the electron temperature and therefore the plasma acceleration of the rear would be decreased. Also vaporization of the film and expansion to an underdense state would be slowed, thereby allowing a smaller part of the tail of the pulse to pass through the film.

However a number of points may be made which cast doubt upon this interpretation:

(i) A plausible alternative explanation for the reduction in transmissivity is that the light transmitted is that which passes through at the beginning of the pulse before the film is sufficiently ionized to become overdense. This is consistent with the observation that the actual amount of light passing through the film, as determined from Fig.9-1c, is constant to within a factor of about two. The correspondence could be closer in view of the large error-bars, although this is not a prerequisite for this theory on account of the complicated non-linear break-down phase of the polystyrene film.

(ii) When the plasma becomes underdense through expansion, first on the axis, the radial variation of refractive index may be sufficient to refract the transmitted beam away from the direction of the detector. Ideally we would obtain information about the onset of an underdense state from time-resolved transmissivity measurements.

(iii) The convergence of arrival times of the rear and front "fast" peaks at high intensities is difficult to understand. Because they obviously contain a substantial proportion of the vaporized mass (see Fig.9-1a), it is unlikely on the grounds of momentum conservation that they both arise from the absorption region on the front of the film as a result of anomalous electrostatic acceleration mechanisms. We prefer to understand the process as a fairly rapid isothermalization of the overdense plasma and

the absorption region, followed by expansion on either side of an approximately symmetric pressure distribution. That this expansion is electrostatic is reflected in the fluid equations which couple the centre of mass motion of the relatively cold ions to the electron pressure gradient via the electric field*.

(iv) The close proximity of the two peaks suggests that the distinction between "fast" and "thermal" may be misleading - the peaks may correspond to the differential accelerations of the different charge species present in the electrostatic field. The "thermal" peak may correspond to a cooler region off-axis where the average intensity is less and where radial velocities are higher, thereby explaining the observed directional dependence, but we can see no simple reason according to this viewpoint why the rear peaks should diverge at high intensities.

(v) The remarkable constancy of the arrival times of the "fast" peaks while the intensity varies over an order of magnitude suggests that at higher intensities a smaller proportion of the laser energy is absorbed - if a constant proportion of the laser energy were converted into kinetic energy it would be reasonable to expect the arrival time of the peak to vary as $I^{-\frac{1}{2}}$. The obvious explanation for this is that at higher intensities the central region becomes underdense sooner; another possibility is that some of the extra energy goes into ionization.

---

*Of course the electric field is not purely electrostatic.

(vi) The explanation of flux-limiting requires the thermal flux to be actually reduced at higher temperature gradients, rather than merely to depend on a lower power of T_e than the 3.5 of the classical formula (Table A.4). Without categorically ruling out such a mechanism we remark that in the theory of anomalous resistivity the electron-ion relative velocity increases less fast with the applied electric field above the ion-acoustic and two-stream instability thresholds.[100] In contrast, the inhibiting effect of magnetic fields increases with intensity and it is possible that this may provide an adequate flux - limiting mechanism, even over a small spatial distance in the high density region between the absorption zone and the solid. Sufficiently large values of $\Omega\tau$ however do not occur in the runs presented in this chapter.

9.1.3 Other experimental and numerical results

Our discussion would be incomplete without reference to the work of Malone et al.[49] on flux-limited electron thermal conduction. They used a one-dimensional Lagrangian code (not described in detail in this reference) in which, in their notation, the electron thermal flux F is given similarly to (4.54) by

$$F^{-1} = F_L^{-1} + F_c^{-1} \qquad (9.1)$$

where F_c is the classical thermal flux and

$$F_L = f(n_e k T_e)\ (kT_e/m_e)^{\frac{1}{2}} \qquad (9.2)$$

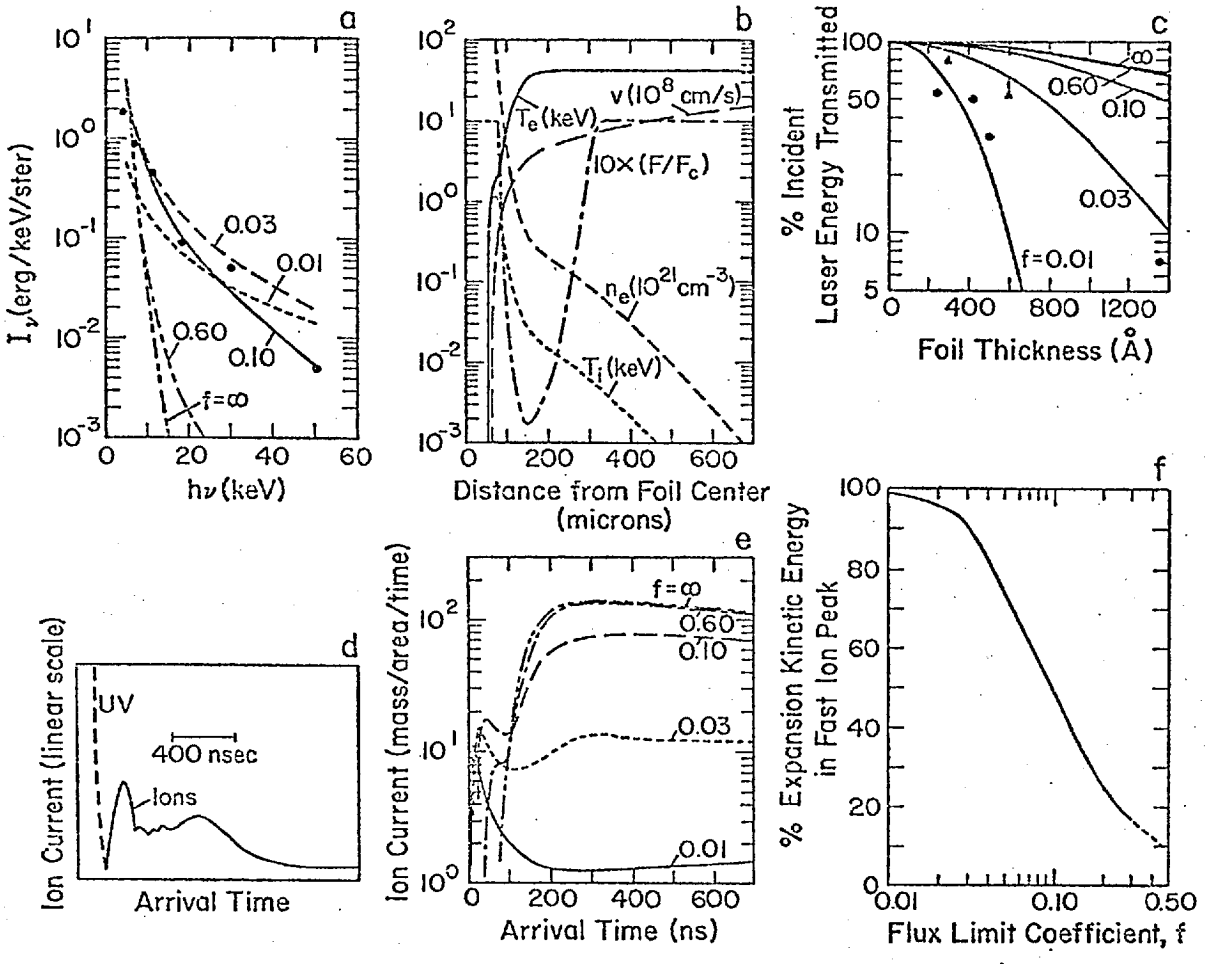

Fig.9-2 Numerical results of Malone et al.[49]

(a) Bremsstrahlung spectra for various f and 10J pulse. Data (.) from Kephart et al.[55]

(b) Calculated T_e, T_i, n_e, v, and F/F_c, for f=0.1 and $I_A = 2\times10^{16}$ W/cm^2.

(c) Calculated thin CH film transmissivity. (.) represents Los Alamos experimental results.

(d) Experimental ion current from a thick CH_2 foil.

(e) Calculated ion current.

(f) Percentage of kinetic energy in fast ion peak.

is the "free streaming" limiting flux. f is varied so as to give correspondence with experimental results for the bremsstrahlung spectra, the transmissivity of thin CH films, and the ion arrival times from thick CH_2 foils. Their laser energies vary between 4 and 40 Joules, giving a peak intensity on axis I_A between 10^{15} and 10^{16} W/cm^2 (from (8.1) with t_{FW} = 25 psec, d_{FW}= 100 μm and $r_{max}=\infty$). This is an order of magnitude greater than the pulses considered in Runs 9A-9C of this chapter where $I_A \sim 10^{14}$ - 3×10^{14} W/cm^2, or in Runs 8A-8D of Chapter 8 where $I_A \sim 3\times10^{14}$ - 10^{15} W/cm^2.

Their results are summarized in Fig.9-2. They obtain a reasonable fit to the x-ray spectrum of Kephart et al.[55] on taking $0.03 \leqslant f \leqslant 0.10$, while without flux-limiting, or with f = 0.60, they cannot generate a significant number of photons with energies around 50 keV. See Fig.9-2a, and Fig.2-6 where we reproduced the experimental results of Kephart et al. An indication of the experimental uncertainty is provided by the difference between the curves D and E of Fig.2-6, curve E corresponding to a slightly higher energy. It is curve D which is quoted in Fig.9-2a.

The rôle of the "flux-limit parameter" f is simply to generate hotter electrons in the absorption region, which we must note can also be effected by magnetic fields. The equation (8.1) for a 10J pulse with t_{FW}= 25 psec and

d_{FW} = 100 μm* gives $I_A \simeq 3.3 \times 10^{15}$ W/cm^2, which on comparison with the peak I_A of Runs 8C-8D (1.3×10^{15} W/cm^2) is expected to produce hot spots.

They also obtain a fit for the transmissivity through a thin CH film for $0.01 \leqslant f \leqslant 0.03$ in Fig.9-2c. It could be argued that the fit is fortuitous; indeed they point out that the experimental results are sensitive to the details of the spatial and temporal dependence of the laser pulse and the true absorption mechanism, all of which are uncertain. It is also notable how sensitive the transmissivity is to f: for a film of thickness 0.1 μm, values for f of ∞, 0.03 and 0.01 give transmissivities of 80%, 30% and 0% respectively.

The proportion transmitted in the initial stages is probably small because of their large laser energies, and their transmissivity is without doubt a function of the time when the plasma becomes underdense. Without substantial flux-limiting this happens very soon and most of the laser energy is transmitted. With point (vi) of Section 9.1.2 in mind we anticipate that their model will predict higher transmissivities at higher intensities in contrast to the experimental results of Pearlman and Anthes.

Their third point of comparison is the ion arrival time graphs. Although their code only treats one ion species they are able to obtain a fast peak on the graph of ion current by decreasing f to below 0.1; the peak is however

---

*The 50μm given by Kephart et al.[55] was later found to be an underestimate[49].

not very pronounced except for $f \lesssim 0.03$. (It is interesting to recall that we obtained a similar double peak in Section 7.1.2 due to magnetic fields). At what value of f the double hump should arise is not immediately apparent as the calculation of this graph involves an inversion of the velocity distribution weighted by the density distribution, but we may make the obvious point that when the laser energy is concentrated into smaller hotter regions the result is likely to be a smaller number of more energetic ions. These ions, like the photons of Fig.9-2a, are not suprathermal - they just correspond to higher temperatures*.

In conclusion, any flux-limiting mechanism which increases the temperature of the absorption region at the expense of thermal conduction into the solid may be expected to reduce the transmissivity of a thin film, and to produce more energetic photons and ions. It is interesting that while a small flux-limit parameter f and large $\Omega\tau$ effects have the common property of producing such hot regions, only the latter mechanism produces a truly localized hot spot: in Fig.9-2b we see an isothermal atmosphere of temperature 40 keV, with ions ablating at the very high speed of 10^9 cm/sec.

---

*It may be argued though that they correspond to "suprathermal temperatures".

9.2 THE NUMERICAL MODEL

9.2.1 Formulation of the problem

We consider a laser pulse, Gaussian in space and time, given by (8.1) and the following parameters:

$$\left.\begin{array}{ll} \text{pulse full width} & t_{FW} = 50 \text{ psec} \\ \text{beam radius} & r_b = 50 \ \mu\text{m} \\ \text{simulation radius} & r_{max} = 100 \ \mu\text{m}, \end{array}\right\} \quad (9.3)$$

which imply the subsidiary parameters:

$$\left.\begin{array}{ll} \text{Gaussian parameter} & t_o \simeq 30 \text{ psec} \\ \text{time of peak power} & t_p \simeq 60 \text{ psec} \\ \text{spot diameter} & d_{FW} \simeq 83 \ \mu\text{m}. \end{array}\right\} \quad (9.4)$$

With these parameters a pulse of J Joules implies a peak intensity on axis I_A given by

$$I_A \simeq 2.44 \times 10^{14} \ J \ \ W/cm^2, \quad (9.5)$$

In particular, pulses of 0.348 and 1.16 Joules give values for I_A of 8.48×10^{13} W/cm^2 and 2.83×10^{14} W/cm^2 respectively.

For purposes of comparison with the experimental results another intensity $\tilde{I}$ is defined by requiring that a uniform intensity $\tilde{I}$ incident on an area πr_b^2 for a time t_{FW} yields a specified fraction f_r of the pulse energy - i.e.

$$\tilde{I} = \frac{f_r \ J}{\pi r_b^2 \ t_{FW}} \ . \quad (9.6)$$

We take $f_r = 0.6$, in which case pulses of 0.348 and 1.16 Joules give values for $\tilde{I}$ of 5.32×10^{13} and 1.77×10^{14} W/cm^2 respectively. $\tilde{I}$ corresponds better than I_A to the experimental graphs of Fig.9-1.(99)

As in the thick target runs of Chapter 8 we consider the target to be composed of a single ion species, C^{4+}, with an initial arbitrarily chosen temperature of 10eV. The associated inaccuracies were discussed in Section 4.5.

The dumping factors (5.86) at the critical density are given by

$$d_i = 1.0,\ 0.4,\ 0.0 \quad \text{for} \quad i = 1,\ 2,\ 3. \qquad (9.7)$$

In the case of a steep initial density profile (see next section) we take $d_2 = 0$, thereby dumping all unabsorbed energy on the first overdense point.

Again, all the equations are implemented in full, except that the Righi-Leduc terms and the distinction between $\underline{V}$ and $\underline{V}_e$ are omitted.

9.2.2 The initial density profile

The representation of a film of thickness 0.1μm on an Eulerian mesh with uniform spacing presents some problems. The radial dimension requires at least 100μm for a beam of 50μm radius, but possibly not many mesh-points; the axial dimension should be large enough for us to follow the ablating plasma during its acceleration, while the axial mesh-step should be as small as possible to treat the

large initial density gradients. Our compromise is to take 21 mesh points over 100 μm radially and 41 mesh points over 40μm axially, the film being situated in the middle of the mesh at z = 20μm. The mesh is not square but has a ratio dr:dz = 5:1 .

In terms of computer time our choice is just tolerable; however, because the timestep is determined from the advective time across a mesh cell in the z- direction, doubling the number of points in that direction would approximately quadruple the computer time required.

We attempt to represent the film by spreading out its mass over a few axial mesh points. It is important that (9.10) below conserves the mass per unit area because the temperatures and expansion velocities depend on the sharing of the laser energy among the particles in the focal region. Specifically, we take a profile

$$\rho(z) = \rho_o + \rho_1 \exp\{-(z-z_o)^2/a^2\} \quad 0 \leqslant z \leqslant 40\mu m \qquad (9,8)$$

where

$$\left.\begin{aligned} \rho_o &= \rho_c/20 \\ \rho_c &\text{ is the critical density} \\ \rho_1 &= 3\rho_c \text{ or } 6\rho_c \\ z_o &= 20\mu m, \end{aligned}\right\} \qquad (9,9)$$

and a is determined by requiring

$$\int_o^{2z_o} \rho(z)\, dz = \rho_s\, t \qquad (9,10)$$

where the solid density ρ_s = 1.06 gm/cc and the film thickness t = 10^{-5}cm*. The density cut-off ρ_o is used for computational convenience and accounts for only 10% of the mass.

The critical density is calculated assuming ions of atomic mass 12 and charge number 4. For a given ratio ρ_1/ρ_c we may easily calculate the Gaussian parameter a, the distance z_c from the peak of the Gaussian to the critical density, and the distance z_{c4} from critical to quarter critical density; the results are given in Table 9.1. We

Table 9.1 Density scale - lengths for profile (9.8). Gaussian parameter (a), peak to critical length (z_c) and critical to ¼ critical length (z_{c4}), all given in μm as functions of ρ_1/ρ_c.

ρ_1/ρ_c	a	z_c	z_{c4}
3	3.66	3.92	2.10
6	1.83	2.48	0.89
12	0.91	1.46	0.39

see that ρ_1/ρ_c = 12 implies z_c < 2μm, in which case only one column of the main submesh "1" (Fig.5-1) is overdense. Our mesh is certainly not fine enough to adequately resolve such a density distribution.

---

*1.1×10^{-5} cm in the experiment.

We shall compare runs with ρ_1/ρ_c taking the less severe values of 3 and 6 to examine the dependence of the results on the initial density profile. Our approximation may not be too bad because once the film is ionized, early in the pulse, expansion may be expected to smooth out somewhat the very large initial density gradients. We shall now give an order of magnitude argument in support of this assertion.

We may estimate that the density scale-length will increase with a speed of the order of the sound speed C_s defined by

$$C_s^2 = \frac{zkT_e}{m_i} . \qquad (9.11)$$

In our case,

$$C_s \simeq 2.84 \times 10^5 \sqrt{zT_e} \text{ cm/sec} \qquad (9.12)$$

where T_e is measured in eV; taking zT_e = 1000eV we have $C_s \simeq 9 \times 10^6$ cm/sec, which would cover 1μm in just over 10psec. If this is correct the development of the density profile should be only weakly dependent on the initial ratio which we choose for ρ_1/ρ_c. If we were to develope a (Lagrangian) code for the early one-dimensional behaviour we might expect the outcome after a few picoseconds to resemble the initial conditions we have just described.

Clearly we must be cautious because this order of magnitude argument does not leave much margin for error. In particular we require that the thermal diffusion time into

the film must also be at the most of the order of a few picoseconds. We may estimate this from Spitzer's formula, the diffusion time τ_k over a lengthscale L being given from Table A.1 by

$$\tau_k \simeq 3.2 \times 10^{-21} \cdot \frac{z^2 n_i L^2}{T_e^{5/2}} \text{ secs} \qquad (9.13)$$

where n_i is measured in cm^{-3}, L in cm and T_e in eV. For example the choice

$$\left.\begin{aligned} n_i &= 5 \times 10^{22} \ cm^{-3} \\ z &= 4 \\ T_e &= 100 \text{ eV} \\ L &= 0.1\mu m \end{aligned}\right\} \qquad (9.14)$$

yields $\tau_k \simeq 2.6$ psec.

τ_k is strongly dependent on T_e - an increase of T_e to 400 eV would not greatly affect z and would reduce τ_k to much less than 1 psec. For this reason we are probably safe, at least for large or moderate laser powers. However these figures should be treated with caution because of our assumption of an initially ionized plasma.

We remark that two errors, operating in opposite directions, will occur in our numerical treatment of thermal diffusion. From (9.13), at constant $n_i L$,

$$\tau_k \propto L, \qquad (9.15)$$

so smoothing out the density by a factor of 30-60 will increase τ_k by that factor. Secondly the poor mesh resolution of even the smoothed-out profile will anomalously increase the speed of propagation of the thermal front on the mesh.

Another interesting but less obvious approximation implicit in our choice of the initial density profile is that the density scale-length is independent of radius and symmetrical about the centre of the film. This is pertinent to such effects as the differential rates of generation of magnetic field on either side of the film.

We also note that equipartition to the ions will be underestimated, although for a short time only. Anticipating our discussion of this in Section 9.3.3, this error is unimportant.

Finally we emphasize that it it the initial phase which is most likely to be treated inadequately. At later times the main defect appears to be the inclusion of only one charge species.

9.3 THE NUMERICAL RESULTS

Three runs will be compared from the point of view of the dependence of the model on the laser power and the initial assumed density gradient. They are the "Standard" Run 9A with $\rho_1/\rho_c = 3$ and J = 0.348 Joules, the "Hot" Run 9B differing from Run 9A in having J = 1.16 Joules, and the

"Steep" Run 9C differing from Run 9A in having ρ_l/ρ_c=6. See Table 9.2.

Table 9.2 Characterization of Runs 9A-9C.

	$\rho_l/\rho_c = 3$	$\rho_l/\rho_c = 6$
Low energy	Run 9A "Standard"	Run 9C "Steep"
High energy	Run 9B "Hot"	

9.3.1 Typical laser-film interaction (Run 9B)

The initial density profile, given by (9.8) with $\rho_l/\rho_c = 3$, is shown in Fig.9-3a. All of the diagrams in this series view the interaction from the origin, on the rear of the target, with the laser incident from the right along the z-axis. The critical density is encountered a few mesh-steps from the centre of the target. Note that these perspective diagrams, which merely plot arrays, are scaled differently in the r and z directions because the mesh is not square.

The early development of T_e is given in Fig.9-3 (b-d). Very early, at 1 psec (Fig.9-3b), some laser energy has been absorbed by the atmosphere, where we have assumed $n_e = n_c/20$, although most is absorbed near the critical density; at 11 psec (Fig.9-3c) conduction is effective

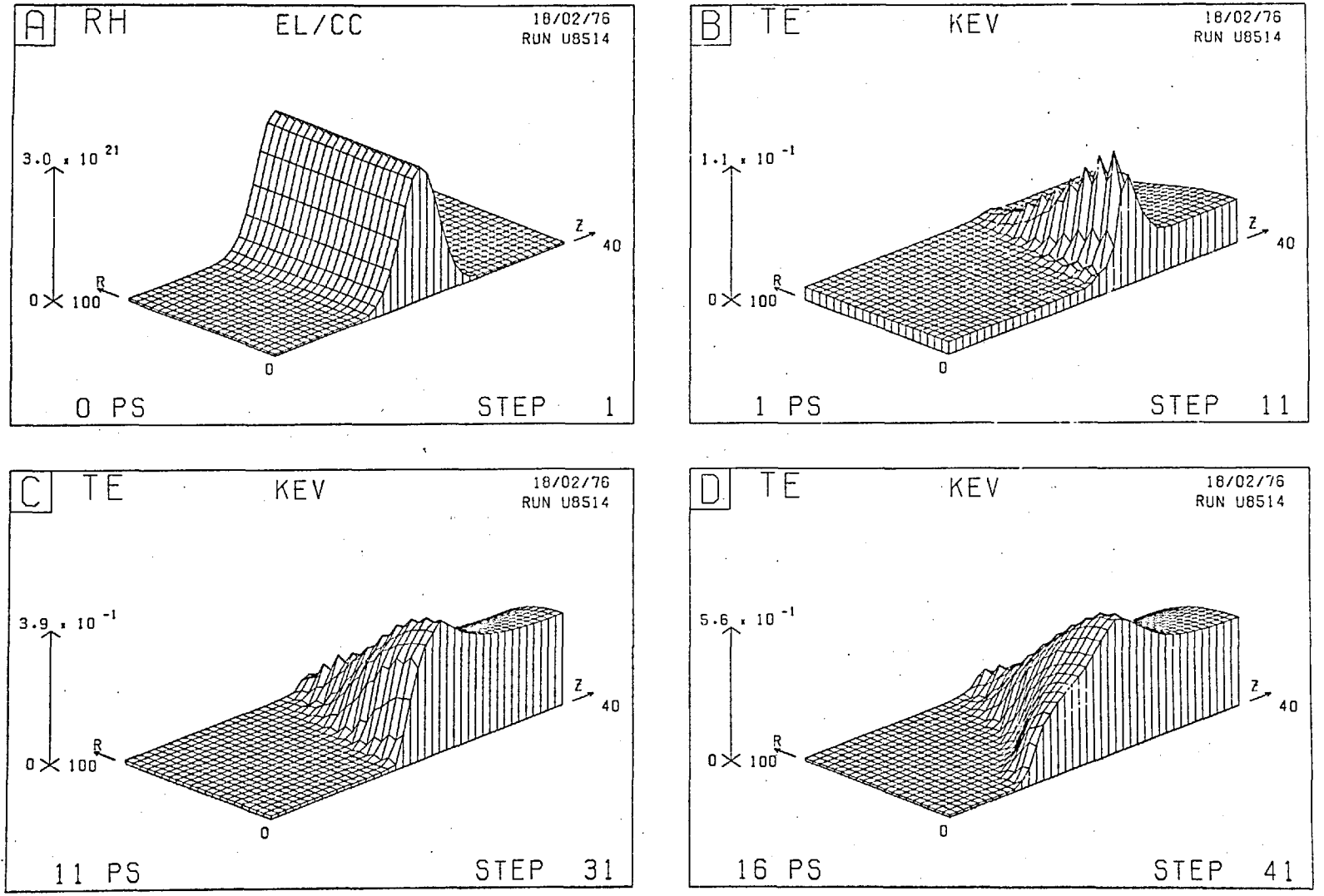

Fig.9-3 Run 9B. (a) Initial density profile (b) T_e at 1 psec
(c) T_e at 11 psec (d) T_e at 16 psec

towards the atmosphere but slow into the film; and at 16 psec (Fig.9-3d) the conduction front is just passing through the film on and near the axis. We shall return to a more detailed consideration of this initial phase in Section 9.3.2.

The behaviour of the six major fluid variables and two diagnostic variables is illustrated in Figs.9-4 and 9-5, which both refer to a time of 41 psec, two-thirds of the time of peak laser power. Fig.9-4a shows T_e to have an approximately symmetrical distribution about the position of the film. A slight peak occurs in the neighbourhood of the absorption region, where there is some reduction in thermal conductivity but not enough to form a hot spot. In the low density region, however, $\Omega\tau$ effects are greater, impeding the advance of the thermal fronts in the $\pm$ z - directions to both ends of the mesh; this is in contrast to Fig.9-3 (c-d). Radial diffusion has caused electron temperature equalization on these two ends of the mesh. Nearer the film it is impeded by large $\Omega\tau$ effects, and in the high density region it is slow because of the high thermal capacity. It would be slower still if ionization effects were included.

Fig.9-4b gives the distribution of V_z, which corresponds to a symmetrical expansion in the front and rear directions with a peak (occurring 10μm off-axis) of about 4.2×10^7 cm/sec (11 keV ions), consistent with a peak zT_e of 9.6 keV.

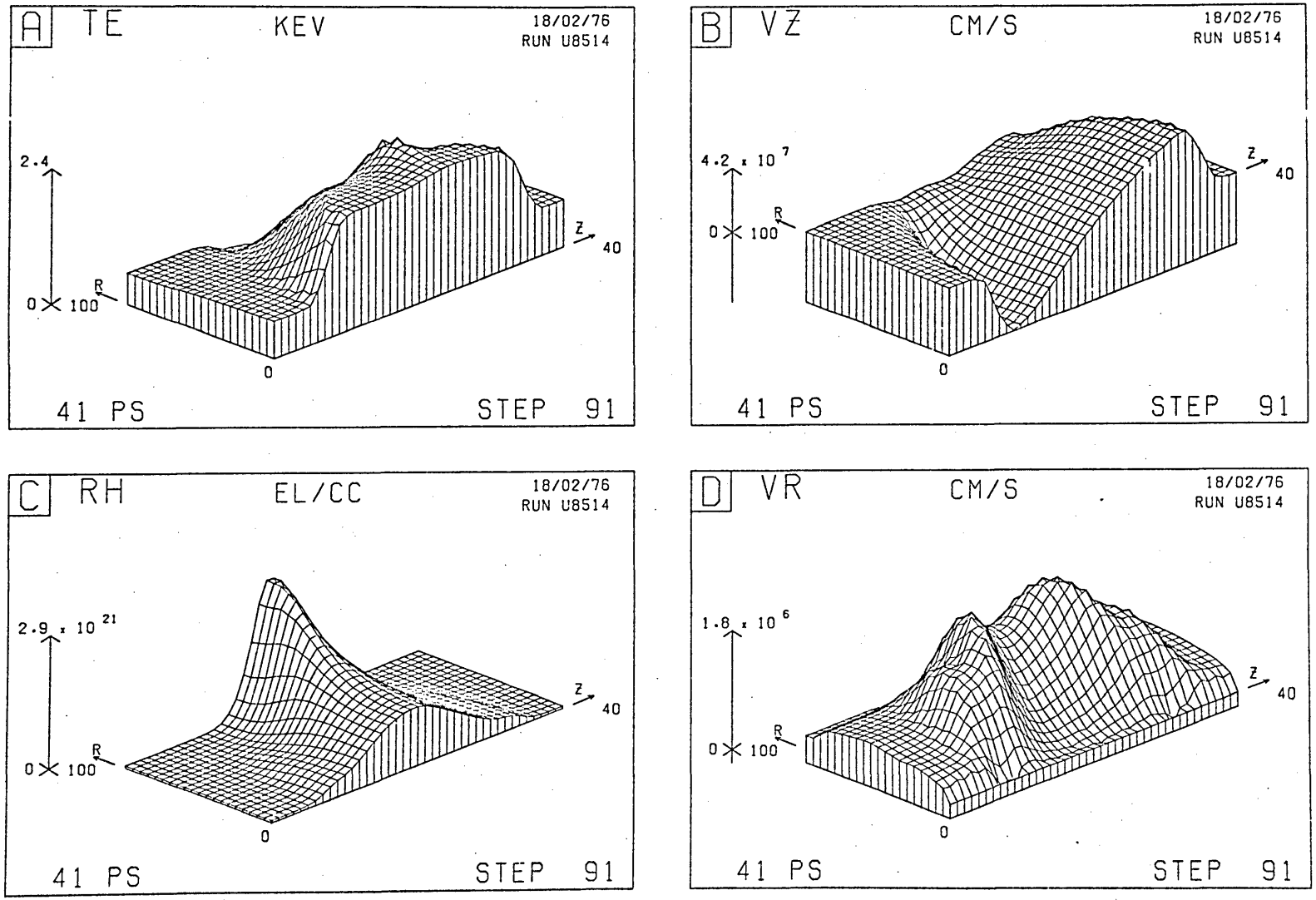

Fig.9-4 Run 9B. At 41 psec: (a) T_e (b) V_z (c) n_e (d) V_r

The peak V_z in fact occurs on the rear of the film, but it only exceeds the peak of the front expansion by 10%. We observe also that the ablation fronts have not yet reached the ends of the simulation region. For this reason nor have the magnetic fields, which is why radial temperature diffusion caused temperature equalization on the ends of the mesh as seen in Fig.9-4a.

The effect of expansion on the density distribution is shown by the plot of n_e (Fig.9-4c). Near the axis the plasma has almost become underdense. By the time of peak power (60 psec) the plasma is underdense up to a radius of 70μm (see Fig.9-6d), and most of the energy incident thereafter passes through the hole. Fig.9-4d shows the radial velocity - a response to the time integral of $\partial(\rho T_e)/\partial r$ it is generally positive, but is reduced near the film where there is a large positive $\partial\rho/\partial r$. It is an order of magnitude smaller than the axial velocity.

Fig.9-5a shows T_i; never very large, with a 96eV maximum, it is determined primarily by equipartition, which is greatest in the high density region. Equipartition is underestimated as discussed earlier, but this may not be very significant. The ripples at $z \approx 10\mu m$ and $z \approx 30\mu m$ correspond to the ripples in density at the ablation fronts.

The last of the six fluid variables, the magnetic field, is shown in Fig.9-5b. According to our convention

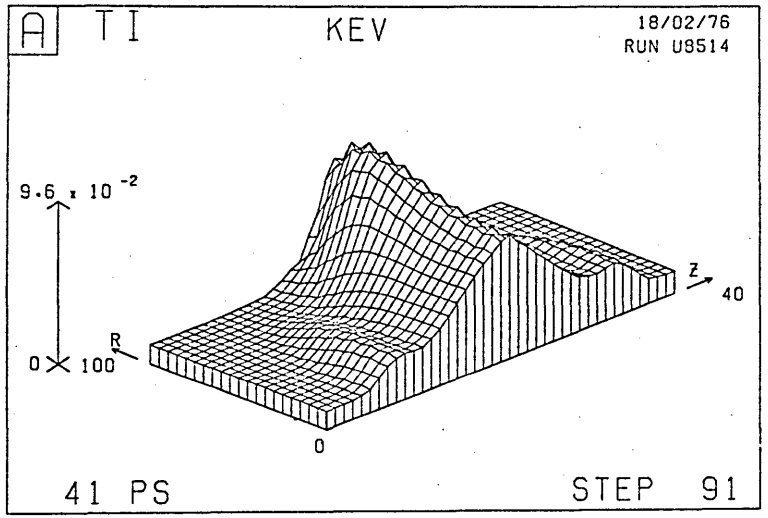

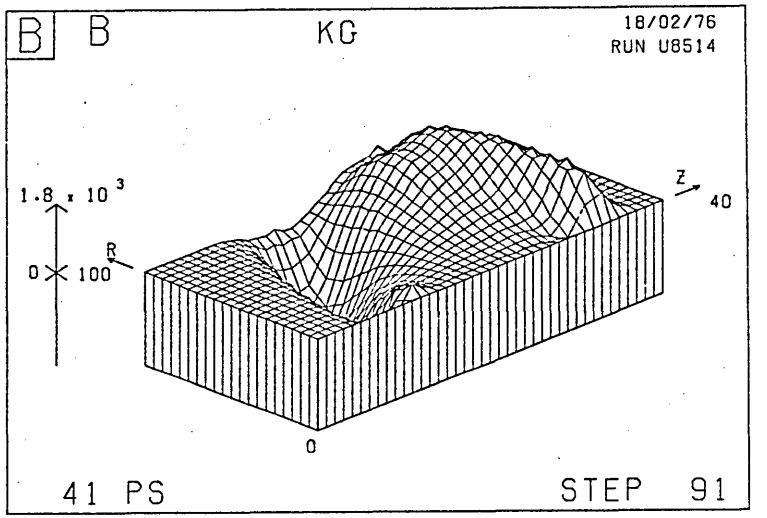

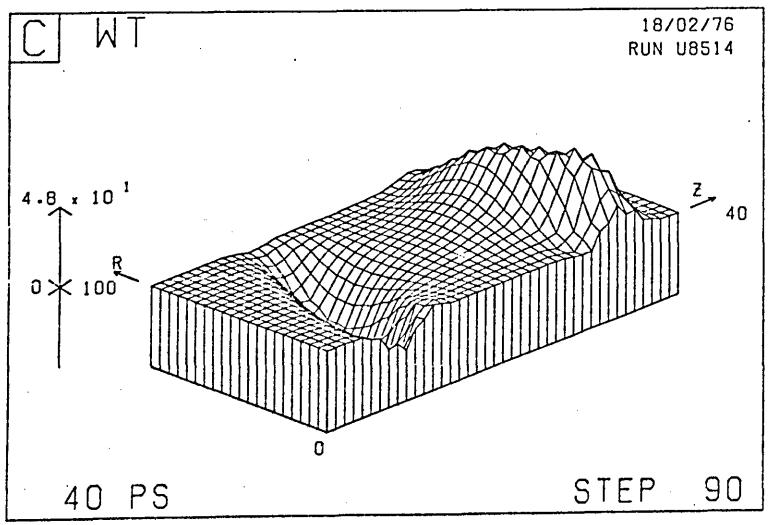

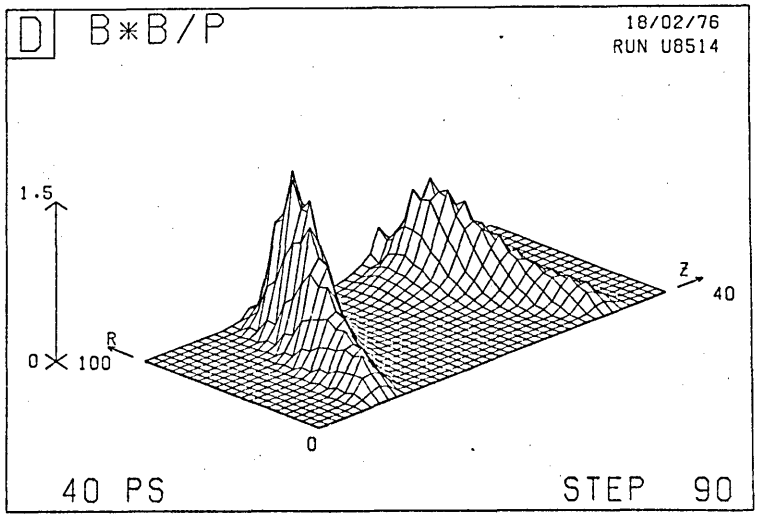

Fig.9-5 Run 9B. At 41 psec: (a) T_i (b) B (c) $\Omega\tau$ (d) B^2/P

it is $-B_\theta$ which is plotted, so that B_θ is negative on the front of the film ($z \gtrsim 20\mu m$) and reversed in sign on the rear where $\partial n_e/\partial z$ is reversed. It peaks at 1.8MG on the front and 2.5 MG on the rear. The slightly larger field on the rear arises because when the temperature field diffuses through the film it is localized nearer to the axis than on the front (see Fig.9-3d), thereby causing larger radial temperature gradients. If in practice the density gradient is also greater on the rear this effect will be enhanced.

Two consequences of the magnetic field are $\Omega\tau$ (Fig.9-5c) and the ratio B^2/P of magnetic to plasma pressure* (Fig.9-5d). The distribution of $\Omega\tau$ has a peak of 48, giving rise to the two regions of reduced thermal conductivity referred to in the discussion of Fig.9-4a. Because the distribution of T_e flattens near the centre, the source of B switches off there, so that the regions of significant B move out with the ablating plasma. The ratio B^2/P is significant in the same regions, although it is greater at larger radii where the pressure is smaller. Its peak of 1.5 occurs away from the region of greatest ablation, and indeed the axial velocity distribution (Fig.9-4b) shows no sign of being affected by $\underline{J} \times \underline{B}$ forces.

Later, $\underline{J}\times\underline{B}$ forces may be seen from Fig.9-6 to have had some effect. Fig.9-6 (a-d) shows respectively B^2/P, V_r, V_z and ρ at 61 psec, the time of peak laser

---

*Strictly speaking we have plotted $3/\beta$: see (8.3).

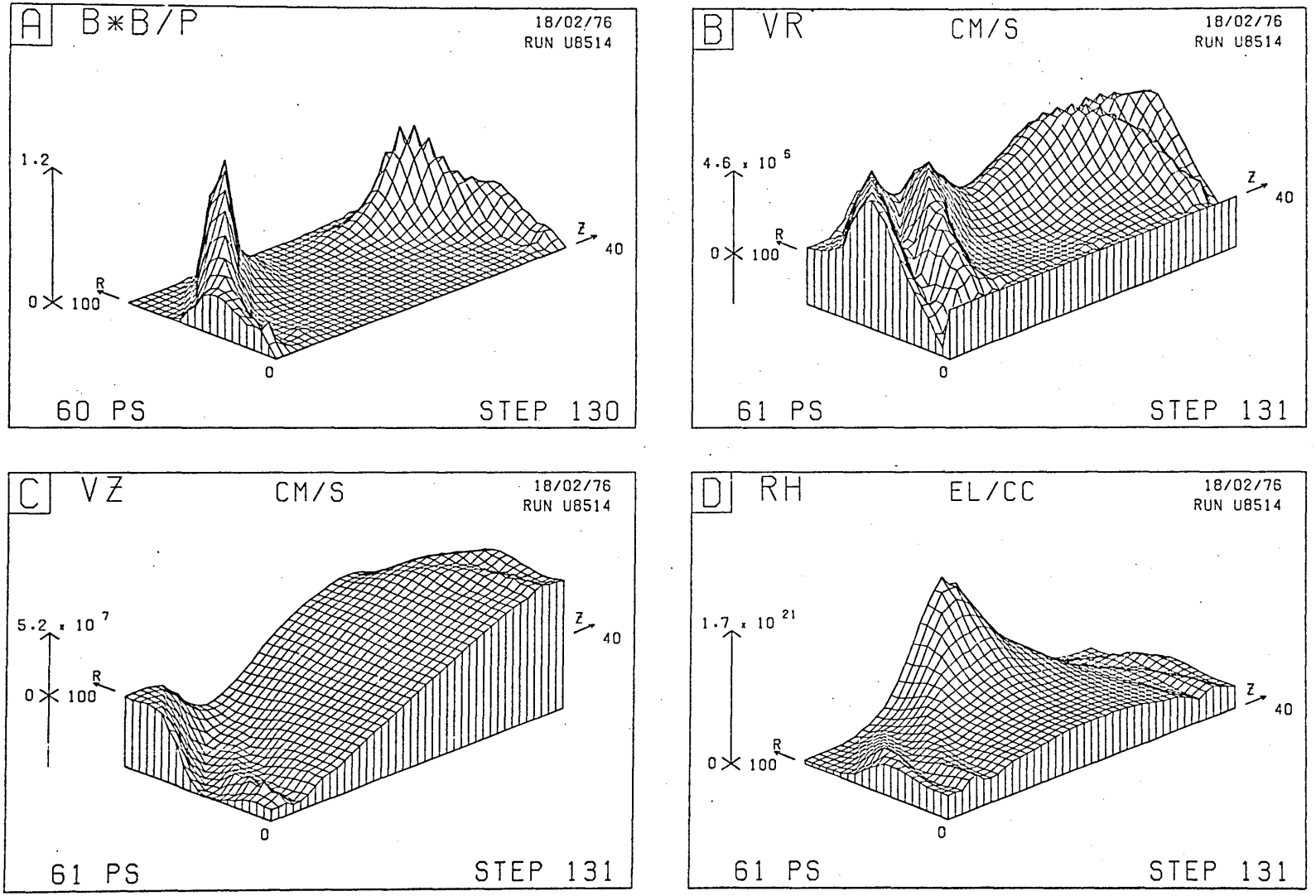

Fig.9-6 Run 9B, At 61 psec: (a) B^2/P (b) V_r (c) V_z (d) n_e

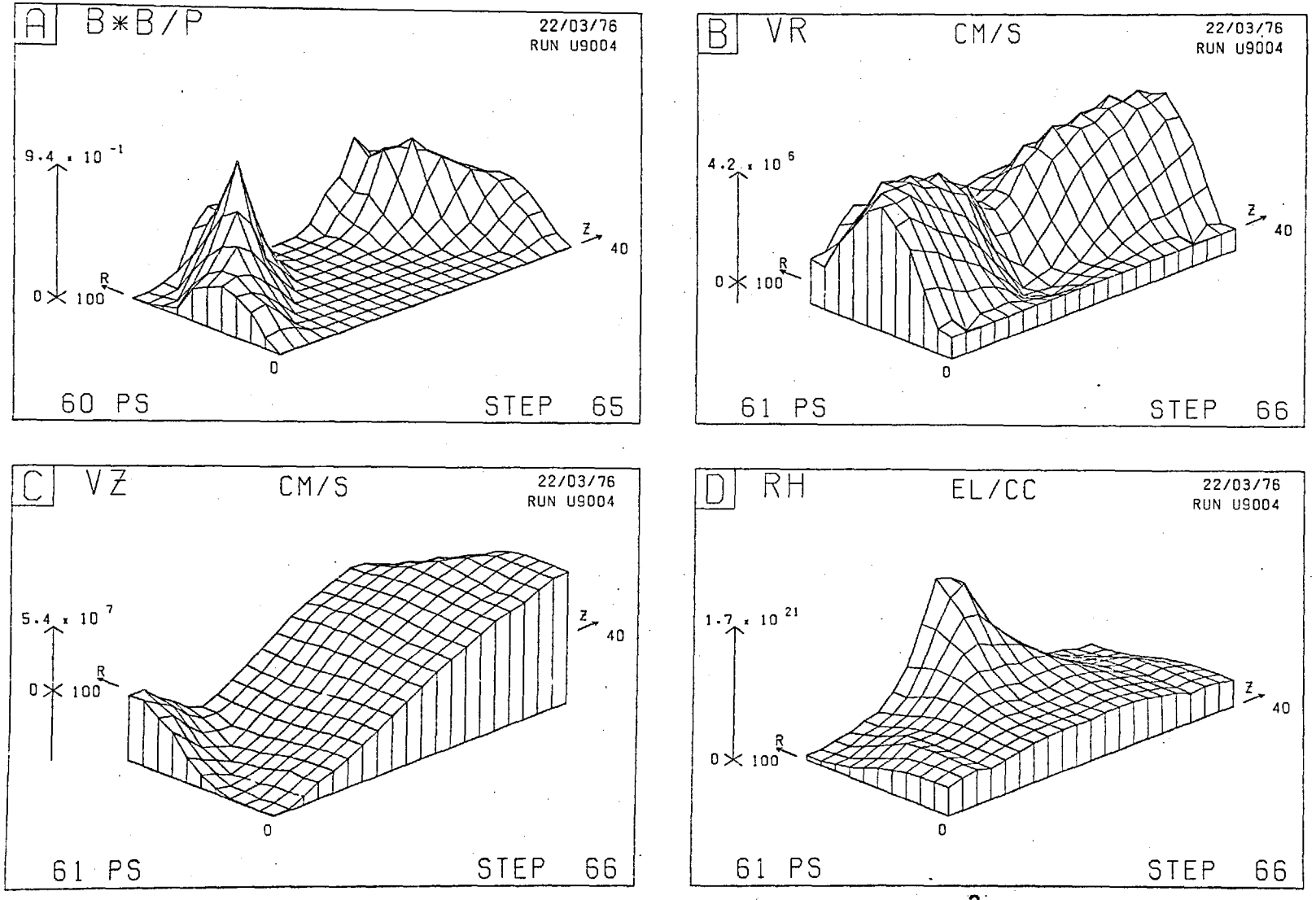

Fig.9-7 Coarse mesh version of Run 9B. At 61 psec: (a) B^2/P (b) V_r (c) V_z (d) n_e

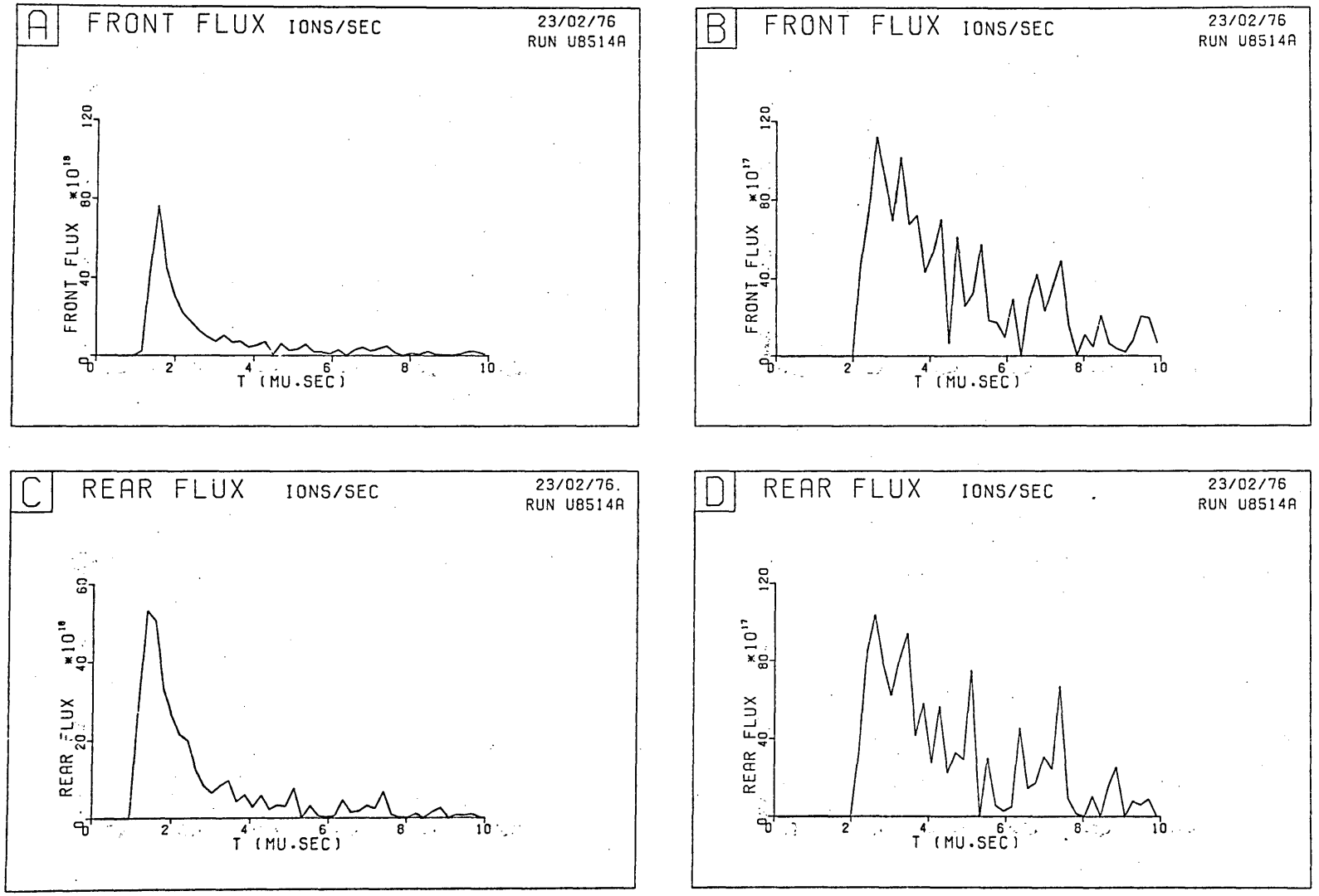

Fig.9-11 Run 9B. Ion flux at collector (calculated at 120 psec)
(a) on front of film (b) on front due to remaining ions only
(c) on rear of film (d) on rear due to remaining ions only

power. The region of large B^2/P has moved out a little further, and has caused significant perturbations to V_r if not to V_z. However the negative pinching radial velocities generated are small in comparison with the axial velocity; they have only a slight effect on the density distribution, whose most important feature is that the plasma is underdense at most radii.

Another run was performed on a coarse mesh, identical to Run 9B except that dr, dz and dt were doubled; the plot corresponding to Fig.9-6 is shown in Fig.9-7. We observe that while very little difference was made to the main features and peak numerical values, the resolution of the structure in V_r was lost.

The later development of T_e is given in Fig.9-8 (a-d) at times of 46, 56, 66 and 86 psec respectively. Fig. 9-8a is very similar to Fig.9-4a (41 psec). At 56 psec the plasma is underdense in the middle and the distribution of T_e has flattened considerably. Eventually the plasma becomes isothermal, although progress towards this state is somewhat impeded by the residual magnetic fields in the two corners distant from the axis.

The time histories of the maximum T_e, B, $\Omega\tau$ and V_z are given in Fig. 9-9. Shortly after 40 psec the maximum T_e drops due to the plasma becoming underdense, and correspondingly so does the maximum $\Omega\tau$. The peak B and V_z occur a little later, the decline being due to

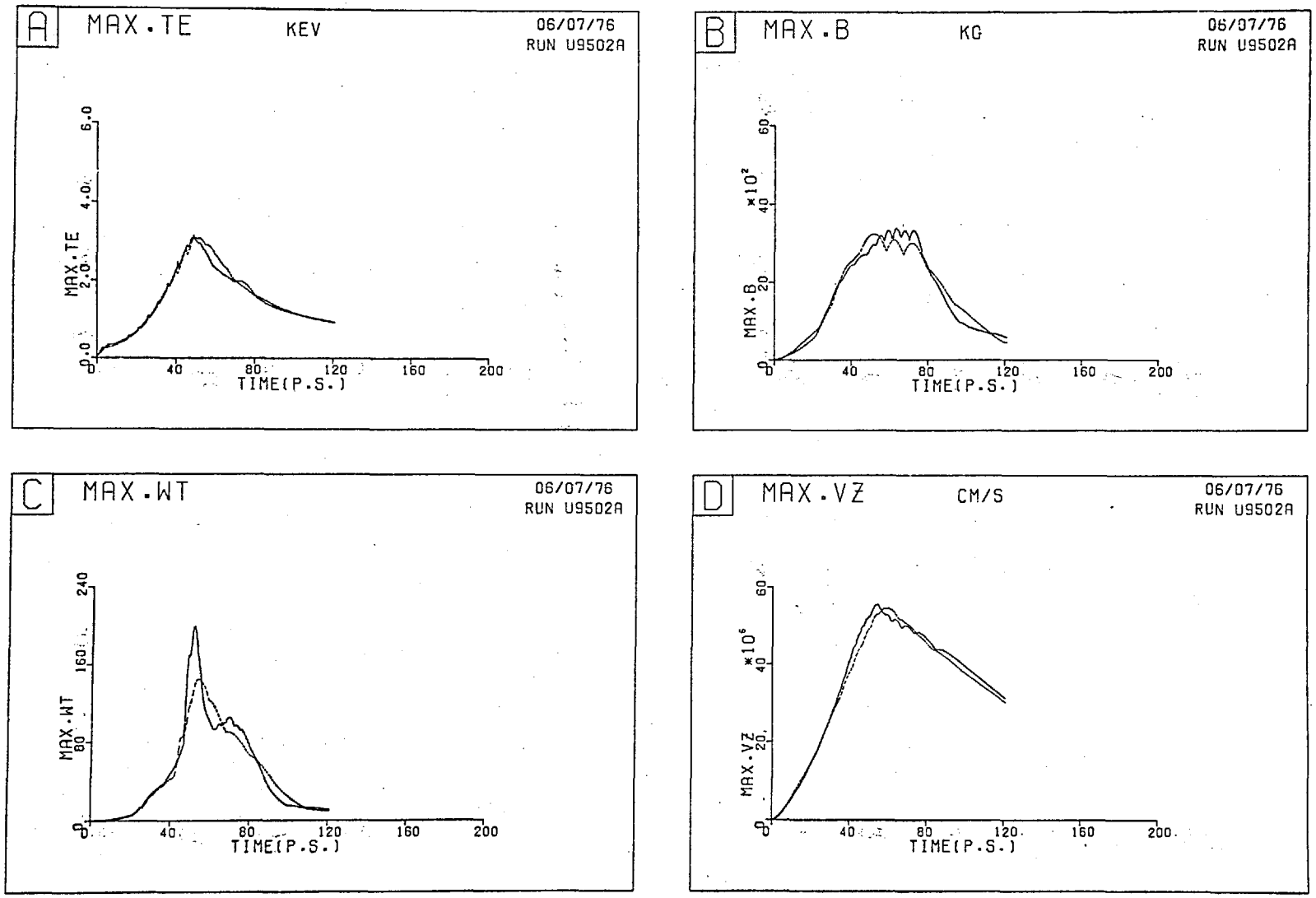

Fig.9-9 Run 9B. Time histories of the maximum on the mesh of:
(a) T_e (b) B (c) $\Omega\tau$ (d) V_z
(Dotted lines refer to coarse mesh version).

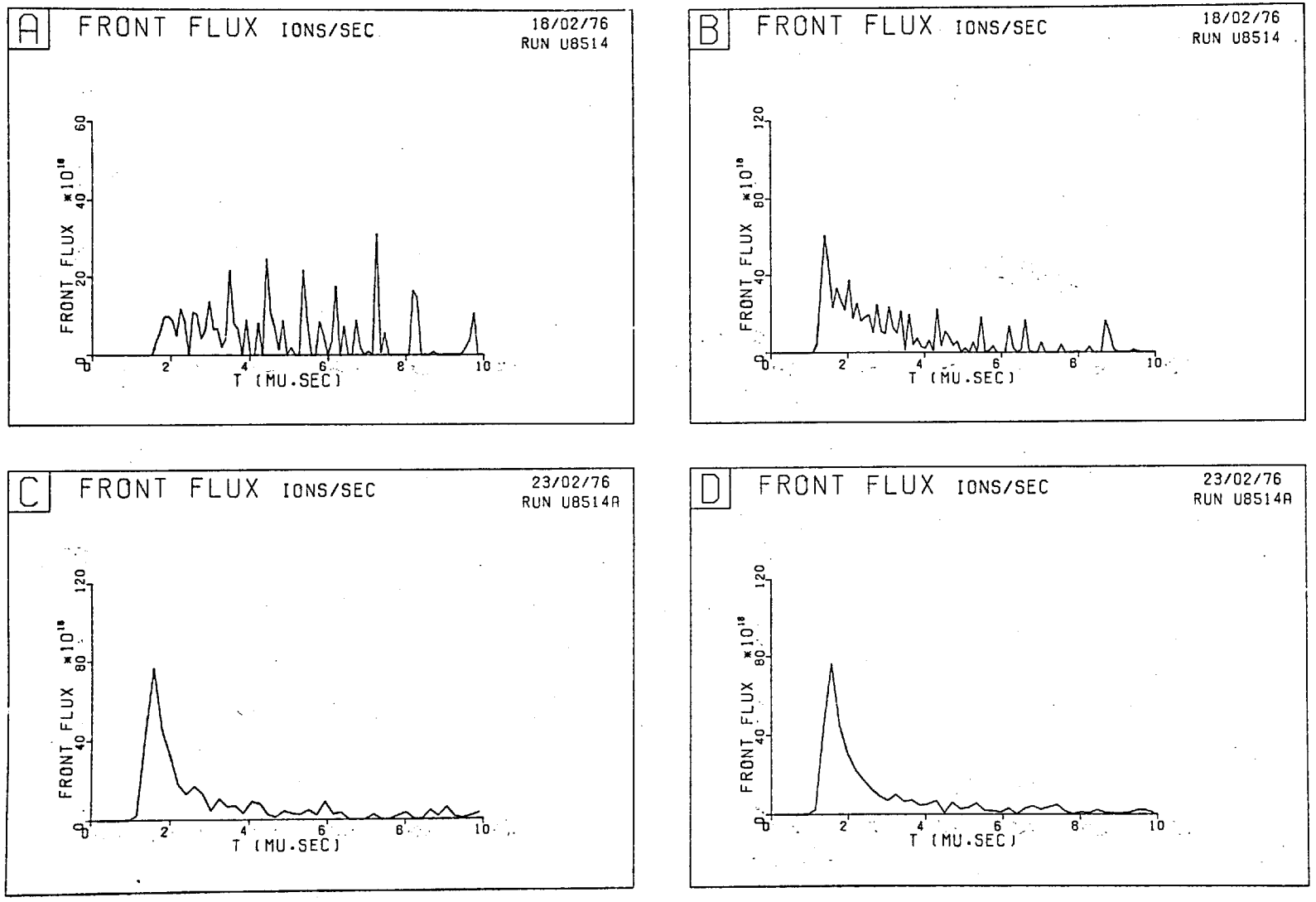

Fig.9-10 Run 9B. Ion flux at collector on front of film based on axial velocity distributions at:

(a) 40 psec (b) 65 psec (c) 100 psec (d) 120 psec

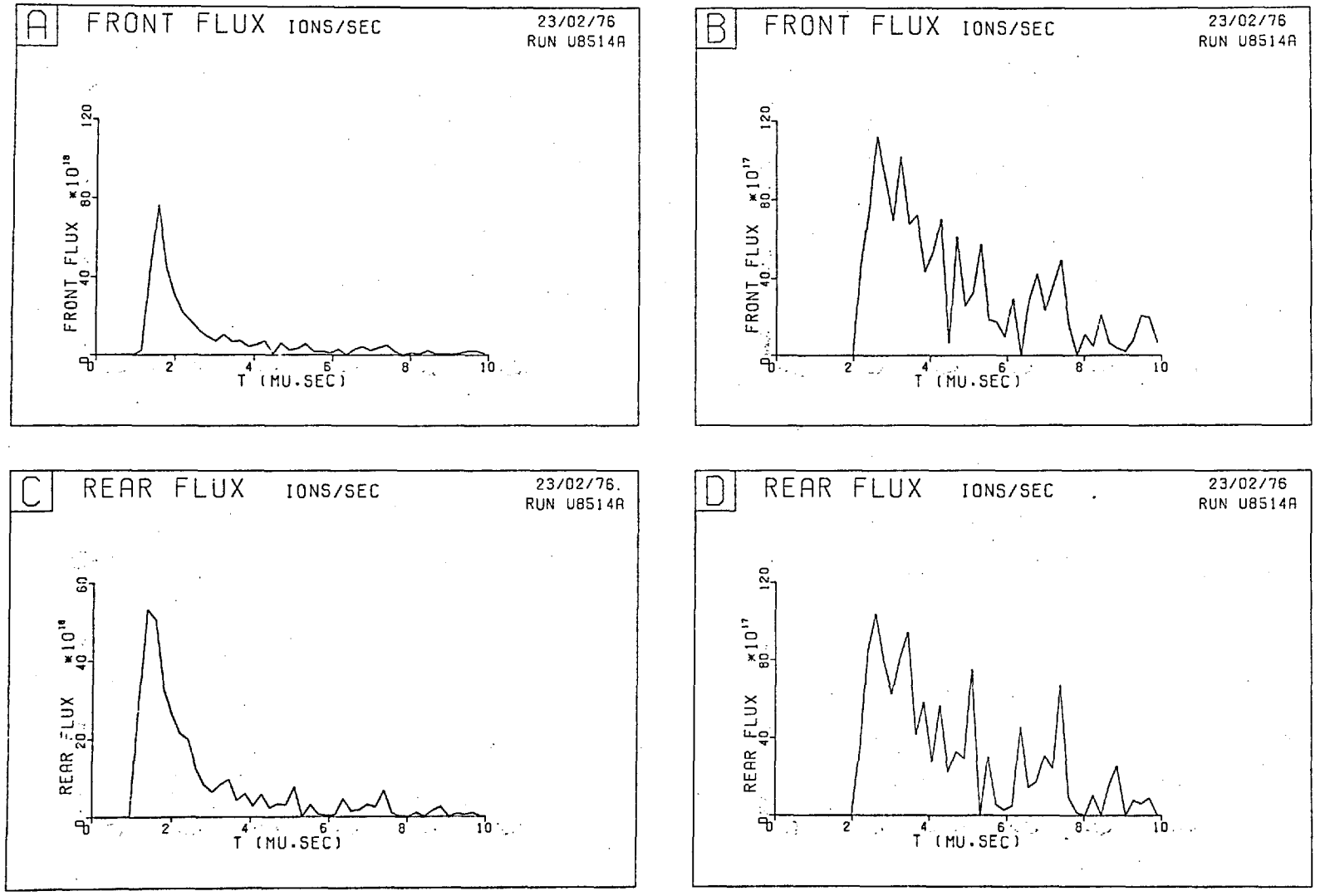

Fig.9-11 Run 9B. Ion flux at collector (calculated at 120 psec)
(a) on front of film (b) on front due to remaining ions only
(c) on rear of film (d) on rear due to remaining ions only

advection off the mesh. Eventually there remains on the mesh a cool isothermal plasma with small magnetic fields and low ablation velocities.

The dotted curves in Fig.9-9 are taken from the coarse mesh run referred to above. Apart from the poorer resolution of the peak in $\Omega\tau$ the agreement is very close, suggesting that we have achieved reasonable accuracy with our 21 x 41 mesh.

We turn to the predictions for the arrival-time graphs, front and rear, the basis of which calculations was discussed in Section 5.2.12. Fig.9-10 (a-d) gives the front arrival-time graphs based on the axial velocity distributions at 40, 65, 100 and 120 psec respectively; the vertical scale of Fig.9-10a is twice that of the rest. 48 velocity groups of an equal temporal width 0.2μsec are used to cover an arrival-time range of 0-10μsec at a collector 66 cms from the target. Convergence is clearly seen to a peak at around 1.6μsec, corresponding to a velocity of 4.1×10^7 cm/sec or an energy of 10.6 keV, and is obtained because by 120 psec only 42% of the original mass remains on the mesh, with velocities that will cause it to arrive after the peak.

This is illustrated in Fig.9-11, which shows the ion fluxes calculated including and excluding those ions which have left the mesh, the front fluxes in Fig.9-11 (a-b) and the rear fluxes in Fig.9-11 (c-d). Fig.9-11a

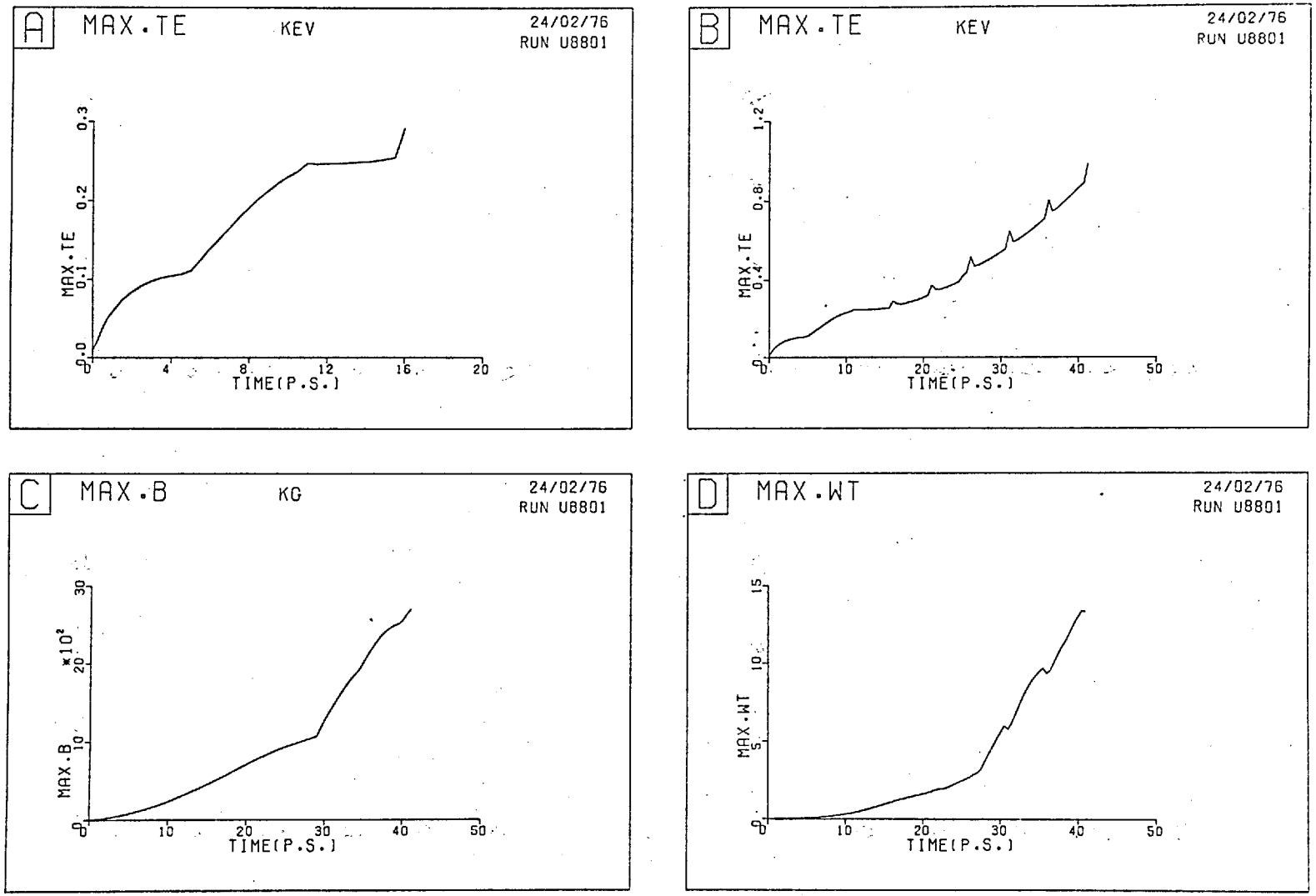

Fig.9-12 Run 9C. Early time histories of the maximum on the mesh of:
(a),(b) T_e (c) B (d) $\Omega\tau$

is the same as Fig.9-10d. The scales of Fig.9-11 are different - the peak of Fig.9-11a (7.6 x 10^{19} ions/sec) is much greater than that of Fig.9-11b (1.1 x 10^{19} ions/sec); also the fastest ions still on the mesh are not expected to arrive before 2μsec.

We obtain peaks at 1.6 and 1.4 μsec for the front and rear respectively, which compare well with the experimental figures of 1.6 and 1.9 μsec for the "fast" peaks taken from Fig.9-1b. The experimental error-bars are 0.2 μsec, the same as the width of our velocity groups: our rear peak would have been given as 1.6 μsec if the flux at 1.4 μsec were only a few per cent less as may be seen from Fig.9-11c.

9.3.2 Initial temperature behaviour of Run 9C

Qualitatively all three runs 9A-9C are very similar and the physics examined in this section applies equally to the other two runs. Under consideration here is Run 9C, the steep initial density gradient, low power run. We wish to explain the apparently complicated time dependence of electron temperature shown in Fig.9-12b, the early stages of which are enlarged in Fig.9-12a. Various discontinuities in slope occur, at times roughly corresponding to the distributions of T_e given in Fig.9-13 (a-d).

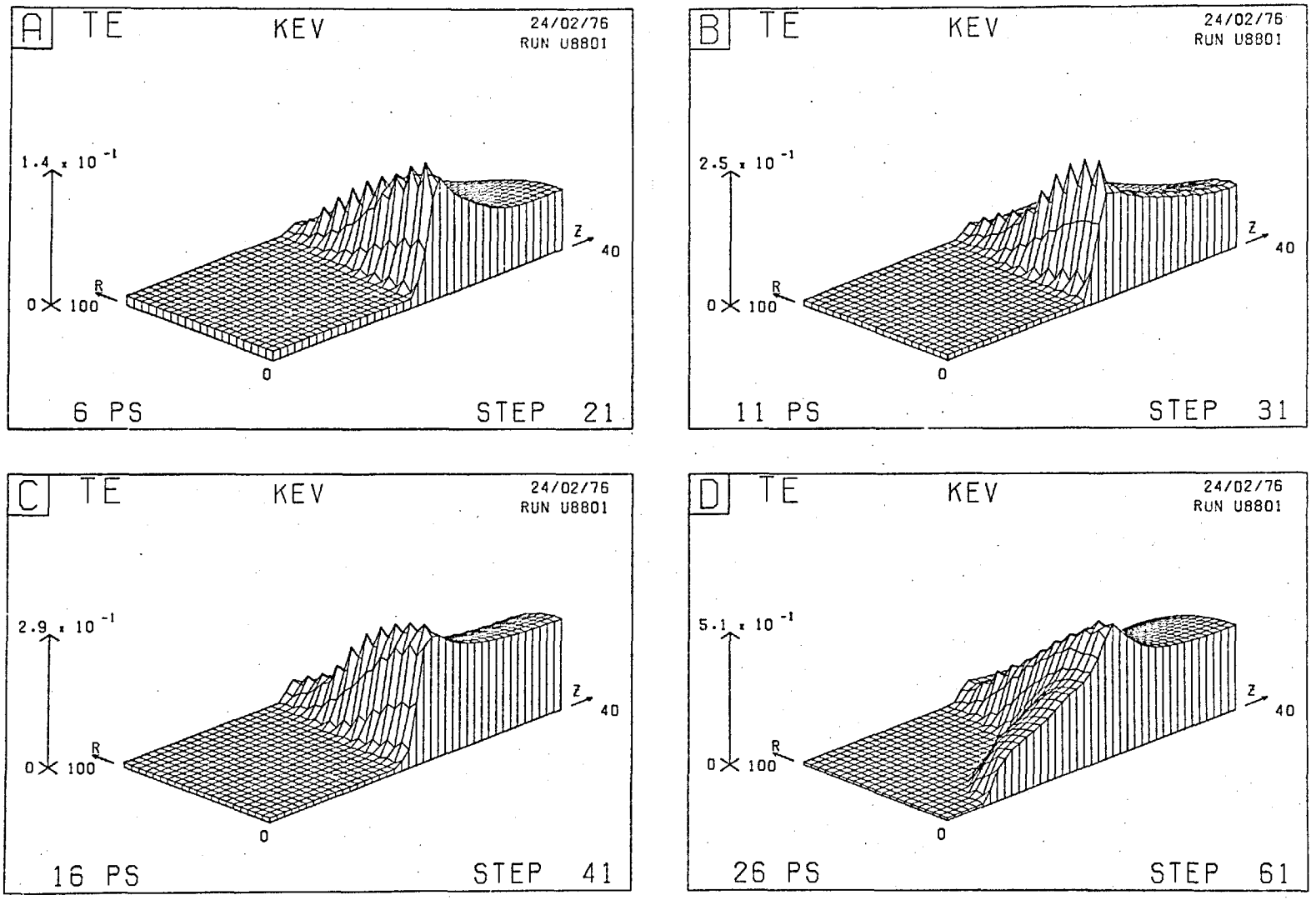

Fig.9-13 Run 9C. T_e at (a) 6 psec (b) 11 psec (c) 16 psec (d) 26 psec

Initially the peak T_e occurs at a point heated by inverse bremsstrahlung. During the first picosecond (10 steps) the I.B. absorption length K_{IB}^{-1} (see Table 8.3) is less than a mesh-length dz at this point, all the remaining laser energy is absorbed here, and the rise is linear. Between 1psec and 5 psec K_{IB}^{-1} exceeds dz, so that what energy is not absorbed by this point is dumped on the next point, the first overdense point. The temperature at the last underdense point therefore increases approximately as $t^{0.4}$ as given by (8.7). At 5 psec the peak temperature occurs at the first overdense point, whose temperature then rises linearly. The transitional distribution of T_e, at 6 psec, is given in Fig.9-13a.

The spiky appearance of Fig.9-13a arises from the decoupling of the two staggered main submeshes near the critical density. Because of the very steep density profile chosen ($\rho_1/\rho_c = 6$ here) the last underdense points on these meshes have electron number densities of 10^{20} and 4×10^{20} cm^{-3} respectively, causing different I.B. absorption profiles. Later when thermal diffusion is effective the diagonal differencing of the diffusion equation (Fig.5-2) ensures coupling. The auxiliary points of the display are calculated as averages of the four surrounding main points.

The linear rise of temperature continues until about 11 psec, when thermal diffusion into the solid is

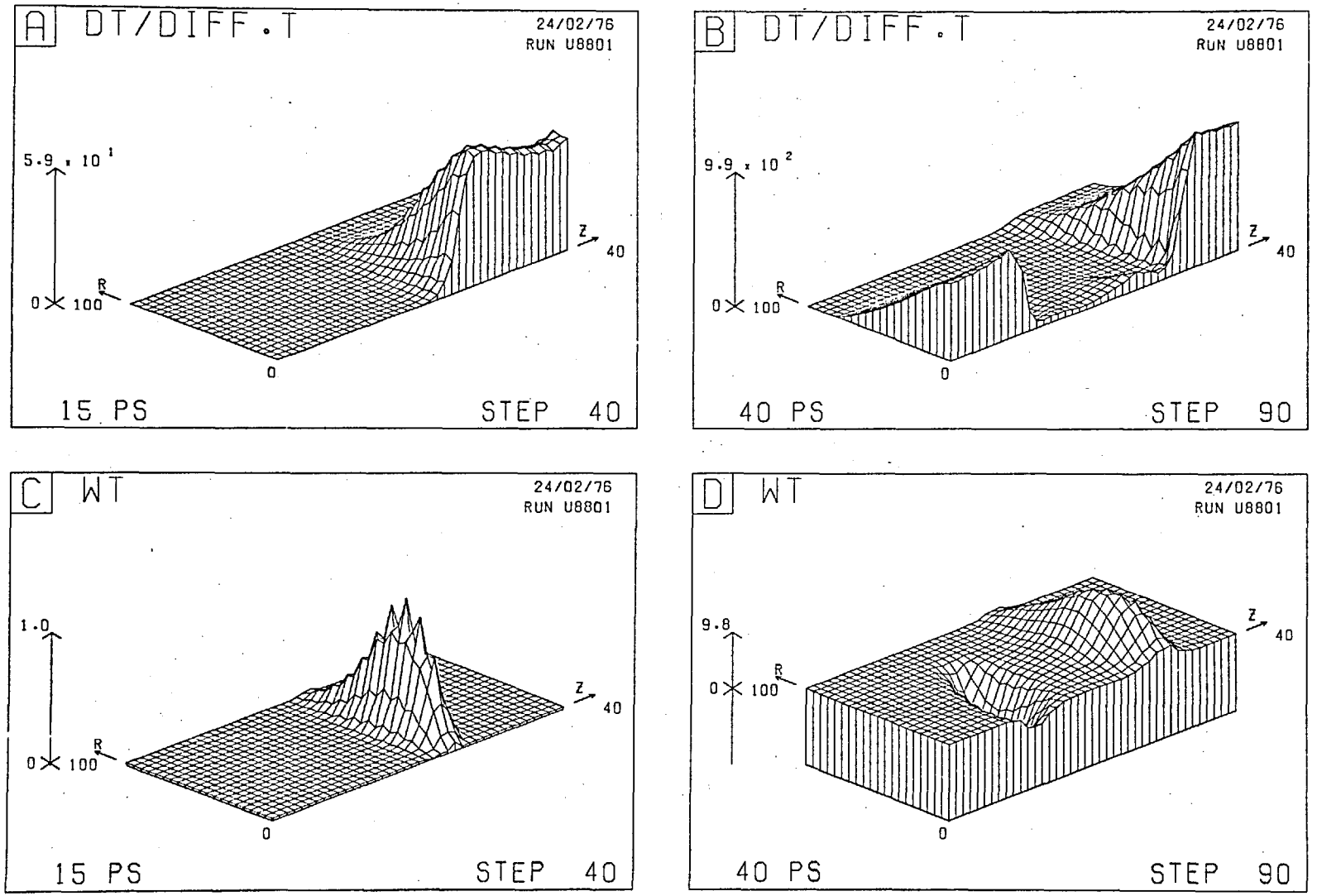

Fig.9-14 Run 9C. Ratio s of timestep to diffusion time at: (a) 15 psec (b) 40 psec
Electron Hall parameter $\Omega\tau$ at: (c) 15 psec (d) 40 psec

beginning to be important and the graph of T_e flattens out. The corresponding temperature plot (Fig.9-13b) shows that diffusion into the low density region is also operative. The temperature at 16 psec (Fig.9-13c) is not very dissimilar from that at 11 psec, but we may note that the decoupling is reduced, in confirmation of diffusion having become important. This also explains the spikes in the graph of Fig.9-12b which commence at the same time - as was pointed out at the end of Section 5.2.5, the solution of the diffusion equation on the diagonal mesh of Fig.5-2 does not provide sufficient diffusion because the mesh is not square. However it is seen that this error does not have a significant effect on the overall graph of Fig.9-12b.

The slight upwards trend of the derivative of this graph after 16 psec is expected from the increase of laser power with time. Possibly this trend would be greater were it not for the increase of thermal conductivity with temperature, despite the inhibiting effects of large $\Omega\tau$ in the low density region which commence at around 30psec according to Fig.9-12d.

The breakthrough of T_e to the rear of the film occurs between 16 psec and 26 psec from Fig.9-13 (c-d); the magnetic field in this region commences to grow at a faster rate than did the magnetic field on the front because of the increased $\partial T_e / \partial r$ as noted earlier. At

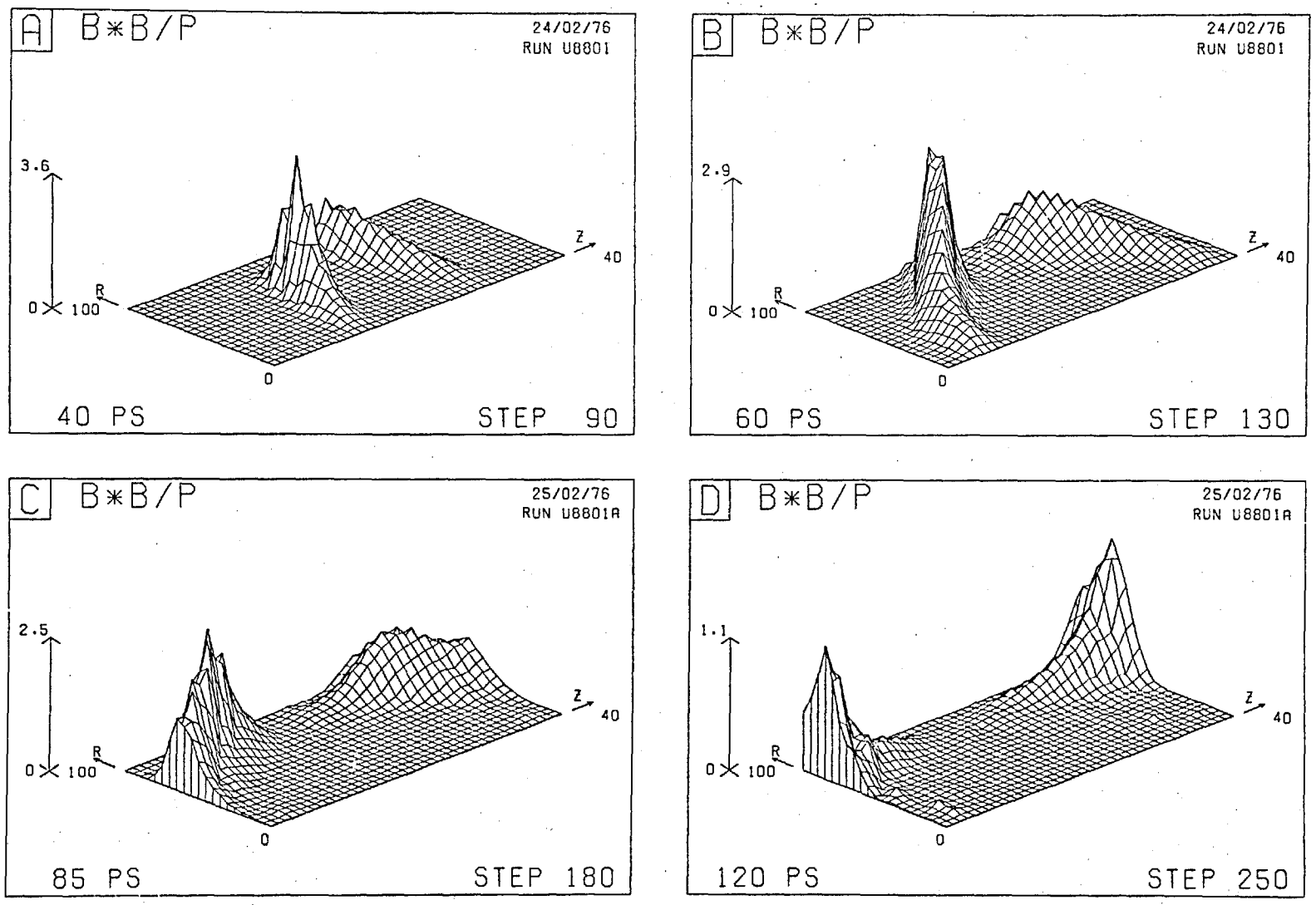

Fig.9-15 Run 9C: B^2/P at (a) 40 psec (b) 60 psec
(c) 85 psec (d) 120 psec

30 psec it is this rear field which determines the peak B, causing the discontinuity in the graph of B (Fig.9-12c).

An indication of the importance of thermal conductivity may be gained from the ratio s defined by

$$s = \frac{dt}{\tau_d} , \qquad (9.16)$$

where

$$\tau_d = \frac{3}{2} n_e k \frac{dz^2}{K_{e\perp}} \qquad (9.17)$$

and $K_{e\perp}$ is the thermal conductivity parallel to the temperature gradient and perpendicular to the magnetic field. The ratio s, and $\Omega\tau$, are shown in Fig.9-14 at 15 psec and at 40 psec. At the earlier time $s \simeq 60$ in the low density region, where gradients in T_e over n mesh-steps (2μm each) are therefore expected to disappear after about $n^2/60$ timesteps, or $n^2/120$ psec in this run. The region of large s is essentially the region of large T_e; $\Omega\tau$ is not yet great enough to be important.

At 40 psec, however, the situation is different, and s is only large in the two low density regions, with a peak of 990. It is clear that the conductivity is reduced in the regions of large $\Omega\tau$, where $(\Omega\tau)^2$ reaches almost 100. In the middle the high density causes s to be low.

The final sequence (Fig.9-15) is unrelated to the main content of this section and is included to illustrate the advection from the mesh of the regions of greatest magnetic field. On account of this, magnetic field effects

Table 9.3 Comparative parameters of Runs 9A-9C.

	Units	Run 9A "Standard"	Run 9B "Hot"	Run 9C "Steep"
Initial ρ_1/ρ_c		3	3	6
Lengthscale z_{c4}	μm	2.10	2.10	0.89
Laser energy	Joules	0.35	1.16	0.35
% absorbed (a)		67.4	40.3	67.6
Peak I_A on axis	W/cm^2	8.5×10^{13}	2.8×10^{14}	8.5×10^{13}
"Mean" intensity $\hat{I}$	W/cm^2	5.3×10^{13}	1.8×10^{14}	5.3×10^{13}
Simulation time	psec	141	121	121
No. of timesteps		251	251	251
Hot spot ?		No	No	No
Time whole plasma underdense	psec	106	76	105
Peak values (b)				
Max. T_e	keV	1.71 (63)	3.03 (49)	1.61 (56)
Max. B	MG	2.92 (85)	3.37 (64)	3.44 (78)
Max. V_z	10^7cm/s	4.22 (68)	5.57 (55)	4.85 (69)
Max. $\Omega\tau$		75 (66)	193 (51)	64 (66)
Arrival time of ion peaks (c) front : rear	μsec	2.3:2.3	1.6:1.4	1.8:2.0
Corresponding velocities	10^7cm/s	2.9:2.9	4.1:4.7	3.7:3.3
Corresponding energies	keV	5.1:5.1	10.6:13.8	8.4:6.8
Energy of first ions to arrive	keV	11.1	19.3	14.6
Mean ion energy (d)	keV	3.51	6.85	3.88
% mass remaining (a)		67	42	65

(a) At 121 psec; (b) Corresponding times (psec) in parentheses;
(c) ± 0.2 psec; (d) K.E. at 121 psec ÷ initial number of ions.

are less marked in this chapter than was the case in Chapters 7 and 8.

9.3.3 A Comparison of Runs 9A-9C

Some comparative data for these three runs is given in Tables 9.3 and 9.4. The information is similar to that of Tables 7.2 and 8.2, but here we also give the time the whole plasma becomes underdense and figures relating to the energy balance.

Table 9.4 Comparative energetics of Runs 9A-9C.

% of absorbed energy in	Run 9A "Standard"	Run 9B "Hot"	Run 9C "Steep"
Electron internal energy	25.1	12.5	21.5
Ion internal energy	0.66	0.13	0.65
Electron enthalpy lost	30.8	45.4	30.6
K.E. (on mesh + lost)	39.8	39.3	44.1

It is clear that in many respects Runs 9A and 9C, differing only in their initial ρ_1/ρ_c, are very similar. In Run 9A (9C), 67.4 (67.6)% of the incident laser energy is absorbed, the whole plasma becomes underdense at 106 (105) psec, the peak electron temperature is 1.71 (1.61) keV, and eventually at 121 psec, 67(65)% of the initial mass remains on the mesh with ion internal energies constituting 0.66 (0.65)% of the absorbed energy. In view of our approximation for the initial density distribution this is reassur-

ing. There are some differences, though, the most significant being that somewhat larger magnetic fields (2.92→3.44 MG) and ablative velocities (4.22→4.85 x 10^7 cm/sec) are generated in Run 9C.

The results appear to be more sensitive to the laser power. In the "Hot" Run 9B larger temperatures, magnetic fields and ablative velocities are found, the film becomes underdense sooner, all quantities attain their peaks earlier, and a smaller proportion of the incident laser energy is absorbed. Recalling that the figure of 1.4μsec for the rear peak is an underestimate, the arrival-times of the fastest ions and of the front and rear peaks are all decreased in much the same proportion: roughly, the corresponding energies are doubled as is the absorbed (as distinct from incident) energy.

Comparing Runs 9A and 9B we may calculate indices s_L and s_A, as in Section 8.3.4, for scaling with the laser energy and the energy absorbed; it is debatable which index is the more meaningful. The results are shown in Table 9-5. We do not offer these figures as more than ad hoc results; extrapolations to a wider range of intensities should be treated with caution.

We note that T_e scales more strongly with the absorbed energy than was the case in the thick target runs 8B and 8C described in Table 8.5. Before conversion into

Table 9.5 Sensitivity to laser power. Scaling indices s_L and s_A derived from Runs 9A and 9B for scaling with laser and absorbed energies respectively.

	s_L	s_A
Peak T_e	0.475	0.84
Peak $\Omega\tau$	0.78	1.39
Peak B	0.12	0.21
Peak V_z	0.23	0.41

kinetic energy takes place the majority of the absorbed energy resides in electron internal energy, shared among the same number of electrons in each case. The fact that the index s_A=0.84 is a little less than unity is presumed to reflect the greater thermal diffusion in the higher energy case. B appears to be less sensitive because the density gradients are smoothed out more quickly, and we are not surprised to find that V_z scales as the square root of T_e. Indeed the conversion of absorbed energy to kinetic energy is about 40% in all cases.

In contrast to the thick target runs, the peak $\Omega\tau$ scales with an index s_A almost as high as would be predicted from (8.11); this is because the approximate isothermality and the more uniform density ensure that the peaks of B and $\Omega\tau$ are approximately coincident.

One concern was the effect of a lower initial density on equipartition to the ions. The relevant stat-

Table 9.6 Equipartition to the ions. Ion energy balance between 0 and 61 psec. Energies are given in mJ.

	Run 9A "Standard"	Run 9B "Hot"	Run 9C "Steep"
Ion equipartition gain	3.09	3.13	4.26
Work done by ions	0.92	1.51	1.92
Ion internal energy gain	2.17	1.56	2.34
Ion internal energy at 61 psec	2.57	1.96	2.74

istics are given in Table 9.6, from which we see that in the "Steep" Run 9C the equipartition is just 40% greater than in the "Standard" Run 9A; this is far less than the difference in peak densities, which is not maintained for long as we have seen. Most of this extra energy goes into work, resulting in an increase of only 10% in the ion internal energy gain. In the "Hot" Run 9B the faster expansion appears to cancel the extra energy the ions would have gained from the hotter electrons, as the ion equipartition gain is not significantly different from that of the "Standard" Run 9A. More work is done on expansion because of the higher velocities, and the net result is less ion internal energy gain.

9.3.4 Overall energy balance

We give in Table 9.7 a detailed energy analysis for Run 9C, at 61 psec when the laser power is maximum, and

Table 9.7 Energy analysis of Run 9C. All energies are given as percentages of the absorbed energy (175 mJ at 61 psec, 234 mJ at 121 psec).

ENERGY IN :	at 61 psec	at 121 psec
Electron internal energy	69.1	21.5
Ion internal energy	1.6	0.7
Magnetic field energy	3.4	0.6
Kinetic energy on mesh	31.5	12.3
Kinetic energy lost	–	31.8
Electron enthalpy lost	0.03	30.6
Ion enthalpy lost	–	0.5
Poynting flux	0.2	6.2
Radiation loss	0.04	0.1
TOTAL	105.87	104.3
DERIVED FROM :		
Initial electron energy	0.9	0.7
Initial ion energy	0.2	0.2
Laser energy absorbed	100.0	100.0
Numerically created	5.2	3.1
TOTAL	106.3	104.0

at 121 psec when the pulse is over. The surface terms are significant only at 121 psec because very little mass has left at the earlier time.

The dominant process is the transfer of laser energy first into electron thermal energy and then into

kinetic energy. Ultimately nearly 100% of the absorbed laser energy is expected to undergo this conversion into ions moving radially outwards from the target, because charge neutrality ensures that the two species expand together, but we have only followed this process to a stage where about 40% has been converted. The electron enthalpy lost (H_e) is the flux of P_e+U_e , where P_e and U_e are the electron pressure and energy per unit volume:

$$U_e = \frac{3}{2} P_e = \frac{3}{2} n_e k T_e \ , \qquad (9,18)$$

The pressure contribution ($0,4H_e$) is work done on the further acceleration of the ions that have left the mesh, and the thermal contribution ($0,6H_e$) will eventually also be converted into kinetic energy.

The ion internal energy and the radiation loss are negligible. Equipartition is ineffective as has already been discussed.

Although the magnetic field energy may exceed the electron internal energy in localized low density regions, overall it accounts for only a few per cent of the absorbed energy. The Poynting flux at 121 psec is largely the convective flux S_c from the west and east boundaries (z=0 and 40μm):

$$S_c = \int_S -\frac{1}{\mu_o} (\underline{V}\times\underline{B})\times\underline{B}.\underline{dS}\ dt \ , \qquad (9,19)$$

$$= \int_S \frac{B^2}{\mu_o}\ \underline{V}.\underline{dS}\ dt \qquad (9,20)$$

in our configuration*. At 61 psec the Poynting flux is very small and arises from the thermal source term S_t on the north boundary (r=100μm):

$$S_t = \int_S \frac{-\nabla P_e}{\mu_o n_e e} \times \underline{B} \cdot \underline{dS}\, dt \,. \qquad (9.21)$$

The only other significant contribution to Table 9.7 is the subject of the next section.

9.3.5 Numerically created energy

Table 9.8 Analysis of created energy in Run 9C. For detailed explanation of the ε_i see Appendix B.

		Energy created (mJ)	
		by 61 psec	by 121 psec
(a) Neglect of $\underline{J}.\nabla P_e$:	ε_{18}	6.70	12.3
(b) Truncation in time:	ε_7	- 0.49	- 1.68
	ε_{11}	0.88	1.15
	ε_{12}	0.79	1.33
(c) Truncation in space:	ε_{14}	0.67	- 0.49
	ε_{15}	- 0.07	- 0.11
	ε_{17}	1.05	- 2.75
	ε_{19}	- 0.42	- 2.42
(d) Matrix inversion:	ε_2	- 0.001	0.0004
Total		9.11	7.33

The origin of numerical errors in the overall

*S_c is not merely the flux of magnetic energy $B^2/2\mu_o$ because of the electromagnetic work done.

energy conservation equation is discussed in Section 5.2.11 and Appendix B. The error terms contributing to the numerically created energy of Run 9C are listed in Table 9.8, where their values are given at 61 psec and 121 psec. From Table 9.7 the corresponding total numerical errors amount to 5% and 3% of the laser energy absorbed. They are made up as follows:

(a) The omission of $\underline{J}.\nabla P_e$ from the electron energy equation. This is motivated by a desire to avoid large electron velocities in low density regions, and provides the largest contribution. It causes the electrons not to lose internal energy when magnetic fields are generated, so that the electrons are a few per cent too hot.

(b) Truncation errors in time.

(c) Truncation errors in space.

(d) The errors arising from the iterative inversion of the quindiagonal matrices. They are negligible in this run.

9.4 COMPARISON WITH THE EXPERIMENT

Further runs were performed in order to provide a comparison with the experimental results (Fig.9-1b,c) over a wider range of intensity. The parameters of these runs were otherwise those of Runs 9A and 9B.

The arrival times of the front and rear peaks are

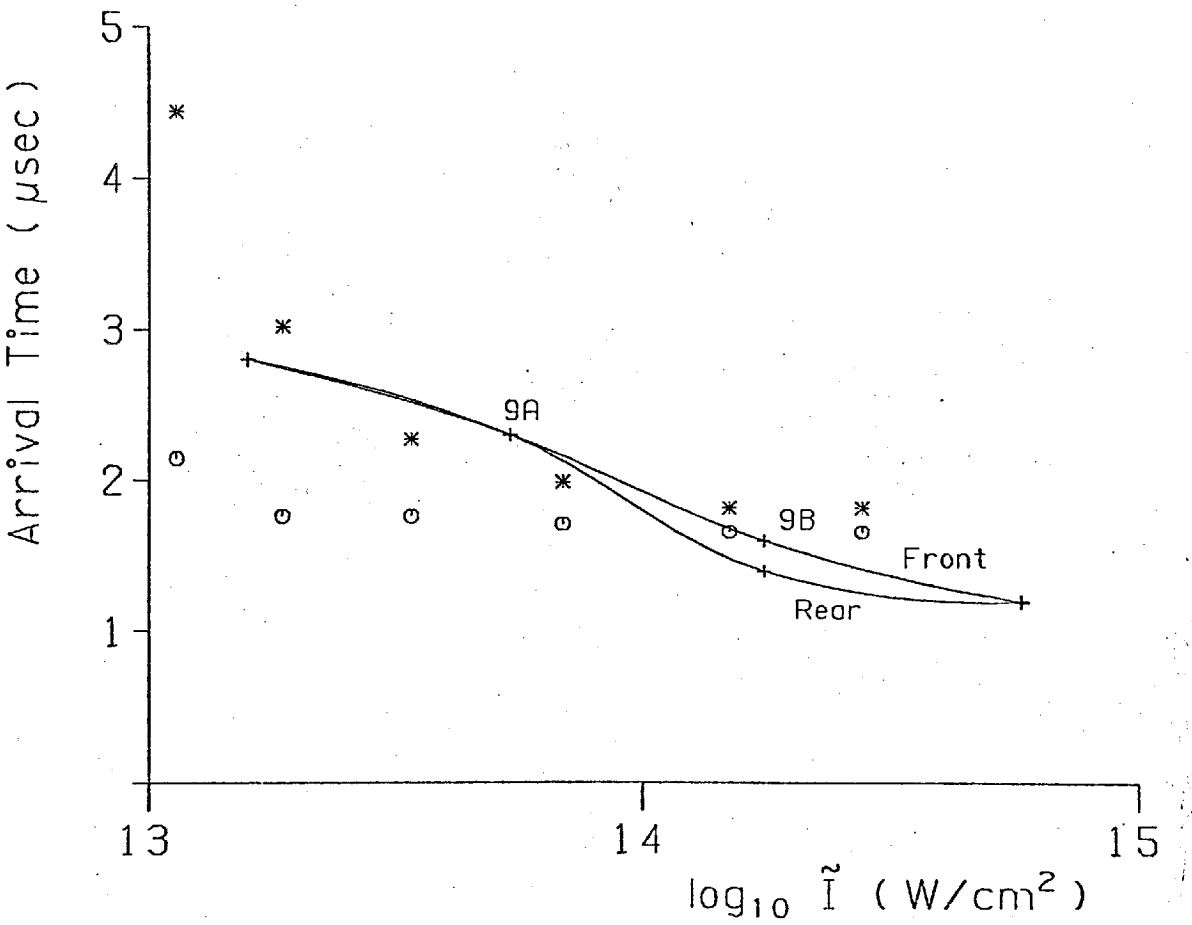

Fig.9-16 Arrival times of front and rear ion peaks as a function of laser intensity. Points (⊙) and (*) indicate experimental "fast" peak data for front and rear respectively.

plotted in Fig.9-16. The resolution is no better than 0.2 μsec, so that no significance may be attached to the difference between the graphs for the front and rear peaks. The order of magnitude comparison with the experimental "fast" peaks is good. The remarkable insensitivity to intensity observed experimentally is less obvious here, but while the incident intensity increases by a factor of over 30 the arrival time decreases by a factor of only 2.3.

This is explained according to our model by the

increased transmissivity obtained at higher intensities - over the above range of incident intensity the absorbed energy increases by a factor of only 8. Within the 0.2 μsec uncertainty, the energy of the peak is proportional to the absorbed energy.

There is however marked disagreement between our results and the experimental results for the transmissivity, as is apparent from Fig.9-1c and Fig.9-17. Our results are consistent with the expansion of the film to an underdense

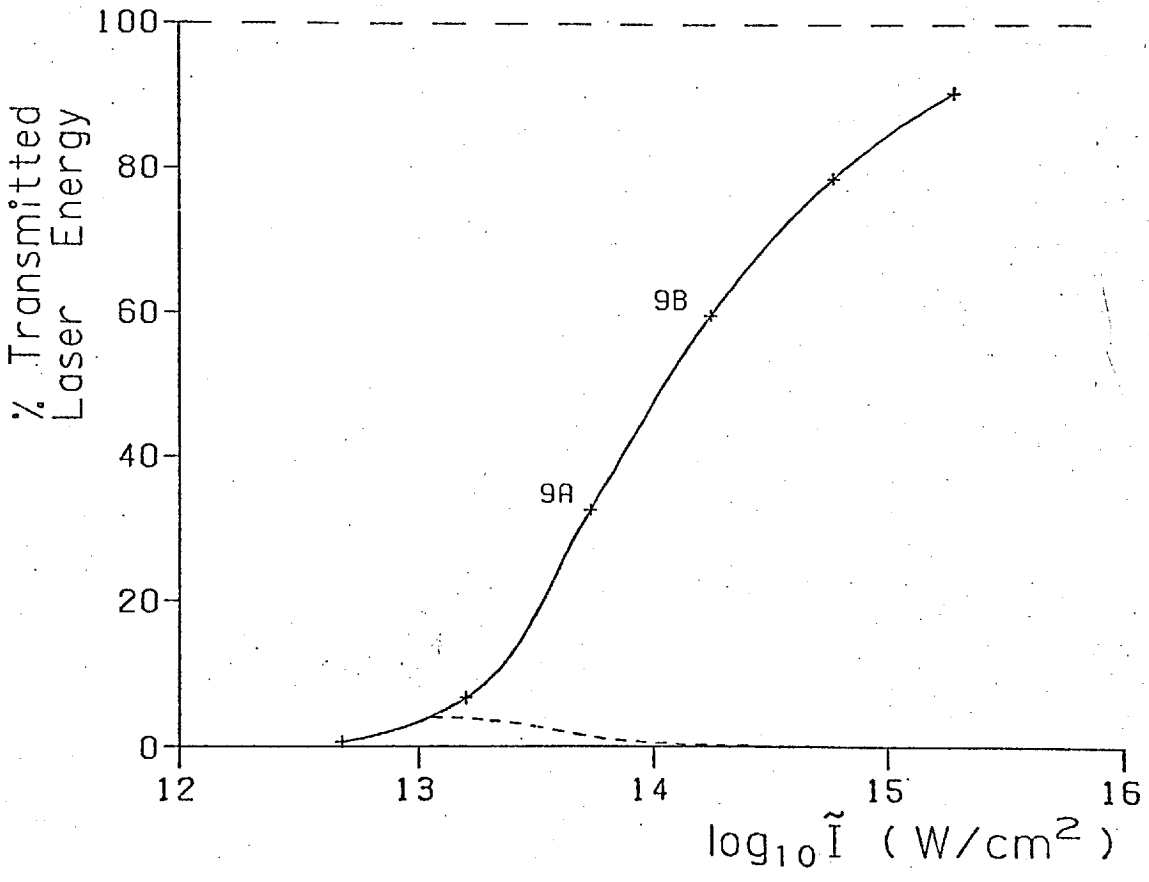

Fig.9-17 Transmissivity as a function of intensity. Dashed line indicates experimental results for the core of the transmitted light.

state occurring earlier in the higher intensity runs. The experimental results were obtained from the core of the transmitted light, and the discrepancy may be explained in terms of refraction in the slightly underdense plasma. (We would expect the curve of Fig.9-17 to be shifted a little to the right if account were to be taken of the proportion of the incident energy which is reflected or goes into ionization. 28 mJ, or 8% of the pulse of Run 9A, is sufficient to ionize fully the 1.7×10^{14} atoms present - see Table 2.2 in Section 2.2.3).

There is also disagreement in that our calculations do not yield a "thermal" peak. However, in view of the reasonable agreement obtained for the "fast" peak, we suggest that ion acceleration proceeds according to the fluid equation

$$\rho \frac{d\underline{V}}{dt} = - \nabla P_e \qquad (9.22)$$

and that the other peak arises from physics omitted from our model; for example:

(a) the other charge species present;

(b) plasma at greater radii than allowed for in our simulation;

(c) conversion of the electron enthalpy flux blown-off (Section 9.3.4);

(d) recombination effects during the flight to the collector.

We believe the first explanation to be the most plausible because on that basis the separation of the "thermal" peaks at high intensities might be understood.

Unlike our assumed initial profile, the actual density distribution is unlikely to be symmetric. A much larger atmosphere is expected on the front as a result of the initial interaction; the fast ion mean free path being a key parameter (see Section 4.1.3), we expect fewer collisions and therefore greater species separation on the rear. The situation is complicated however by the observation that each peak contains a mixture of charge species.

In conclusion, the application of LASERB to thin film interactions for which it was not originally designed has nevertheless yielded interesting results. The work could be extended by

(a) including a larger simulation radius and calculating the angular dependence of the plasma expansion;

(b) including refraction and calculating the angular distribution of transmitted light; or

(c) allocating more mesh points to the density gradient so as to examine the penetration of the thermal front through the film.

However, if it is desired to obtain a better quantitative comparison with experiment, a physically more realistic code should be developed including separate

equations for all ion species and a full treatment of ionization effects. Also, a one-dimensional Lagrangian code might yield interesting information about the early stages of ionization and the electron temperature breakthrough to the rear.

CHAPTER 10

CONCLUSION

As we remarked in the introduction there are intrinsic limitations to all three approaches to laser-plasma interactions, experimental, theoretical and computational. We have not attempted to conceal the inadequacies of our computational model, because only when we know its weaknesses can we assess its strength.

The principal limitations of our model are the lack of atomic physics and the treatment of electrons as near-Maxwellian. In the first case our code is patently not suited to experiments where the target material is chosen specifically because of its ionization and radiation characteristics. In the second case, the electron distribution function actually present remains an uncertainty. The large collision times and long mean free paths of hot electrons imply the presence of a "suprathermal" electron component. The question of how to incorporate these electrons into a fluid code and the extent to which they modify the transport coefficients deserves more attention, even in the spherically symmetric case where magnetic fields are absent. In the presence of large magnetic fields, possibly strongly spatially varying and possibly turbulent, the situation is far more complicated.

While heated electron distribution functions are being produced by resonant absorption, magnetic fields are

generated near the critical density. These fields may in turn affect the absorption process; further work is appropriate here.

Further runs with the present code are worth performing, either with different parameters (such as a varying laser wavelength) or with minor modifications to the equations (such as the inclusion of refraction). The bremsstrahlung spectra could also be calculated and the numerical techniques could be improved.

The direction in which code development should move is not obvious. A key question is whether one should aim at a universal code capable of solving all laser fusion problems or be content with smaller codes tailor-made for specific problems. There is much to be said for the latter approach. For example, if we are interested in the differential accelerations of a mixture of different charge species, time dependent ionization equations should be included together with separate hydrodynamic equations for the various species. If we are interested in a closer comparison with thin film experiments a non-uniform two-dimensional mesh could also be introduced, with occasional rezoning; however, such a code would be unsuitable for the similar problem of a spherical shell. Another important consideration is whether the code is required for the interpretation of experimental results or for theoretical studies.

It would be unwise to predict the future develop-

ment of laser fusion research as more powerful lasers and improved diagnostics become available. About one thing however we may be certain - there will be no shortage of work for the computational physicist.

APPENDIX A

CHARACTERISTIC PARAMETERS

This Appendix summarizes in four tables various timescales, velocities, lengthscales and other plasma parameters, of general interest to plasma physics and of particular interest to laser-plasma interactions. The defining algebraic formulae in the middle columns are in S.I. units, whereas all results and quantities appearing in the numerical formulae of the right-hand columns are expressed in "conventional" units, defined as follows:

Time	sec
Length	cm
Number density	cm^{-3}
Velocity	cm/sec
Temperature	eV
Energy	eV
Energy flux	W/cm^2
Magnetic field	Gauss
Electric field	Volts/cm
Pressure	atm.

The formulae apply to a plasma with one ion species of charge number z ($n_e = zn_i$) and atomic number A. Our definitions of τ_{ei} and τ_{ii} are taken from Shkarofsky et al.[62], but including the z - dependence (they consider only z=1). The numerical factors occurring in the algebraic formulae for the thermal, resistive and viscous

diffusion times and the classical heat flux are from the same source, and because they are calculated on the basis of a z=1 plasma must be considered approximate for z>1.

Λ and b_o, related via the definition

$$\Lambda = \lambda_D / b_o , \tag{A.1}$$

are taken from Rosenbluth et al.[64] and used by Shkarofsky et al.[62] As only the logarithm of Λ appears in the transport formulae we make the approximation throughout that $\ln\Lambda = 10$.

The factor $f(\omega_p/\omega_{las})$ appearing in the formulae for the inverse bremsstrahlung length and the Faraday rotation angle is defined by

$$f(x) = \sqrt{1 - x^2} . \tag{A.2}$$

The formula for the inverse bremsstrahlung length K_{IB}^{-1} is taken from Johnston and Dawson[63], who use the same value of τ_{ei} as Shkarofsky et al.[62] The equipartition time is taken from Spitzer.[8]

The notation is generally self-explanatory or defined within the tables. L is a spatial length of variation, and E_o is the peak electric field of a laser beam of intensity I Watts/cm^2. The one quantity not defined in the tables (for reasons of length) is the bremsstrahlung radiation rate P_{rad}:

$$P_{rad} = \left(\frac{2\pi kT_e}{3m_e}\right)^{\frac{1}{2}} \frac{32\pi}{3hm_e c^3} \left(\frac{e^2}{4\pi\varepsilon_o}\right)^3 Z^2 n_e n_i . \tag{A.3}$$

It should be noted that the transport formulae have their accuracy limited for the following reasons (at least):

(a) The variation of the Coulomb logarithm is ignored.

(b) The dependence on z for z>1 is approximate. For example, according to Spitzer[8], the electron thermal conductivity should be multiplied by a factor $\delta_T(z)/0.225$ where $\delta_T(z)$ varies from 0.225 at z=1 to 1.0 at $z=\infty$.

(c) The plasma equations are considered valid to only about 10% anyway. See for example Robinson and Bernstein[65]: this is due to the neglect of terms of order unity in comparison with terms of order $\ln\Lambda$.

(d) It may be that they are being applied in regimes where the conditions for the validity of their derivations are not well satisfied.

The physics implied by these formulae is discussed in the main text (Chapter 4).

Table A.1 Characteristic timescales

Electron plasma frequency	$\omega_p = \sqrt{\frac{n_e e^2}{\varepsilon_o m_e}}$	5.641×10^{4}	$n_e^{\frac{1}{2}}$
Ion plasma frequency	$\omega_{pi} = \sqrt{\frac{n_i e^2}{\varepsilon_o m_i}}$	1.321×10^{3}	$\frac{n_i^{\frac{1}{2}}}{A^{\frac{1}{2}}}$
Electron - ion collision time	$\tau_{ei} = 6\pi\sqrt{2\pi}\frac{\varepsilon_o^2 m_e^{\frac{1}{2}}(kT_e)^{3/2}}{e^4 \ln\Lambda\, z^2 n_i}$	3.441×10^{4}	$\frac{T_e^{3/2}}{z^2 n_i}$
Ion - ion collision time	$\tau_{ii} = 6\pi\sqrt{2\pi}\frac{\varepsilon_o^2 m_i^{\frac{1}{2}}(kT_i)^{3/2}}{e^4 \ln\Lambda\, z^4 n_i}$	1.469×10^{6}	$\frac{A^{\frac{1}{2}}T_i^{3/2}}{z^4 n_i}$
Electron - ion equipartition time	$\tau_{eq} = \frac{m_i}{2m_e}\tau_{ei}$	3.136×10^{7}	$\frac{A\, T_e^{3/2}}{z^2 n_i}$
Electron Larmor frequency	$\Omega_e = \frac{eB}{m_e}$	1.759×10^{7}	B
Ion Larmor frequency	$\Omega_i = \frac{eB}{m_i}$	9.649×10^{3}	$\frac{B}{A}$
Thermal diffusion time	$\tau_k = \frac{3}{2}\frac{0.654}{5}\frac{m_e L^2}{kT_e\tau_{ei}}$	3.242×10^{-21}	$\frac{z^2 n_i L^2}{T_e^{5/2}}$
Resistive diffusion time	$\tau_\eta = \frac{1}{0.5064}\frac{\omega_p^2\tau_{ei}L^2}{c^2}$	2.406×10^{-7}	$\frac{T_e^{3/2}L^2}{z}$
Viscous diffusion time	$\tau_v = 0.7326\frac{m_i L^2}{kT_i\tau_{ii}}$	5.169×10^{-19}	$\frac{A^{\frac{1}{2}}z^4 n_i L^2}{T_i^{5/2}}$
Ion thermal diffusion time	$\tau_{ki} = \frac{3}{2}\frac{0.896}{5}\frac{m_i L^2}{kT_i\tau_{ii}}$	1.896×10^{-19}	$\frac{A^{\frac{1}{2}}z^4 n_i L^2}{T_i^{5/2}}$

(continued)

Table A.1 Continued

Bremsstrahlung radiation time	$\tau_{rad} = \frac{3}{2} n_e k T_e / P_{rad}$	1.565×10^{13}	$\frac{T_e^{\frac{1}{2}}}{z^2 n_i}$
Light travel time	$\tau_l = \frac{L}{c}$	3.336×10^{-11}	L
Laser frequency	$\omega_{las} = \frac{2\pi c}{\lambda_{las}}$	1.884×10^{11}	$\frac{1}{\lambda_{las}}$

Table A.2 Characteristic velocities

Electron thermal velocity	$V_{th,e} = \sqrt{\frac{3kT_e}{m_e}}$	7.264×10^{7}	$\sqrt{T_e}$
Ion thermal velocity	$V_{th,i} = \sqrt{\frac{3kT_i}{m_i}}$	1.701×10^{6}	$\sqrt{\frac{T_i}{A}}$
Sound speed	$C_s = \sqrt{\frac{zkT_e}{m_i}}$	9.823×10^{5}	$\sqrt{\frac{zT_e}{A}}$
Alfvén speed	$V_A = \sqrt{\frac{B^2}{\mu_o n_i m_i}}$	2.189×10^{11}	$\frac{B}{\sqrt{A n_i}}$
Current velocity	$V_{rel} = \frac{\nabla \times B}{n_e e \mu_o}$	4.967×10^{18}	$\frac{B}{n_e L}$
Quiver velocity	$V_o = \frac{eE_o}{m_e \omega_{las}}$	2.563×10^{5}	$\lambda_{las}\sqrt{I}$

Table A.3 Characteristic lengthscales

Impact parameter	$b_o = \frac{ze^2}{12\pi\varepsilon_o kT_e}$	4.800×10^{-8}	$\frac{z}{T_e}$
Inter-particle distance	$n_e^{-1/3}$		$n_e^{-1/3}$
Debye length	$\lambda_D = \sqrt{\frac{\varepsilon_o kT_e}{n_e e^2}}$	7.434×10^{2}	$\sqrt{\frac{T_e}{n_e}}$
Electron mean free path	$\lambda_e = \tau_{ei} V_{th,e}$	2.499×10^{12}	$\frac{T_e^2}{z^2 n_i}$
Ion mean free path	$\lambda_i = \tau_{ii} V_{th,i}$	2.499×10^{12}	$\frac{T_i^2}{z^4 n_i}$
Electron Larmor radius	$a_e = \Omega_e^{-1} V_{th,e}$	4.130	$\frac{\sqrt{T_e}}{B}$
Ion Larmor radius	$a_i = \Omega_i^{-1} V_{th,i}$	1.763×10^{2}	$\frac{\sqrt{AT_i}}{B}$
Collisionless skin depth	$\delta_s = \omega_p^{-1} c$	5.314×10^{5}	$\frac{1}{\sqrt{n_e}}$
Inverse bremsstrahlung length	$K_{IB}^{-1} = \frac{c\tau_{ei}\sqrt{1-\omega_p^2/\omega_{las}^2}}{\omega_p^2/\omega_{las}^2}$	1.150×10^{28}	$\frac{T_e^{3/2} f(\omega_p/\omega_{las})}{z^2 n_i n_e \lambda_{las}^2}$
Electron excursion in em wave	$x_o = V_o/\omega_{las}$	1.361×10^{-6}	$\lambda_{las}^2\sqrt{I}$

Table A.4 Miscellaneous parameters

Electron Hall parameter	$(\Omega\tau)_e =$	$\Omega_e \tau_{ei}$	6.052×10^{11}	$\frac{BT_e^{3/2}}{z^2 n_i}$
Ion Hall parameter	$(\Omega\tau)_i =$	$\Omega_i \tau_{ii}$	1.417×10^{10}	$\frac{BT_i^{3/2}}{A^{\frac{1}{2}} z^4 n_i}$
Lambda	$\Lambda =$	λ_D / b_o	1.549×10^{10}	$\frac{T_e^{3/2}}{z n_e^{\frac{1}{2}}}$
No. of electrons in Debye sphere	$n_D =$	$\frac{4}{3}\pi\lambda_D^3 n_e$	1.721×10^{9}	$\frac{T_e^{3/2}}{n_e^{\frac{1}{2}}}$
Peak em electric field	$E_o =$	$\sqrt{2c\mu_o I}$	2.745×10^{1}	$\sqrt{I}$
Peak radiation÷thermal pressure	$\eta^2 =$	$\frac{\varepsilon_o E_o^2}{n_e k T_e}$	4.164×10^{8}	$\frac{I}{n_e T_e}$
Plasma beta	$\beta =$	$\frac{3\mu_o k(n_e T_e + n_i T_i)}{B^2}$	6.040×10^{-11}	$\frac{n_e T_e + n_i T_i}{B^2}$
Classical heat flux	$Q_c =$	$\frac{5 n_e k^2 T_e \tau_{ei}}{0.654\, m_e} \frac{T_e}{L}$	7.413×10^{1}	$\frac{T_e^{7/2}}{zL}$
Free-streaming heat flux	$Q_{fs} =$	$\frac{3}{2} n_e k T_e\, V_{th,e}$	1.746×10^{-11}	$n_e T_e^{3/2}$
Free-streaming transition temperature	T_{fs} at which $Q_c = Q_{fs}$		4.853×10^{-7}	$\sqrt{zLn_e}$
Faraday rotation	$\Delta\phi =$	$\frac{\Omega_e L}{2c} \frac{\omega_p^2/\omega_{las}^2}{f(\omega_p/\omega_{las})}$	2.631×10^{-17}	$\frac{BLn_e\lambda_{las}^2}{f(\omega_p/\omega_{las})}$

(continued)

Table A.4 Continued

Quiver energy	ε_q	$= \frac{1}{2}m_e V_o^2$	1.867×10^{-5}	$\lambda_{las}^2 I$
Peak em magnetic field	B_o	$= E_o/c$	9.156×10^{-2}	$\sqrt{I}$
Fermi energy	ε_F	$= \frac{h^2}{8m_e}\left[\frac{3n_e}{\pi}\right]^{2/3}$	3.646×10^{-15}	$n_e^{2/3}$
Fermi pressure	P_F	$= \frac{2}{5}n_e\varepsilon_F$	2.306×10^{-33}	$n_e^{5/3}$
Electron pressure	P_e	$= n_e k T_e$	1.581×10^{-18}	$n_e T_e$
Photon energy	ε_ν	$= hc/\lambda_{las}$	1.240×10^{-4}	$\frac{1}{\lambda_{las}}$
Critical number density	n_c	$= \frac{\varepsilon_o m_e}{e^2}\left[\frac{2\pi c}{\lambda_{las}}\right]^2$	1.115×10^{13}	$\frac{1}{\lambda_{las}^2}$
Energy of ablating ion	ε_v	$= \frac{1}{2}m_H A V^2$	5.182×10^{-13}	AV^2
Swelling factor	S	$= 3.6\left[\frac{\omega_{las} L}{c}\right]^{1/3}$	6.643	$\left[\frac{L}{\lambda_{las}}\right]^{1/3}$

APPENDIX B

THE OVERALL CONSERVATION OF ENERGY

We derive in detail the equation in difference form for the overall conservation of energy, illustrating the origin of the various possible numerical errors. For simplicity the equations are all given in difference form, although it is the volume and surface summations which are calculated in the code.

We find it convenient to make the following notational definitions:

$$\theta_e \equiv kzT_e/m_i = P_e/\rho$$

$$g \equiv 1/(\gamma-1)$$

$$\nu_{eq} \equiv 1/\tau_{eq}$$

and

$$\Delta_t f \equiv \frac{f(t+\Delta t)-f(t)}{\Delta t}$$

Δ_t^* and Δ_t^D are similarly defined, and refer to the two stages (5,19) and (5.20) of the electron temperature calculation.

We now list 19 equations for error quantities ε_i which would all be zero in the continuous case:

The integration of T_e to T_e^*:

$$\varepsilon_1 = g\rho\Delta_t^*(\theta_e)-g\theta_e\nabla.(\rho\underline{V})^{(1)}+P_e\nabla.\underline{V}_e+g\nabla.(P_e\underline{V}_e)-n_e k\nu_{eq}(T_i-T_e)^{(1)}$$

$$+P_{rad}-P_{las}-\eta\underline{J}^2. \qquad (B.1)$$

The diffusion equation for T_e:

$$\varepsilon_2 = g\rho\Delta_t^D(\theta_e)+\nabla\cdot\underline{Q}_e. \qquad (B.2)$$

$\underline{B}/\mu_o$ times the magnetic field equation:

$$\varepsilon_3 = (B/\mu_o)\Delta_t(B)+(\underline{B}/\mu_o)\cdot\nabla x(-\underline{V}_e x\underline{B})+(\underline{B}/\mu_o)\cdot\nabla x(-\nabla P_e/n_e e) + (\underline{B}/\mu_o)\cdot\nabla x(\eta\underline{J}). \qquad (B.3)$$

The ion energy equation:

$$\varepsilon_4 = \Delta_t(gP_i)+P_i\nabla\cdot\underline{V}+g\nabla\cdot(P_i\underline{V})+\nabla\cdot\underline{Q}_i+ n_e k\nu_{eq}(T_i-T_e)^{(2)}. \qquad (B.4)$$

The equipartition term might have been different:

$$\varepsilon_5 = n_e k\nu_{eq}(T_i-T_e)^{(1)}- n_e k\nu_{eq}(T_i-T_e)^{(2)}. \qquad (B.5)$$

$g\theta_e'$ times the density equation:†

$$\varepsilon_6 = g\theta_e'\Delta_t(\rho)+g\theta_e'\nabla\cdot(\rho\underline{V})^{(2)}; \qquad (B.6)$$

The above used a different $\nabla\cdot(\rho\underline{V})$ and θ_e:

$$\varepsilon_7 = g\theta_e\nabla\cdot(\rho\underline{V})^{(1)} - g\theta_e'\nabla\cdot(\rho\underline{V})^{(2)}. \qquad (B.7)$$

$\underline{V}$, the momentum equation:

$$\varepsilon_8 = \underline{V}\cdot\Delta_t(\rho\underline{V})+\underline{V}\cdot\nabla\cdot(\rho\underline{V}\underline{V})+\underline{V}\cdot\nabla P_e+\underline{V}\cdot\nabla P_i-\underline{V}\cdot\underline{J}x\underline{B}. \qquad (B.8)$$

$(V^2/2)$ times the density equation:

$$\varepsilon_9 = -(V^2/2)\Delta_t(\rho) - (V^2/2)\nabla\cdot(\rho\underline{V}), \qquad (B.9)$$

The total change of electron energy:

---

† θ_e' is θ_e evaluated at the new time,

$$\varepsilon_{10} = \Delta_t(g\rho\theta_e) - g\rho\Delta_t^*(\theta_e) - g\rho\Delta_t^D(\theta_e) - g\theta_e'\Delta_t(\rho). \quad (B.10)$$

The total change of magnetic energy:

$$\varepsilon_{11} = \Delta_t(B^2/2\mu_o) - (B/\mu_o)\Delta_t(B). \quad (B.11)$$

The total change of kinetic energy:

$$\varepsilon_{12} = \Delta_t(\rho V^2/2) - \underline{V}.\Delta_t(\rho\underline{V}) + (V^2/2)\Delta_t(\rho). \quad (B.12)$$

Absorption of the laser energy:

$$\varepsilon_{13} = P_{las} + \nabla.\underline{I}. \quad (B.13)$$

Electron work:

$$\varepsilon_{14} = -P_e\nabla.\underline{V}_e + \nabla.(P_e\underline{V}_e) - \underline{V}.\nabla P_e + (\underline{J}/n_e e).\nabla P_e \quad (B.14)$$

Ion work:

$$\varepsilon_{15} = -P_i\nabla.\underline{V} + \nabla.(P_i\underline{V}) - \underline{V}.\nabla P_i \quad (B.15)$$

Poynting theorem for each electric field component:

$$\varepsilon_{16} = \eta\underline{J}^2 - (\underline{B}/\mu_o).\nabla x(\eta\underline{J}) + \nabla.(\eta\underline{J}x\underline{B}/\mu_o). \quad (B.16)$$

$$\varepsilon_{17} = \underline{V}.\underline{J}x\underline{B} - (\underline{B}/\mu_o).\nabla x(-\underline{V}_e x\underline{B}) + \nabla.(-(\underline{V}_e x\underline{B})x\underline{B}/\mu_o) \quad (B.17)$$

$$\varepsilon_{18} = -(\underline{J}/n_e e).\nabla P_e - (\underline{B}/\mu_o).\nabla x(-\nabla P_e/n_e e) + \nabla.(-(\nabla P_e/n_e e)x\underline{B}/\mu_o) \quad (B.18)$$

Velocity vector identity:

$$\varepsilon_{19} = -\underline{V}.\nabla.(\rho\underline{V}\underline{V}) + (V^2/2)\nabla.(\rho\underline{V}) + \nabla.(\rho V^2\underline{V}/2). \quad (B.19)$$

On the summation of (B.1)-(B.19) most of the terms cancel in pairs and we obtain the overall conservation equation

$$\varepsilon_{tot} = \Delta_t(g\rho\theta_e + gP_i + B^2/2\mu_o + \rho V^2/2)$$

$$+\nabla.\left[(g+1)(P_e\underline{V}_e + P_i\underline{V}) + \rho V^2\underline{V}/2 + \underline{Q}_e + \underline{Q}_i + \underline{E}x\underline{B}/\mu_o + \underline{I}\right]$$

$$+ P_{rad} \qquad \text{(B.20)}$$

where

$$\underline{E} = \eta\underline{J} - \underline{V}_e x\underline{B} - \nabla P_e/n_e e \qquad \text{(B.21)}$$

and

$$\varepsilon_{tot} = \sum_{1}^{19} \varepsilon_i \qquad \text{(B.22)}$$

Note that g is generally 3/2.

The derivation of (B.20) in the continuous case requires most but not all of the 19 steps: the extra steps arise here because

(i) the total electron energy changes three times, during the electron hydrodynamic and diffusion stages and consequent upon density changes in the Lax-Wendroff stage;

(ii) a check is made to ensure that the equipartition energy transfers exactly balance;

(iii) the $\nabla.(\rho\underline{V})$ used in the equation (3.48) for T_e is evaluated at a different time from the $\nabla.(\rho\underline{V})$ used in (3.1) to integrate ρ.

The equation (B.13) relating the total energy absorbed to the laser flux across the east boundary provides a check in runs where all the incident energy is absorbed. In the thin film runs, where some energy is transmitted, (B.13) is used to give the overall transmissivity and $-P_{las}$ rather than $\nabla.\underline{I}$ is needed to balance (B.20).

The ε_i may be divided into five classes:

(a) ε_1, ε_{3-6}, ε_{8-10} : these should be zero to within the machine rounding error, and serve as a check on the code;

(b) ε_7, ε_{11-12}: truncation errors in time;

(c) ε_{14-19}: truncation errors in space;

(d) ε_2 : error incurred during the iterative inversion of quindiagonal matrices;

(e) ε_{13} : the difference between absorbed and incident energy discussed above.

REFERENCES

Work associated with six major U.S. Laboratories is identified as follows:

KMSF	KMS Fusion, Inc.
LASL	Los Alamos Scientific Laboratory
LLE	Laboratory for Laser Energetics
LLL	Lawrence Livermore Laboratory
NRL	Naval Research Laboratory
SL	Sandia Laboratories.

1 J.NUCKOLLS, L.WOOD, A.THIESSEN & G.ZIMMERMAN. Laser compression of matter to super-high densities: thermonuclear (CTR) applications. Nature 239 139 (1972) (LLL)

2 J.S.CLARKE, H.N.FISHER & R.J.MASON. Laser-driven implosion of spherical DT targets to thermonuclear burn conditions. Phys.Rev.Lett. 30 89 (1973) (LASL)

3 G.S.FRALEY, E.J.LINNEBUR, R.J.MASON & R.L.MORSE. Thermonuclear burn characteristics of compressed deuterium microspheres. Phys.Fluids 17 474 (1974) (LASL)

4 G.YONAS, J.W.POUKEY, K.R.PRESTWICH, J.R.FREEMAN, A.J.TOEPFER & M.J.CLAUSER. Electron beam focusing and application to pulsed fusion. Nucl.Fusion 14 731 (1974) (SL)

5 F.F.CHEN. In 'Laser interaction and related plasma phenomena', ed. H.J.Schwarz & H.Hora. Plenum, New York Vol.3A, p.291 (1973)

6 J.J.THOMSON, C.E.MAX & K.ESTABROOK. Magnetic fields due to resonance absorption of laser light. Phys. Rev.Lett. 35 663 (1975) (LLL)

7 R.L.MORSE & C.W.NIELSON. Occurrence of high energy electrons and surface expansion in laser-heated target plasmas. Phys.Fluids 16 909 (1973) (LASL)

8 L.SPITZER. 'Physics of fully ionized gases'. Wiley, New York (1967)

9 Lawrence Livermore Laboratory Semiannual report, July-December 1972.

10 G.S.FRALEY & R.J.MASON. Preheat effects on micro-balloon laser-fusion implosions. Phys.Rev.Lett. 35 520 (1975) (LASL)

11 K.A.BRUECKNER, S.JORNA & R.JANDA. Hydrodynamic stability of a laser-driven plasma. Phys. Fluids 17 1554 (1974) (KMSF)

12 J.N.SHIAU, E.B.GOLDMAN & C.I.WENG. Linear stability analysis of laser-driven spherical implosions. Phys.Rev.Lett. 32 352 (1974) (LLE)

13 B.H.RIPIN, P.G.BURGHALTER, F.C.YOUNG, J.M.McMAHON, D.G.COLOMBANT, S.E.BODNER, R.R.WHITLOCK, D.J. NAGEL, D.J.JOHNSON, N.K.WINSOR, C.M.DOZIER, R.D. BLEACH, J.A.STAMPER & E.A.McLEAN. X-ray emission spectra from high-power-laser-produced plasmas. Phys.Rev.Lett. 34 1313 (1975) (NRL)

14 K.A.BRUECKNER. Energy deposition in laser-heated plasmas. Phys.Rev.Lett. 36 677 (1976)

15 V.V.KOROBKIN & R.V.SEROV. Investigation of the magnetic field of a spark produced by focusing laser radiation. JETP Lett. 4 70 (1966)

16 J.A.STAMPER, K.PAPADOPOULOS, R.N.SUDAN, S.O.DEAN, E.A.McLEAN & J.M.DAWSON. Spontaneous magnetic fields in laser-produced plasmas. Phys.Rev. Lett. 26 1012 (1971) (NRL)

17 J.A.STAMPER. Laser-induced sources for magnetic fields. NRL Report 7411, 1972.

18 R.S.BIRD, L.L.McKEE, F.SCHWIRZKE & A.W.COOPER. Pressure dependence of self-generated magnetic fields in laser-produced plasmas. Phys Rev.A 7 1328 (1973)

19 L.L.McKEE, R.S.BIRD & F.SCHWIRZKE. Self-generated magnetic fields associated with a laser-produced plasma. Phys.Rev.A 9 1305 (1974)

20 R.S.CASE & F.SCHWIRZKE. Background gas pressure dependence and spatial variation of spontaneously generated magnetic fields in laser-produced plasmas. J.Appl.Phys. 46 1493 (1975)

21 F.SCHWIRZKE. Measurements of spontaneous magnetic fields in laser-produced plasmas. In 'Laser interaction and related plasma phenomena', ed H.J.Schwarz & H.Hora. Plenum, New York Vol.3, p213 (1973)

22 J.N.OLSEN & C.W.MENDEL. Near-field measurements of subnanosecond-created laser plasmas. J.Appl. Phys. 46 4407 (1975) (SL)

23 R.SEROV & M.C.RICHARDSON. Measurement of intense magnetic fields associated with laser-produced plasmas. Appl.Phys.Lett. 28 115 (1976)

24 M.G.DROUET & R.BOLTON. Distribution of self-generated current in laser-produced plasmas. Phys.Rev.Lett. 36 591 (1976)

25 M.G.DROUET & H.PÉPIN. Parametric study of the current induced in a CO_2 laser plasma. Appl. Phys.Lett. 28 426 (1976)

26 J.A.STAMPER & B.H.RIPIN. Faraday-rotation measurements of megagauss magnetic fields in laser-produced plasmas. Phys.Rev.Lett. 34 138 (1975) (NRL)

27 L.M.GOLDMAN, J.SOURES & M.J.LUBIN. Saturation of stimulated backscattered radiation in laser plasmas. Phys.Rev.Lett. 31 1184 (1973) (LLE)

28 B.H.RIPIN, J.M.McMAHON, E.A.McLEAN, W.M.MANHEIMER & J.A.STAMPER. Time-resolved laser-plasma backscatter studies. Phys.Rev.Lett. 33 634 (1974) (NRL)

29 C.YAMANAKA, T.YAMANAKA, T.SASAKI, J.MIZUI & H.B.KANG. Brillouin backscattering and parametric double resonance in laser-produced plasma. Phys.Rev.Lett. 32 1038 (1974)

30 P.LEE, D.V.GIOVANIELLI, R.P.GODWIN & G.H.McCALL. Harmonic generation and frequency mixing in laser-produced plasmas. Appl.Phys.Lett. 24 406 (1974) (LASL)

31 K.B.MITCHELL, T.F.STRATTON & P.B.WEISS. Backscatter measurements from laser-produced plasmas at 10.6μm. Appl.Phys.Lett. 27 11 (1975) (LASL)

32 R.MASSEY, K.BERGGREN & Z.A.PIETRZYK. Observation of Brillouin backscattering from an underdense plasma. Phys.Rev.Lett. 36 963 (1976)

33 J.J.TURECHEK & F.F.CHEN. Detection of Brillouin backscattering in underdense plasmas. Phys. Rev.Lett. 36 720 (1976)

34 A.A.OFFENBERGER, M.R.CERVENAN, A.M.YAM & A.W. PASTERNAK. Stimulated Brillouin scattering of CO_2 laser radiation from underdense plasma. J.Appl.Phys. 47 1451 (1976)

35 J.W.SHEARER, S.W.MEAD, J.PETRUZZI, F.RAINER, J.E. SWAIN & C.E.VIOLET. Experimental indications of plasma instabilities induced by laser heating. Phys.Rev.A 6 764 (1972) (LLL)

36 J.L.BOBIN, M.DECROISETTE, B.MEYER & Y.VITEL. Harmonic generation and parametric excitation of waves in a laser-created plasma. Phys.Rev. Lett. 30 594 (1973)

37 K.EIDMANN & R.SIGEL. Second-harmonic generation in an inhomogeneous laser-produced plasma. Phys. Rev.Lett. 34 799 (1975)

38 H.A.BALDIS, H.PÉPIN, T.W.JOHNSTON & K.J.PARBHAKAR. Second-harmonic light from the interaction of a nanosecond CO_2 laser pulse with the plasma produced from polyethylene sheet. Phys.Rev.Lett. 35 37 (1975)

39 H.A.BALDIS, H.PÉPIN & B.GREK. Third harmonic generation from laser-produced plasma. Appl.Phys. Lett. 27 291 (1975)

40 J.P.FRIEDBERG, R.W.MITCHELL, R.L.MORSE & L.I. RUDSINSKI. Resonant absorption of laser light by plasma targets. Phys.Rev.Lett. 28 795 (1972) (LASL)

41 K.G.ESTABROOK, E.J.VALEO & W.L.KRUER. Two-dimensional relativistic simulations of resonance absorption. Phys.Fluids 18 1151 (1975) (LLL)

42 S.JACKEL, J.ALBRITTON & E.GOLDMAN. Critical-density scale-length measurements in laser-produced plasmas. Phys.Rev.Lett. 35 514 (1975) (LLE)

43 T.P.DONALDSON & I.J.SPALDING. Density cavitons and x-ray filamentation in CO_2 - laser-produced plasmas. Phys.Rev.Lett. 36 467 (1976)

44 R.A.HAAS, M.J.BOYLE, K.R.MANES & J.E.SWAIN. Evidence of localized heating in CO_2 - laser-produced plasmas. J.Appl.Phys. 47 1318 (1976) (LLL)

45 A.W.EHLER. High-energy ions from a CO_2 laser-produced plasma. J.Appl.Phys. 46 2464 (1975) (LASL)

46 C.W.MENDEL & J.N.OLSEN. Charge-separation electric fields in laser plasmas. Phys.Rev. Lett. 34 859 (1975) (SL)

47 Handbook of Chemistry and Physics, ed. R.C.Weast. Chemical Rubber Co., 56th edition (1975)

48 D.COLOMBANT & G.F.TONON. X-ray emission in laser-produced plasmas. J.Appl.Phys. 44 3524 (1973)

49 R.C.MALONE, R.L.McCRORY & R.L.MORSE. Indications of strongly flux-limited electron thermal conduction in laser-target experiments. Phys. Rev.Lett. 34 721 (1975) (LASL)

50 D.J.NAGEL, P.G.BURKHALTER, C.M.DOZIER, J.F. HOLZRICHTER, B.M.KLEIN, J.M.McMAHON, J.A. STAMPER & R.R.WHITLOCK. X-ray emission from laser-produced plasmas. Phys.Rev.Lett. 33 743 (1974) (NRL)

51 P.J.MALLOZZI, H.M.EPSTEIN, R.G.JUNG, D.C.APPLEBAUM, B.P.FAIRAND, W.A.GALLAGHER, R.L.UECKER & M.C. MUCKERHEIDE. Laser-generated plasmas as a source of x rays for medical applications. J.Appl. Phys. 45 1891 (1974)

52 F.C.YOUNG. Measurements of energetic x rays from laser-produced plasmas. Phys.Rev.Lett. 33 747 (1974) (NRL)

53 U.FELDMAN, G.A.DOSHEK, D.K.PRINZ & D.J.NAGEL. Space-resolved spectra of laser-produced plasmas in the XUV. J.Appl.Phys. 47 1341 (1976) (NRL)

54 D.A.TIDMAN & J.A.STAMPER. Role of magnetic fields in suprathermal particle generation by laser-produced plasmas. Appl.Phys.Lett. 22 498 (1973)

55 J.F.KEPHART, R.P.GODWIN & G.H.McCALL. Bremsstrahlung emission from laser-produced plasmas. Appl.Phys. Lett. 25 108 (1974) (LASL)

56 J.G.DOWNWARD. Intensity variation of reflected energy from spherical glass shell laser fusion targets. J.Appl.Phys. 46 2147 (1975) (KMSF)

57 P.M.CAMPBELL, G.CHARATIS & G.R.MONTRY. Laser-driven compression of glass microspheres. Phys.Rev.Lett. 34 74 (1975) (KMSF)

58 R.R.GOFORTH. Detection of core-gas ions from ^{3}He-filled pellets in laser-driven fusion studies. Appl.Phys.Lett. 27 598 (1975) (KMSF)

59 T.A.LEONARD & F.J.MAYER. Helium blast-wave measurements of laser-heated microshell targets. J.Appl. Phys. 46 3562 (1975) (KMSF)

60 V.W.SLIVINSKY, H.G.AHLSTROM, K.G.TIRSELL, J.LARSEN, S.GLAROS, G.ZIMMERMAN & H.SHAY. Measurement of the ion temperature in laser-driven fusion. Phys.Rev.Lett. 35 1083 (1975) (LLL)

61 I.P.SHKAROFSKY, T.W.JOHNSTON & M.P.BACHYNSKI. 'The particle kinetics of plasmas'. Addison-Wesley (1966)

62 I.P.SHKAROFSKY, I.B.BERNSTEIN & B.B.ROBINSON. Condensed presentation of transport coefficients in a fully ionized plasma. Phys.Fluids 6 40 (1963)

63 T.W.JOHNSTON & J.M.DAWSON. Correct values for high-frequency power absorption by inverse bremsstrahlung in plasmas. Phys.Fluids 16 722 (1973)

64 M.N.ROSENBLUTH, W.M.MacDONALD & D.L.JUDD. Fokker-Planck equation for an inverse-square force. Phys.Rev. 107 1 (1957)

65 B.B.ROBINSON & I.B.BERNSTEIN. A variational description of transport phenomena in a plasma. Ann. Phys.(N.Y.) 18 110 (1962)

66 V.L.GINZBURG. 'The propagation of electromagnetic waves in plasmas'. Pergamon, New York. (1964)

67 P.KAW & J.DAWSON. Relativistic nonlinear propagation of laser beams in cold overdense plasmas. Phys.Fluids 13 472 (1970)

68 J.A.STAMPER. Laser radiation forces in laser-produced plasmas. Phys.Fluids 18 735 (1974) (NRL)

69 J.A.STAMPER & D.A.TIDMAN. Magnetic field generation due to radiation pressure in a laser-produced plasma. Phys.Fluids 16 2024 (1973) (NRL)

70 S.I.BRAGINSKII. Transport properties in a plasma. In 'Reviews of plasma physics', ed. M.A. Leontovich. Consultants Bureau, New York. Vol.1, p205 (1965)

71 W.L.KRUER & K.G.ESTABROOK. Laser light absorption with self-generated magnetic fields. Bull.Am.Phys.Soc. 21 597 (1976) (LLL)

72 D.A.TIDMAN & R.A.SHANNY. Field-generating thermal instability in laser-heated plasmas. Phys. Fluids 17 1207 (1974)

73 D.A.TIDMAN. Seeded megagauss turbulence in dense fusion-target plasmas. Phys.Rev.Lett. 35 1228 (1975)

74 D.A.TIDMAN. Mega-Gauss turbulence due to seeded composition fluctuations in dense plasma, and electron beam scattering. Phys.Fluids 19 321 (1976)

75 D.A.TIDMAN. Thermally generated magnetic fields in laser-driven compressions and explosions. Phys. Fluids 18 1454 (1975)

76 D.E.T.F.ASHBY & J.P.CHRISTIANSEN. The effect of the electron free-streaming limit on laser compression. 6th European Conference on Controlled Fusion and Plasma Physics,Moscow, p431. (1973)

77 R.J.BICKERTON. Thermal conduction limitations in laser fusion. Nucl.Fusion 13 457 (1973)

78 D.E.POTTER. Numerical studies of the plasma focus. Phys.Fluids 14 1911 (1971)

79 R.S.VARGA. 'Matrix iterative analysis'. Prentice Hall, New Jersey (1962)

80 J.P.BORIS & D.L.BOOK. Flux-corrected transport. I. SHASTA, a fluid transport algorithm that works. J.Comput.Phys. 11 38 (1973) (NRL)

81 R.D.RICHTMEYER & K.W.MORTON. 'Difference methods for initial value problems'. Interscience, New York 2nd Edition (1967)

82 D.L.BOOK, J.P.BORIS & K.HAIN. Flux-corrected transport II: Generalizations of the method. J.Comput.Phys. 18 248 (1975) (NRL)

83 J.S.PEARLMAN & J.P.ANTHES. Reduction of classical thermal conductivity under the influence of high-power lasers. Appl.Phys.Lett. 27 581 (1975) (SL)

84 M.M.WIDNER. Self-generated magnetic fields in laser plasmas. Phys.Fluids 16 1778 (1973) (SL)

85 M.M.WIDNER & T.P.WRIGHT. Alternating-direction implicit code for simulating laser plasmas. Sandia Laboratory report SC-DR-72 0733 (1973)

86 I.R.LINDEMUTH. The alternating-direction implicit numerical solution of time-dependent, two-dimensional, two-fluid magnetohydrodynamic equations. Ph.D. Thesis, Lawrence Livermore Laboratory report UCRL-51103 (1971)

87 J.B.CHASE, J.M.LeBLANC & J.R.WILSON. Role of spontaneous magnetic fields in a laser-created deuterium plasma. Phys.Fluids 16 1142 (1973) (LLL)

88 N.K.WINSOR & D.A.TIDMAN. Laser target model. Phys. Rev.Lett. 31 1044 (1973) (NRL)

89 D.G.COLOMBANT, K.G.WHITNEY, D.A.TIDMAN, N.K.WINSOR & J.DAVIS. Laser target model. Phys.Fluids 18 1687 (1975)

90 G.BIRKHOFF, R.S.VARGA & D.YOUNG. Alternating direction implicit methods. In 'Advances in Computers', ed. F.L.Alt & M.Rubinoff. Academic, New York Vol.3, p189 (1962)

91 H.L.STONE. Iterative solution of implicit approximations of multidimensional partial differential equations. SIAM J.Numer.Anal. 5 530 (1968)

92 J.H.WILKINSON. 'The algebraic eigenvalue problem'. Clarendon, Oxford 1965

93 A.BRACHA-BARAK & P.E.SAYLOR. A symmetric factorization procedure for the solution of elliptic boundary value problems. SIAM J. Numer.Anal. 10 190 (1973)

94 A.BRACHA-BARAK. A factorization procedure for the solution of multidimensional elliptic partial differential equations. SIAM J. Numer.Anal. 11 887 (1974)

95 P.E.SAYLOR. Second order strongly implicit symmetric factorization methods for the solution of elliptic difference equations. SIAM J.Numer.Anal. 11 894 (1974)

96 R.J.WRIGHT. Private communication (1976)

97 T.A.HALL. Private communication (1975)

98 J.N.OLSEN, G.W.KUSWA & E.D.JONES. Ion-expansion energy spectra correlated to laser plasma parameters. J.Appl.Phys. 44 2275 (1973) (SL)

99 J.S.PEARLMAN. Private communication (1976) (SL)

100 V.L.SIZONENKO & K.N.STEPANOV. On the non-linear stage of plasma hydrodynamic current instability in a strong electric field. Plasma Phys. 13 1033 (1971)

Hot Spots in Laser Plasmas

R. S. Craxton* and M. G. Haines
Department of Physics, Imperial College, London SW7 2BZ, England
(Received 21 July 1975)

Spontaneously generated magnetic fields can substantially reduce the thermal conductivity in pellet atmospheres and give rise to localized hot spots, which may lead to the ablation of anomalously fast ions.

Magnetic fields have been observed in laser-target experiments and are believed to be thermoelectrically generated as a result of nonparallel density and temperature gradients in the absorption region.[1] In laser-fusion experiments they may grow through a lack of spherical symmetry in the laser irradiation, as is considered in this paper, or from instabilities in an otherwise uniform illumination.[2]

The electron thermal conduction, essential for the efficient transfer of heat into the compression region, may be drastically reduced by the large value of $\Omega\tau$ generated; this may give rise to "hot spots"—regions where heat is deposited by the laser but prevented from escaping by large confining magnetic fields. By virtue of ion acceleration in the large associated electric fields, these hot spots may be the origin of the suprathermal fast ions observed to carry away an anomalous proportion of the absorbed energy in ablative kinetic energy. Three other mechanisms are possible: (1) The magnetic fields generated in the absorption region and convected outwards may cause substantial acceleration of the lower-density plasma through the $\vec{J}\times\vec{B}$ force. Although in our simulations the magnetic pressure is generally lower than the plasma pressure we do not rule out this effect on longer time scales. (2) Flux-limited electron thermal conduction (to within a few percent of the free-streaming limit[3]) may increase the temperature in the absorption region without requiring lack of spherical symmetry. The authors of Ref. 3 mention $\Omega\tau$ effects as an alternative flux-limiting process,[4] which appears very plausible because of the dependence of conductivity on the square of $\Omega\tau$. (3) Suprathermal electrons, generated where the effect on the local average tem-

perature is small, may convect to a lower-density region, causing a substantial increase in the average temperature there, resulting in ion acceleration to the corresponding energy, again without requiring asymmetry.

A two-dimensional Eulerian code has been developed which focuses attention on the generation of magnetic fields, the electron temperature distribution, and their effect on each other. We describe the model used and a typical run.

If many separate laser beams irradiate a spherical target, local intensity maxima can occur. We consider a region centered on one beam and extending to a boundary of symmetry, equidistant from this beam and neighboring beams, across which all fluxes are zero. We approximate this by taking a Nd-glass laser beam incident from large z along the axis of a cylindrical simulation region, defined by $0 \leq r \leq r_{max} = 300$ μm and $0 \leq z \leq z_{max} = 220$ μm, $r = r_{max}$ being this boundary of symmetry (at which radial velocity and magnetic field are zero). Zero flux is imposed on $z = 0$, the center of the pellet, while free flux is allowed on $z = z_{max}$. The laser beam has a Gaussian radial profile of half-width $0.5 r_{max}$; its power increases linearly to a maximum of 2×10^{12} W at 40 psec, when the peak intensity is 4×10^{15} W/cm^2, and the peak deposition rate almost 10^{18} W/cm^3. A small proportion of the energy is absorbed by inverse bremsstrahlung up to the critical density where the remainder is dumped over the next few mesh points. An initial deuterium plasma of arbitrary temperature 50 eV is assumed; the electron density is a uniform 4×10^{22} cm^{-3} for $0 \leq z \leq 0.25 z_{max}$, drops exponentially through the critical density at $0.5 z_{max}$, to 2.5×10^{19} cm^{-3} at $0.75 z_{max}$, and is uniform for $0.75 z_{max} \leq z \leq z_{max}$.

We use two-temperature fluid equations for the six variables ρ, T_e, T_i, V_r, V_z, and B_θ, differenced on a 29×41 Eulerian mesh. They include the laser energy dump, electron thermal conduction, the magnetic-field source term, hydrodynamics, $\vec{J} \times \vec{B}$ forces, equipartition, the Hall term, bremsstrahlung loss, inverse bremsstrahlung absorption, ion thermal conduction, magnet-

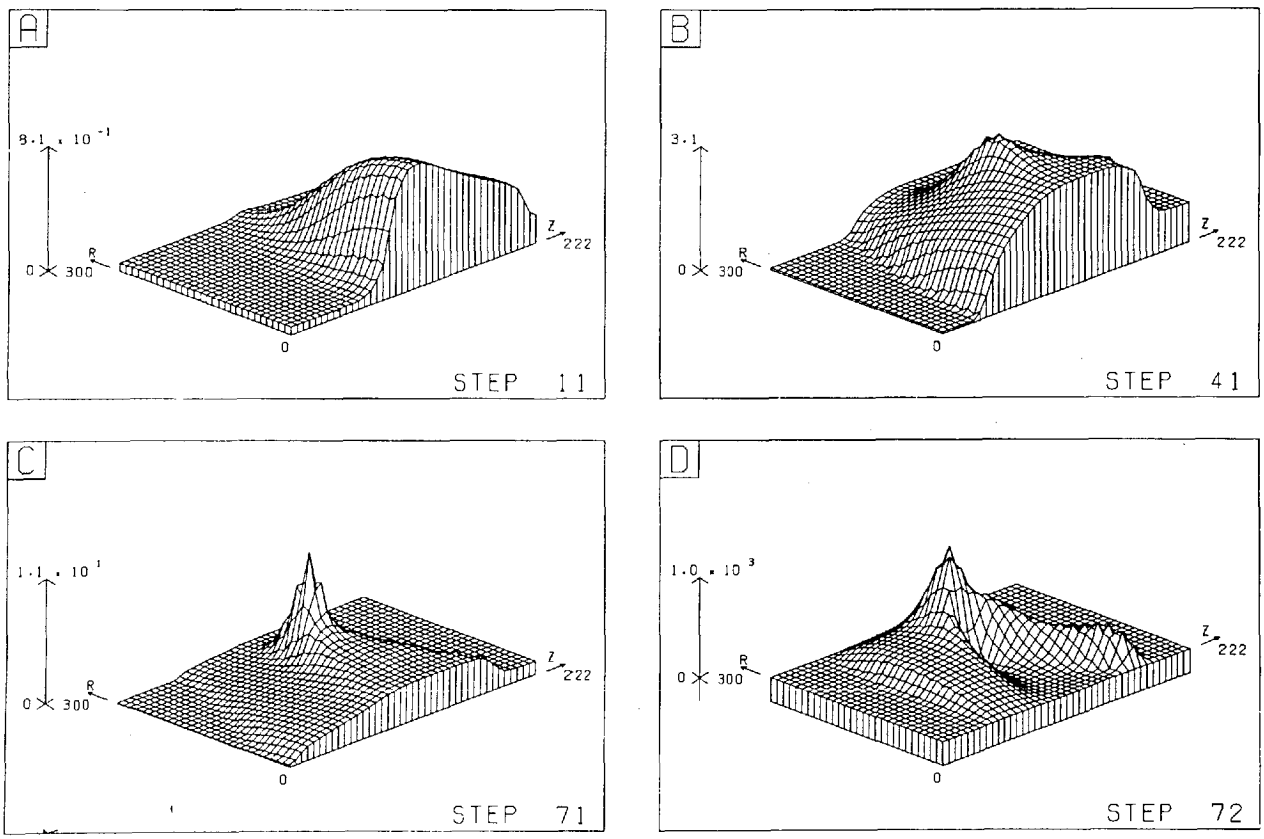

FIG. 1. (a)–(c) Distributions of electron temperature (T_e), in keV, at 6, 35, and 65 psec, respectively. (d) Distribution of azimuthal magnetic field (B), in kG, at 65 psec. The plots are scaled to the maximum, which is indicated by the arrow on the left.

ic field convection, and the perfect-gas equation of state. The first three phenomena dominate, and are associated with picosecond time scales; resistivity, which is unlikely to be important in our parameter regimes, is excluded.

The equation for azimuthal magnetic field is

$$\frac{\partial B_\theta}{\partial t} = \left\{ -\nabla \times \left[-\vec{V}_e \times \vec{B} - \frac{1}{ne} \nabla (nkT_e) \right] \right\}_\theta \quad (1)$$

$$= -\frac{1}{ne} \frac{\partial T_e}{\partial r} \frac{\partial n}{\partial z} + \text{smaller terms}, \quad (2)$$

the source term largely determined by $\partial T_e/\partial r$, and the electron heat flux is given by

$$q_e = -\frac{K_0}{1+(\Omega\tau)^2} \nabla T_e, \quad (3)$$

where $K_0 = \text{const} T_e^{5/2}$ is the classical conductivity,[5] Ω the electron Larmor frequency, and τ the electron collision time.

To treat mesh diffusion times $< 10^{-2}$ psec the diffusion terms in the equation for T_e are differenced fully implicitly, and the resulting quindiagonal matrix is solved by use of the alternating-direction-implicit iterative method. The hydronamics makes use of the two-step Lax-Wendroff method in a section based on the code FOCUS of Potter.[6]

Figure 1(a) shows the distribution of T_e at 6 psec. The laser beam is incident from the right along the z axis; the electron temperature is essentially determined by the local absorption of laser energy and thermal conduction is only effective as yet in the low-density region.

Figure 1(b) shows T_e at 35 psec; we note the thermal front advancing towards the solid, but the dominant feature is the hot spot, with a peak temperature of 3.1 keV. The hot spot always occurs in a region of absorption and large $\Omega\tau$; at this time the maximum values of $\Omega\tau$ and B_θ are 102 and 145 kG, respectively. Figure 1(c) shows T_e at 65 psec; the hot spot is more pronounced, with a peak of 11 keV, and is more distant from the axis.

From (2), B_θ is largely a response to $\partial T_e/\partial r$, so that the souce term is reversed on the axial

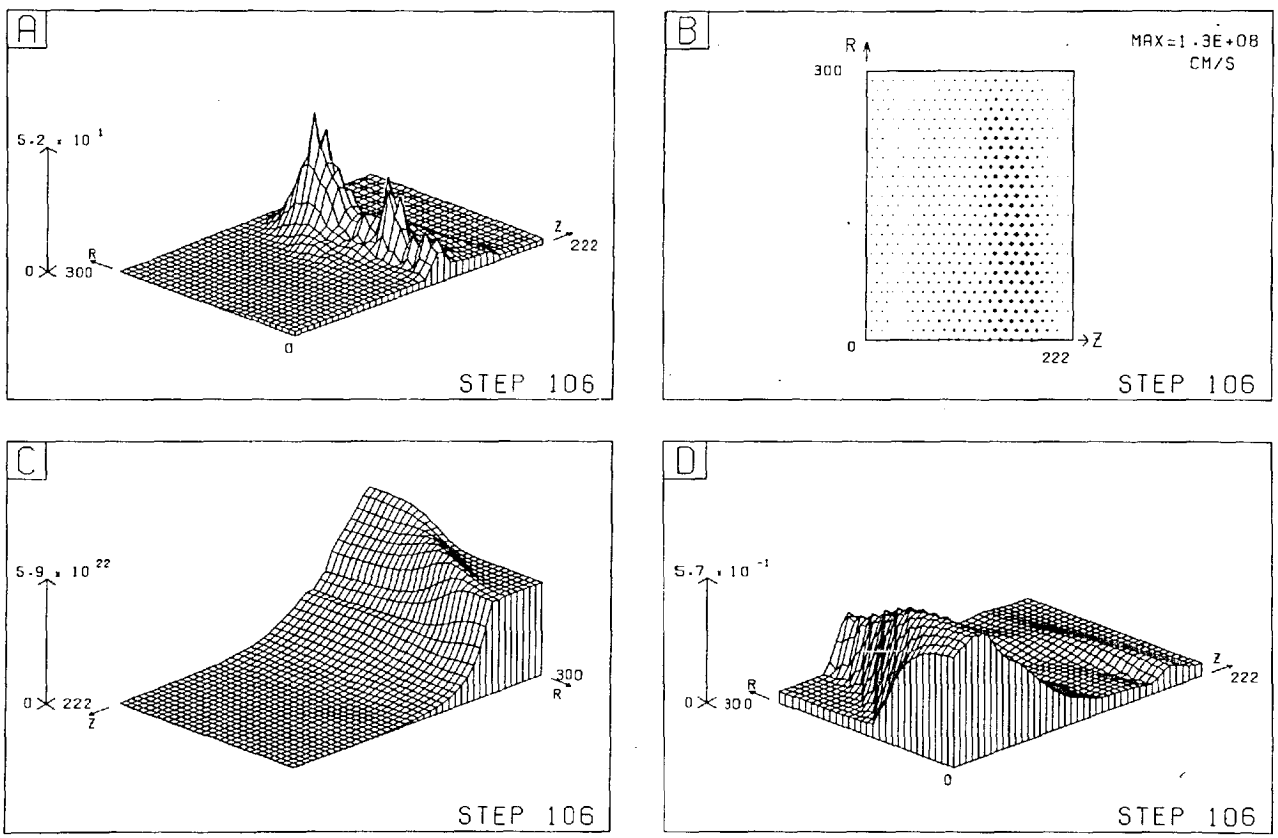

FIG. 2. (a)–(d) Distributions of T_e, in keV, ion velocity in cm/sec, density ρ, in electrons/cm^3, and ion temperature T_i, in keV, respectively, at 99 psec.

side of a hot spot but enhanced on the other side. Consequently the region of most restricted conductivity (and therefore the hot spot) gradually moves away from the axis. Figure 1(d) shows the distribution of $-B_\theta$ at 65 psec and illustrates this point. The peak of 1 MG occurs at slightly larger radius than the hot spot. Between the hot spot and the axis are regions of reduced and reversed magnetic field. This implies a conduction path along which $\Omega\tau$ is zero, in addition to the obvious conduction paths at the axis and the "symmetry" boundary $r = r_{max}$. The peak magnetic field reaches 3 MG at 88 psec and 5 MG at 99 psec.

Figure 2(a) shows T_e at 99 psec. The hot spot peaks at 52 keV, dwarfing by comparison the remainder of the distribution. The structure has fragmented somewhat, with a second hot spot appearing nearer the axis. The two hot spots are each surrounded by large magnetic fields, of opposite signs, and therefore with a conduction path in between. The scale length of this structure is related to the original scale length of the incident laser profile.

The velocity field generated by the pressure gradient is shown in Fig. 2(b) at 99 psec, the peak velocity of 1.3×10^8 cm/sec corresponding to an ion energy of 17 keV. Over all, 79% of laser energy has gone into electron thermal energy, 15% into ion thermal energy (in the denser region), and 6% into kinetic energy of ablation, although the rate of transfer to ablating ions is increasing.

Figure 2(c) shows ρ at 99 psec, viewed from the opposite direction to previous plots. Slight compression is observed, with a peak of 1.4 times the initial solid density. The thermal front has not yet reached the region around $(r, z) = (300\ \mu\text{m}, 0)$, whereas if $\Omega\tau$ effects are excluded T_e rapidly diffuses radially and the compression front is uniform over r.

Figure 2(d) shows T_i at 99 psec. Equipartition is effective only in the higher-density and lower-temperature region, while in the hot-spot region large ablative velocities cause expansion and cooling of the ions.

We have performed various other runs, hot spots appearing in most cases. The source term for B_0 [Eq. (2)] may be reduced by choosing a lower density gradient or greater laser spatial half-width. Initially conduction may be sufficiently effective to produce an almost flat $T(r)$, and only later when $\Omega\tau$ becomes large enough to reduce the conductivity will the hot spot form. A fluctuating radial profile, e.g.,

$$f(r) \propto 1 + 0.5\cos(2\pi r/r_{max}), \tag{4}$$

gives rise to two hot spots, originating near $r = 0$ and $r = r_{max}$, and moving towards each other. From Eq. (2) it is clear that a reversed magnetic field configuration is set up, with an $\Omega\tau = 0$ conduction path in the middle. We have obtained similar results for a CO_2 laser, although smaller laser intensities are needed to give similar temperatures at similar times because of the lower density of the absorption region. For the same reason $\Omega\tau$ effects are enhanced. Also, we have considered the heat flow perpendicular to the temperature gradient (the Righi-Leduc effect) which presents computational difficulties.

We conclude with a note of caution: These hot spots are driven by a largely assumed energy-absorption mechanism, and while azimuthal magnetic fields may not in themselves inhibit the absorption there must come a temperature beyond which the efficacy of the anomalous mechanisms decreases. Unfortunately this is outside the scope of the present work.

Note added.—Our attention has been drawn to work by D. Colombant *et al.* (to be published). Studying a computer model of x-ray emission from an aluminum target, these authors also find an off-axis maximum of the electron temperature, though less pronounced than here.

---

*Work supported by Culham Laboratory Agreement CUL/926.

[1]J. A. Stamper, K. Papadopoulos, R. N. Sudan, S. O. Dean, E. A. McLean, and J. M. Dawson, Phys. Rev. Lett. 26, 1012 (1971).

[2]D. A. Tidman and R. A. Shanny, Phys. Fluids 17, 1207 (1974).

[3]R. C. Malone, R. L. McCrory, and R. L. Morse, Phys. Rev. Lett. 34, 721 (1975).

[4]N. K. Winsor and D. A. Tidman, Phys. Rev. Lett. 31, 1044 (1973).

[5]B. B. Robinson and I. B. Bernstein, Ann. Phys. (N.Y (N.Y.) 18, 110 (1962).

[6]D. E. Potter, Phys. Fluids 14, 1911 (1971).